IN-24
37965
P-338

NASA Contractor Report 195381

Characterization of Metal Matrix Composites

I.M. Daniel, H.J. Chun, and D. Karalekas
McCormick School of Engineering and Applied Science
Northwestern University
Evanston, Illinois

November 1994

Prepared for
Lewis Research Center
Under Grant NAG3–950

National Aeronautics and
Space Administration

(NASA-CR-195381) CHARACTERIZATION OF METAL MATRIX COMPOSITES Final Report, 15 Nov. 1988 - 31 Mar. 1993 (Northwestern Univ.) 338 p

N95-18940

Unclas

G3/24 0037965

CHARACTERIZATION OF METAL MATRIX COMPOSITES

Final Report

by

I. M. Daniel
H. J. Chun
D. Karalekas

McCormick School of Engineering and Applied Science
Northwestern University
Evanston, IL 60208

NASA Grant NAG3-950

August 1994

National Aeronautics and
Space Administration

Lewis Research Center
Cleveland, OH 44135

FOREWORD

This is the Final Report on Northwestern University project "Characterization of Metal Matrix Composites," prepared for NASA-Lewis Research Center under Grant NAG3-950. The work described in this report was conducted in the period November 15, 1988 to March 31, 1993. Dr. C. C. Chamis was the NASA-Lewis Project Manager. Professor I. M. Daniel was the Principal Investigator. Contributions to the work reported herein were made by Mr. H. J. Chun, Drs. D. Karalekas and S. C. Wooh, and Professor E. E. Gdoutos.

Respectfully submitted,

I. M. Daniel
Professor
Theoretical and Applied Mechanics

CHARACTERIZATION OF METAL MATRIX COMPOSITES

ABSTRACT

Experimental methods were developed, adapted and applied to the characterization of a metal matrix composite system, namely, silicon carbide/aluminum (SCS-2/6061 Al), and its constituents. The silicon carbide fiber was characterized by determining its modulus, strength and coefficient of thermal expansion. The aluminum matrix was characterized thermomechanically up to 399° C (750° F) at two strain rates. The unidirectional SiC/Al composite was chartacterized mechanically under longitudinal, transverse and in-plane shear loading up to 399° C (750° F). Isothermal and non-isothermal creep behavior was also measured. The applicability of a proposed set of multifactor thermoviscoplastic nonlinear constitutive relations and a computer code was investigated. Agreement between predictions and experimental results was shown in a few cases. The elastoplastic thermomechanical behavior of the composite was also described by a number of new analytical models developed or adapted for the material system studied. These models include the rule of mixtures, composite cylinder model with various thermoelastoplastic analyses and a model based on average field theory. In most cases satisfactory agreement was demonstrated between analytical predictions and experimental results for the cases of stress-strain behavior and thermal deformation behavior at different temperatures. In addition, some models yielded detailed three-dimensional stress distributions in the constituents within the composite.

TABLE OF CONTENTS

FOREWORD		i
ABSTRACT		ii
TABLE OF CONTENTS		iii
1.	INTRODUCTION	1
2.	GENERAL BACKGROUND	8
2.1	Metal Matrix Composites	8
2.2	Basic Mechanics of Unidirectional Composite	10
2.3	Thermal Properties	14
3.	NONLINEAR CONSTITUTIVE EQUATIONS FOR MODELING THE THERMOMECHANICAL BEHAVIOR OF METAL MATRIX COMPOSITES	17
3.1	Introduction	17
3.2	Equation Form and Features	17
3.3	METCAN - The Metal Matrix Composite Analyzer	23
4.	THERMOMECHANICAL CHARACTERIZATION OF CONSTITUENT MATERIALS	26
4.1	Introduction	26
4.2	Characterization of SiC Fiber	26
4.3	Characterization of 6061-T4 Aluminum	41
4.4	Creep Properties of 6061-T4 Aluminum	53
4.5	Characterization of 6061-0 Aluminum	58
5.	THERMOMECHANICAL CHARACTERIZATION OF SILICON CARBIDE/ALUMINUM COMPOSITE	65
5.1	Specimen Geometry and Preparation	65
5.2	Physical Characterization	65
5.3	Mechanical Characterization	73
5.4	Creep Behavior	93
5.5	Non-Isothermal Creep Behavior	98

6. APPLICATION OF THERMOVISCOPLASTIC NONLINEAR CONSTITUTIVE RELATIONSHIPS (TVP-NCR) AND METCAN COMPUTER CODE 114

7. THERMAL STRESS ANALYSIS OF SIC/Al COMPOSITE 148

7.1 Introduction 148

7.2 Rule of Mixtures Model (ROM) 150

7.3 Composite Cylinder Model (CCM) 152

7.4 Results and Discussion (ROM and CCM) 157

7.5 Thermo-elastoplastic Analysis Model 169

8. THERMOMECHANICAL ANALYSIS OF SiC/Al COMPOSITE 173

8.1 Introduction 173

8.2 Composite Cylinder Model 175

8.3 Thermo-elastoplastic Analysis Model - Successive Appromixation Scheme 179

8.4 Thermo-elastoplastic Analysis - Average Field Theory Model 181

9. SUMMARY, CONCLUSIONS AND RECOMMENDATIONS FOR FUTURE WORK 188

REFERENCES 192

APPENDICES

1. INTRODUCTION

Energy producing, transportation and space systems expose materials to high temperature environments. For example, the skin temperature of the space shuttle reaches 1100° C (2000° F); skin temperatures of future aircraft are expected to reach 1650° C (3000° F). In addition, precision space structures which must have strict tolerances on dimensional control require structural materials that possess a high specific stiffness and low coefficient of thermal expansion (CTE).

The design of structures and systems capable of operating at these elevated temperatures and possessing exceptional stability across a wide range of temperatures poses great challenges to materials and structures engineers. The development of efficient systems has been hampered up to now, because the only materials capable of withstanding these high temperatures have been ceramic materials with their inherent limitations of brittleness, low strain to failure, low tensile strength, and low fracture toughness. Recent and current developments in materials science and processing technology are overcoming these limitations with the introduction of high temperature composites, such as metal-matrix, ceramic-matrix and carbon-carbon composites.

Advanced metal-metrix composite (MMC's) possess some unique mechanical and physical characteristics which make them highly desirable for specific applications. In addition to the advantages afforded by the anisotropic characteristics common to all composite materials, they have many additional advantages. In general, they exhibit high shear strength and shear modulus, high transverse tensile strength, excellent stability over a wide temperature range, good strength retention, excellent fatigue and creep properties, and high impact strength. In addition, they offer many advantages over polymer-matrix composites, such as higher electrical and thermal conductivities, better radiation resistance, and no outgassing. They are easily formed and machined, easily repaired, and amenable to

typical aerospace sheet metal design and fabrication. Already, methods have been developed for producing extra-strong lightweight metal-matrix composite structures. Superior dimensional stability is also possible, as well as tailored thermal expansion rates which match those of mating materials. All of this potentially can be done at a cost comparable to that of the unreinforced metal.

Even the simplest of fillers can do remarkable things for metals. One of the most common examples is that of 6061 aluminum alloy reinforced with 40% by volume particulate carbide. Compared with the unreinforced metal the modulus of elasticity increases from 10 to 21 Msi. Ultimate strength increases from 42 Ksi to 65 Ksi. Wear resistance improves significantly, and the coefficient of expansion is about half that of aluminum alone. Increasing the fiber percentage to 50-55% increases the modulus to 25.5 Msi. Meanwhile density remains almost exactly the same as that of the matrix metal. Thus, properties comparable to steel are possible in a material with the weight of aluminum. Moreover, these properties can be tailor made to fit a design. Instead of being tied to the normal thermal-expansion rate of a metal, for example, the amount, shape, and size of reinforcement material may be varied to control the rate. In some instances, the lowest expansion possible is clearly ideal. But in others, the expansion rate might be matched to that of other materials in the design. For example, if both aluminum-matrix composites and steel are utilized in the same design, the ideal composite may be one that matches the expansion rate of the steel. In this way, distortion, high stress, or loose joints, which may result from different expansion rates, can be eliminated.

A great deal of effort has been devoted in the past few years to research and development of metal matrix composites due to their superiority over conventional and other composite materials in advanced engineering applications. A wide variety of metallurgical processes including diffusion-bonding, plasma spray bonding, electroforming, liquid metal infiltration, to mention just a few, have been used for

fabrication of fiber reinforced metal matrix composites. A major problem which arises is the compatibility between the fiber and the matrix which includes the relevant chemical reactions taking place at the fiber-matrix interface during manufacturing and in service conditions. Such reactions generally have a detrimental effect on the load transfer capability between the composite constituents.

A number of studies have appeared on manufacturing and characterization of the mechanical and physical behavior of a number of aluminum based filamentary composites with graphite, boron and silicon carbide coated boron (borsic) fibers. The use of boron/aluminum composites, however, at temperatures higher than 900° C (1652° F) is seriously questioned as boron fibers react rapidly with molten aluminum resulting in degradation of the mechanical properties of the composite. This hampers the use of boron fibers for high-temperature applications or for fabrication methods, as fo example, low pressure high-temperature pressing that might be more economically feasible. Such disacvantages have resulted in the development of silicon carbide (SiC) fibers.

Recently, much work has been done on the development of continuous fiber, whisker and particulate reinforced silicon carbide/aluminum metal matrix composites. Silicon carbide (SiC) fibers have surfaces that readily bond to various aluminum alloys and resist degradation at high temperatures. Such composites can therefore be consolidated with more economical processes using high temperatures and low pressures.

The characterization of the mechanical and physical behavior of SiC/Al composites has not received much attention in the literature. Flom and Arsenault [1] performed an experimental study of the plastic strains and the plastic zone developed in the aluminum matrix around a short SiC cylinder during a thermal cycle due to the different thermal expansion coefficients of the two materials. A theoretical model was also developed to explain the plastic deformations in the

matrix. The same authors [2] also determined the strength of the interfacial bond between SiC and 6061 aluminum for particulate composites and found it to be at least 1690 Mpa. McDanels [3] investigated the tensile stress-strain behavior of SiC/Al composites containing SiC whisker, nodule or particulate reinforcement. He found that the elastic modulus of the composite is isotropic and depends only on the volume ratio of the reinforcement, while the strength and ductility are mainly influenced by the matrix alloy and temper condition. The mechanical properties of the composites are better than those of the unreinforced metal. Results on the mechanical behavior of discontinuous SiC/Al composites have also been published by Divecha et al. [4]. The effect of strengthening of 6061 aluminum alloy by SiC short fibers and platelets was studied by Arsenault [5]. He found that the strength of the fiber composite is greater than that of the platelet composite and that the strengths of both composites are higher than those predicted by continuum mechanics theories. This is attributed to the high dislocation density of the matrix resulting from the difference between the thermal expansion coefficients of silicon carbide and aluminum. Tsangarakis et al. [6] investigated the mechanical properties of several particulate and continuous fiber silicon carbide/aluminum composites and gave results for the tensile strength, fracture toughness and fatigue crack growth rate.

In many metal matrix composites a high thermal expansion mismatch between the matrix and the fiber exists resulting in high thermal stresses. High residual thermal stresses are developed in the matrix during cooling from consolidation temperatures which may result in premature yielding even before application of external loading. The study of the thermal expansion behavior and the resulting thermal stresses is an important task in the characerization of the composite.

A number of studies have been devoted to the problem of thermal expansion

behavior of MMC's. Levin [7] derived the macroscopic coefficients of thermal expansion (CTE's) of an elastic two-phase composite with perfectly bonded isotropic phases from the thermoelastic constants of the phases and the macroscopic elastic moduli of the composite. Bounds on the CTE's of fiber reinforced composites were given using bounds for the macroscopic elastic moduli of the composite. Expressions for CTE's of fiber reinforced composites with a doubly periodic array of circular hollow or solid fibers were derived by Van Fo Fy [8,9] who performed a thorough stress analysis. Schapery [10] calculated upper and lower bounds of multiphase media by employing extremum principles of thermoelasticity. Levin's results were extended to two-phase composites with anisotropic constituents by Rosen and Hashin [11]. They also gave bounds for the CTE's of anisotropic composites with any number of anisotropic phases. Dvorak and Chen [12] presented exact expressions for the CTE's of a composite consisting of three cylindrical perfectly bonded phases having transverse isotropy and arbitrary transverse geometry.

The above works were concerned with the micromechanical prediction of the linear thermal expansion behavior of composites. However, when the composite is subjected to temperatures above a critical value, plastic stresses are developed in the matrix and the strain versus temperature curve of the composite becomes nonlinear. A relatively limited number of investigations has dealt with the problem of nonlinear thermal expansion behavior of composites. Hoffman [13] studied the elastic and elastoplastic stresses in tungsten fiber reinforced 80 Ni + 20 Cr matrix composites subjected to heating or cooling in the range of 27 to 1090° C (80 to 2000° F). Dvorak et al. [14] determined the initial yield surfaces of boron/aluminum composites for mechanical and thermal loading using a finite element analysis of a regular hexagonal array model. They found that small temperature changes in the range of 10 to 38° C (50 to 100° F) can introduce plastic

strains in composites with a matrix tensile yield stress of the order of 10 ksi. These plastic strains were proportional to the yield stress. Flom and Arsenault [1] determined experimentally the plastic strains and the elastic-plastic boundaries produced in the aluminum matrix around a short SiC cylinder during a thermal cycle and developed a theoretical model for the prediction of the plastic zone. Kural and Min [16] presented an elastoplastic theoretical model for the study of plastic deformation in the matrix material of graphite fiber reinforced MMC's caused by thermal cyclic loading and residual thermal stresses. Experimental results verified the elastoplastic stresses predicted by the theory. In another paper Min and Crossman [17] used the above theoretical model for the study of the thermomechanical behavior of Gr/A*l* composites.

In conclusion, there is an urgent need for adequate characterization of the mechanical and physical behavior of continuous SiC/A*l* composites under a variety of loading and environmental conditions. A review of the literature revealed that relatively few experimental data on MMC's are available to compare the predictions of the various analytical models with the actual response observed in the laboratory. In particular, there appears to be an absence of systematic investigation of the nonlinear response of unidirectional composites subjected to various loading and environmental conditions. In addition, results from such characterization tests are urgently needed as input into finite element structural analysis programs. More specifically, data are needed for input into and verification of multifactor-dependent nonlinear constitutive relationships developed at NASA-Lewis Research Center [18].

The objective of the present work is to conduct a systematic experimental study of the mechanical and thermal properties of SCS-2 continuous fiber reinforced 6061 aluminum composite and its constituents at temperatures up to 399° C (750° F). Theoretical predictions are made by several elastoplastic

micromechanical models based on a one-dimensional rule-of-mixtures model, an axisymmetric composite cylinder model, a successive approximation scheme with the Prandl-Reuss plastic flow model, and an average field theory. The experimental results are used in conjunction with a least squares analysis to determine the unknown exponents of multifactor-dependent nonlinear constitutive relationships developed at NASA-Lewis Research Center [18] for the composite and its constituents.

2. GENERAL BACKGROUND

2.1 Metal Matrix Composites

As with all composite materials, metal matrix composites have a continuous matrix phase within which is embedded a second phase that can be particulates, whiskers, chopped or discontinuous fibers, or continuous fibers. As the name implies, metal matrix composites have this second phase embedded in a metallic matrix. In many structural applications the fiber properties are the most important and the matrix may be chosen based on cost and minimum weight. There are, however, a significant number of applications in aircraft and spacecraft design where the matrix must possess particular properties if the composite is to perform as desired. In addition to the desired high stiffness to weight ratio, for space structures applications, for example, it is often necessary to have dimensional stability which requires a coefficient of thermal expansion approaching zero. In a significant number of cases the material is subjected to high temperatures, where epoxy composites are quite unusable, so that either metal or, in the extreme temperatures, ceramic matrix composites must be considered.

There is a large variety of metals available for use as the matrix. The one chosen depends on the particular application, the use temperature, the environment, and more importantly, the interaction of the fiber and the matrix. Interaction refers to the wetting of the fiber by the matrix and the potential for a detrimental reaction between the fiber and the matrix [19]. The fiber and the matrix may react chemically, especially at elevated temperatures, degrading the ability of the fiber to performe its function. This may also result in reaction products that further degrade the performance of the composite. Some of the most commonly used matrix materials include nickel superalloys, titanium alloys, aluminum alloys, magnesium, copper and steels. Fibers used are generally grouped into five classes: refractory metal wires, oxides, boron, silicon carbide and carbon/graphite. Typically, fibers

have high modulus, high strength and low weight, so that the stiffness and strength of the composite are mainly due to the fiber. A more detailed discussion on available matrices and fiber reinforcements can be found in the literature [19,20,21,22].

A number of metallurgical processes have been used for the fabrication of filament reinforced metal matrix composites. The techniques vary from those employing conventional powder metallurgy and slip casting methods to techniques such as diffusion bonding and plasma-spray bonding. However, with the method used great care must be exercised to:

1. Preserve the fiber strength during all stages of the fabrication process.
2. Minimize fiber breakage.
3. Promote wetting and bonding between the matrix and fiber.

The choice of fabrication method used depends primarily on the mechanical and chemical properties of the fiber and matrix, the fiber length and size, the fiber packing, and the desired fiber configuration. Furthermore, it is necessary to know the thermodynamics and kinetics of possible fiber matrix reactions, as well as the fabrication and service temperatures to which the composites are subjected. A detailed description of the various existing fabrication methods can be found in references [19,20,21,22,23,24].

Compared to metals, metal matrix composites have the potential of: (1) Higher specific mechanical properties like modulus/density and strength/density ratios, (2) improved fatigue life, and (3) higher use temperature because of the stable metallic phase. When compared to epoxy matrix composites, they have the following potential benefits: (1) Good electrical and thermal conductivity, (2) no out-gassing in a vacuum, (3) metallic joining concepts may be more directly usable, (4) higher temperature utilization, (5) no moisture absorption, and (6) less degradation of properties. In summary, it is clear that there is a definite potential for metal

matrix composites in the future. However, considerable work remains to be done before widespread use of these materials becomes possible.

2.2 Basic Mechanics of Unidirectional Composite

The response of unidirectionally reinforced composites in various loading environments is usually predicted by the rule of mixtures. It is the approach generally employed to determine whether a metal matrix composite has interesting properties initially, and as a measure of optimizing fabrication parameters or bonding conditions [25]. By assuming an isostrain criterion, i.e., both fiber and matrix are strained equally and uniformly, the modulus, stiffness and Poisson's ratio of the composite can be obtained. The major assumptions of this theory are: (1) elastic (or plastic) isotropy, (2) the displacements are continuous across the fiber/matrix interface (no interfacial slip), (3) no chemical reaction between constituents and (4) absence of residual stresses. Experimental data have shown [25] that only the longitudinal modulus and major Poisson's ratio can be reliably predicted by the rule of mixtures which takes the following form:

$$E_1 = E_f V_f + E_m (1 - V_f) \tag{2.1}$$

and

$$\nu_{12} = \nu_f V_f + \nu_m (1 - V_f) \tag{2.2}$$

where

E_1 = Longitudinal Young's modulus of composite (in the fiber direction)

E_f = Young's modulus of fiber

E_m = Young's modulus of matrix

ν_{12} = Major Poisson's ratio of the composite

ν_f = Poisson's ratio of fiber

ν_m = Poisson's ratio of matrix

V_f = Fiber volume ratio

Experimental data fit these approximations well, but Hill [26] showed, theoretically, that these predictions were really the lower bounds of the moduli and applicable when the Poisson's ratios of the constituents were equal. The modulus prediction can be extended to the region where the matrix has yielded by substituting $d\sigma_m/d\varepsilon_m$ and ν for E_m and ν_m in equations (2.1) and (2.2).

$$E_1 = E_f V_f + \left(\frac{d\sigma_m}{d\varepsilon_m}\right)(1 - V_f) \tag{2.3}$$

$$\nu_{12} = \nu_f V_f + \nu (1 - V_f) \tag{2.4}$$

where $(d\sigma_m/d\varepsilon_m)$ is the slope of the matrix stress-strain curve at the equivalent strain of the composite, and ν is Poisson's ratio of the matrix at the same strain, varying from the elastic value to 0.5 for an ideally plastic material.

For perfectly bonded fibers and for the case when the ultimate tensile strain of the fiber is lower than that of the matrix, the longitudinal tensile strength of the composite is approximated by the relation [27]:

$$F_{1t} \cong F_{ft} V_f + \sigma_m' V_m \tag{2.5}$$

where

F_{1t} = Longitudinal composite tensile strength

F_{ft} = Longitudinal fiber tensile strength

σ_m' = Average longitudinal matrix stress when the ultimate fiber strain is reached

Although this simple strength prediction correlates well with experimental data, Lynch [28] emphasizes that there is no reason to expect it to be highly accurate. Fabrication problems would be expected to decrease composite strength.

In the case of transverse normal loading, there are so simple predictions for the modulus and strength of a unidirectional composite. The mechanics of materials approach predicts the following transverse modulus:

$$E_2 = \frac{E_{2f} E_m'}{V_f E_m' + V_m E_{2f}} \tag{2.6}$$

where

E_{2f} = transverse fiber modulus

E_m' = $E_m/(1 - \nu_m^2)$

ν_m = matrix Poisson's ratio

E_m = matrix modulus

The self-consistent field model and the variational bounding method yield complex expressions for transverse modulus in terms of other properties, such as bulk modulus and transverse shear modulus [29,30].

The Halpin-Tsai semi-empirical relationship is a practical one, once the right choice is made for the parameter ξ [31]:

$$E_2 = E_m \frac{1 + \xi_1 \eta_1 V_f}{1 - \eta_1 V_f} \tag{2.7}$$

where

$$\eta_1 = \frac{E_{2f} - E_m}{E_{2f} + \xi_1 E_m}$$

and ξ_1 = reinforcing efficiency factor for transverse loading. The prediction above tends to agree with experimental results for values of ξ_1 between 1 and 2. If a reliable experimental value of E_2 is available for a composite, then the value of ξ_1 can be obtained by using Eq. (2.7) and can then be used to predict E_2 for a wide range of fiber volume ratios of the same composite.

Prediction of transverse tensile strength, which is a matrix-dominated property, is more difficult because this type of loading results in high stress and strain concentrations in the matrix and interface/interphase. Reliable predictions are based on elastoplastic finite element analysis and average field theory.

For in-plane shear loading the mechanics of materials approach uses a series model under uniform stress and yields the following relation for the composite shear modulus

$$\frac{1}{G_{12}} = \frac{V_f}{G_{12f}} + \frac{V_m}{G_m} \tag{2.8}$$

or

$$G_{12} = \frac{G_{12f}\, G_m}{V_f\, G_m + V_m\, G_{12f}} \tag{2.9}$$

where G_{12f} and G_m are the shear moduli of the fiber and matrix, respectively. As in the case of transverse modulus, this approach tends to underestimate the in-plane shear modulus.

The Halpin-Tsai semi-empirical relation in this case is

$$G_{12} = G_m \frac{1 + \xi_2\, \eta_2\, V_f}{1 - \eta_2\, V_f} \tag{2.10}$$

where

$$\eta_2 = \frac{G_{12f} - G_m}{G_{12f} + \xi_2\, G_m}$$

and ξ_2 = reinforcing efficiency factor for in-plane shear

Best agreement with experimental results has been found for $\xi_2 = 1$. For $\xi_2 = 1$, the relation (2.10) becomes

$$G_{12} = G_m \frac{(G_{12f} + G_m) + V_f (G_{12f} - G_m)}{(G_{12f} + G_m) - V_f (G_{12f} - G_m)} \tag{2.11}$$

This expression is identical to that derived by the self-consistent field model

and to the lower bound of the variational approach.

Prediction of in-plane shear strength, being a matrix dominated property, would require elastoplastic analysis as in the case of transverse strength.

2.3 Thermal Properties

Many different analyses exist for predicting the coefficients of thermal expansion (CTE) for unidirectional composites. A brief description of some of the more widely used current analyses will be given here. The basic assumptions that are common to all of the analyses to be presented are: (1) the fibers are circular in cross-section and infinitely long, (2) the displacements are continuous across the fiber/matrix interface, and (3) the temperature is uniform and the constituent material properties do not vary with temperature.

Approximate micromechanical relations for the coefficients of thermal expansion were given by Schapery for isotropic constituents [10]. The longitudinal coefficient for a continuous fiber composite is given by the relation:

$$\alpha_l = \frac{E_f \alpha_f V_f + E_m \alpha_m V_m}{E_f V_f + E_m V_m} = \frac{(E\alpha)_l}{E_l} \tag{2.12}$$

where

E_f, E_m = fiber and matrix moduli, respectively

α_f, α_m = fiber and matrix coefficients of thermal expansion, respectively

V_f, V_m = fiber and matrix volume ratios, respectively

$(E\alpha)_l = E_f \alpha_f V_f + E_m \alpha_m V_m$

This relation is similar to the rule of mixtures for longitudinal modulus and gives fairly accurate results. It is identical to that obtained by the self consistent scheme.

The relation for the transverse coefficient of thermal expansion based on energy principles is [10]:

$$\alpha_2 = \alpha_f V_f (1 + \nu_f) + \alpha_m V_m (1 + \nu_m) - \nu_{12} \alpha_1 \tag{2.13}$$

where

ν_f, ν_m = Poisson's ratios of fiber and matrix, respectively

$\nu_{12} = \nu_f V_f + \nu_m V_m$ = major Poisson's ratio of composite lamina as obtained by the rule of mixtures

α_1 = longitudinal CTE of lamina as obtained by eq. (2.12)

In many cases, the fibers are orthotropic, i.e., they have different properties in the axial and transverse directions. Properties for composites with orthotropic constituents were obtained by Hashin [32]. The relation for the transverse CTE is

$$\alpha_2 = \alpha_{2f} V_f \left(1 + \nu_{12f} \frac{\alpha_{1f}}{\alpha_{2f}}\right) + \alpha_{2m} V_m \left(1 + \nu_{12m} \frac{\alpha_{1m}}{\alpha_{2m}}\right) - (\nu_{12f} V_f + \nu_{12m} V_m) \frac{(E\alpha)_l}{E_l} \tag{2.14}$$

where

α_{1f}, α_{2f} = axial and transverse CTE's of fiber, respectively

α_{1m}, α_{2m} = axial and trasnverse CTE's of matrix, respectively

ν_{12f}, ν_{12m} = axial Poisson's ratios of fiber and matrix, respectively

$$(E\alpha)_l = E_{1f} \alpha_{1f} V_f + E_{1m} \alpha_{1m} V_m \tag{2.15}$$

$$E_l = E_{1f} V_f + E_{1m} V_m \tag{2.16}$$

In most cases the matrix can be considered isotropic and the orientation designation of the matrix properties in eqs. (2.14) through (2.16) can be dropped.

Chamberlain used a plane stress thick walled cylinder solution to derive expressions for α_1 and α_2 for the case of transversely isotropic fibers in an isotropic matrix. A discussion of this analysis and comparisons with experimental data were given by Rogers [33]. The derived expression for α_1 is identical to equation (2.12). The expression for α_2 takes the form

$$\alpha_2 = \alpha_m + \frac{2\,(\alpha_{2f} - \alpha_m)\,V_f}{\nu_m\,(F - 1 + V_m) + (F + V_f) + \left(\frac{E_m}{E_{1f}}\right)(1 - \nu_{12f})\,(F - 1 + V_m)} \tag{2.17}$$

where F is a packing factor which accounts for fiber packing geometry, and is equal to 0.9069 and 0.7854 for hexagonal and square packing geometries, respectively.

Chamis [34] used a simple force-balance, or strength of materials approach to derive expressions for the thermal properties of unidirectional composites with transversely isotropic fibers. The derived expression for α_1 is again identical to equation (2.12). The expression for α_2 is

$$\alpha_2 = \alpha_{2f}\sqrt{V_f} + (1 - \sqrt{V_f})\left(1 + \frac{V_f\,\nu_m\,E_{1f}}{E_1}\right)\alpha_m \tag{2.18}$$

where E_1 is the longitudinal elastic modulus of the composite and is given by the simple rule-of-mixtures formula (2.1).

Several investigators [35-37] have used finite element analyses to study the stress fields in unidirectional composites on a micromechanics level. A special finite element code was developed by Bowels [38] to determine the thermal and mechanical response of unidirectional composites.

3. NONLINEAR CONSTITUTIVE EQUATIONS FOR MODELING THE THERMOMECHANICAL BEHAVIOR OF METAL MATRIX COMPOSITES

3.1 Introduction

A set of thermoviscoplastic nonlinear constitutive relationships (TVP-NCR) have been developed by Chamis and Hopkins [17] mainly for application to high-temperature metal matrix composites. These equations consist of products of terms with unknown exponents determined from experimental data. Each term expresses the dependence of mechanical and thermal properties of the constituent materials and the composite itself on such quantities as, temperature, stress and time. A micromechanical model for high temperature metal matrix composites has also been developed by Hopkins and Chamis [39]. The model is based on a mechanics of materials analysis of a single square array unit cell consisting of a single fiber, surrounding interface and matrix. Based on the model, equations were extablished to predict mechanical properties, thermal properties, and constituent microstresses for the unidirectional fiber reinforced ply. The micromechanical equations were combined with the TVP-NCR equation [17] to develop a computer program (METCAN) for the analysis of fiber reinforced metal matrix composites. The computational capability of the program is schematically shown in Fig. 3.1. The program is integrated with finite element computer programs to determine the response of complex high-tempera;ture metal matrix structural composites.

3.2 Equation Form and Features

The proposed [17] thermoviscoplastic nonlinear constituent relationships (TVP-NCR) for the constituents as well as the composite itself, can be expressed in a generic form applicable to all properties, mechanical and thermal. They relate the dependence of material properties on such quantities as temperature, stress and strain. These relationships are expressed in terms of dimensionless products as

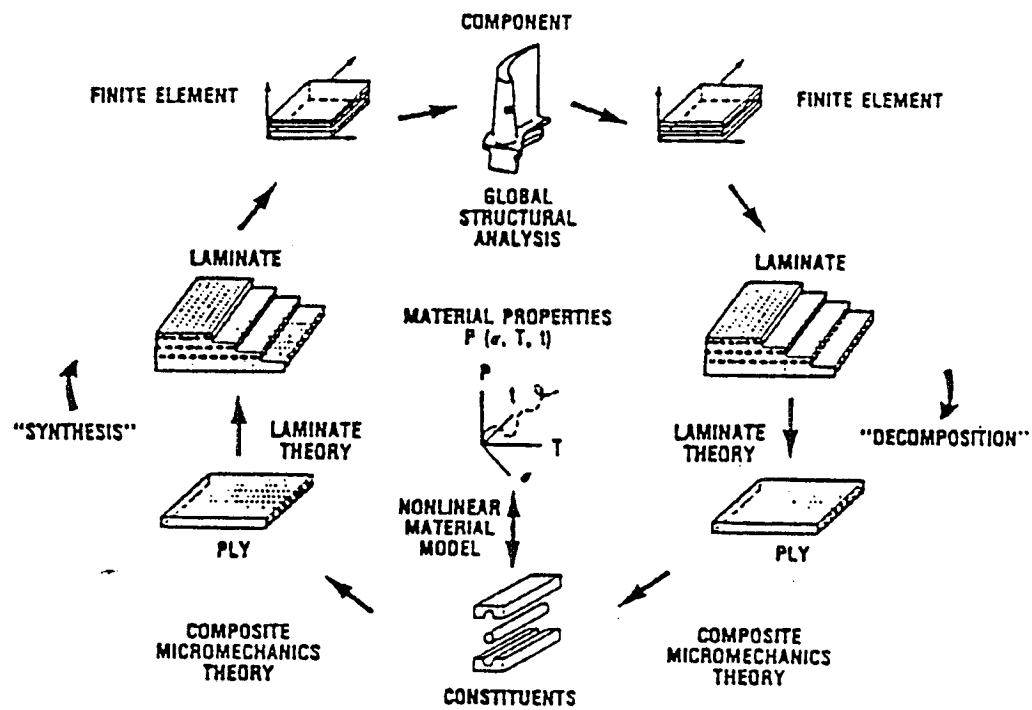

Figure 3.1 Integrated Nonlinear Composite Structural Analysis [1].

$$\frac{P}{P_o} = \left[\frac{T_u - T}{T_u - T_o}\right]^n \left[\frac{F_u - \sigma}{F_u - \sigma_o}\right]^m \left[\frac{\dot{F}_u - \dot{\sigma}_o}{\dot{F}_u - \dot{\sigma}}\right]^l \left[\frac{\dot{T}_u - \dot{T}}{\dot{T}_u - \dot{T}_o}\right]^k$$

$$\left[\frac{R_u - R}{R_u - R_o}\right]^p \left[\frac{N_M - n_M}{N_M - n_{Mo}}\right]^q \left[\frac{N_T - n_T}{N_T - n_{To}}\right]^r \left[\frac{t_u - t}{t_u - t_o}\right]^s \tag{3.1}$$

where

P = Property

T = Temperature

F = Strength Parameter

R = Reaction

N = Number of Cycles to Failure

n = Current Number of Cycles

t = Time

The subscripts signify the following:

u = Ultimate or Final Value

o = Reference State

M = Mechanical

T = Thermal

Symbols without subscripts "u" or "o" denote current values of the variables. Letters with a dot above them designate differentiation with respect to time. The exponents n, m, l, k, p, q, r, s are empirical parameters which can be determined from available experimental data.

Each term on the right hand side of the equation above describes a monotonic functional variation of P/P_o from some initial property value to a final or ultimate state. For instance, the first term represents the temperature dependence, where T_o could be room temperature, T_u the melting temperature of the matrix and T the current temperature. In a similar fashion, the second term represents the stress dependence and the third the stress rate dependence. Equation (3.1)

describes the material behavior in the temperature-stress-stress rate-temperature rate-reaction-mechanical and thermal fatigue-time space. The specific shape of the dependence of P/P_o on each term is dictated by the value of the exponent and the reference and final values of the respective quantity in the term. It is seen that $P=P_o$ when the variable on the right hand side of the above equation becomes equal to its reference value. In addition, P=0 when the variable in the term becomes equal to its final value. When the reference value of each variable is well defined and corresponds to the conditions under which the value P_o is measured, the only condition that is known for the final value is that at that value the corresponding quantity P becomes zero if the exponent is positive. On the other hand, P becomes infinite when the exponent is negative.

The final value of the variable may or may not have a physical meaning, depending on the property under consideration. If it does have a physical meaning, then the final value is well known. Otherwise, the final value should be determined from the available experimental data. For instance, let us consider the temperature dependence of the mechanical properties of a metal alloy. It is known that the mechanical properties of the alloy are zero at its melting temperature (T_m) and therefore $T_u=T_m$ in equation (3.1). Similarly, when the stress dependence of the tangent modulus of the metal is considered, the quantity F in equation (3.1) can be taken as the ultimate stress since at that point the tangent modulus becomes zero. However, when the secant modulus is considered the ultimate stress cannot be used for quantity F since at that stress the secant modulus does not become zero. In this case F does not have a physical meaning and its value must be determined by fitting euqation (3.1) to the experimental data.

As was mentioned before, the specific form of the function depends on the exponent. By selecting various values of an exponent and by selecting the initial and terminal values, a variety of functional dependencies can be simulated using

equation (3.1). In order to obtain the form of dependence of P/P_o on the value of a variable, for instance temperature (T), the variation of P/P_o with T/T_u for $T_o = 0°$ F and various values of the exponent n is shown in Fig. 3.2. It is observed that for positive values of n, P/P_o varies between one and zero when T/T_u varies in the interval (0,1). For n<1 the curve is convex, while for n>1 it is concave with respect to the horizontal axis. For negative values of n, P/P_o is always greater than one and tends to infinity as T/T_u tends to one.

As was previously discussed the form of the TVP-NCR expressed by equation (3.1) implies that the value of a quantity at the ultimate value of the variable is equal to zero or infinity depending on whether the corresponding exponent is positive or negative. While this condition applies to a number of mechanical or thermal properties, there are others which do not become zero or infinite at the ultimate value of the variable. Consider, for example, the variation of Poisson's ratio of a metalic material with stress. Its value is constant up to the yield stress of the material and it increases with stress up to the limiting value of 0.5 at the ultimate stress. Similarly, the secant modulus of a material does not become zero at the ultimate stress.

In order to use the TVP-NCR for material properties which do not satisfy the end condition at the ultimate value of a variable, equation (3.1) should be modified accordingly. The modified TVP-NCR which incorporates all material properties can be put in the following form

$$\frac{\Delta P}{\Delta P_o} = \left[\frac{T_u - T}{T_u - T_o}\right]^n \left[\frac{F_u - \sigma}{F_u - \sigma_o}\right]^m \left[\frac{\dot{F}_u - \dot{\sigma}_o}{\dot{F}_u - \dot{\sigma}}\right]^l \left[\frac{\dot{T}_u - \dot{T}}{\dot{T}_u - \dot{T}_o}\right]^k \left[\frac{R_u - R}{R_u - R_o}\right]^p \left[\frac{N_M - n_M}{N_M - n_{Mo}}\right]^q \left[\frac{N_T - n_T}{N_T - n_{To}}\right]^r \left[\frac{t_u - t}{t_u - t_o}\right]^s \tag{3.2}$$

where

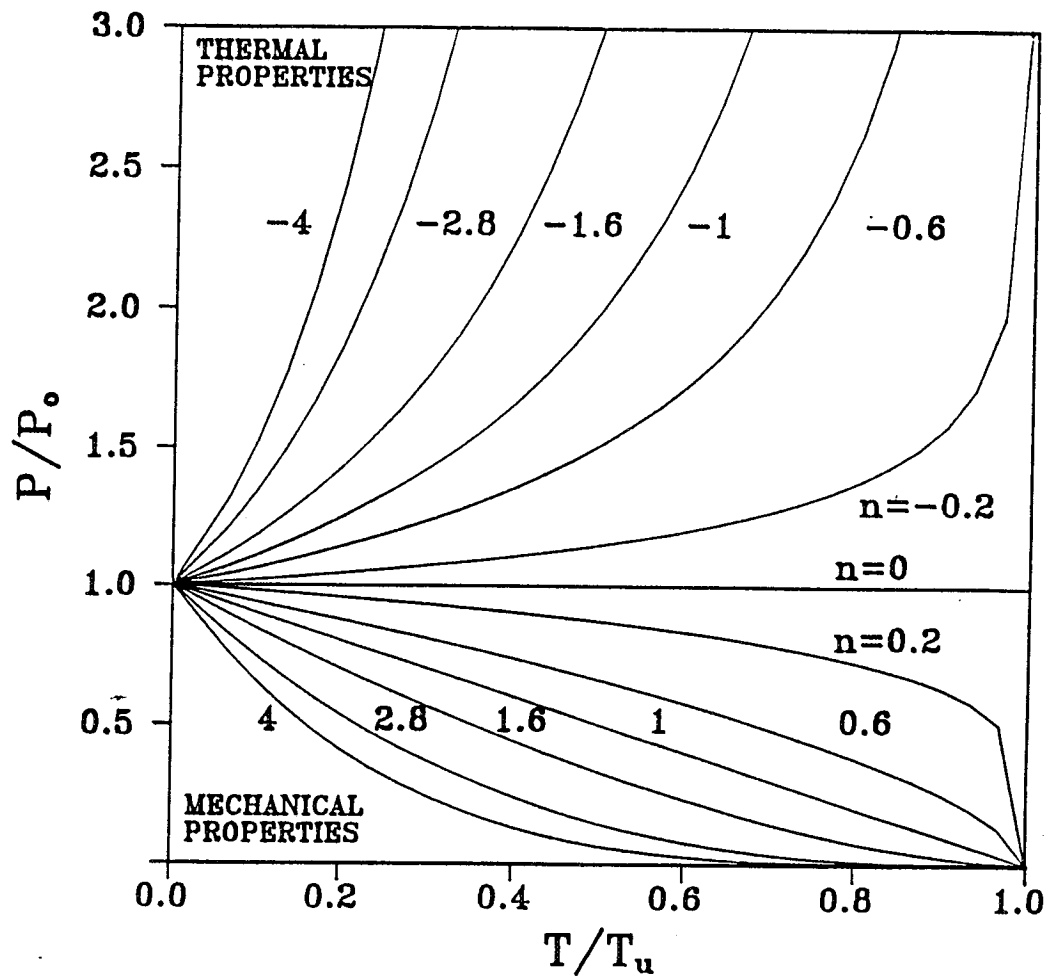

Figure 3.2 Variation of Normalized Material Property P/P_o versus Normalized Variable T/T_u for Different Values of the Exponent n of the Nonlinear Constitutive Relationships.

$$\Delta P = P - P_u$$

$$\Delta P_o = P_o - P_u$$

The features of the TVP-NCR can be summarized into three groups: (1) physical, (2) fundamental, and (3) computational, as follows [17]:

(1) Physical - The constitutive relationships describe dependence on temperature, time, stress, stress rate, and complete property degradation as the ultimate value is approached.

(2) Fundamental - The constitutive relationships are:

- generic - they are applicable to all constituent material properties.
- evolutionary - they are easily extended to include additional dependence.
- isomorphic - they have the same form for all the properties.
- unified - they are fully coupled from the initial to the terminal material state.
- universal - they are fully applicable to any three constituents (fiber, matrix, interface).
- nondimensional - they are normalizable with respect to reference and ultimate values.

(3) Computational - the constitutive relationships are:

- computationally efficient - they only require simple substitution and exponentiation.
- easily integrated into nonlinear composite mechanical and structural analysis codes.

3.3 METCAN - The Metal Matrix Composite Analyzer [18]

Predicting the mechanical and thermal behavior and the structural response of components fabricated from MMC requires the use of a variety of mathematical

models. An extensive research in computational mechanics methods for predicting the nonlinear behavior of MMC's has been undertaken at NASA-Lewis Research Center. This research has led to the development of the METCAN (Metal Matrix Composite Analyzer) computer code.

The integrated approach implemented in the METCAN computer code is illustrated in Fig. 3.1. The cyclic arrangement defines the computational effort for each load increment. Material nonlinearity is treated at the constituent (fiber, matrix, interface) level, where the current material model describes a time-temperature-stress dependence of a constituent's mechanical and thermal properties at any instant in its "material history space." Characteristic properties of the composite, at the various levels of simulation, are approximated from the instantaneous constituent properties by composite mechanics. These properties then could be used, for example, to specify elemental properties for a subsequent global structural analysis by finite element analysis. In the "decomposition" process, global response variables are decomposed into localized response, again at the various levels of simulation.

Some of the basic features of METCAN with its flow chart shown in Fig. 3.3 are:

- Linear Analysis - Thermal/Mechanical Room/High Temperature Properties.
- Nonlinear Analysis - Thermal/Mechanical Monotonic Load Histories.
- Microstresses - Due to Thermal/Mechanical Loads.
- Ply Stress/Strain Influence Coefficients.
- Ply Thermo-Visco-Plastic Response.
- Stress/Strain Behavior Data for Uniaxial Loading.
- Residual Stresses Due to Processing/Curing Conditions.
- Stress Concentration Factors around a Circular Hole in an Infinite Plate.

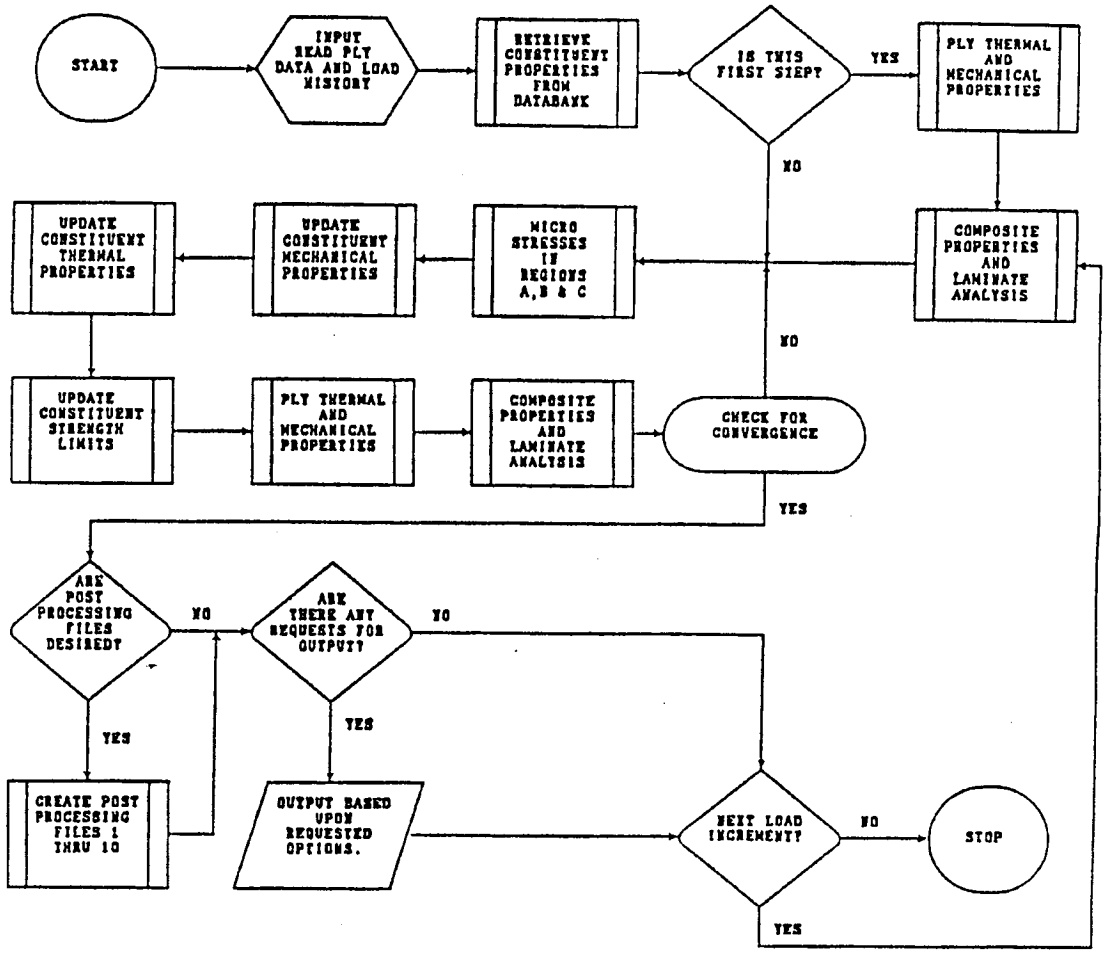

Figure 3.3 METCAN Flow Chart [3].

4. THERMOMECHANICAL CHARACTERIZATION OF CONSTITUENT MATERIALS

4.1 Introduction

The behavior of the composite is intimately related to the properties of the constituents, therefore, it is important to determine these properties under a variety of loading and environmental conditions. Micromechanical analyses used for prediction of composite properties rely on the properties of the constituents and their interaction. In the present case it is desired to characterize as fully as possible the stress-strain and thermal deformation behavior of the silicon carbide fiber (SCS-2) and the aluminum matrix at various temperatures.

4.2 Characterization of SiC Fiber

The silicon carbide fiber (SCS-2) studied is produced by chemical vapor deposition (CVD) and is used as the reinforcement in metal matrix composites. Specifically, these fibers are used in titanium and aluminum metal matrix composites because of their high-modulus, high strength, thermal stability, and compatibility with the matrix materials. These fibers have high strength and modulus, but show some deterioration in tensile strength at temperatures above 800° C [40]. There are two commercial processes for making continuous silicon carbide fibers: one is by vapor deposition over a tungsten or carbon core that produces a large diameter fiber (100 - 150 μm), and the other is by melting and spinning an organic polymer containing silicon atoms as a precursor fiber followed by heating at an elevated temperature that produces a smaller diameter fiber (10-30 μm).

The SiC fiber used in this study is a continuous filament produced by Textron in a tubular glass by CVD as shown in Fig. 4.1. The process occurs in two steps on a carbon monofilament substrate which is resistively heated. During the first step, pyrolytic graphite (PG) approximately 1 μm thick is deposited to

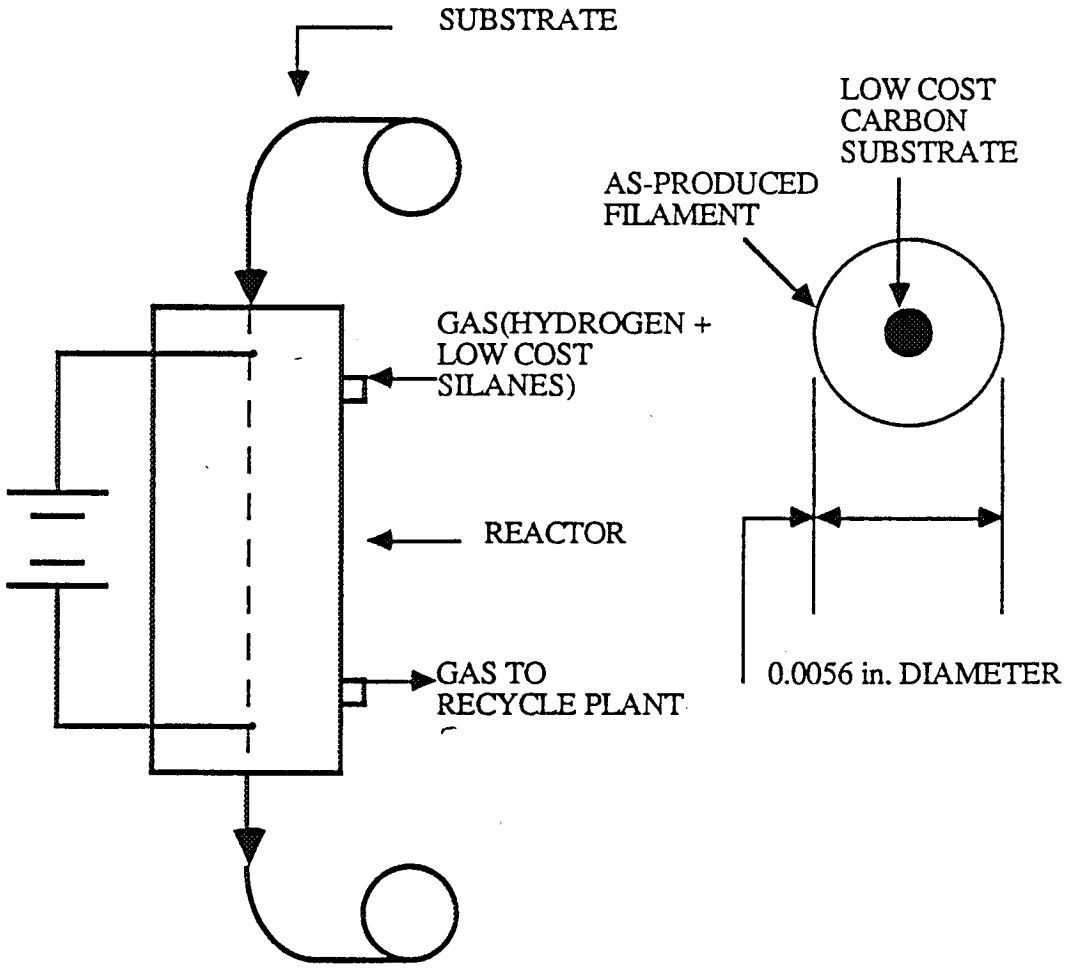

Figure 4.1 Fabrication of Silicon Carbide Fiber.

smooth the substrate and enhance electrical conductivity. In the second step, the PG coated substrate is exposed to form beta silicon carbide (βSiC) continuously on the substrate. The resulting filament, like most high-strength high-modulus reinforcements, is brittle and exhibits a distribution of strengths. The filament is extremely sensitive to surface defects and abrasion. To overcome this problem, the filament manufacturers have developed a protective carbon silicon coating called SCS, which is also applied by CVD. The coating consists mostly of carbon and is slightly enriched in silicon at the surface. The presence of the SCS surface layer causes a twofold increase in filament strength, presumably by reducing the severity of stress concentration at the filament surface. The fibers produced by CVD can be categorized into three types depending on the surface composition [41]. SCS-2 fiber has a 1 μm (39 μin.) carbon rich coating, which increases in silicon content as the outer surface is approached. This fiber has been used extensively to reinforce aluminum. SCS-6 fiber has a 3 μm (118 μin.) carbon rich coating in which the silicone content exhibits maxima at the outer surface and at 1.5 μm (59 μin.) from the outer surface. The SCS-6 fiber is primarily used to reinforce Titanium. SCS-8 fiber was developed to give better mechanical properties than SCS-2 in aluminum composite transverse to the fiber direction. It consists of 6 μm (236 μin.) of very fine grained SiC, a carbon rich region of about 0.5 μm (20 μin.), and a less carbon rich region of 0.5 μm (20 μin.). Figure 4.2 is a photomicrograph and a schematic representation of a fiber cross section showing the interior of the fiber and the carbon monofilament substrate.

Several methods exist for measuring the elastic modulus of a fiber, three of which are briefly reviewed here. They are the sonic modulus method, direct strain measurement test, and the standard ASTM test [42].

The sonic test is based on measurement of the time it takes for a sonic pulse to travel a given distance in the fiber. The modulus is given by

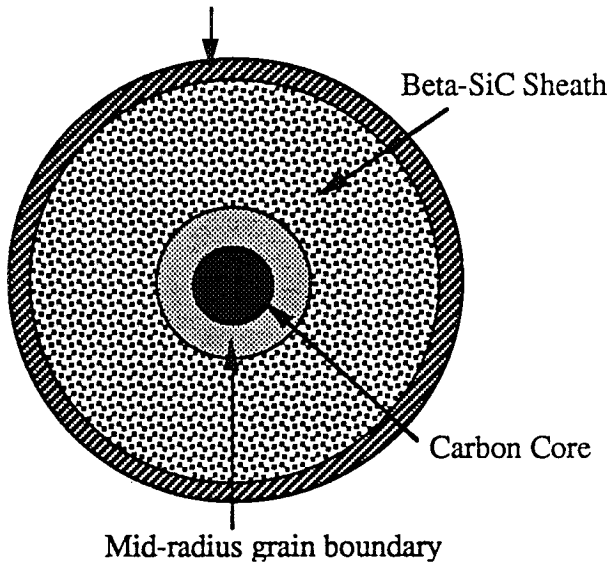

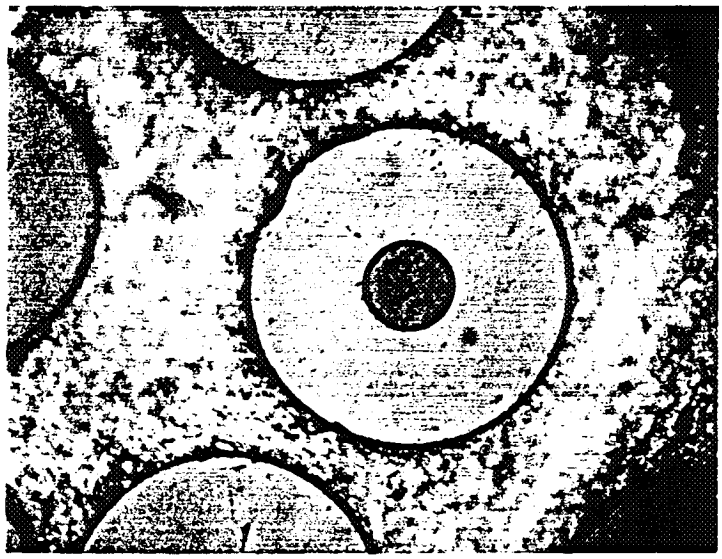

Figure 4.2 Cross-Section of a Silicon Carbide Fiber.

$$E_f = \rho_f c^2 \tag{4.1}$$

where,

E_f = modulus of fiber

ρ_f = density of fiber

c = sonic velocity

In the direct strain measurement test, the fiber strain under loading is measured directly with a noncontact extensometer, usually one based on a laser system. The fiber modulus is then obtained directly as

$$E_f = \frac{\sigma_f}{\varepsilon_f} \tag{4.2}$$

where σ_f and ε_f are the stress and strain in the fiber, respectively.

The method used in this study was the standard ASTM method described in ASTM specification D3379-75 [42,43]. Silicon carbide SCS-2 fibers were obtained from the composite manufacturer, Textron Specialty Materials Inc. They were tested in tension under constant strain rate to determine strength, elastic modulus and failure strain. The method is limited to fibers with an elastic modulus greater than 21 GPa (3 x 10^6 psi). The filament is centerline mounted on paper with slotted tabs (Figure 4.3) and axial alignment is accomplished without damaging the filament. After the specimen is mounted in the test machine the paper tab is cut to allow for filament elongation. Originally, the specimens were tested in an Instron servohydraulic machine using a 25 lb. load cell and specially made grips. Subsequent tests were conducted on a small frame designed for low load testing. The test system consists of a reaction frame, a 50 lb. load cell (Hottinger Baldwin Measurements), LVDT (Trans-Tek, Inc.), grips and a pneumatic cylinder. The specimen with the grips was mounted in this loading frame with one set of grips connected to the moving piston of the pneumatic cylinder and the other set connected to the other end of the reaction frame through the load cell.

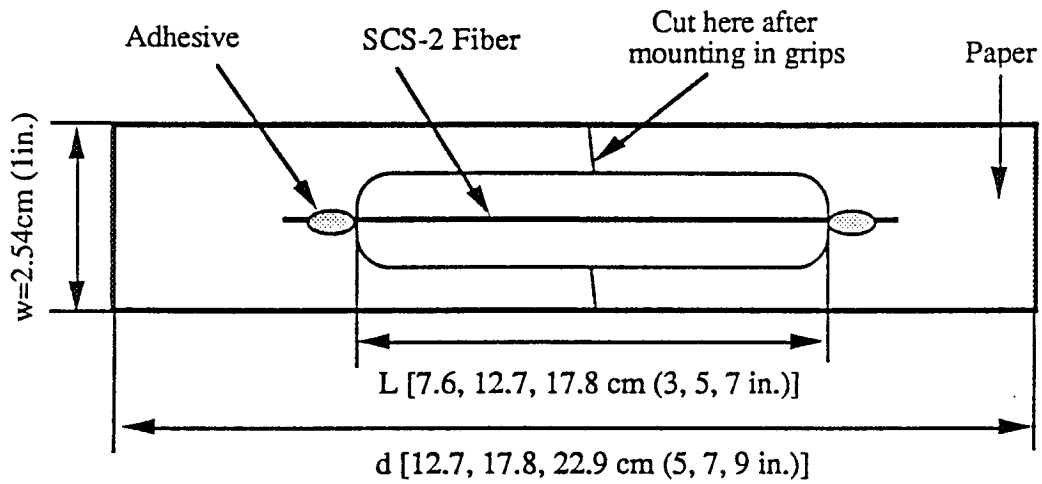

Figure 4.3 SCS-2 Fiber Center Mounted on Paper with Sloted Tabs.

Twelve specimens of gage lengths of 1, 1.5, 1.75, 2, and 2.25 in. were tested. They were loaded to failure and load-displacement curves were obtained and recorded digitally and stored on the computer. The cross-sectional area of the fiber, A, was determined from measurements of a representative number of fiber cross sections in highly magnified photomicrographs. The average cross sectional area was determined as follows:

$$A = \frac{\Sigma a_f}{NM^2} \tag{4.3}$$

A = average fiber cross sectional area

a_f = area of one fiber cross section in photomicrograph

N = number of fibers measured

M = photomicrograph magnification factor

The measurements showed that the SCS-2 fiber has a uniform diameter of 140 μm (0.0055 in.) with a carbon core diameter of 34 μm (0.00134 in.). The elastic modulus of the filament cannot be determined from the slope alone of the load-displacement curve since the system compliance must be taken into consideration. The system compliance is the portion that indicates elongation contributed by the loading train and the specimen gripping system. It must be determined experimentally for a given combination of test machine conditions, grip system and specimen mounting and subtracted from the indicated elongation to yield true specimen elongation in the gage length. An apparent compliance, C_a, can be determined from the initial straight line portion of the load-displacement curve.

$$C_a = \frac{u}{P} \tag{4.4}$$

where P and u are the load and cross-head displacement, respectively, associated with the slope of the straight line portion of the load-displacement curve. The term apparent compliance is used because cross-head travel, due to system compliance,

is not a true measure of filament displacement. This difficulty is overcome by assuming that the system compliance is constant. Thus

$$C_a = \frac{u}{P} = \frac{u_f}{P} + C_s = \frac{L}{AE_f} + C_s \tag{4.5}$$

where u_f and E_f are the actual fiber displacement and modulus, respectively. By determining values of C_a for different gage length specimens, the true value of E_f can be determined from equation (4.5). In particular, E_f can be determined from the slope of the best-fit straight line plot of measured values of C_a as a function of gage length (Fig. 4.4). The intercept of this straight line with the compliance axis represents the system compliance, C_s, from which u_s is determined as

$$u_s = C_s P \tag{4.6}$$

The elastic modulus of the filament is determined from eq. (4.5) as

$$E_f = \frac{L}{A(C_a - C_s)} \tag{4.7}$$

The fiber strain at failure, ε_f, is simply

$$\varepsilon_f = \frac{u_{max} - u_s}{L} \tag{4.8}$$

and the tensile strength is

$$F_{ft} = \frac{P_{max}}{A} \tag{4.9}$$

From the load-deflection curves it is seen that the fiber behaves linearly up to failure. The mean value of the modulus was found to be 400 GPa (58 Msi). The tensile strength showed large scatter with a range of 3,460 - 5,310 MPa (502 - 770 ksi). A size effect trend is seen in Fig. 4.5 where the tensile strength appears to decrease with increasing gage length. The mean value of the strengths measure was 4,000 MPa (580 ksi) with a variance of 15%. An approximate modulus was calculated by using the rule of mixtures. The modulus of the carbon core and SiC

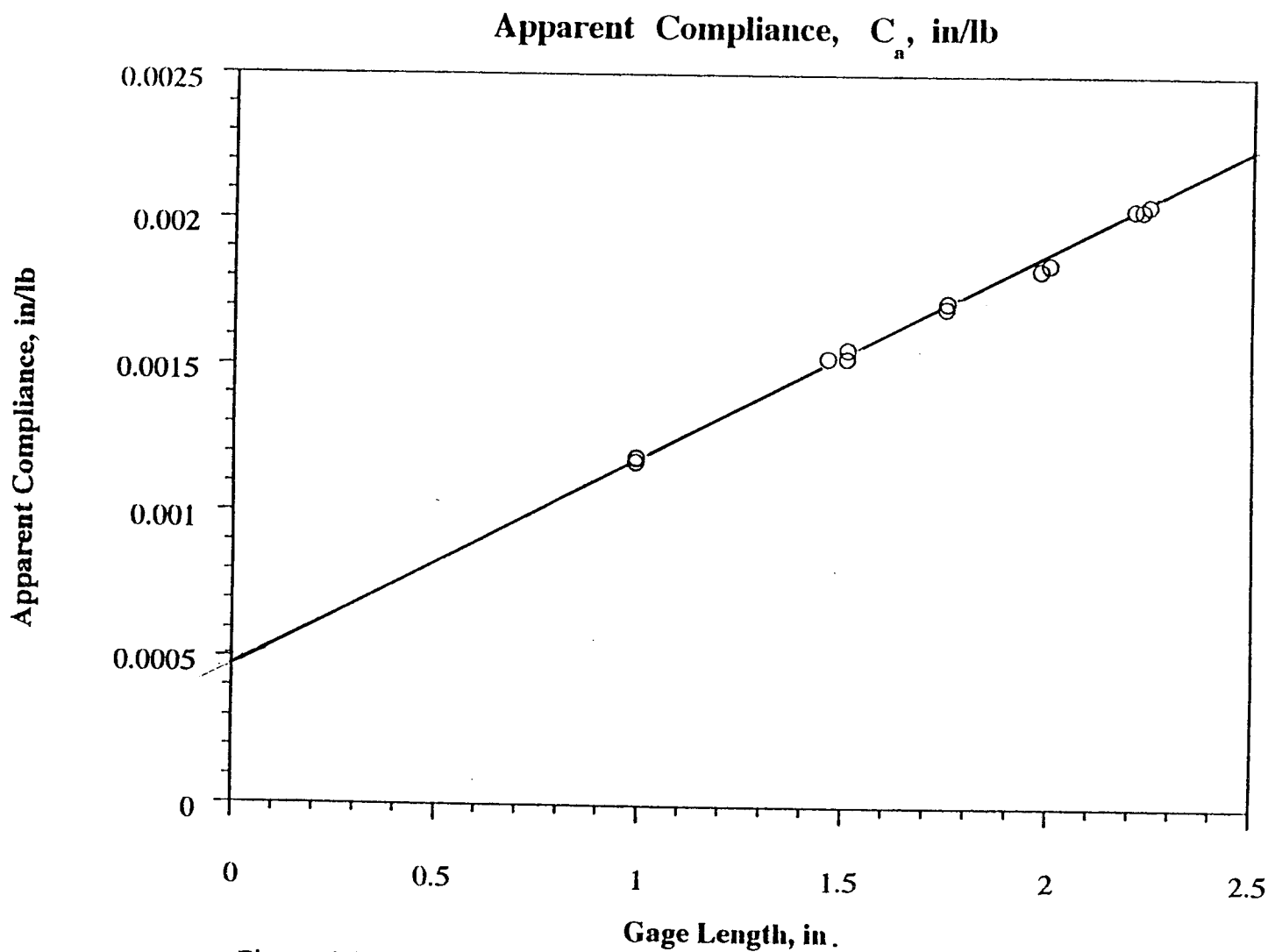

Figure 4.4 Apparent Compliance versus Gage Length for SCS-2 Fiber

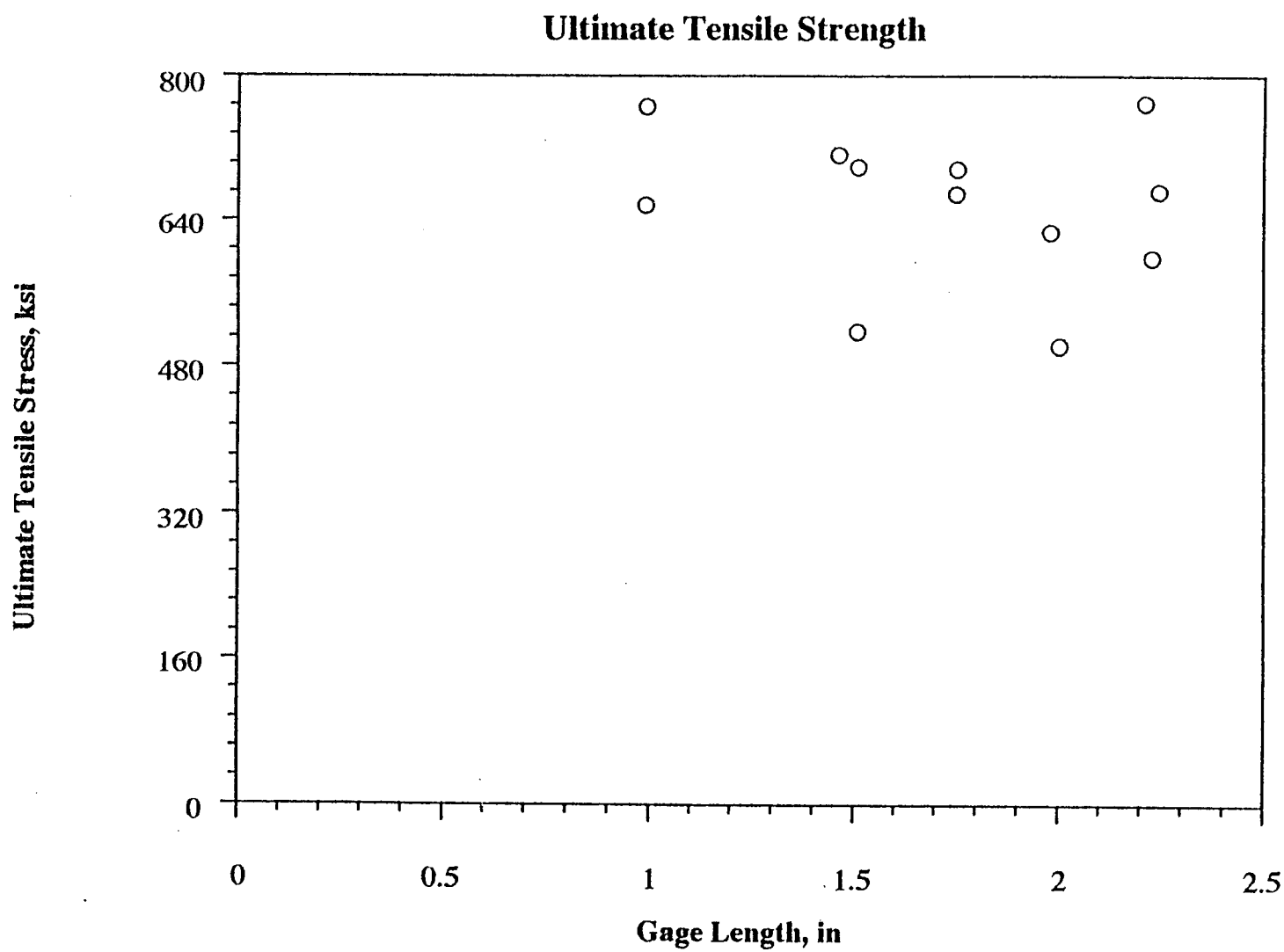

Figure 4.5 Tensile Strength of SCS-2 Fiber as a Function of Gage Length

sheath in the fiber are 41.4 GPa (6 Msi) and 414 GPa (60 Msi), respectively. The volume fraction represented by the carbon core is 5.9%. The calculated modulus of SCS-2 fiber was obtained as

$$E_f = V_c E_c + V_s E_s \tag{4.10}$$

where

V_c = volume fraction of carbon core

V_s = volume fraction of SiC sheath

E_c = elastic modulus of carbon core

E_s = elastic modulus of SiC sheath

The modulus obtained from the above equation is 392 GPa (57 Msi).

The manufacturer's values for the elastic modulus and fracture strength of the fiber are given as 4,000 MPa (580 ksi) and 407 GPa (60 Msi), respectively. Similar results are found in the literature. Nunes [44] in his study of the tensile properties of several spools of silicon carbide filaments (SCS-2) gives an experimentally measured modulus of 386.2 ± 9.66 GPa (56.0 ± 1.4 Msi) for each of the spools tested and a failure stress range of 2,993 MPa (434 ksi) to 3,290 MPa (477 ksi). He also found that examination of the broken filaments from each of the spools tested revealed a normal tensile failure that originated at the relatively weak interface of the carbon monofilament substrate. Similar values for ultimate tensile strength and tensile modulus are given by Skinner et al. [45]. The reported values for the elastic modulus and strength of SCS-6 fiber of 4,000 GPa (58 Msi) and 3,350 MPa (485 ksi), respectively. They also found that the tensile strength exhibits a strong size effect. The fracture appears to be flaw density limited, since increasing the gage length increases the statistical probability of a surface flaw in the gage length. According to Skinner et al. fracture in SiC fibers can be initiated at surface flaws, inclusions and defects in the core-sheath interface and occasionally in the core. In addition, he noticed that the overall failure trend of the SiC fiber

indicates insensitivity to thermal exposure. This is substantiated by Crane and Krukonis [46], who have shown that SiC fiber strength remains fairly uniform below 600° C (1,112° F), above which rapid strength degradation occurred, and by Nutt and Wawner [40] who showed that the SiC fiber strength remains fairly uniform below 800° C.

Thermal expansion properties for SiC fibers are scarce in the literature. Hillmer showed that thermal expansion of SCS fibers is controlled by the SiC sheath and does not depend on the fiber coating or the carbon core [47]. He also found that after a relatvely small initial expansion from room temperature to 450° C (842° F), the expansion of the fiber increases linearly with temperature from 450° C (842° F) to 1500° C (2732° F). Above 1300° C (2372° F) a hysteresis effect was observed involving a temporary 50% reduction in expansion. No results were obtained over the low range between room temperature and 450° C because of inadequate resolution.

A new method was developed for measuring longitudinal thermal expansion in the fiber [48]. A fiber specimen of length l is freely supported at the ends on V-grooves in a titanium silicate support plate as shown in Fig. 4.6. The fiber is straight at room temperature, T_o. When the temperature increases to T_i the fiber bends because its coefficient of thermal expansion is higher than that of the support plate. Assuming a parabolic shape for the deformed fiber we obtain the deflection curve, then we calculate the total length of the fiver at temperature T_i, and finally we calculate the thermal strain as follows:

$$\varepsilon_t = \alpha_r \Delta T + \frac{8\,\delta_i^2}{3l^2\left(1 + \alpha_r \Delta T\right)} \tag{4.11}$$

where

α_r = coefficient of thermal expansion of support (reference) titanium silicate material

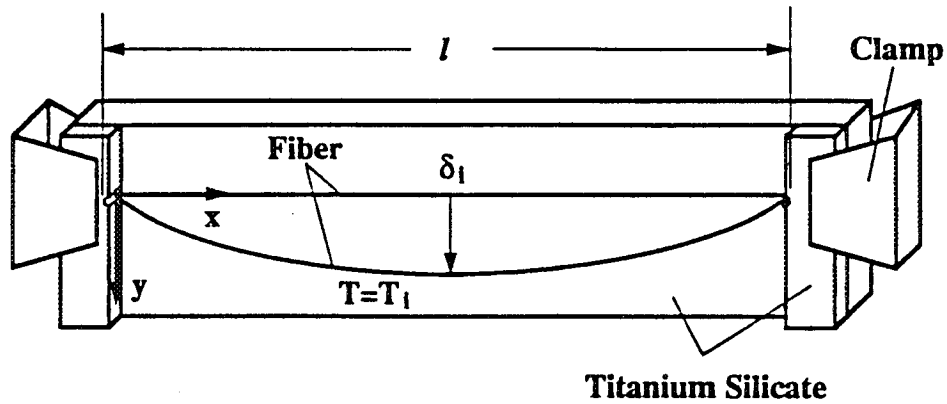

Figure 4.6 **Fixture for Thermal Expansion Coefficient Measurement of Rigid Fiber**

$\Delta T = T_i - T_o$ = temperature change

δ_i = central deflection of fiber

If a sine function is assumed for the deformed shape of the fiber

$$y = \delta_i \sin\left[\frac{\pi x}{l\left(1 + \alpha_r \Delta T\right)}\right] \tag{4.12}$$

the thermal strain is calculated as

$$\varepsilon_t = \sqrt{\left(1 + \alpha_r \Delta T\right)^2 + \left(\frac{\pi \delta_i}{l}\right)}\left(1 + \sum_{n=1}^{\infty}\left[\frac{(2n-1)!!}{2^n\, n!}\right]^2 \frac{k^{2n}}{2n-1}\right) - 1 \tag{4.13}$$

The difference between the strains given by eqs. (4.11) and (4.13) is less than 4%.

The coefficient of thermal expansion is obtained by plotting the thermal strain versus temperature as shown in Fig. 4.7, and taking the slope of this curve. The coefficient of thermal expansion of the SCS-2 fiber varies with temperature, starting with a value of 0.9×10^{-6}/°C (0.5×10^{-6}/°F) at 24° C (75° F) and increasing nonlinearly to 2.6×10^{-6}/°C (1.4×10^{-6}/°F) at temperatures between 120° C (250° F) and 200° C (400° F).

The transverse mechanical and thermal properties of the SCS-2 fiber are not known and cannot be measured easily, but it is assumed that they are close to the longitudinal properties despite the presence of the carbon core. More exact values of transverse properties can be obtained indirectly from transverse properties of the composite.

Properties of the SCS-2 fiber measured in this program or obtained from the literature are summarized in Table 4.1

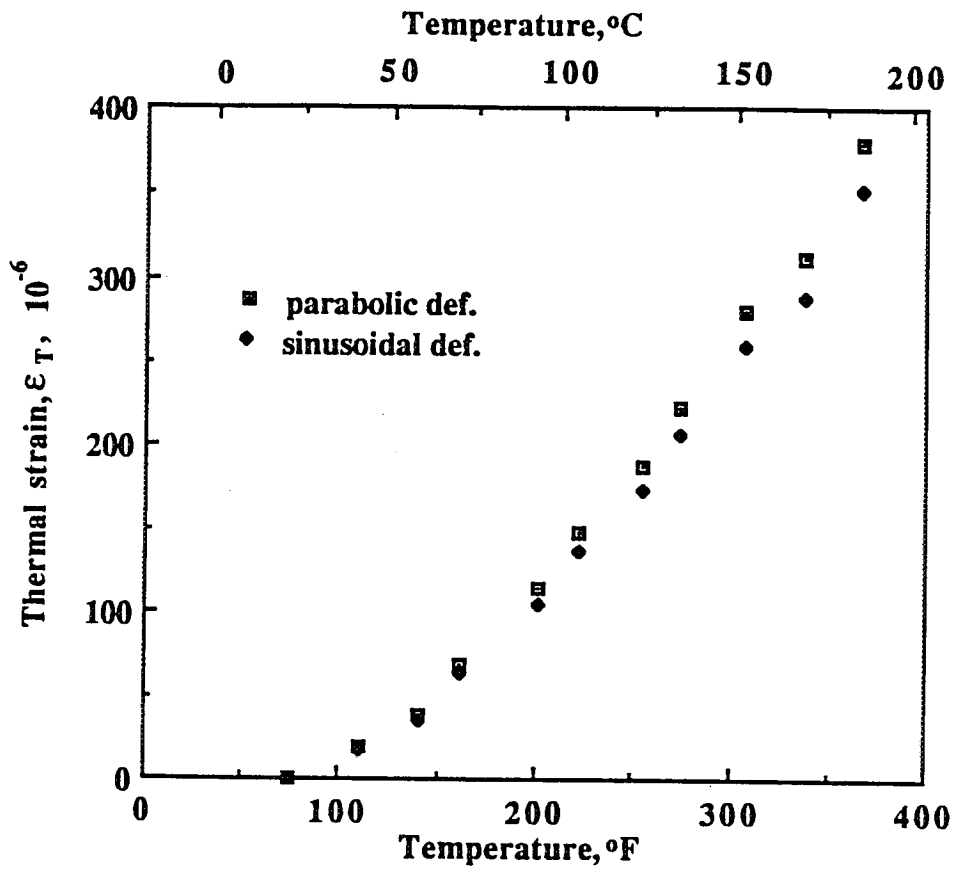

Fig. 4.7 Thermal Strain vs. Temperature for Silicon Carbide/Carbon Fiber (SCS-2)

Table 4.1 Properties of Silicon Carbide SCS-2 Fiber

Young's Modulus, E	400 GPa (58 Msi)
Poisson's Ratio, ν	0.22
Ultimate Tensile Strain, ε_{ft}^{u}	0.010
Tensile Strength, F_{ft}	4,000 MPa (580 ksi)
Coefficient of Thermal Expansion, α_f	
At 24°C (75° F)	0.9×10^{-6}/°C (0.5×10^{-6}/° F)
120 - 200° C (250 - 400° F)	2.6×10^{-6}/°C (1.4×10^{-6}/° F)
450 - 1500° C (842 - 2,732° F)	4.9×10^{-6}/°C (2.7×10^{-6}/° F)
Density, ρ	2.72g/cm^3 (0.0981 lb/in^3)

4.3 Characterization of 6061-T4 Aluminum

The aluminum alloy used in manufacturing the composite studied is 6061 with T6 temper. This aluminum alloy contains silicon and magnesium in approximately equal proportions to form magnesium silicide, thus, making it capable of heat treatment. Although this alloy is not stronger than other aluminum alloys, it possesses good formability and corrosion resistance with intermediate strength. During consolidation of the composite the aluminum experiences a heat treatment process which changes its temper. It was suggested by the manufacturer (Textron) that the aluminum matrix in the composite system has properties close to those of 6061 with T4 temper. Aluminum of 6061-T4 type was obtained in plate form for thermomechanical characterization. Later on, it was found that, following the composite specimen preparation process, the matrix experiences a further heat

treatment so that its effective in situ properties become closer to those of fully annealed 6061 Aluminum.

Rectangular specimens of dimensions 20.32 x 1.27 x 0.16 cm. (8.0 x 0.5 x 0.062 in.) were prepared. For testing at elevated temperatures steel tabs were bonded onto the specimen ends with a high strength-high temperature adhesive (FM-36). The aluminum specimens were loaded in tension in an Instron testing machine. The specimens were loaded at a crosshead rate of 0.06 in./min up to failure. Particular care was taken in aligning the coupons in the grips. Special grips capable of withstanding temperatures up to 540° C (1000° F) were used. The specimens were tested inside a thermal chamber set to the desired temperature. A water-cooling system was used to protect the loadcell from the extensive heat generated at elevated temperatures. The experimental setup for this testing is shown schematically in Fig. 4.8. Axial strains were monitored with strain gages and a special high temperature extensometer (Model 632.11B-45, MTS Corp.). WK gages (Micro Measurements Group) made of karma alloy and encapsulated in phenolic resin were used at temperatures up to 550° F. RKO gages (J. P. Technology) made of karma alloy and encapsulated in polyimide resin were used at 750° F. In some cases axial strains were also double-checked with another water-cooled high temperature extensometer (2630 series, Instron) with a 1 in. gage length and capable of operating in the temperature range of 15 - 500° C (59-930° F). A data acquisition system (Metrabyte Corp.) was used to acquire, process and plot the data.

Stress-strain curves for 6061-T4 aluminum at various temperatures and at a strain rate of 0.02% per second are shown in Fig. 4.9. Figure 4.10 shows the same stress-strain curves zoomed to the 1% strain range. At this relatively low strain rate it takes several minutes to fail the specimen. It is seen that as the temperature increases the yield stress or the proportional limit, σ_{my}, decreases. The

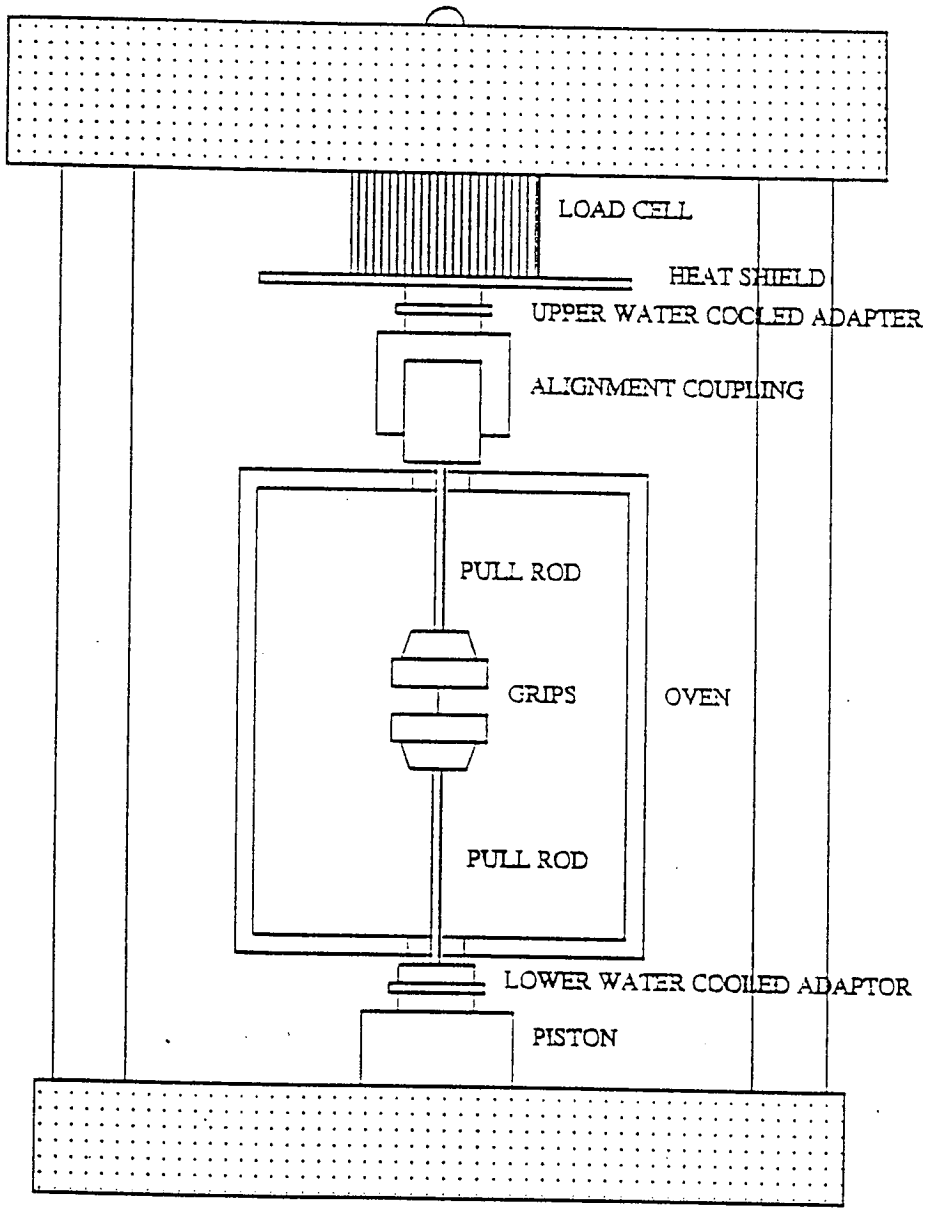

Fig. 4.8 Schematic Diagram of Elevated Temperature Tensile Test System

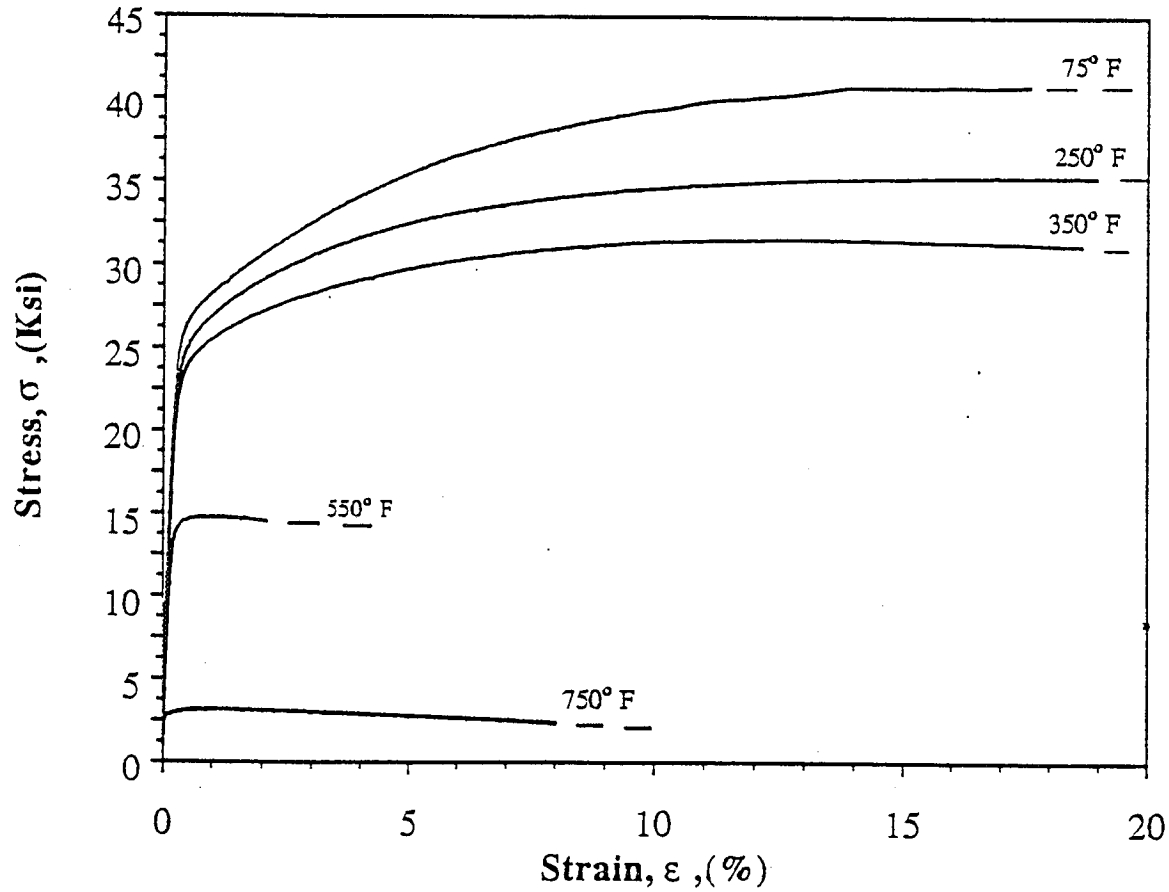

Fig. 4.9 'Stress-Strain Curves of Aluminum 6061-T4 Specimens under Tensile Loading at Various Temperatures at a Strain Rate of 0.02%/sec

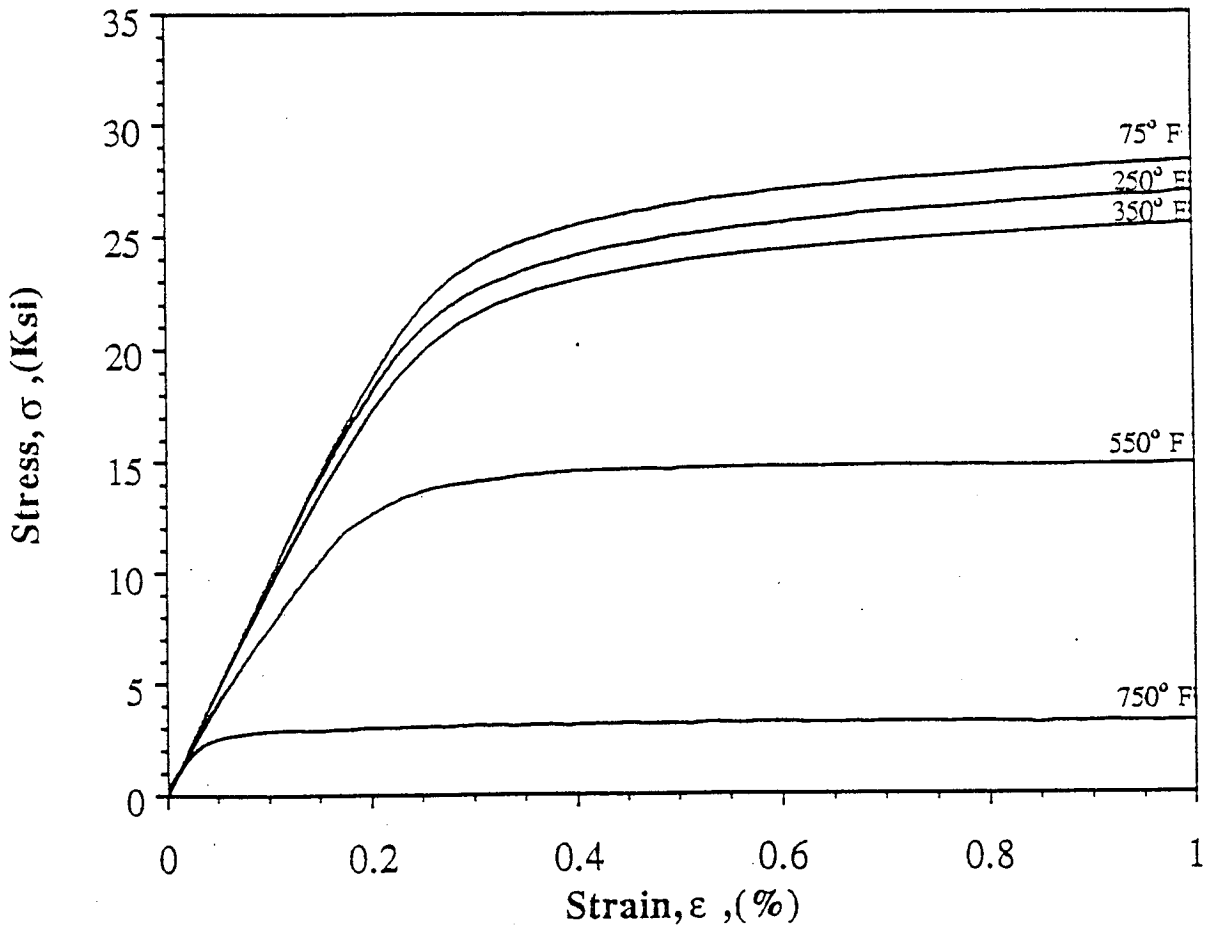

Fig. 4.10 Stress-Strain Curves of Aluminum 6061-T4 Specimens under Tensile Loading at Various Temperatures up to 1% at a Strain Rate of 0.02%/sec

tensile strength also decreases with increasing temperature. The ultimate strain does not follow a consistent trend with temperature, but in general it decreases with increasing temperature due to the reduced degree of work hardening.

Figures 4.11and 4.12 show stress-strain curves for 6061-T4 aluminum at various temperatures obtained at a strain rate of 115% per second. The yield stress and strength are higher at this higher strain rate. However, no consistent trend in ultimate strain is observed with increasing strain rate.

Figures 4.13 and 4.14 show the decrease in ultimate strength and yield stress with temperatuere for both strain rates used. The relative increase in tensile strength at the higher strain rate is plotted versus temperature in Fig. 4.15. It is seen that the effect of strain is small at room temperature but increases rapidly at higher temperatures. This increase begins rather abruptly at a specific temperature which corresponds roughly to the recrystallization temperature. In addition to increased strain rate sensitivity, high temperature behavior above the recrystallization point is characterized by a breakdown of low temperature strengthening mechanisms as a result of a higher rate of self diffusion. Poor resistance to creep and an inability of the metal to workharden are invariably associated with high temperature behavior. Tensile properties at low strain rate deteriorate considerably because of the transition to high temperature behavior. At high rates of strain, under high temperature conditions, higher strength properties are maintained, probably because plastic flow occurs more rapidly than diffusion. Therefore, structural metals can be used safely at high temperatures under conditions of rapid loading. The initial tengential modulus remains constant but the secant modulus decreases at low rates and high temperatures. This decrease is due to a small amount of plastic deformation and creep that occur during the initial phase of the tensile test as the specimen is loaded slowly through the elastic region. This plastic deformation decreases the slope of the stress-strain curve causing a decrease

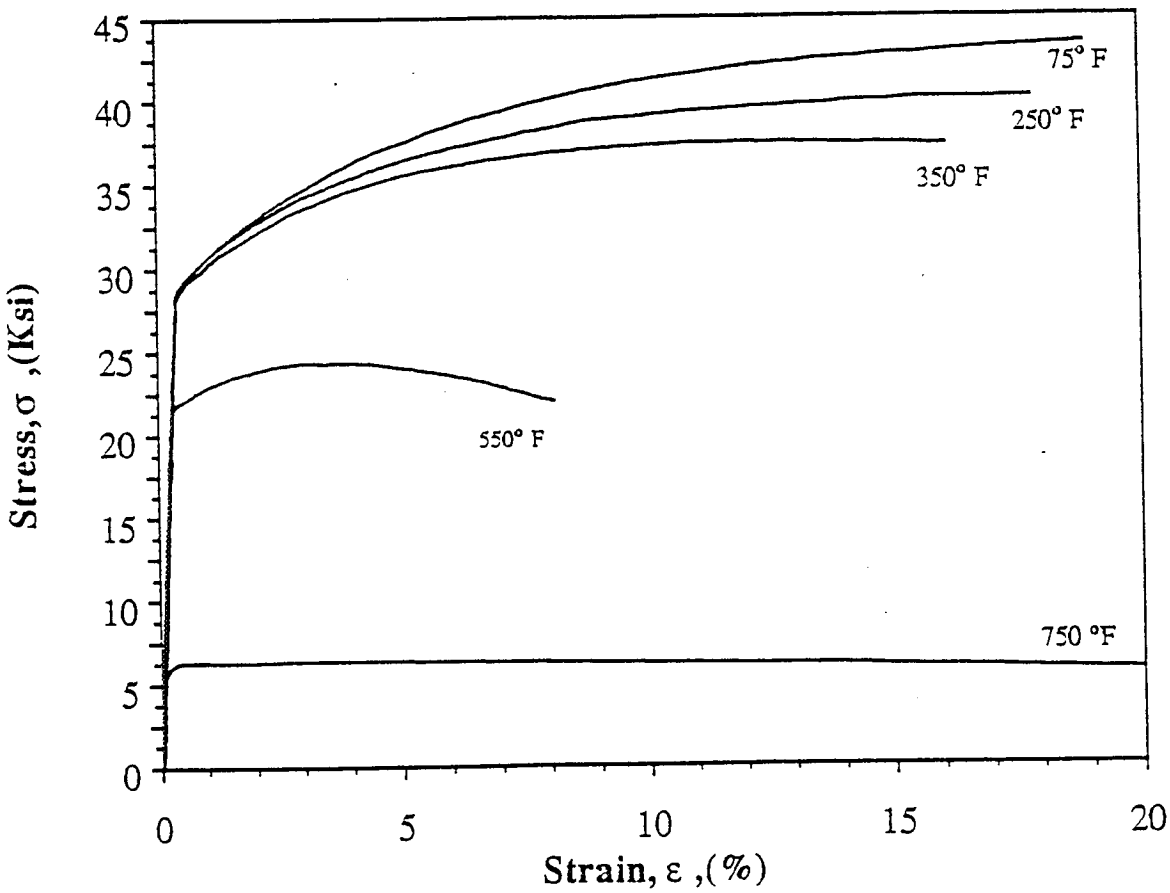

Fig. 4.11 Stress-Strain Curves of Aluminum 6061-T4 Specimens under Tensile Loading at Various Temperatures at a Strain Rate of 115%/sec

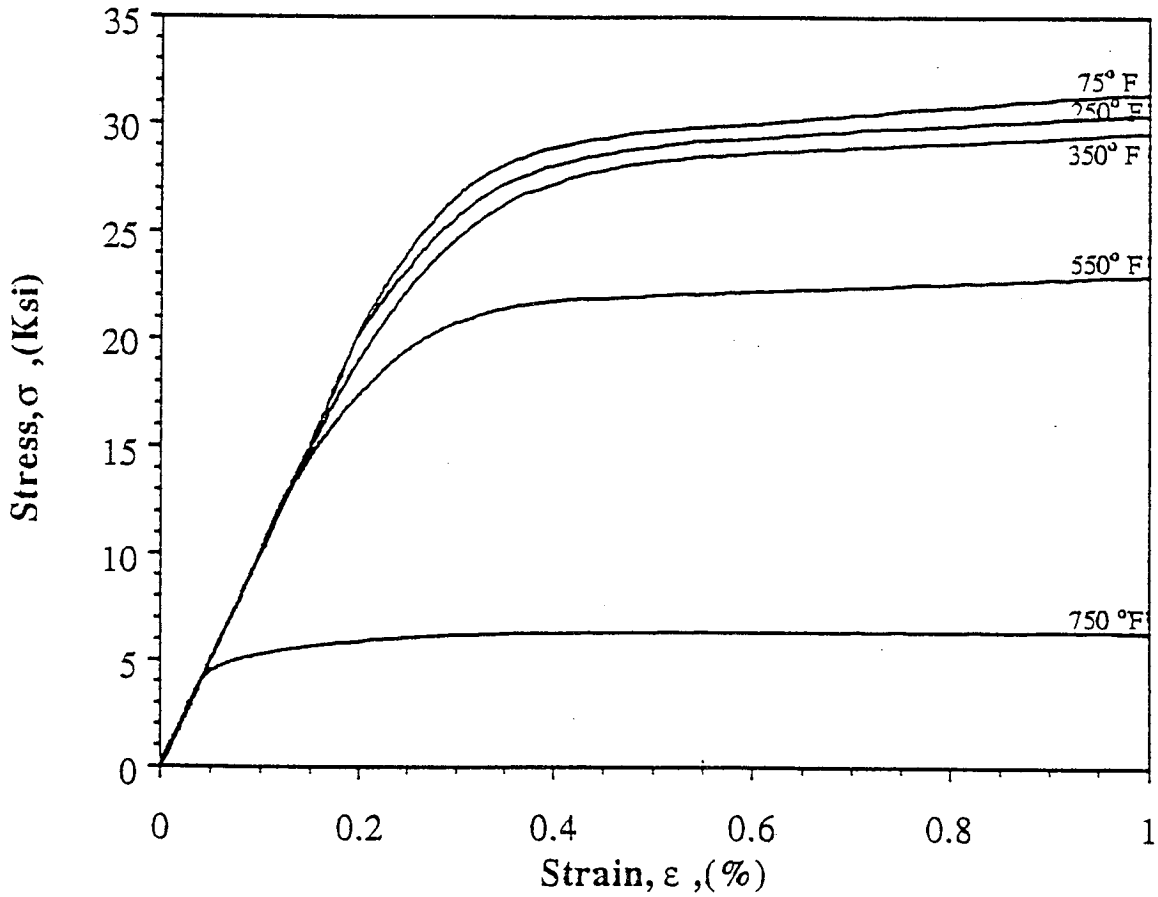

Fig. 4.12 Stress-Strain Curves of Aluminum 6061-T4 Specimens under Tensile Loading at Various Temperatures up to 1% at a Strain Rate of 115%/sec

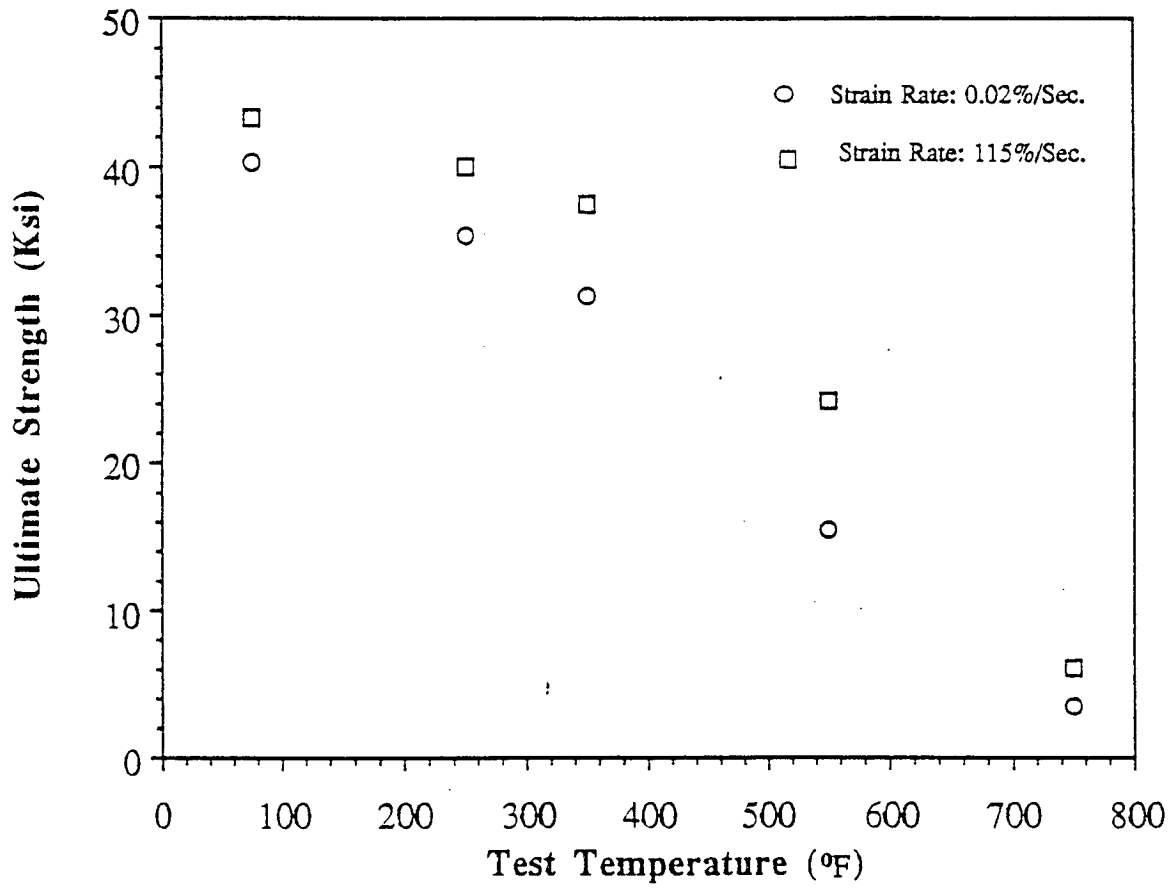

Fig. 4.13 Variation of Ultimate Tensile Strength with Test Temperatures for Aluminum 6061-T4

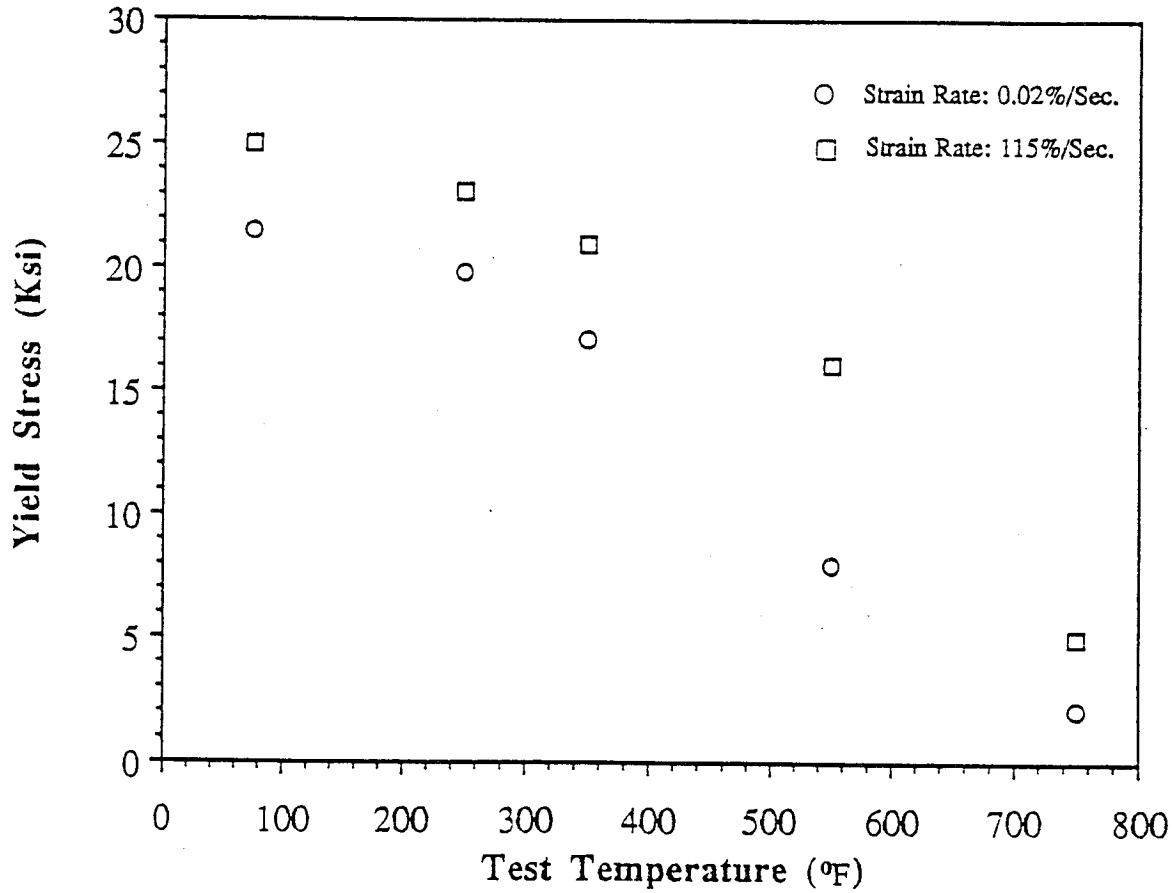

Fig. 4.14 Variation of Yield Stress with Test Temperatures for Aluminum 6061-T4

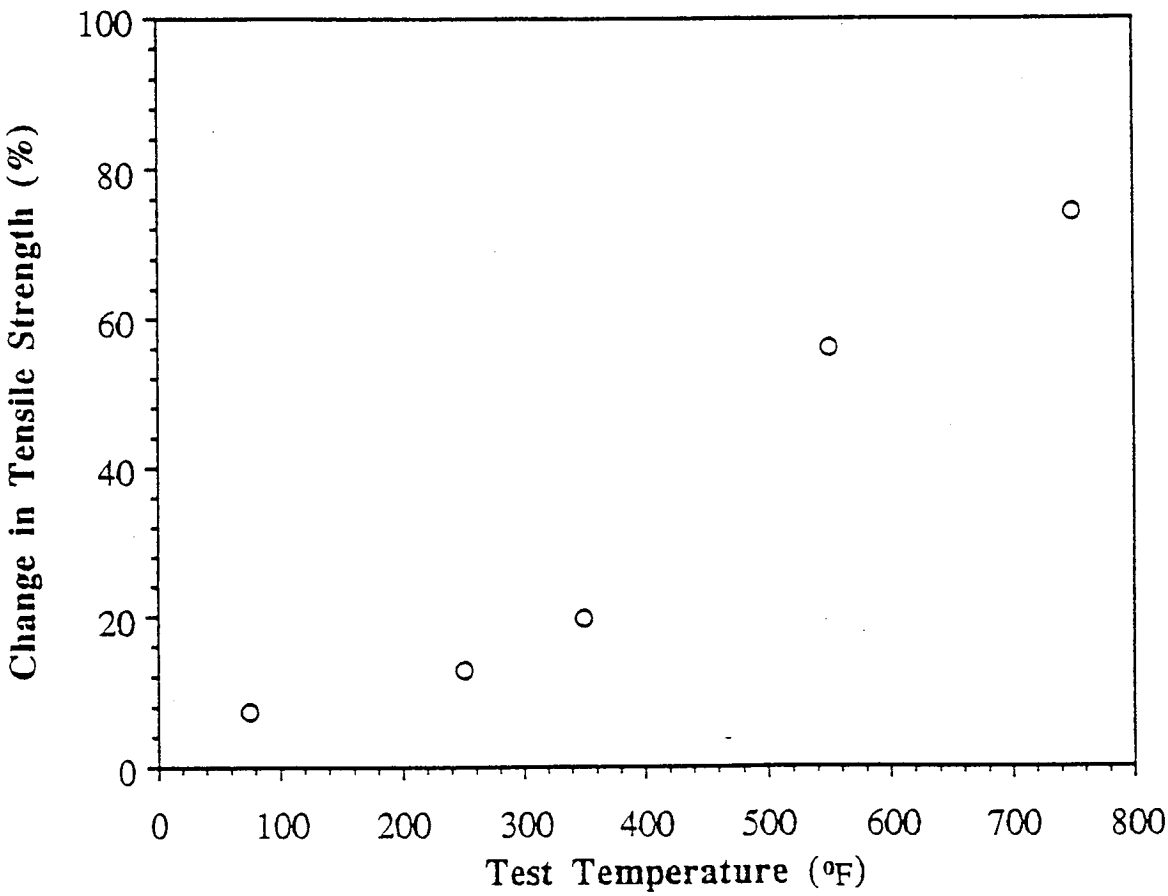

Fig. 4.15 Relative Change in Tensile Strength at High Strain Rate as a Function of Temperature for 6061-T4 Aluminum

in modulus. Since creep is time dependent, the modulus determined at a high strain rate is representative of true elasticity. In the case of low temperature behavior, modulus values are unaffected because creep is negligible.

At 750° F, both at low and high strain rates, super plastic elongation is observed. The superplasticity of aluminum 6061 is triggered at a certain strain rate and temperature. Superplastic behavior occurs above these threshold levels. The superplastic elongation is believed to result from grain boundary sliding. The strain of superplastic elongation is reported to be several hundred percent.

In addition to mechanical properties, physical properties such as density and coefficient of thermal expansion were measured. The density of the matrix material, measured by the method described in ASTM D792-66 specification, was 2.72 g/cm^3 (0.0981 lb/in.^{3}).

The coefficient of thermal expansion, α_m, was obtained by measuring thermal strain as a function of temperature. Aluminum specimens were instrumented with EA-00 or WK-00 gages for thermal cycling up to 340° F or 500° F, respectively. At least three thermocouples per specimen were used to monitor the temperature. Strain gages have been shown to be a practical and adequate means of measuring thermal strain [49, 50]. However, they must be properly compensated for the purely thermal output. One method of temperature compensation employs an identical gage bonded to a reference material of known thermal expansion exposed to the same temperature as the test specimen.

The true thermal strain in the material is given by

$$\varepsilon_{tc} = \varepsilon_{ac} - \varepsilon_{ar} + \varepsilon_{tr} \tag{4.14}$$

where

ε_{tc} = true thermal strain in test specimen

ε_{ac} = apparent strain in test specimen

ε_{tr} = $\alpha_r \Delta T$ = true thermal strain in reference specimen

ε_{ar} = apparent strain in reference specimen.

Reference materials used are usually ceramics of low and stable coefficient of thermal expansion. In this case titanium silicate, having a coefficient of thermal expansion of $\alpha_r = 0.03 \times 10^{-6}/^\circ$ C, was used. The thermal strain is plotted versus temperature and is shown in Figure 4.16. The thermal expansion coefficient α_m is obtained from the slope of the thermal strain versus temperature curve. The thermal deformation of 6061-T4 aluminum was also determined by using a 10 mm (0.39 in.) long and 3 mm (0.12 in.) diameter cylindrical specimen with a dilatometer. The thermal strain curve up to 482° C (900° F) is shown in Figure 4.17. The thermal strain curves of aluminum are linear up to 120° C (250° F). Above this temperature the strain-temperature curves become nonlinear and the coefficient of thermal expansion increases.

Thermomechanical properties of both SCS-2 fiber and 6061-T4 aluminum are summarized in Table 4.2.

4.4 Creep Properties of 6061-T4 Aluminum

Creep behavior is a very important characteristic of high temperature composites. The important issue in creep behavior of composites is the determination of the mechanism by which the creep behavior is introduced by the creeping matrix and the less creeping fibers. The general definition of creep is time dependent strain caused by a constant applied load at constant temperature. Usually creep is undesirable and a limiting factor in the life of parts such as blades on the spinning rotors of turbine engines. Creep can occur at any temperature, but the behavior can be different for different temperature ranges. There is low temperature creep behavior and high temperature creep behavior. The boundary between these temperature ranges depends on the homologous temperature of the material. For our matrix material the homologous temperature is approximately 188° C (370° F).

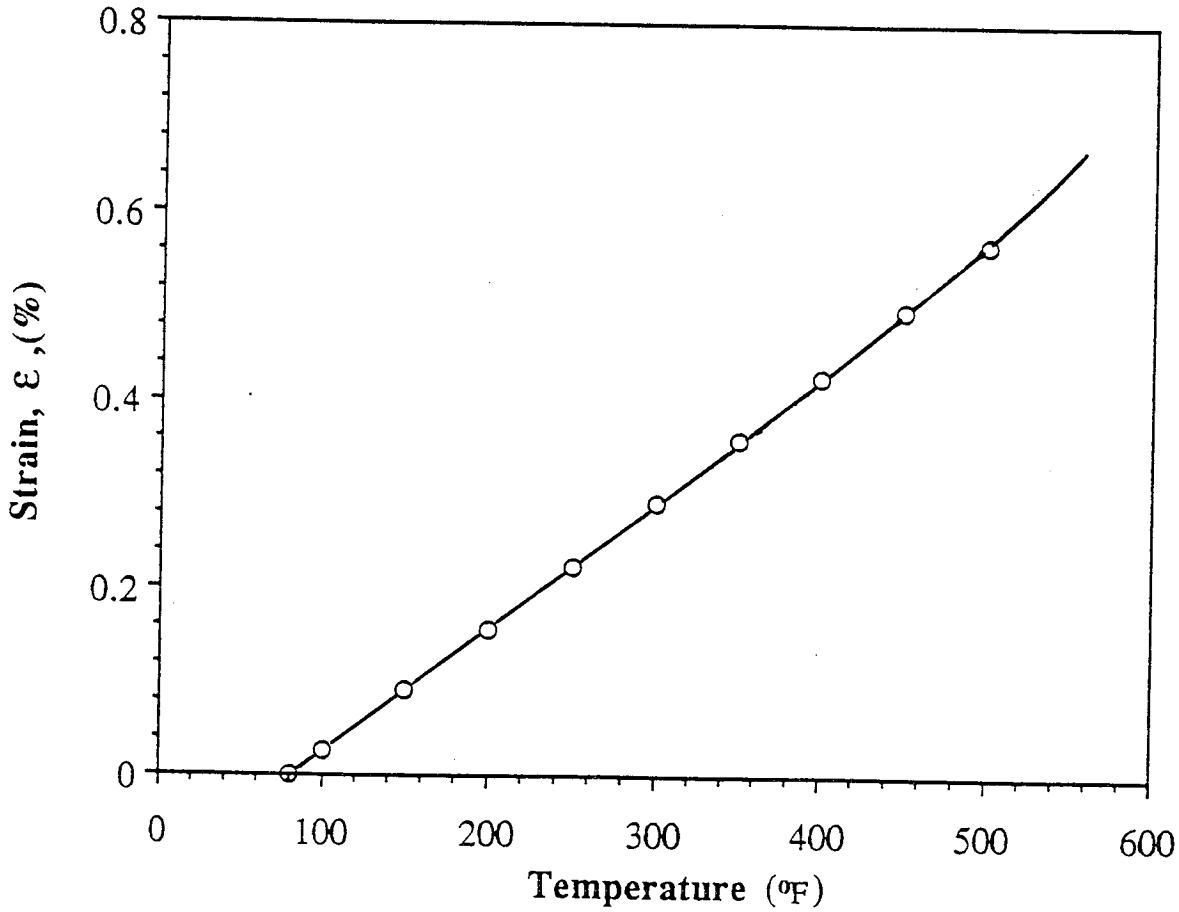

Fig. 4.16 Thermal Strain versus Temperature Curve of Aluminum 6061-T4

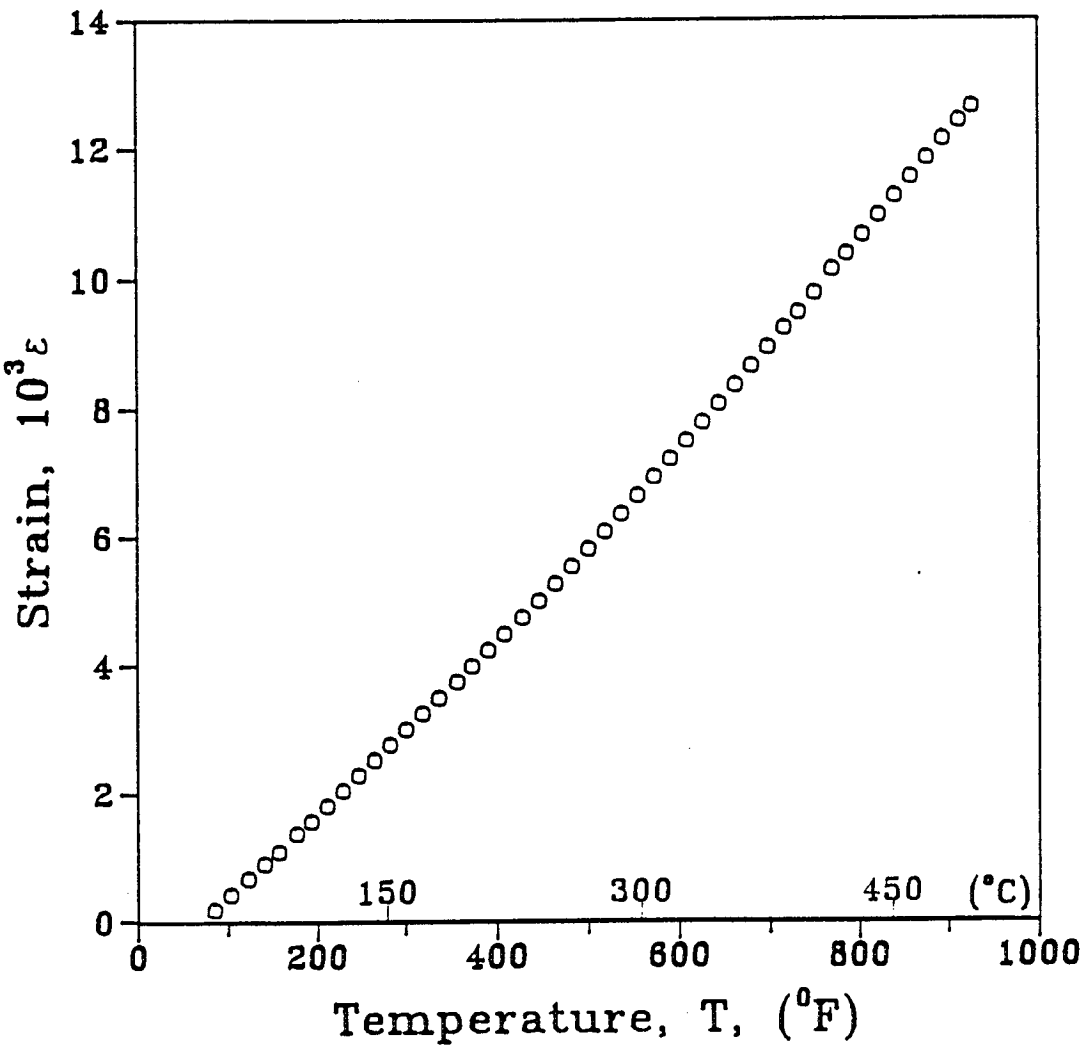

Fig. 4.17 Strain versus Temperature Curve of Aluminum 6061-T4 up to 482 °C (900 °F).

Table 4.2. Properties of Constituent Materials

Property	SCS-2 Fiber	6061-T4 Aluminum 24° C (75° F)	121° C (250° F)	177° C (350° F)	288° C (550° F)	399° C (750°F)
Density, ρ, g/ cm^3 (lb/in.^{3})	3.05 (0.110)	2.72 (0.098)	2.72 (0.098)	2.72 (0.098)	2.72 (0.098)	2.72 (0.098)
Coefficient of Thermal Expansion, α, 10^{-6}/°C (10^{-6}/°F)	0.9 - 4.9 (0.5 - 2.7)	23.2 (12.9)	23.4 (13.0)	24.3 (13.5)	25.4 (14.1)	28.8 (16.0)
Young's Modulus, E, GPa (Msi)	400 (58)	69 (10)	69 (10)	69 (10)	69 (10)	69 (10)
Poisson's Ratio, ν	0.22	0.33	0.33	0.33	0.33	0.33
Yield Stress, σ_y, MPa (ksi)	-	148 (21.5)	137 (19.8)	117 (17.0)	53 (7.7)	14.5 (2.1)
Tensile Strength, F_t, MPa (ksi)	4000 (580)	278 (40.3)	244 (35.4)	216 (31.3)	167 (24.2)	42 (6.1)
Ultimate Tensile Strain, ε_t^u, %	1.0	25	~ 20	~ 20	5 - 8	> 20

Creep is not only affected by temperature but also by stress level. Once loaded, the material initially deforms at a very rapid rate. If the applied load is sufficiently high an initial plastic deformation also occurs, but significant deformation ceases after the initial application of the load and an increase in load is needed to cause further deformation. For low temperatures, this type of behavior can continue indefinitely. At high temperatures, the region of constantly decreasing strain rate leads to the condition where the rate of deformation becomes independent of time and strain. When this occurs, creep is in its second stage. This steady state creep rate depends significantly on stress and temperature and is used frequently to characterize the creep resistance of the material. Although considerable deformation can occur under these steady-state conditions, eventually the strain rate begins to accelerate with time. Creep behavior can be simply explained by the Bailey-Orowan model. It views creep as a result of competition between recovery and work-hardening processes. After the load is applied, fast deformation begins, but it is not maintained as the material workhardens and becomes increasingly more resistant to further deformation. At low temperatures recovery cannot occur which leads to steady state in which the recovery and hardening processes balance one another. As the temperature increases, recovery becomes easier to activate and overcomes hardening. Thus, the transition from primary to secondary creep generally occurs at lower strains as the temperature increases. The third stage of creep cannot be rationalized in terms of the Bailey-Orowan model. Instead, tertiary creep is the result of microstructural instabilities. For instance, defects in the microstructure, such as cavities, grain boundary separation and cracks develop. This results in a local decrease in cross sectional area that corresponds to a slightly higher stress in the region.

Aluminum specimens were subjected to constant load in the Instron servo-hydraulic machine operating in the load control mode. Both high temperature strain

gages and a high temperature extensometer were used to monitor the time-varying strain. Creep tests were conducted inside the thermal chamber at three temperatures, 177° C (350° F), 288° C (550° F) and 399° C (750° F). Figure 4.18 shows creep curves for 6061-T4 aluminum for an applied stress equal to 85% of the yield stress corresponding to the test temperature. At 177° C (350° F) the material exhibits the typical low temperature creep behavior. At 288° C (550° F) all three stages of creep are shown. At 399° C (750° F) high creep deformation is observed with a very short second stage. From these creep curves it is apparent that creep deformation increases sharply at higher temperatures for the same effective load in relation to the corresponding yield stress. Figure 4.19 and 4.20 show creep rate and creep compliance curves obtained from the creep curves of Fig. 4.18.

4.5 Characterization of 6061-0 Aluminum

Although according to the manufacturer the in-situ properties of the aluminum matrix are close to those of 6061 aluminum with T4 temper, it was subsequently realized that all micromechanical predictions of composite properties were in better agreement with experimental results when based on matrix properties of fully annealed aluminum. Furthermore, during specimen preparation the curing process for bonding the tabs to the specimen exposes the specimen to a temperature history similar to that of the annealing process of aluminum. Other investigators, such as Pindera and Lin [51] also assumed that the in-situ properties of the matrix are reasonably close to those of the fully annealed state. For the reasons above, an additional test program was conducted to characterize the 6061 aluminum in the annealed state.

Stress-strain curves for 6061-0 aluminum at various temperatures are shown in Fig. 4.21. Thermal strains were also measured as in the case of 6061-T4

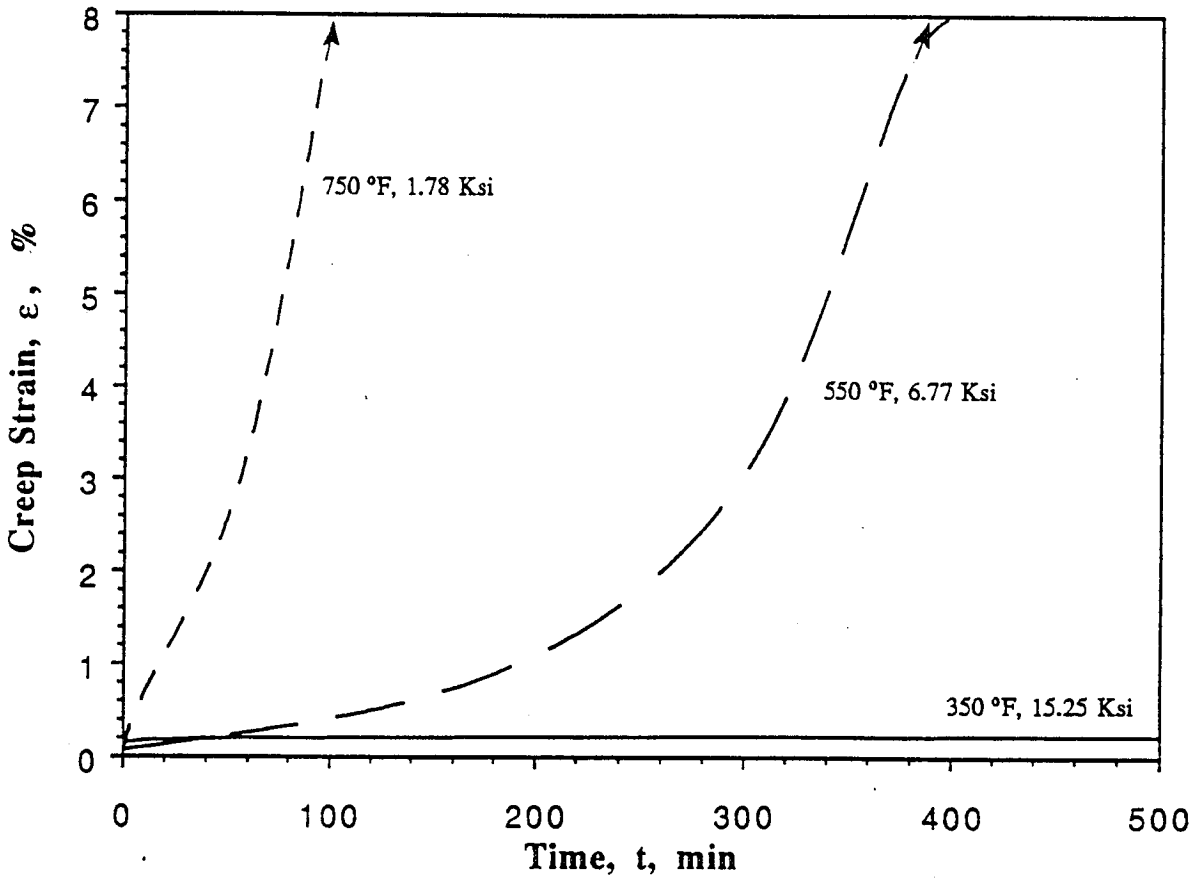

Fig. 4.18 Creep Curves of Aluminum 6061-T4 at Three Different Temperatures

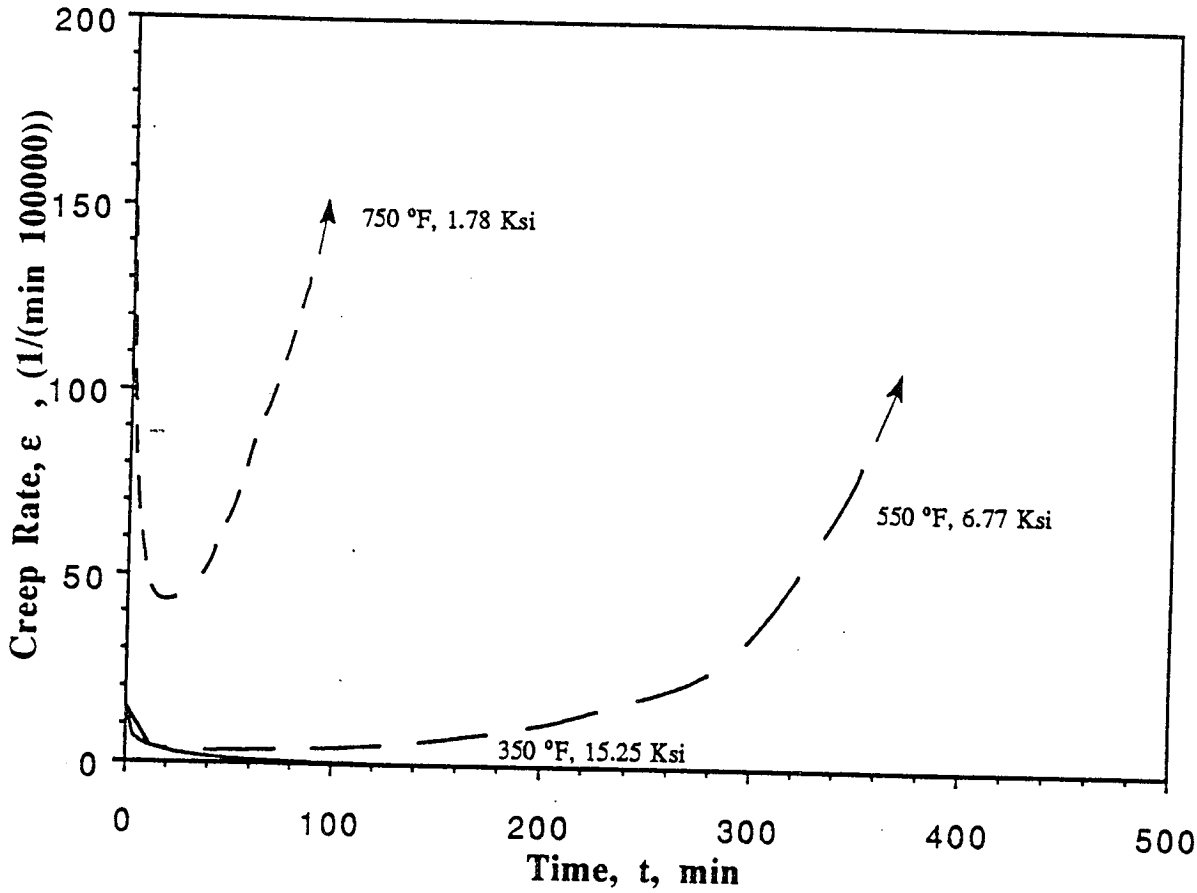

Fig. 4.19 Creep Rate Curves of Aluminum 6061-T4 at Three Different Temperatures

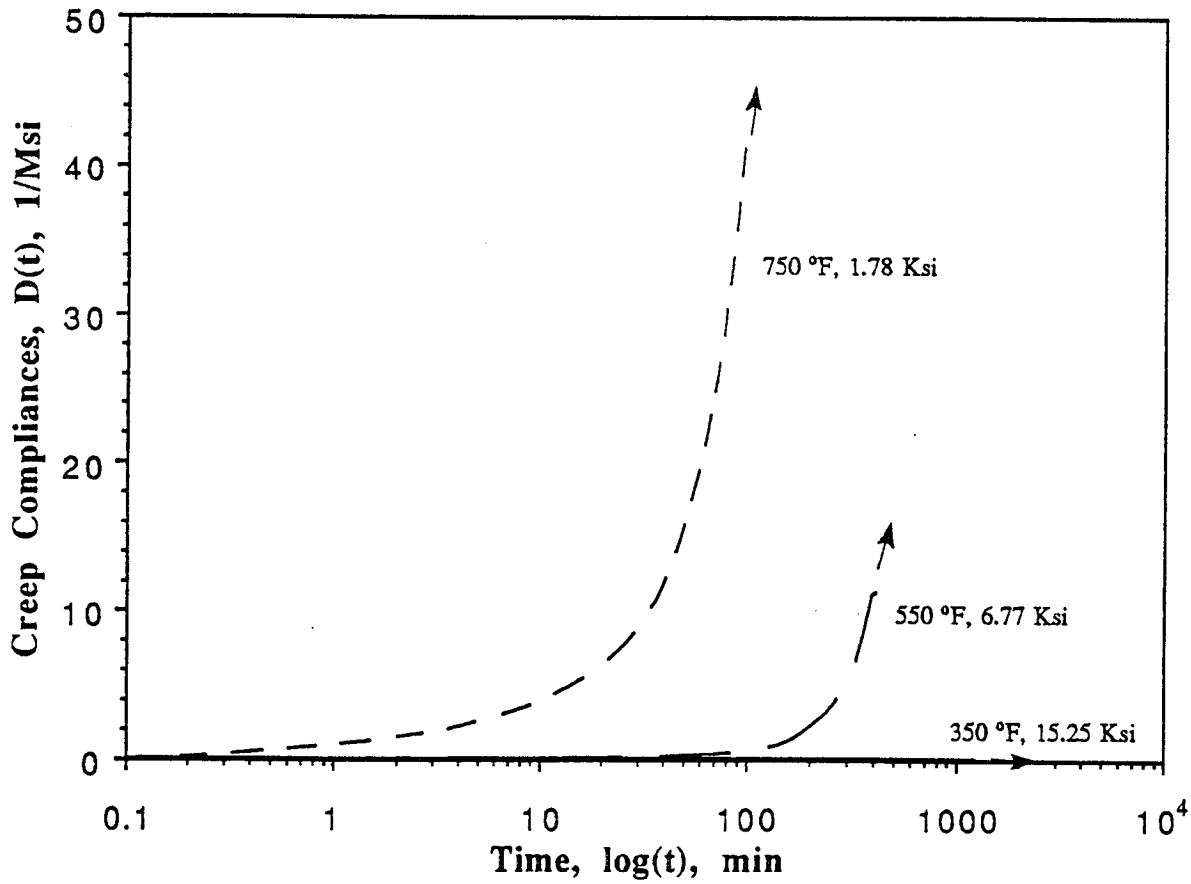

Fig. 4.20 Creep Compliances of Aluminum 6061-T4 at Three Different Temperatures

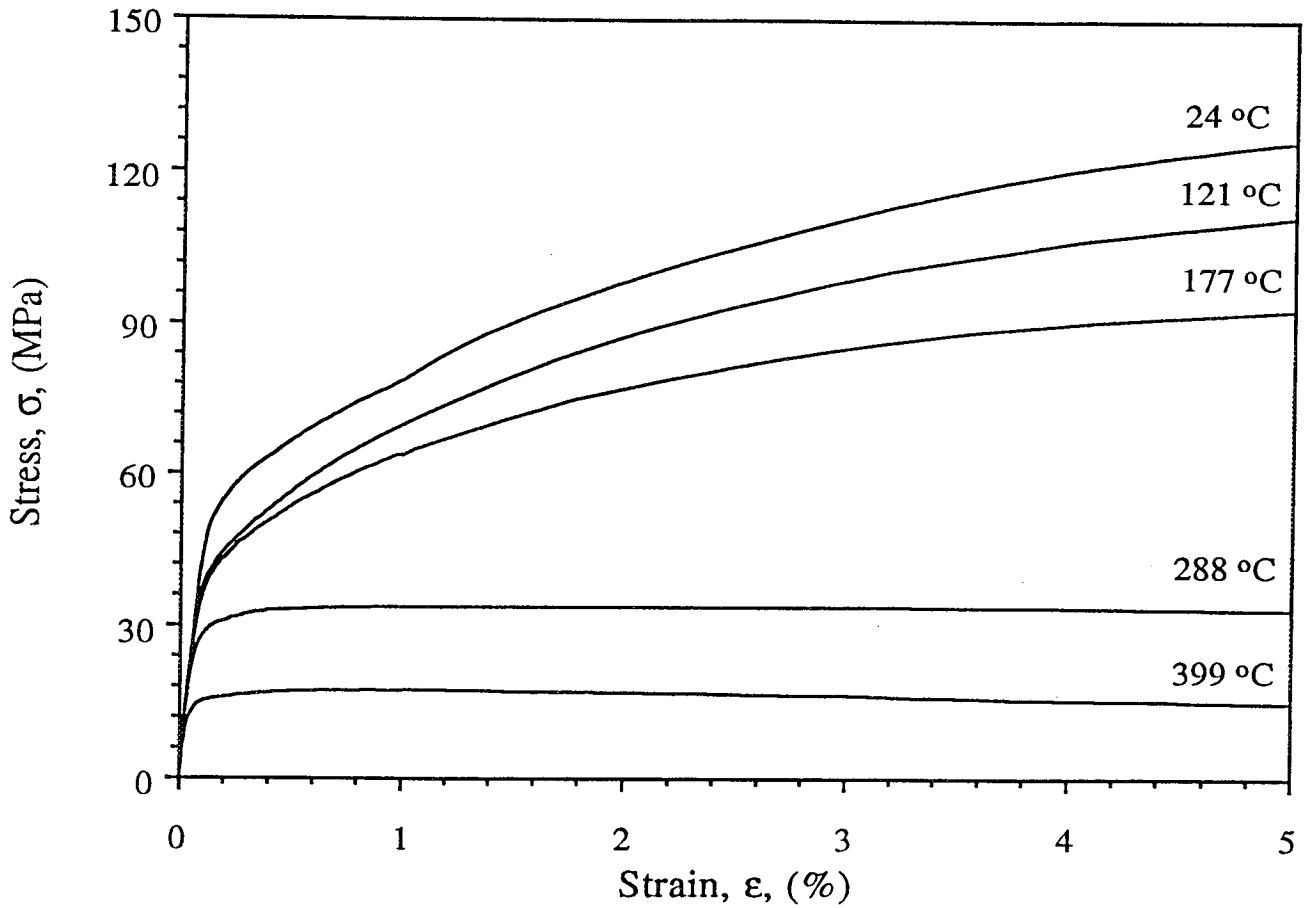

Fig. 4.21 Stress-strain Curves of 6061-0 Aluminum at Various Temperatures

discussed before and plotted versus temperature in Fig. 4.22. Properties of the annealed aluminum are summarized in Table 4.3. The yield stress and the tensile strength of the material at room temperature are 55.2 MPa (8 ksi) and 124.1 MPa (18 ksi), respectively.

Table 4.3 Properties of 6061-0 Aluminum

Temperature	Elastic Limit Stress σ_y, MPa (ksi)	Coefficient of Thermal Expansion, α 10^{-6}/° C (10^{-6}/° F)
24° C (75° F)	41.4 (6.0)	23.4 (13.0)
121° C (250° F)	39.3 (5.7)	23.6 (13.1)
177° C (350° F)	37.4 (5.4)	23.9 (13.3)
288° C (550° F)	33.1 (4.8)	24.8 (13.5)
399° C (750° F)	15.9 (2.3)	---

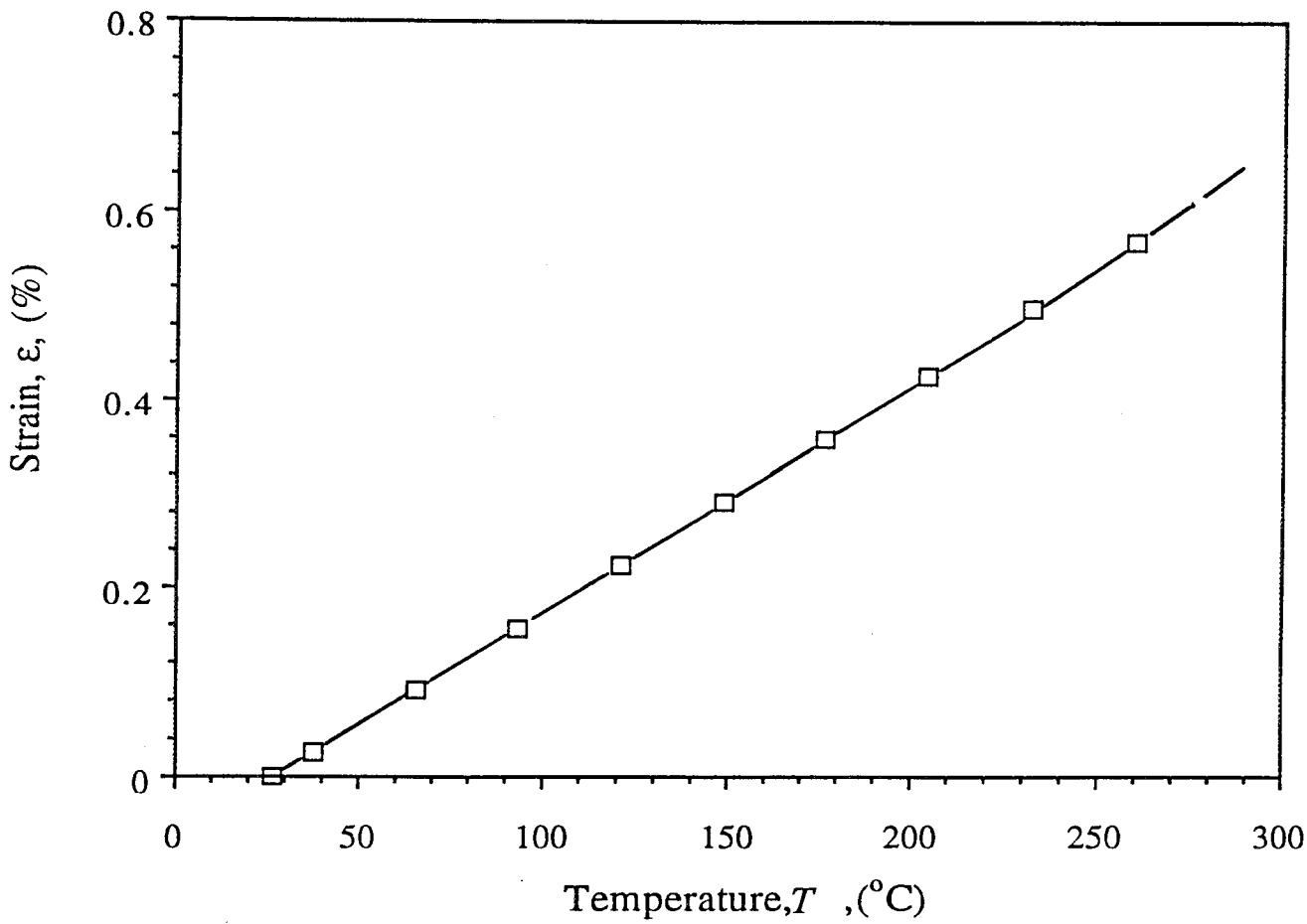

Fig. 4.22 Thermal Strain versus Temperature for 6061-0 Aluminum

5. THERMOMECHANICAL CHARACTERIZATION OF SILICON CARBIDE/ALUMINUM COMPOSITE

5.1 Specimen Geometry and Preparation

The material was obtained in the form of unidirectionally reinforced eight-ply 30.5 x 30.5 cm (12 x 12 in.) SCS-2/6061 Al plates. These plates were produced by using the diffusion bonding consolidation technique. Rectangular specimens 15.24 cm (6 in.) long, 1.27 cm (0.5 in.) wide and 1.42 mm (0.056 in.) thick were cut from these plates with a water-cooled thin diamond saw. The specimen design is shown in Fig. 5.1. Longitudinal specimens were cut with the long dimension parallel to the fibers and transverse specimens were cut perpendicular to the fiber orientation. The test coupons were lightly sanded with silicon carbide 340 grit sand paper and then tabbed along two opposite sides with 2.54 x 1.27 x 0.122 cm (1 x 0.5 x 0.048 in.) strips of steel. The steel tabs were bonded onto the specimen grip sections using a high strength-high temperature adhesive (FM-36, American Cyanamid Co.). The function of the tabs is to provide a cushion between the rough grip surface and the specimen surface to prevent any damage to the specimen material. The tab length was long enough to provide a shear area large enough to transfer the load to the specimen.

The specimens were instrumented with WK gages (Micro Measurements Group) for temperatures up to 288° C (550° F) and RKO gages (J. P. Technology) for testing at 399° C (750° F). In addition to the strain gages, high temperature extensometers (Instron and MTS) were used.

5.2 Physical Characterization

The density of the material was determined by the immersion method described in ASTM specification D792-66. It was found to be 2.86 g/cm^3 (0.1033 lb/in^3).

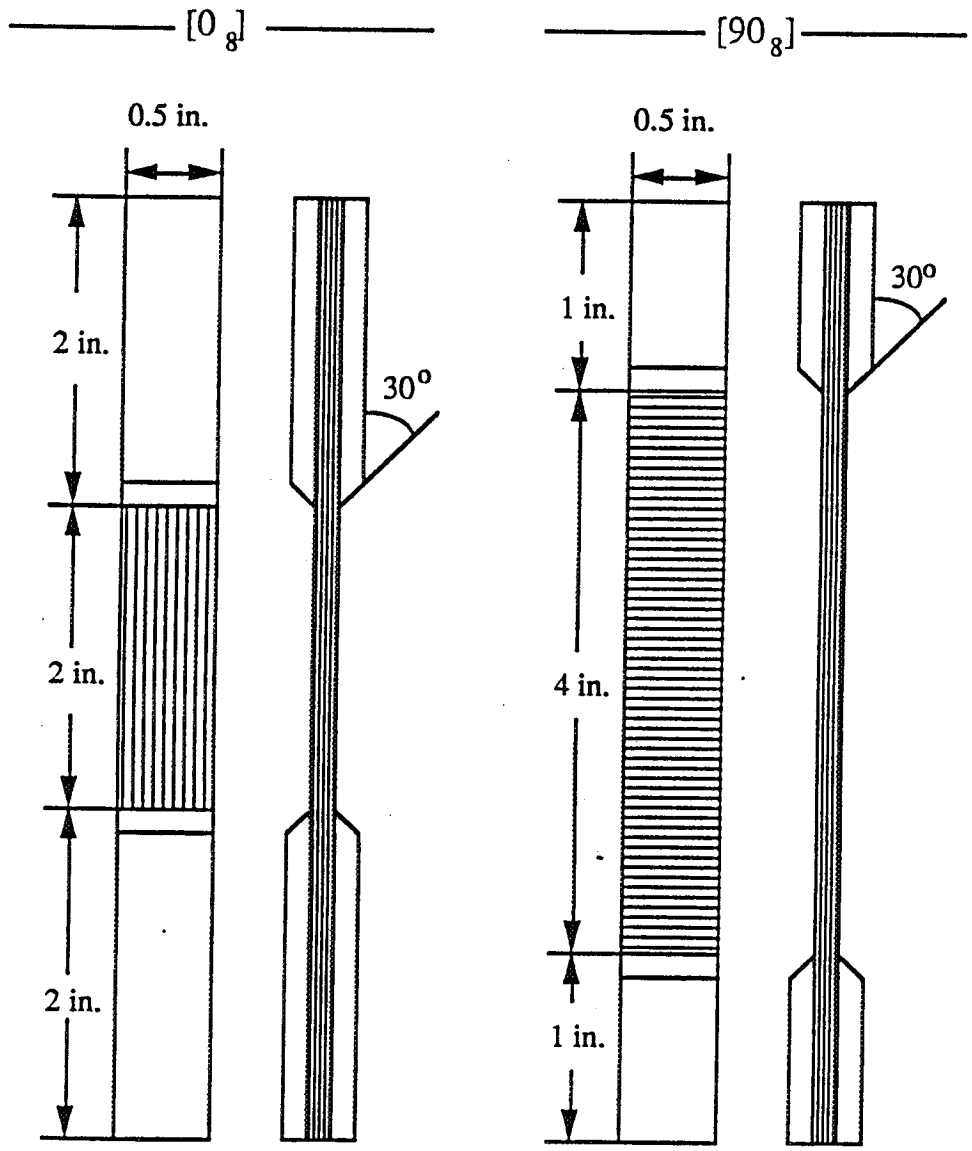

Fig. 5.1 Specimen Geometries.

The fiber volume ratio was determined by analyzing photomicrographs of transverse sections of the composite (Fig. 5.2). It was determined by two methods. In the first method the total area of fiber cross sections was measured and divided by the total area of the region covered. In the second method a number of lines are randomly drawn on the photomicrograph. The fiber volume ratio, V_f, is determined as the ratio of the cumulative length of the fiber intersections along the lines to the total length of the lines drawn. The result obtained by these two methods is

$$V_f = 0.44$$

A unidirectional specimen of the composite was subjected to thermal loading in order to determine the thermal expansion coefficients along the longitudinal (α_1) and transverse (α_2) directions. Unidirectional 8-ply specimens of dimensions 15.2 x 12.7 cm (6.0 x 0.5 in.) were instrumented with EA-00 and WK-00 type gages (Micromeasurements Group) for temperature cycling up to 177° C (350° F) and 288° C (550° F), respectively (Fig. 5.2). Three thermocouples per specimen were used to measure temperature. A programmable press (MTP-14, Tetrahedron) was used to control the temperature increments. The specimens were thermally cycled between room temperature and 177° C (350° F) or 288° C (550° F), for the two types of gages. Longitudinal and transverse strains and temperature readings were recorded at 14° C (25° F) intervals using a BC-8SSG strain gage bridge conditioner (KAYE Instruments) and a data logger. Strains were recorded only when all three thermocouples on the same specimen exhibited the same temperature reading. The true thermal strains were obtained by subtracting the pure thermal output by means of the reference specimen method described before [49,50]. The true longitudinal and transverse strains were then plotted versus temperature and are shown in Figures 5.3 and 5.4. The thermal expansion coefficients α_1 and α_2 were obtained from the slopes of the corresponding thermal strain versus temperature curves.

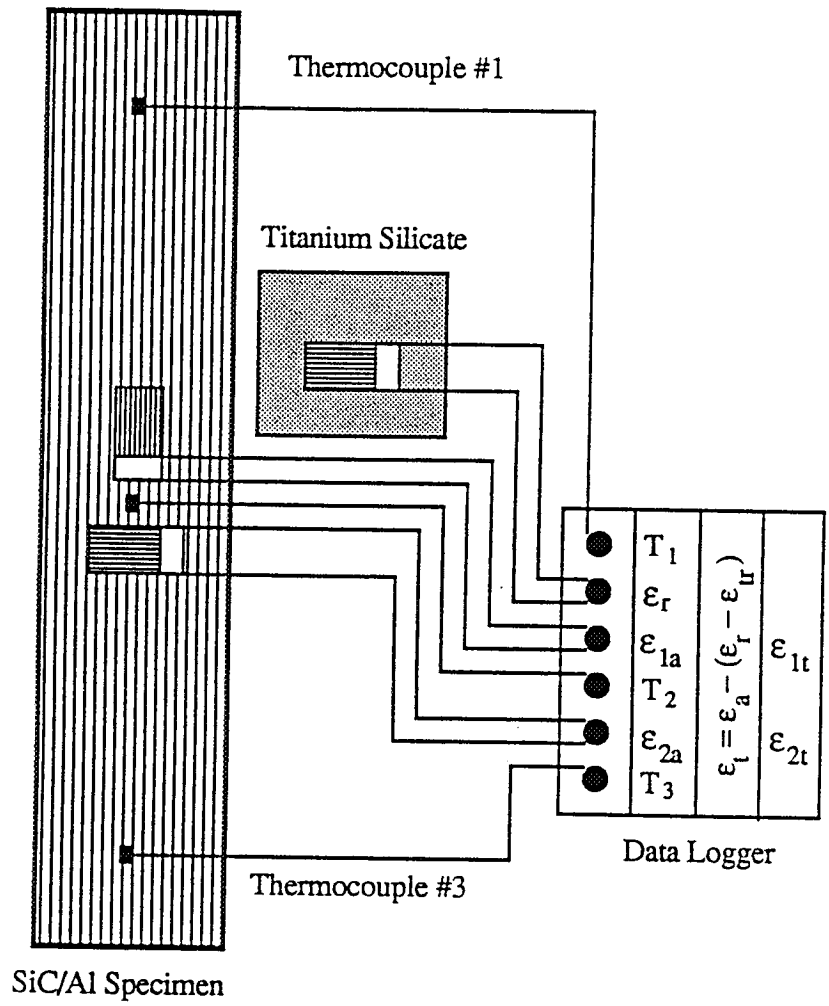

Fig. 5.2 Schematic Representation of a Unidirectional SiC/Al $[0_8]$ Specimen along with a Titanium Silicate Reference and a Data Logger Used for Measuring the Coefficients of Thermal Expansion along the Two Principal Directions of the Composite by Means of Strain Gages.

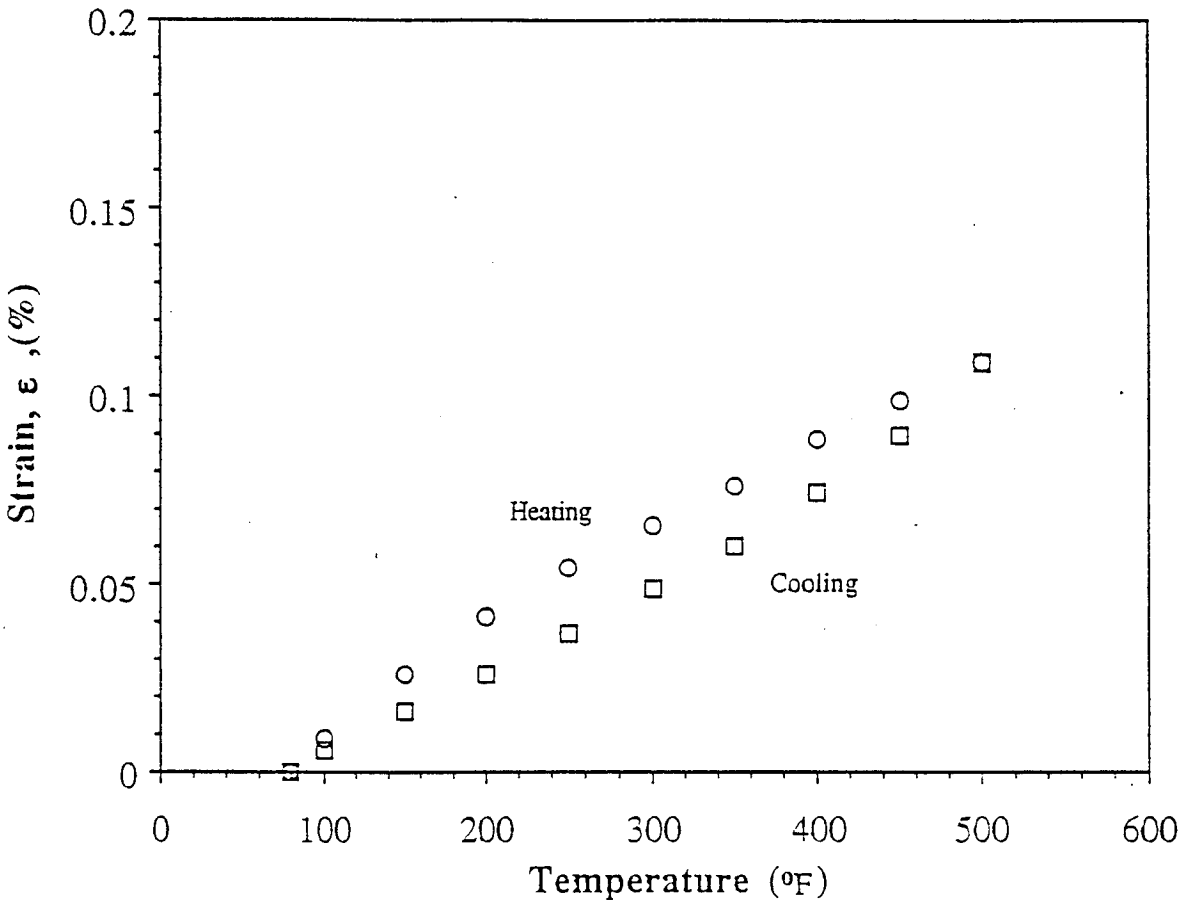

Fig. 5.3 Longitudinal Thermal Strain versus Temperature of SiC/Al Composite

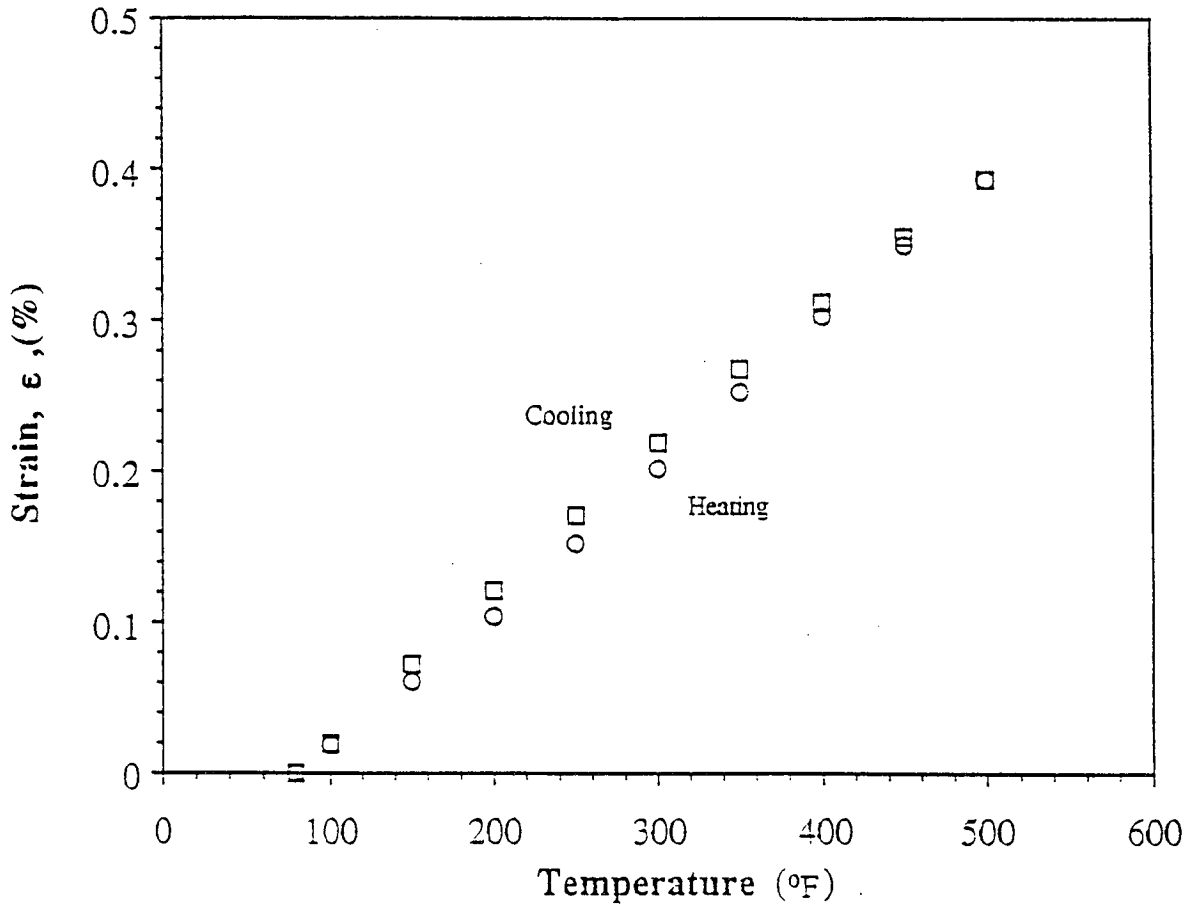

Fig. 5.4 Transverse Thermal Strain versus Temperature of SiC/Al Composite

In a second type of experiment, longitudinal and transverse thermal strains were obtained for temperatures up to 482° C (900° F) using a dilatometer. Special cylindrical specimens 10 mm (0.39 in.) long and 3 mm (0.12 in.) in diameter were used. For this purpose three layers of composite plate were first glued together to produce sufficient thickness for preparation of the cylindrical specimens. The longitudinal and transverse thermal strain curves are shown in Fig. 5.5. The results of the two types of experiments are in agreement over the common temperature range.

From Fig. 5.3 it is observed that the longitudinal thermal strain varies nonlinearly with temperature, with a decreasing rate as the temperature increases. This corresponds to a gradually decreasing longitudinal coefficient of thermal expansion with increasing temperature. This behavior is attributed to yielding of the aluminum matrix with decreasing amount of strain hardening. The transverse thermal strain displays the opposite behavior increasing at a faster rate as the temperature increases. This corresponds to a gradually increasing transverse coefficient of thermal expansion with increasing temperature.

For both longitudinal and transverse thermal strains a "hysteresis loop" is observed when the specimen is thermally unloaded down to room temperature. The hysteresis loop is more pronounced for the longitudinal thermal strain. This behavior may be explained, qualitatvely, by the following series of events. During the initial heat up from room temperature both fiber and matrix expand linearly. At higher temperatures the matrix yields under compression, the expansion becomes strongly influenced by the fiber, and the composite coefficient of thermal expansion decreases. The matrix continues to yield up to the maximum temperature of the cycle. On cool down from the maximum temperature the fiber and the matrix are unloaded linearly elastically until the matrix yields under tension. As the matrix yields the expansion is primarily influenced again by the fiber response. On the

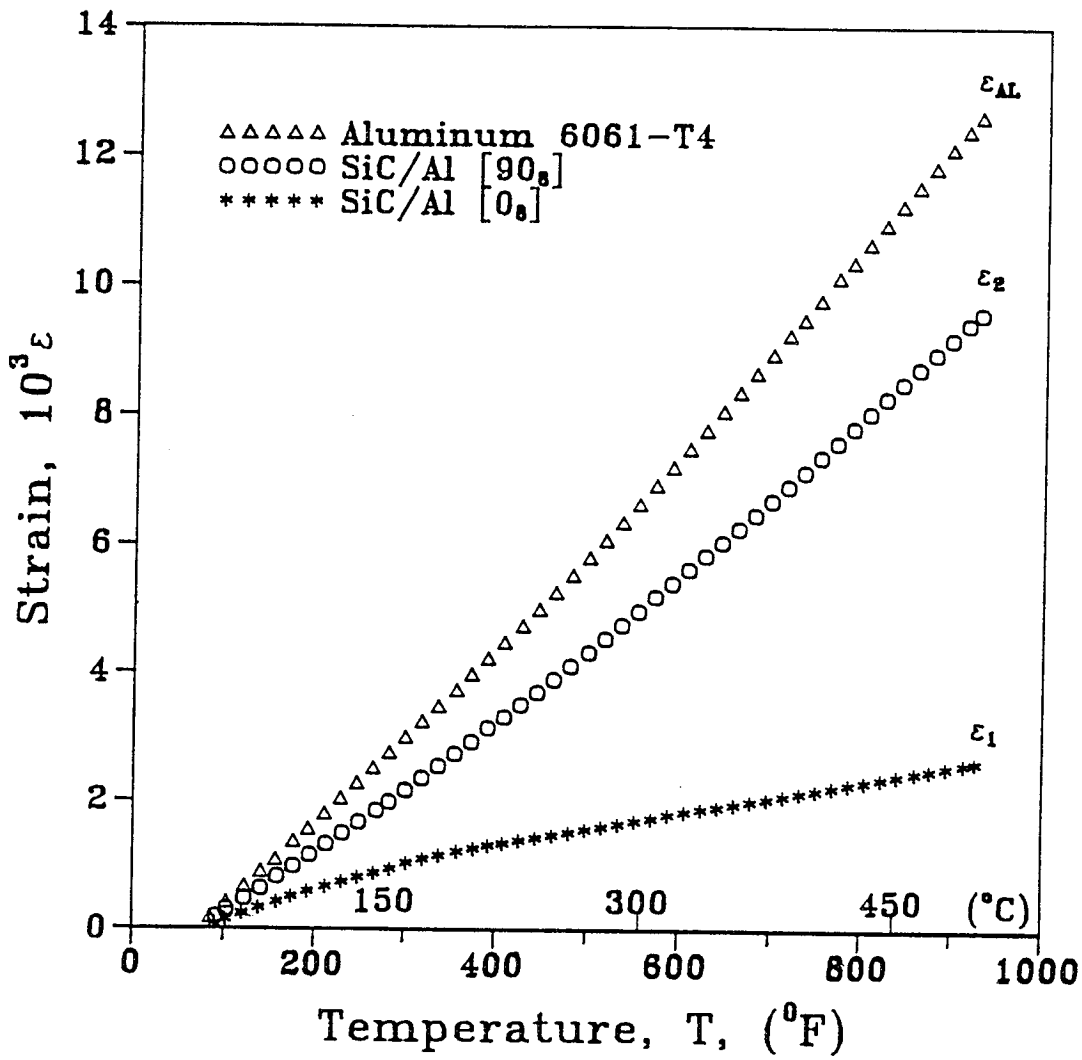

Fig. 5.5 Strain versus Temperature Curves of SiC/Al Composite along the Fiber and Transverse to the Fiber Direction as Obtained by the Dilatometer.

other hand, the transverse thermal expansion is mainly controlled by the matrix behavior, resulting in a smaller hysteresis loop. The reduced hysteresis in the transverse direction is due to the fact that it is influenced by the product of Poisson's ratio and the change in longitudinal coefficient of thermal expansion. Furthermore, it was found that when the same cycle of thermal loading and unloading was repeated several times the same loop was reproduced.

5.3 Mechanical Characterization

Standard characterization tests were conducted on the unidirectional lamina to determine the following properties at various temperatures:

- Longitudinal Modulus, E_1
- Transverse Modulus, E_2
- Major Poisson's Ratio, ν_{12}
- Minor Poisson's Ratio, ν_{21}
- Longitudinal Tensile Strength, F_{1t}
- Ultimate Longitudinal Tensile Strain, $\varepsilon^u{}_{1t}$
- Transverse Tensile Strength, F_{2t}
- Ultimate Transverse Tensile Strain, $\varepsilon^u{}_{2t}$

The minor Poisson's Ratio can be determined by

$$\nu_{21} = \nu_{12}\frac{E_2}{E_1} \tag{5.1}$$

A high temperature testing facility was used for thermomechanical characterization of the SiC/Al metal matrix composite. The testing facility consists of an Instron 1331 Servo-hydraulic Testing System with a 22,480 lb tension compression load cell, Instron 8500 Controller, a 20 gpm capacity hydraulic pump and an ATS (Applied Test Systems, Model 3620) split box type oven with a view-port and temperature range of -155 to 425° C (-250° to 800° F) controlled by ATS series 2010 controller.

A standard test procedure, which includes specimen preparation, testing, and data reduction was followed for each test to promote reproducibility. Particular care was taken in aligning the upper and lower grips. The alignment was checked by loading an aluminum specimen in the elastic region. The specimen was equipped with single strain gages. The alignment was considered acceptable when the values of the three strains were within 2.5% of the average strain.

ATS high temperature grips were used with water cooled rods (Series 4043, ATS) which were mounted on the load cell through a double knife- edge alignment coupling (Series 4021, ATS). The double knife - edge alignment coupling was implemented in the assembly to minimize specimen bending moment caused by misalignment due to eccentric pull rods. The water cooled rod was installed to protect the load cell from heat conduction directly from the grips. In addition, the load cell was covered with insulating material and shielded with an insulating square plate wrapped with aluminum foil to cut down heat convection and radiation from the oven. Two large fans were also installed on top of the oven to blow away the heat and cool the loadcell. Figure 4.8 shows a schematic diagram of the elevated temperature tensile test system.

The strain gage output is conditioned through a Wheastone bridge conditioner (BC-8SG, KAYE Instruments Inc.) amplified and then recorded by a data acquisition system (Metrabyte Corp.). Axial strains are also double checked by a water cooled high temperature extensometer (2630 Series, Instron) with a 1 in. gage length and operating temperature range of 15° C to 500° C (59° F to 930° F). The acquired data were transferred to a microcomputer and stored on a floppy disk. For the high temperature tests, temperature induced effects were nulled out by adjusting the output of the bridge conditioner or putting a dummy gage on an identical but unloaded reference specimen placed inside the environmental chamber and subtracting the temperature effect by connecting the dummy gage to an adjacent

arm of the Wheastone bridge. In the case of the extensometer, the thermal effect was nulled out by balancing the 8500 Controller (Instron) strain output at the test temperature. When the specimen was heated to the test temperature, it was loaded to failure and outputs were recorded by the data acquisition system as the net induced mechanical strain. The temperature of the specimen was sensed by a K-type thermocouple (Chromel - Alumel) attached to the specimen surface with high temperature ceramic adhesive or Kapton tape. The cement and Kapton tape provide some shielding of the thermocouple from the heat. All specimens were held at the test temperature for 15 minutes to assure a uniform temperature throughout the specimen then pulled at the desired rate. The tensile tests were carried out in the Instron at a constant stroke rate of 0.06 in./min up to specimen failure. Experiments were carried out at room temperature, 288° C (550° F) and 399° C (750° F). The high temperature tests were conducted in the ATS oven which was controlled to within 0.6° C (1° F).

The testing procedure was as follows:

1. Measure the width and thickness of the flat specimen at several points and average them.
2. Place the specimen in the grips of the testing machine and carefully align specimen and grips using spacers.
3. For elastic modulus determinations attach the extensometer or strain gage leads to the strain recording equipment. Make a preliminary check of settings and adjust the amplification scale.
4. Check the control settings and cross head speed on the Instron 8500 Controller panel.
5. Heat the oven to the desired temperature and keep that temperature stable for uniformity.

6. Start applying load and continue up to specimen failure and record the load and strain.

Typical stress-strain curves for the unidirectional reinforced composite tested parallel (0°) and perpendicular 90°) to the direction of the reinforcement are shown in Figures 5.6 to 5.9. There are several interesting features of these stress-strain curves which deserve special consideration.

When the 0° curve is carefully examined, three distinct regions are noted (Fig. 5.10). On initial application of the tensile load, both matrix and fiber respond completely elastically (Stage I). Eventually, the yield strength of the matrix is exceeded and the matrix begins to flow plastically (Stage II). In this stage the matrix contributes little to the elastic modulus. The slope of the stress-strain curve in this region is referred to as the system's secondary modulus and was measured to be 83% of the initial modulus. The system experiences permanent deformation because of matrix flow and breakage of severely weakened filaments. This second stage continues until fiber breakage is encountered, whereupon the slope of the stress-strain curve is again observed to decrease (Stage III), eventually resulting in composite failure. Because of the extreme brittleness of the fibers in the composite, the extent of Stage III is limited. In cases where the yield strain of the matrix exceeds the failure strain of the fiber, Stage II-type behavior will not be observed. The transition from Stage I to Stage II depends on the yield strain of the metal matrix and the magnitude of residual consolidation stresses. The three stages of strain response to increasing tensile loading can be termed as "elastic-elastic" (Stage I), "elastic-plastic" (Stage II) and "plastic-plastic" (Stage III), respectively [52].

Figures 5.6 and 5.7 show stress-strain curves for the SiC/Al composite at room temperature, 24° C (75° F), and at 288° C (550° F). Both curves exhibit a linear elastic portion that extends up to strains $\varepsilon = 0.12$ percent and 0.07 percent, for temperatures of 24° C and 288° C, respectively. Note that the stress-strain

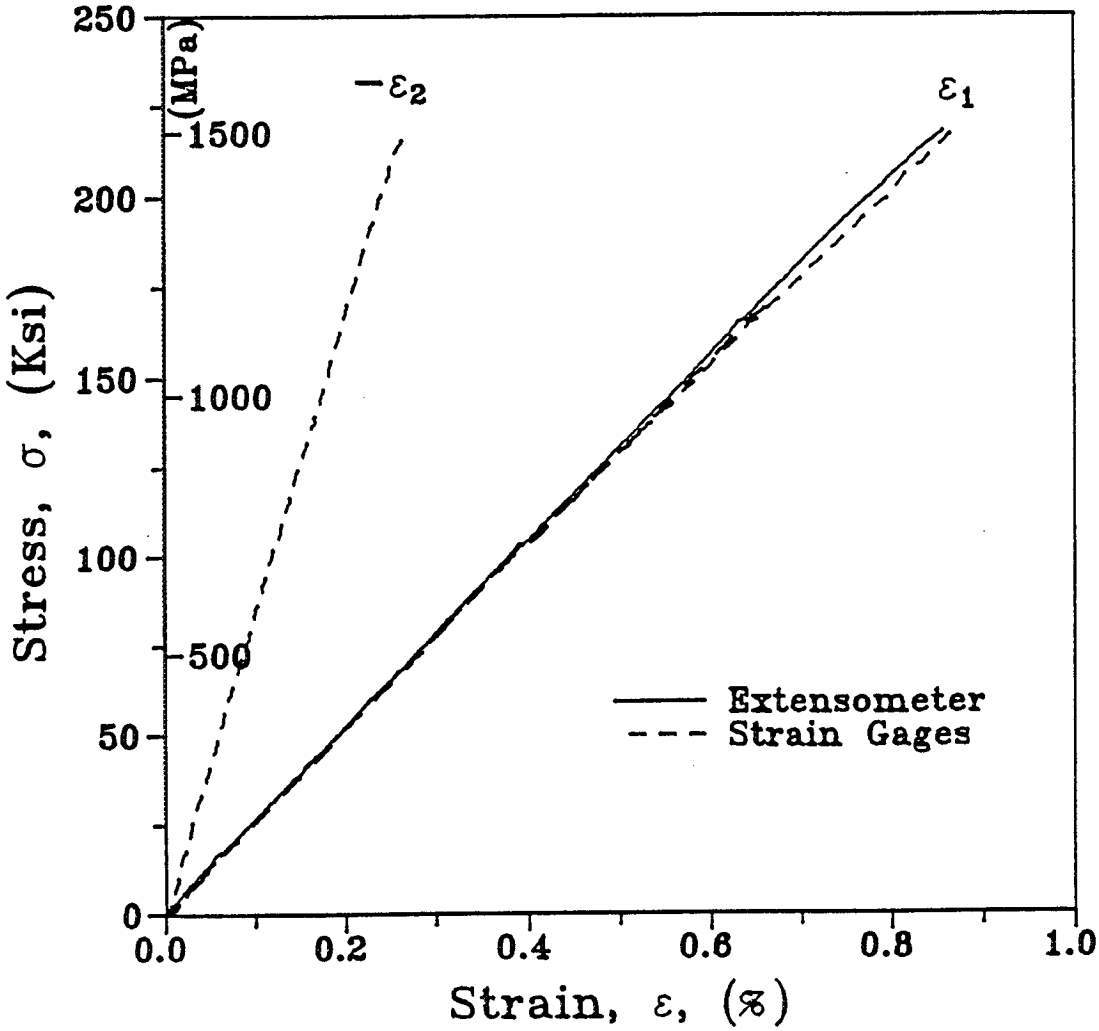

Fig. 5.6 Stress-Strain Curves for [0_8] SCS-2/6061 Aluminum Composite Specimen Under Tensile Loading at 24 °C (75 °F).

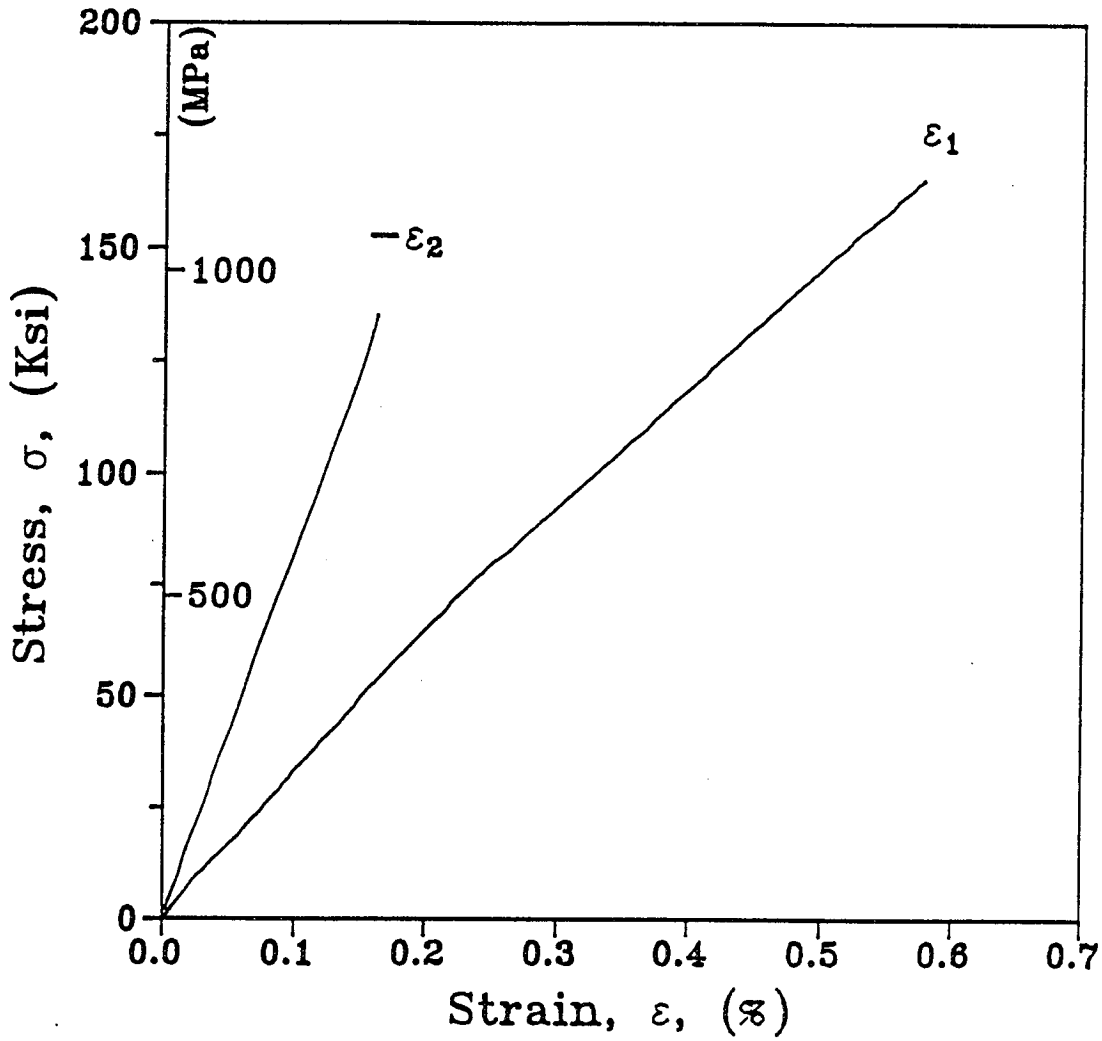

Fig. 5.7 Stress-Strain Curves for $[0_8]$ SCS-2/6061 Aluminum Composite Specimen Under Tensile Loading at 288 °C (550 °F).

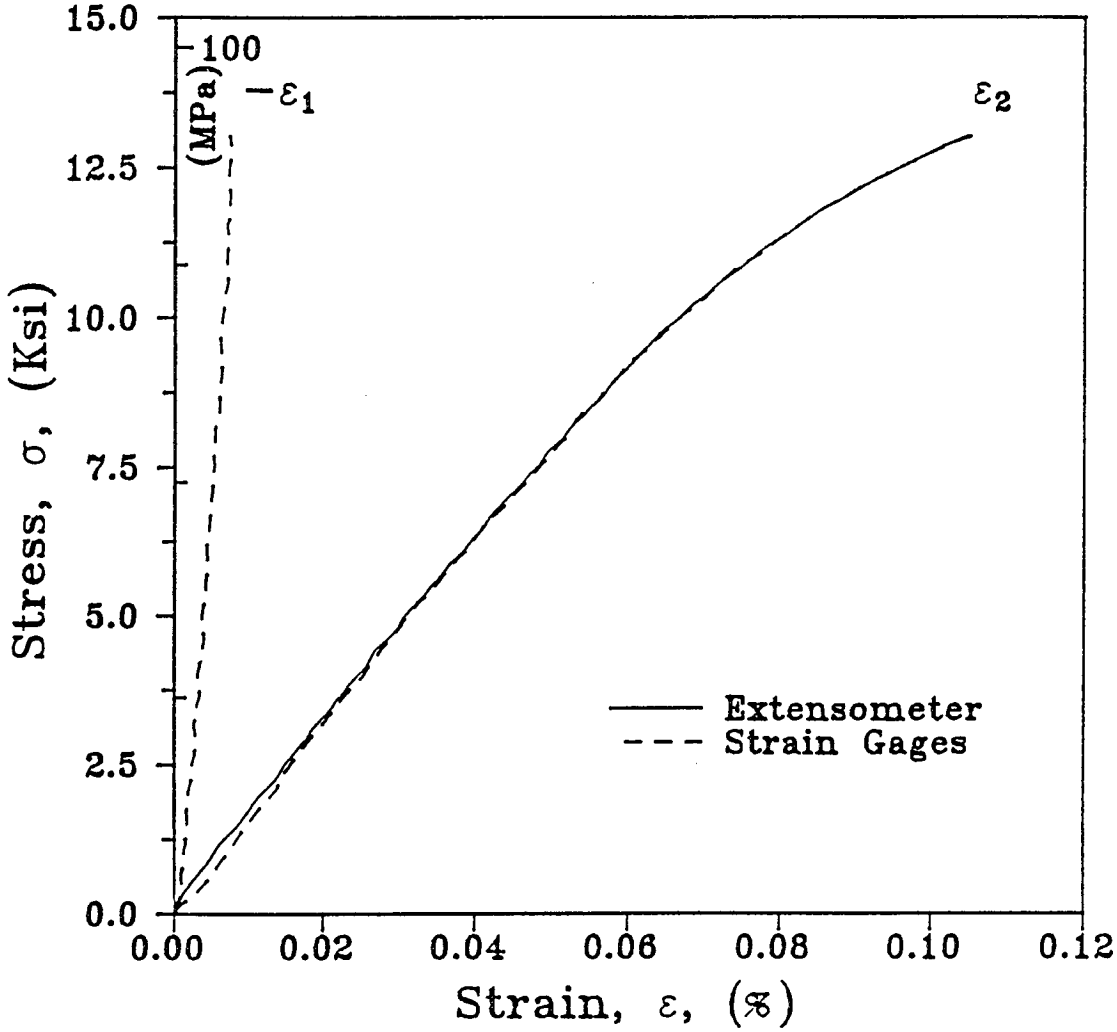

Fig. 5.8 Stress-Strain Curves for [90_8] SCS-2/6061 Aluminum Composite Specimen Under Tensile Loading at 24 °C (75 °F).

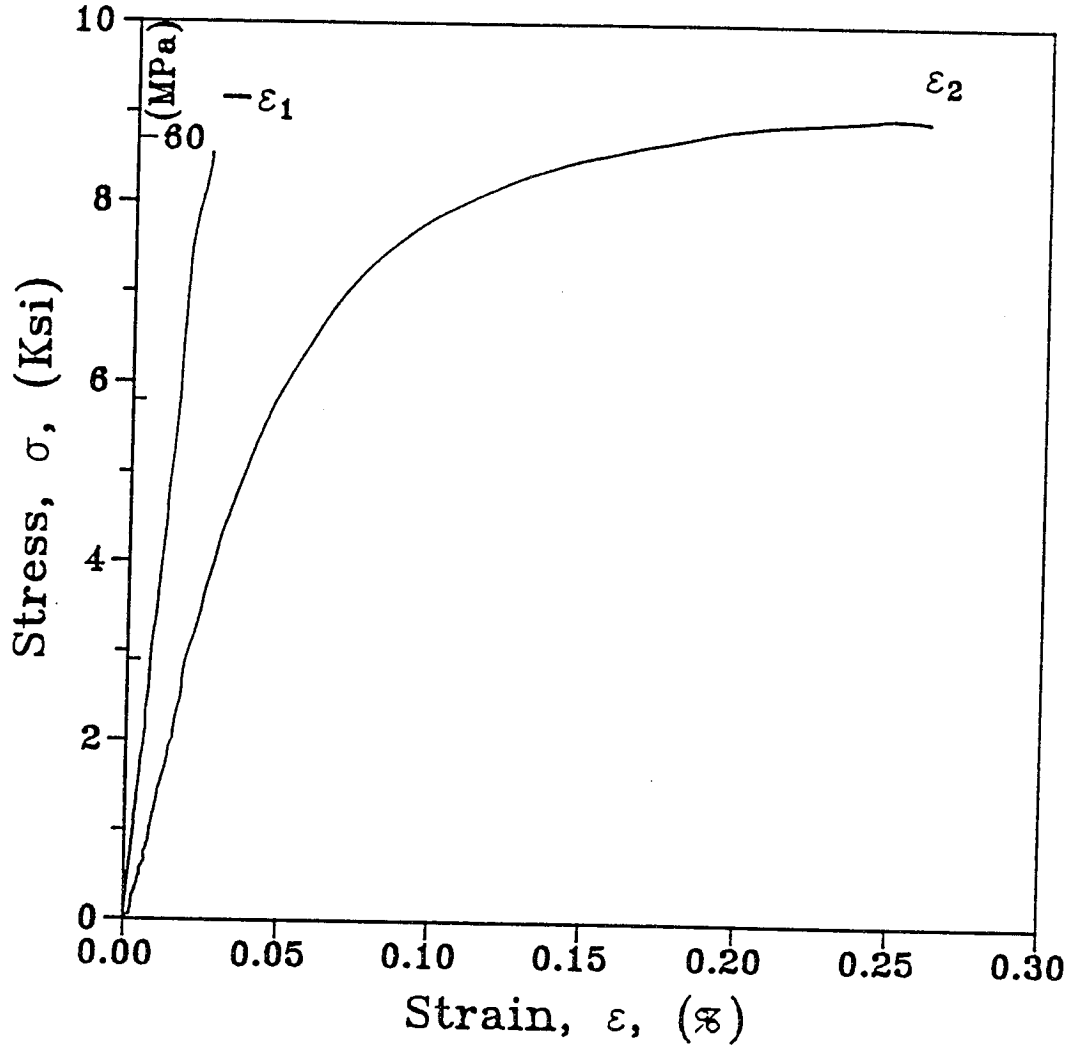

Fig. 5.9 Stress-Strain Curves for [90_8] SCS-2/6061 Aluminum Composite Specimen Under Tensile Loading at 288 °C (550 °F).

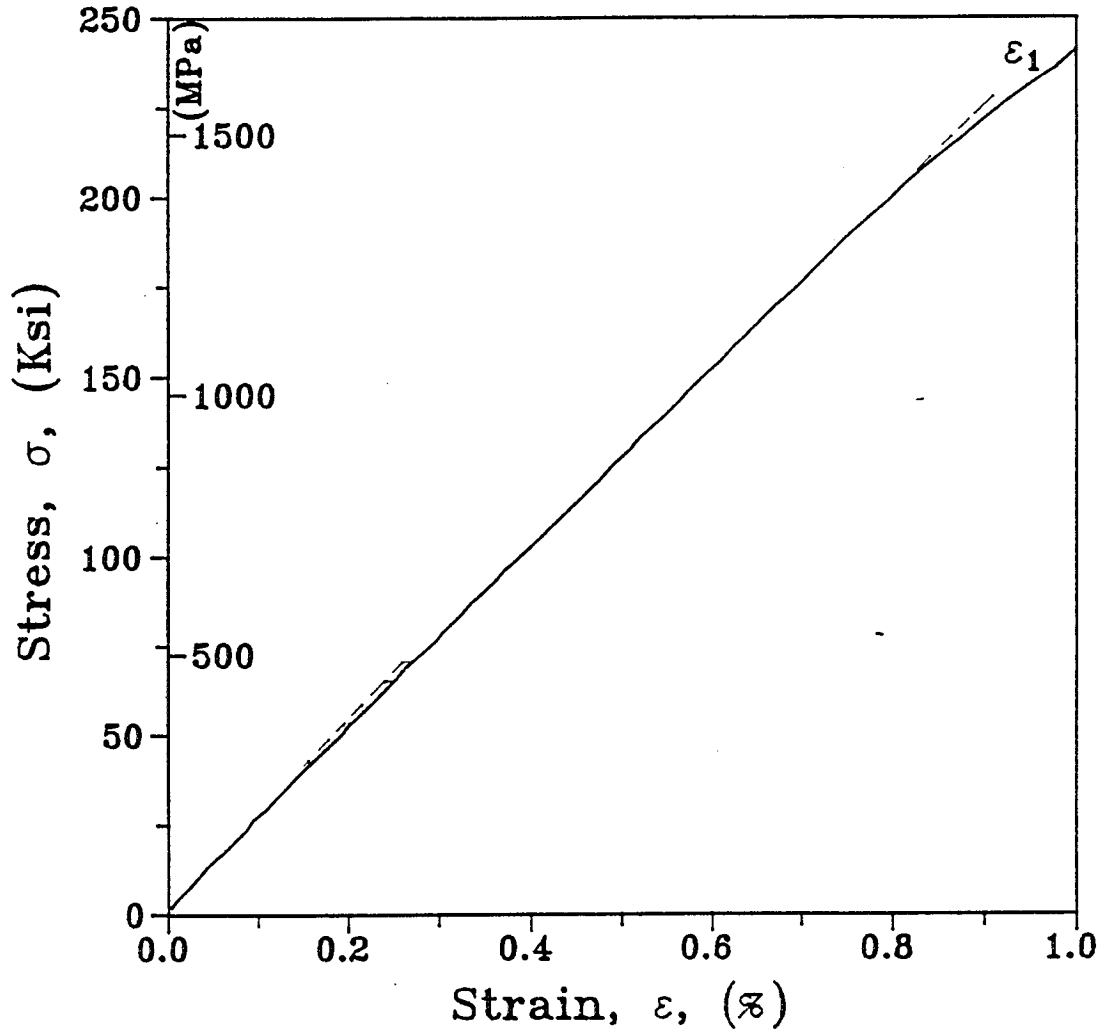

Fig. 5.10 Stress-Strain Curves for [0_8] SCS-2/6061 Aluminum Composite Specimen Under Tensile Loading at 24 °C (75 °F) Showing Three Regions.

curves up to failure deviate little from linearity which is attributed to the fact that most of the applied load is carried by the fibers due to their much higher elastic modulus. The deviation from linearity is more pronounced at 288° C. The stress vs. transverse strain curve at 24° C and 288° C (Figures 5.6 and 5.7) are almost linear up to fracture. Figures 5.11 to 5.13 show scanning electron photomicrographs of the tensile fracture surface of unidirectional SCS-2/6061 aluminum composite specimens. Extensive fiber/matrix interface debonding is observed in the photographs. In addition, a large amount of fiber pullout is apparent, indicated by the number of empty fiber sites, since the pulled-out fibers did not remain intact after failure. A variety of fiber damage is observed, including fiber splitting, fiber shattering and pulled-out cores.

At room temperature the rule-of-mixtures prediction of 1531 MPa (222 ksi) for the composite tensile strength is very close to the experimentally obtained one of 1524 MPa (221 ksi). Furthermore, at 288° C (550° F) the predicted strength of the composite is 1463 MPa (212 ksi) and the experimental one 1241 MPa (180 ksi). It is seen that the observed composite strength at 288° C is lower than the rule-of-mixtures prediction. However, the direct application of filament tensile strength is often misleading [53], particularly at elevated temperatures where the chemical reactivity of the filament with the atmosphere or the metal matrix introduces an additional complexity.

The transverse properties of SiC/Al composite, tensile modulus, strength, and ductility, are all lower than longitudinal properties. The lower modulus and strength are in part due to the fact that the isostrain criterion no longer applies. That is the matrix is free to flow nearly independently of the fibers. Under these conditions it becomes more difficult to predict composite stiffness and strength. If the fibers are well bonded to the matrix and free of defects, the transverse strength should approach or exceed the strength of the bulk matrix alloy. Unfortunately,

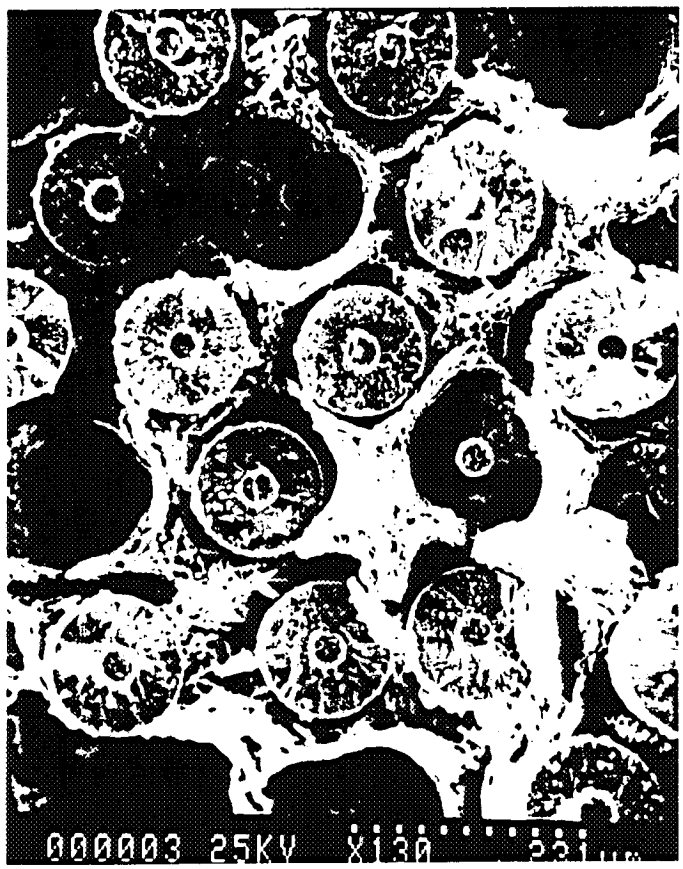

Fig. 5.11 Scanning Electron Photomicrograph of the Tensile Fracture Surface of $[0_8]$ SCS-2/6061 Aluminum Composite Specimen Showing Debonding at Fiber/Matrix Interfaces.

Fig. 5.12 Scanning Electron Photomicrograph of the Tensile Fracture Surface of $[0_8]$ SCS-2/6061 Aluminum Composite Specimen Showing Fiber Pullout.

Fig. 5.13 Scanning Electron Photomicrograph of the Tensile Fracture Surface of $[0_8]$ SCS-2/6061 Aluminum Composite Specimen Showing Fiber Damage.

these strength levels are not usually attained in SiC/Al composites at room temperature. The explanation for low transverse strength of SiC/Al composite seems to be related to the transverse strength of the fiber and partial debonding. If the fibers split and debond under transverse tensile loading at a low stress level, the load carrying cross section would be sharply reduced and stress concentrations would be introduced which would account for the observed low composite strength and ductility. Examination of the transverse tensile fracture surface establishes the degrading influence of fiber splitting and debonding. For a weak matrix, transverse failure is controlled by matrix strength and failure takes place predominantly through the matrix. If the matrix is solution treated and aged so that it can introduce higher loads into the fibers, transverse failure can be controlled by filament splitting and fracture occurs through fibers as in the case of SiC/Al composite. Also, the relative area of split filaments on the fracture surface is found to be larger than the V_f of the composite, which indicates that the fibers offer the least resistance to crack propagation and control of composite failure. Also, fiber splitting has been observed only at, or in the immediate vicinity of, the composite fracture surface. These observations reflect the susceptibility of aluminum alloy to severe stress concentrations associated with split SiC filaments and their probable low transverse strength. Also, the strength reduction can be attributed to structural imperfections or initial filament quality or consolidation technique.

The effect of temperature was further studied by conducting tests at 399° C (750° F). Longitudinal and transverse stress-strain curves at three test temperatures are shown in Figs. 5.14 and 5.15.

In-plane shear properties were obtained by means of the 10° off-axis test [50]. In-plane shear stress-strain curves at three different temperatures are shown in Fig. 5.16. The initial shear modulus is 34.5 MPa (5 Msi) or 33% higher than the shear modulus of 6061-T4 aluminum. The measured shear strength was

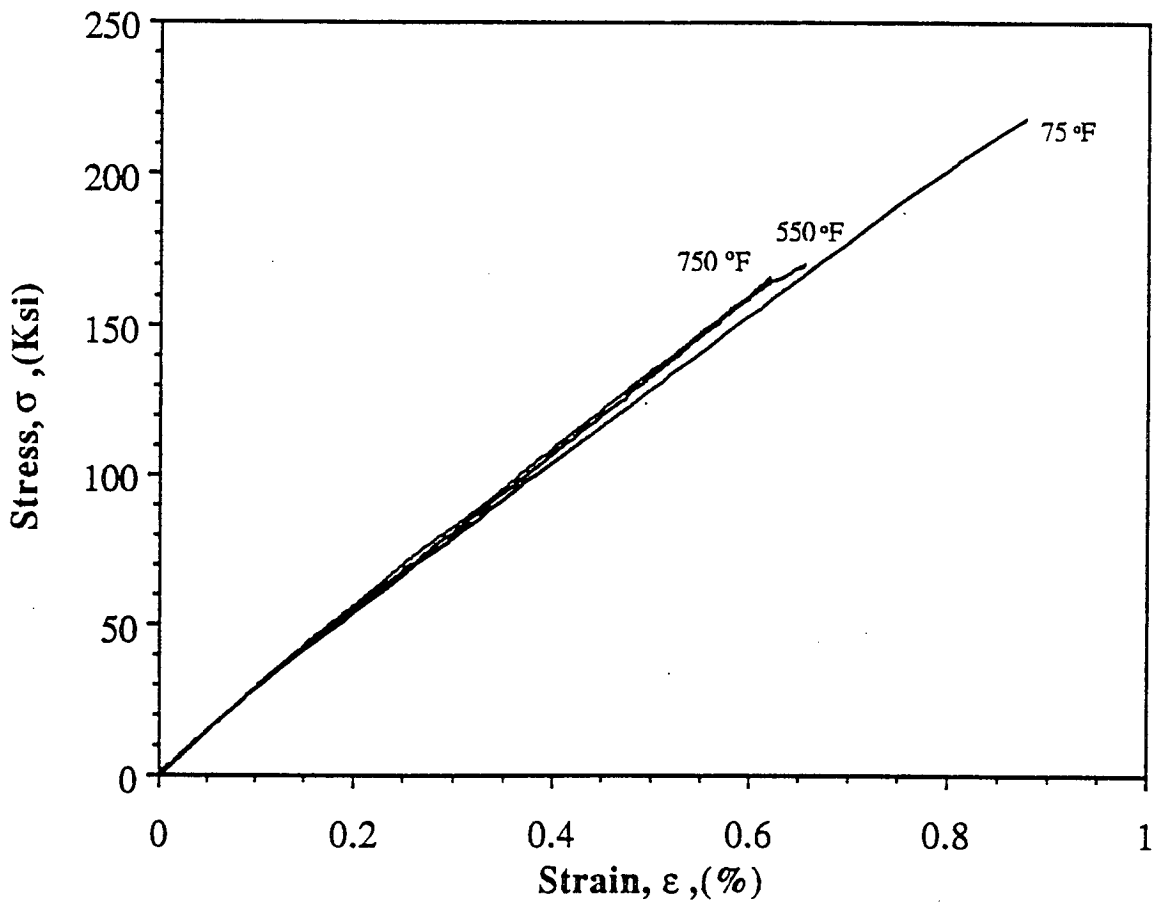

Fig. 5.14 Stress-Strain Curves of Unidirectional SiC/Al Composite Specimens under Longitudinal Tensile Loading at Various Temperatures

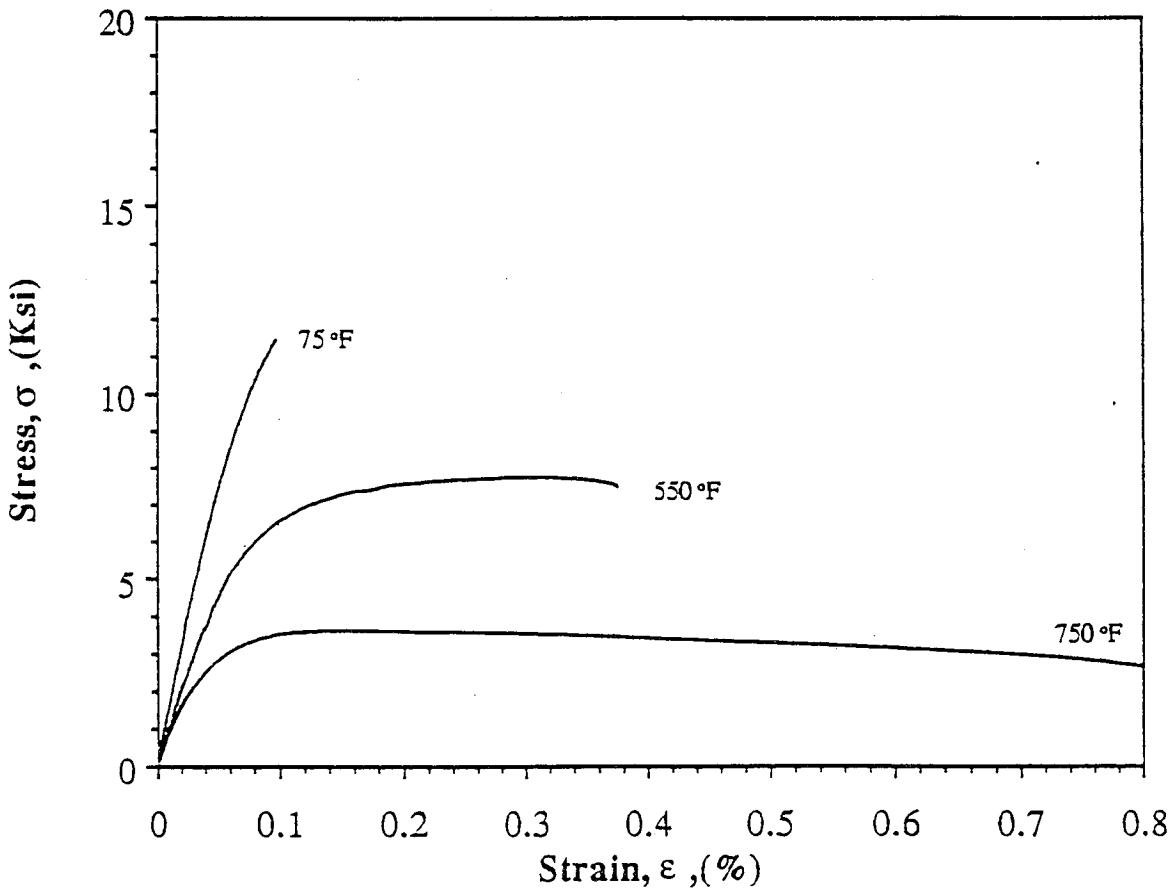

Fig. 5.15 Stress-Strain Curves of Unidirectional SiC/Al Composite Specimens under Transverse Tensile Loading at Various Temperatures

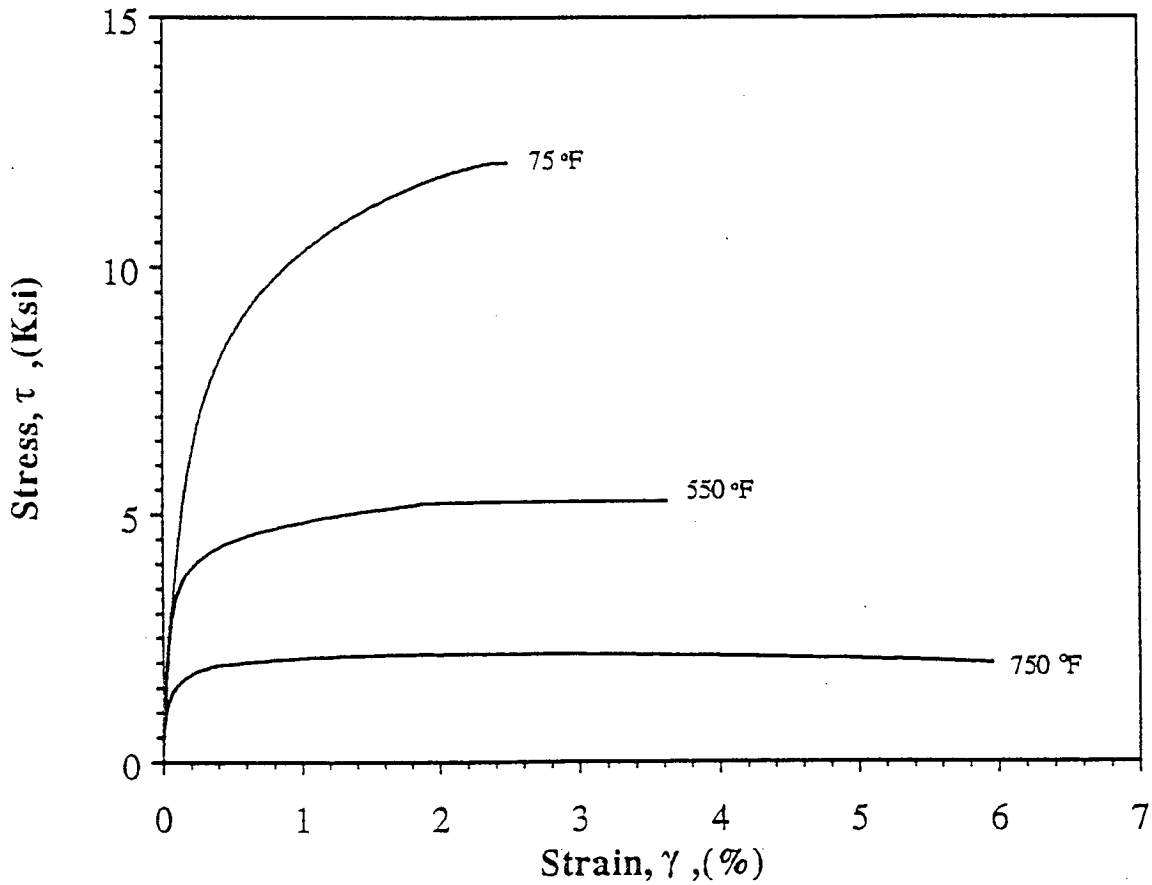

Fig. 5.16 In-Plane Shear Stress-Shear Strain Curves of SiC/Al Composite Specimens at Various Temperatures

approximately 51% lower than that of the matrix material. The fracture surface is parallel to the fiber, that is at 10° with the direction of loading. It indicates that the failure is dominated by debonding of the fiber under shear loading. This interfacial debonding reduces the shear loading cross section in the matrix, thus propagating the matrix crack to failure. If the fibers were perfectly bonded to the matrix without any defects, the shear strength of the composite would be close to the shear strength of the matrix assuming that the fiber has a higher shear strength than the matrix. The residual stress in the composite also plays a role in shear strength reduction.

Figure 5.17 shows the variation with test temperature of the longitudinal tensile strength of SiC/A*l* composite and aluminum for comparison purposes. It is seen that the composite retains its longitudinl strength exceptionally well up to 399° C (750° F). At higher temperatures the composite tensile strength is still much higher than that of the aluminum alloy. The observed composite strengths at high temperature are lower than the rule of mixtures prediction. This is due to the influence of residual stresses. Probably the strength reduction of the SiC fiber with temperature is the other cause, although this is not clear. As mentioned previously, the direct application of fiber tensile data to composite strength prediction is oftentimes quite misleading, particularly at high temperatures where the chemical reactivity of the fiber with the atmosphere or metal matrix introduces an additional complexity.

The temperature dependence of the transverse strength is shown in Fig. 5.18. The transverse strength drops more severely than the longitudinal strength with temperature because of the large reduction in strength of the matrix with temperature. Examination of the transverse tensile fracture surface of the specimen tested at 750° F shows less fiber splitting and debonding and more failure in the matrix, because at high temperatures the matrix becomes relatively weaker than at room temperature so that the transverse failure of the composite at high temperature

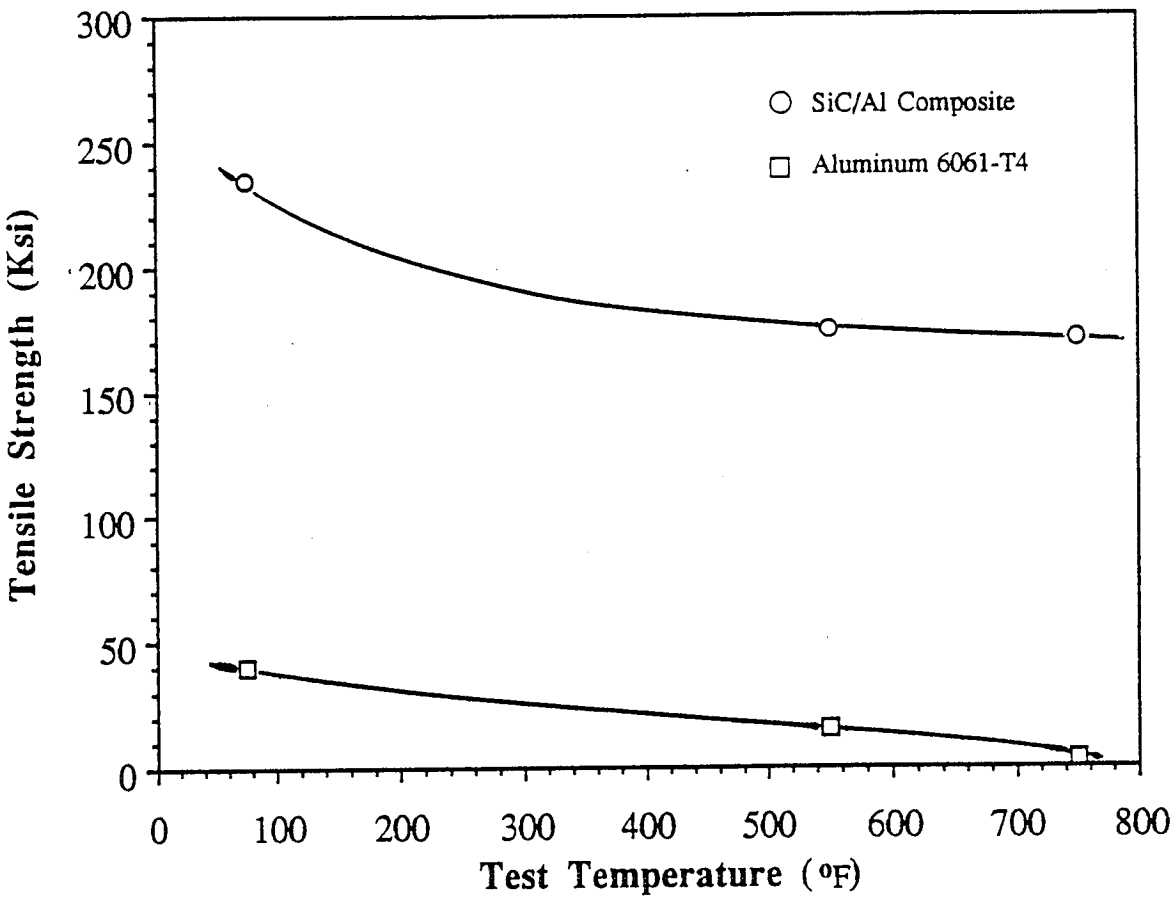

Fig. 5.17 Variation of Longitudinal Tensile Strength with Test Temperature for Unidirectional SiC/Al Composite and Aluminum 6061-T4

C-2

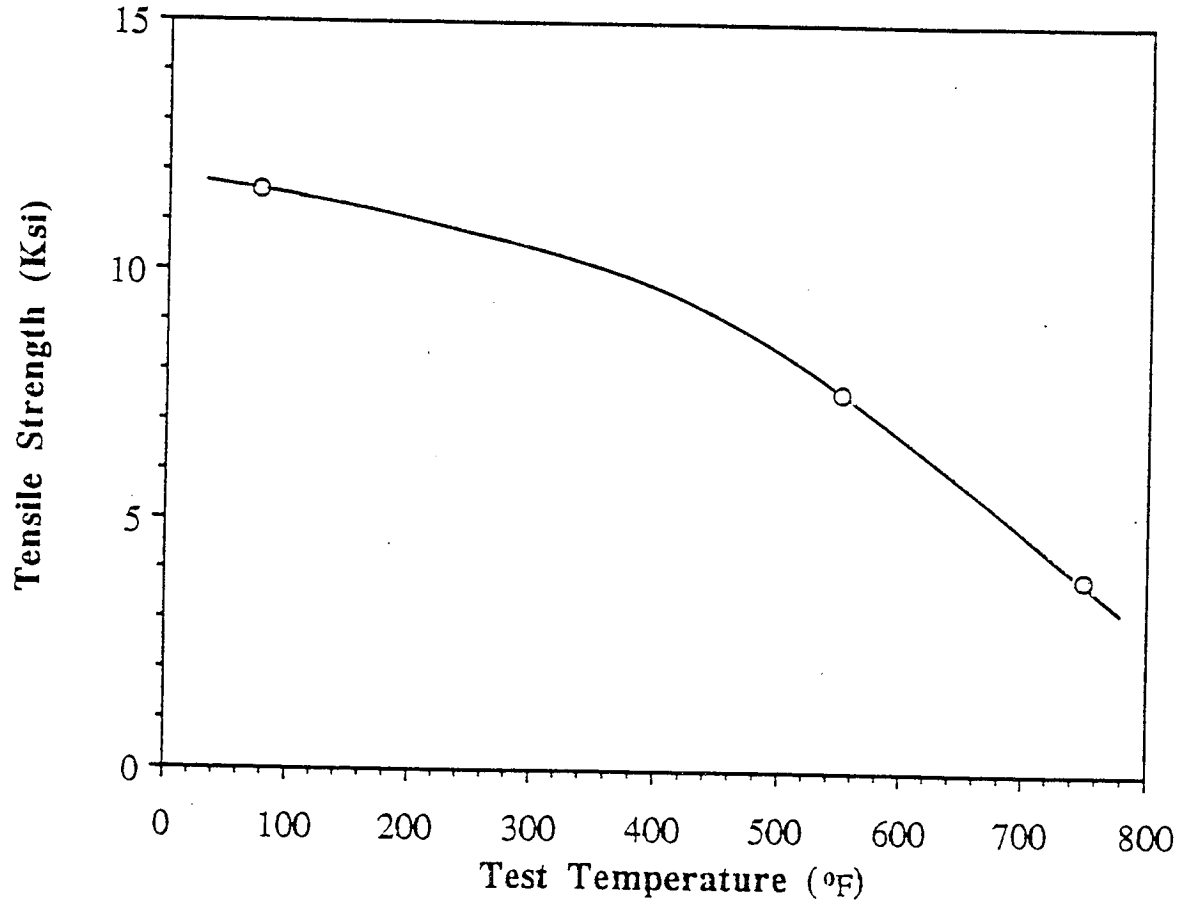

Fig. 5.18 Variation of Transverse Tensile Strength with Test Temperature for Unidirectional SiC/Al Composite

is more matrix deominated. At room temperature the transverse strength is only about 30% of that of the matrix but at 750° F it is very close to that of the matrix.

Figure 5.19 shows the change of in-plane shear strength with temperature. The in-plane shear strength drops very much with temperature somewhat similarly as the transverse strength because both of them are matrix dominated properties.

Not much change in the longitudinal modulus is observed. The initial modulus seems to remain stable with a little drop at 399° C (750° F), but the secondary modulus increased slightly at 288° C (550° F) which is probably associated with relief of residual stresses, both in the matrix and fiber, but this behavior is not clearly understood.

The transverse modulus drops gradually with temperature. Figure 5.20 shows the change of transverse modulus with test temperature. For perfect bonding of fiber and matrix the transverse modulus is expected to remain unchanged. But because of the temperature rise and the few hours of exposure to high temperature, the interfacial zone is extended by chemical reaction between fiber and matrix degrading the properties of the interface. This causes the drop in transverse modulus.

Figure 5.21 shows the shear modulus change with temperature. The initial shear modulus of the composite remains almost unchanged with temperature. The shear modulus of the fiber is unknown but from the above result it seems that the shear modulus of the fiber changes very little with temperature.

Table 5.1 summarizes the measured mechanical properties of SiC/A*l* composite at three different temperatures.

5.4 Creep Behavior

Creep tests on unidirectional SiC/A*l* composite were conducted in a similar manner as in the case of 6061-T4 aluminum described earlier. For the composite

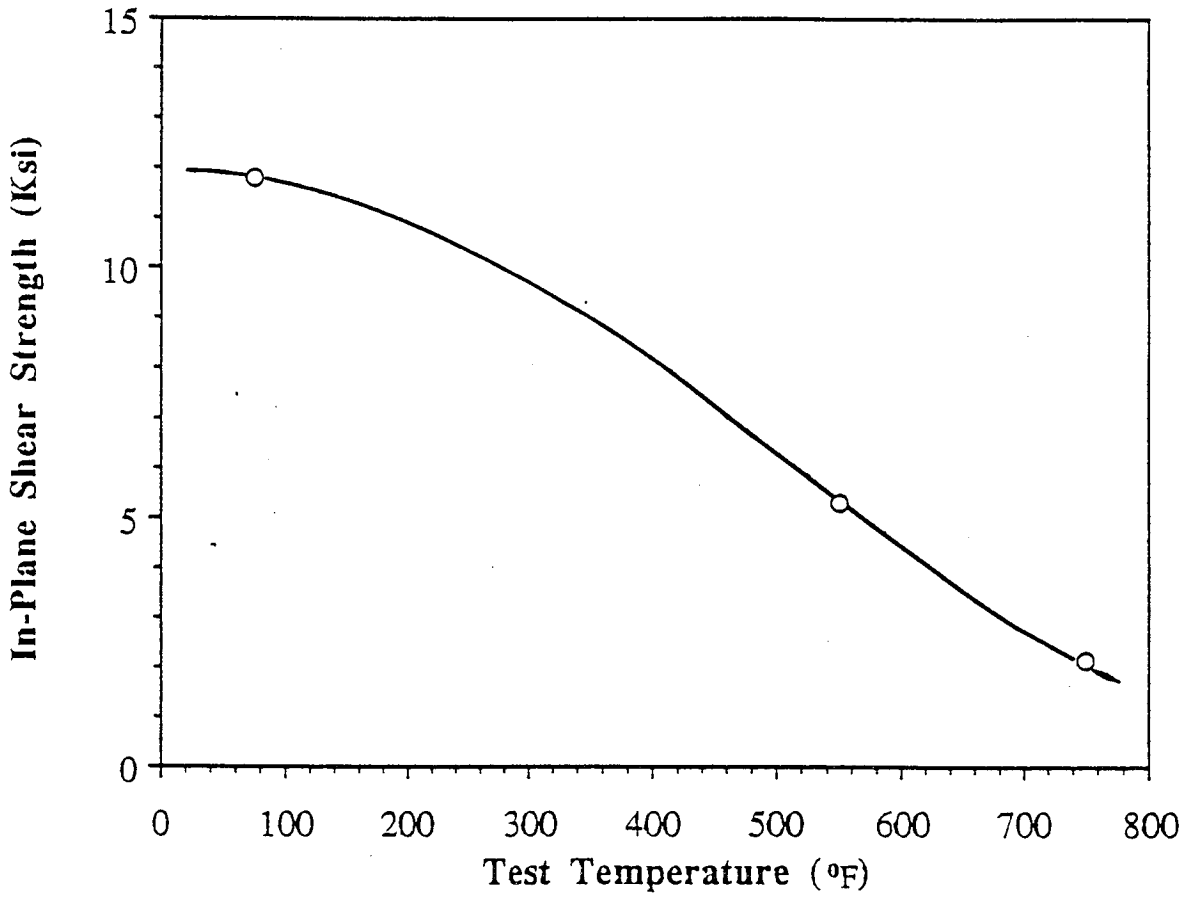

Fig. 5.19 Variation of In-Plane Shear Strength with Test Temperature for Unidirectional SiC/Al Composite

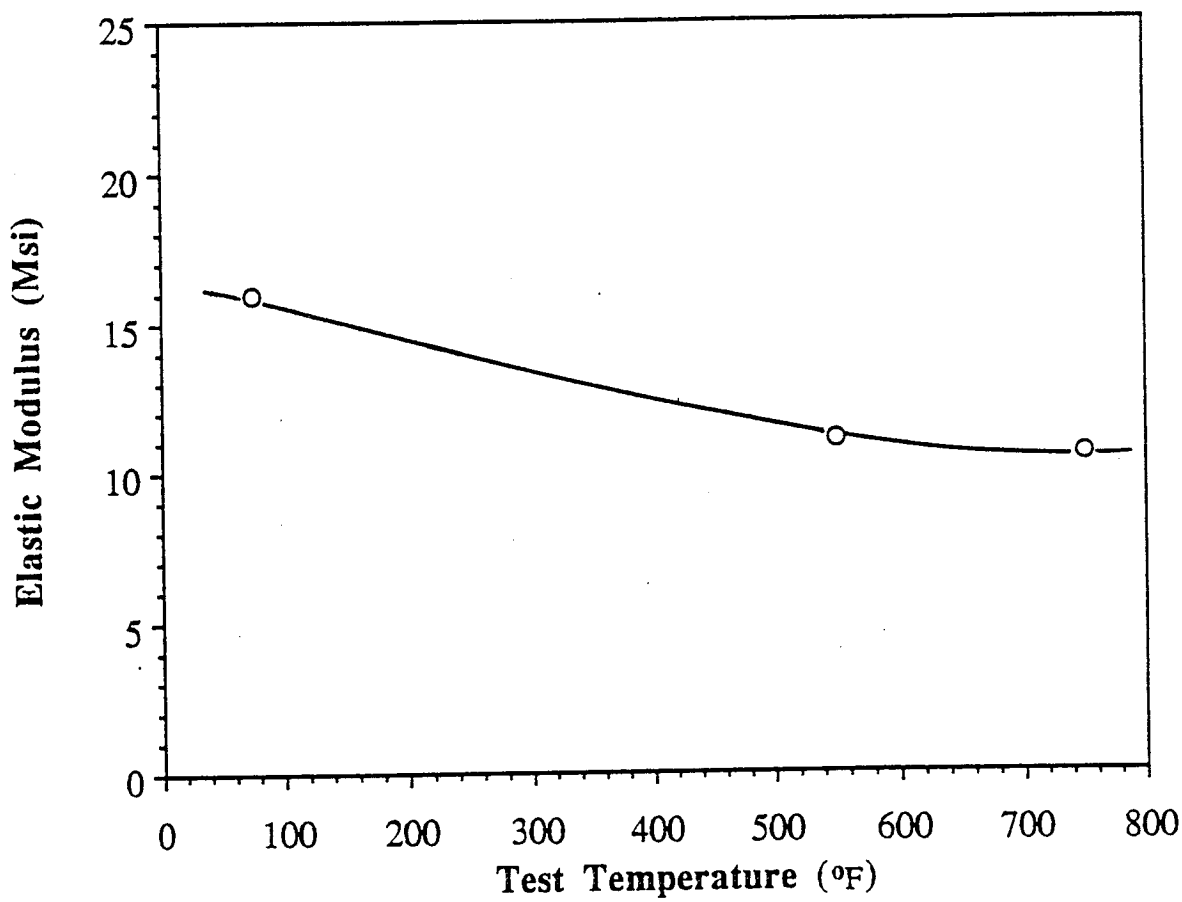

Fig. 5.20 Variation of Transverse Modulus with Test Temperature for Unidirectional SiC/Al Composite

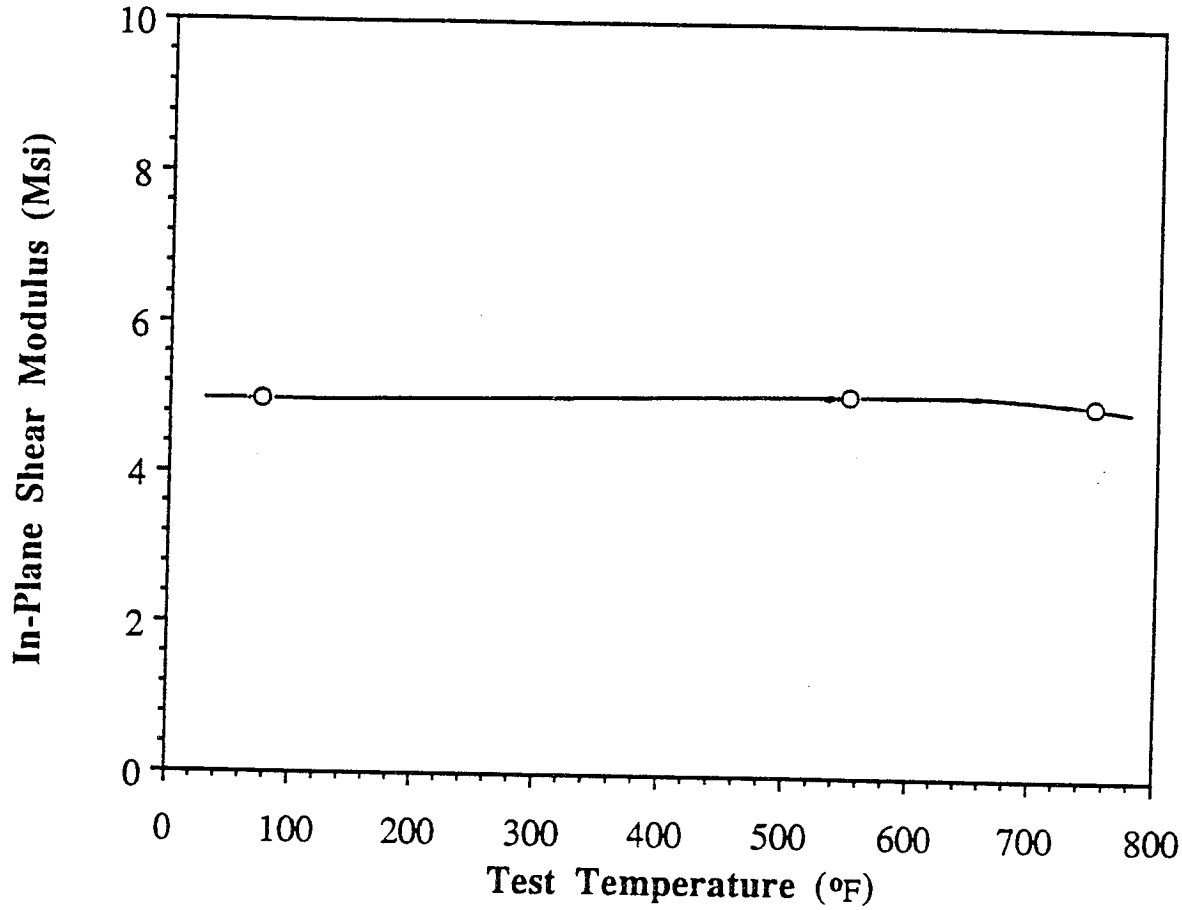

Fig. 5.21 Variation of In-Plane Shear Modulus with Test Temperature for Unidirectional SiC/Al Composite

Table 5.1 Mechanical Properties of Unidirectional SiC/Al Composite at Different Temperatures

Property	Temperature, T, °C (° F) 24 (75)	288 (550)	399 (750)
Fiber Volume Ratio, V_f	0.44	0.44	0.44
Density, ρ, g/cm³ (lb/in³)	2.86 (0.103)	2.86 (0.103)	2.86 (0.103)
Longitudinal Modulus, E_1, GPa (Msi)	207 (30)	207 (30)	207 (30)
Transverse Modulus, E_2, GPa (Msi)	110 (16.0)	76.6 (11.1)	73.1 (10.6)
In-Plane Shear Modulus, G_{12}, GPa (Msi)	34.5 (5.0)	34.5 (5.0)	34.5 (5.0)
Major Poisson's Ratio, ν_{12}	0.28	0.29	0.32
Longitudinal Tensile Strength, F_{1t}, MPa (ksi)	1,622 (235)	1,208 (175)	1,187 (172)
Transverse Tensile Strength, F_{2t}, MPa (ksi)	80.0 (11.6)	52.4 (7.6)	24.2 (3.5)
In-Plane Shear Strength, F_6, MPa (ksi)	81.4 (11.8)	36.6 (5.3)	14.5 (2.1)
Ultimate Longitudinal Tensile Strain, ε^u_{1t}	0.0096	0.0066	0.0063
Ultimate Transverse Tensile Strain, ε^u_{2t}	0.0011	0.0038	0.0101
Ultimate In-Plane Shear Strain, γ^u_6	0.0280	0.0201	0.060
Longitudinal Thermal Expansion Coefficient, α_1, 10^{-6}/°C (10^{-6}/°F)	5.9 (3.3)	-	-
Transverse Thermal Expansion Coefficient, α_2, 10^{-6}/°C (10^{-6}/°F)	16.0 (8.9)	-	-

the major factor influencing its creep behavior is the internal geometry. For unidirectional reinforcement with continuous fibers, the creep rate is minimum in the fiber direction and maximum at an angle to the fiber. The reason is that longitudinal creep of the composite is effectively inhibited by the fibers due to the extremely high elastic modulus and negligible creep properties of the fiber. However, transverse creep is significant even at an applied stress level below that necessary to cause creep in the unreinforced aluminum. Because creep rate is dependent on stress, the strain and strain rate in the vicinity of a fiber will be high due to stress concentration. This will increase the number and size of microstructural faults, which in turn further decrease the local cross sectional area and increase the strain rate. Additionally, microstructural defects as well as other heterogeneities, can act as a site for necking.

Creep tests were conducted under transverse and in-plane shear loading. No creep tests were conducted in the longitudinal (fiber) direction because very little creep is expected in that direction as discussed before. Figure 5.22 shows the creep curves and Figure 5.23 shows the creep rate curves of the composite in the transverse direction. The transverse creep compliance of the composite is shown in Figure 5.24. The shear creep curves and corresponding strain rate curves are shown in Figs. 5.25 and 5.26. The shear creep compliance of the composite is shown in Fig. 5.27.

The prediction of composite creep behavior on the basis of creep properties of the constituents is being investigated by several investigators. However, the problem is difficult because of the nonuniform stress fields involved under transverse loading and shear.

5.5 Non-Isothermal Creep Behavior

Many composites in service are exposed to fluctuating or varying

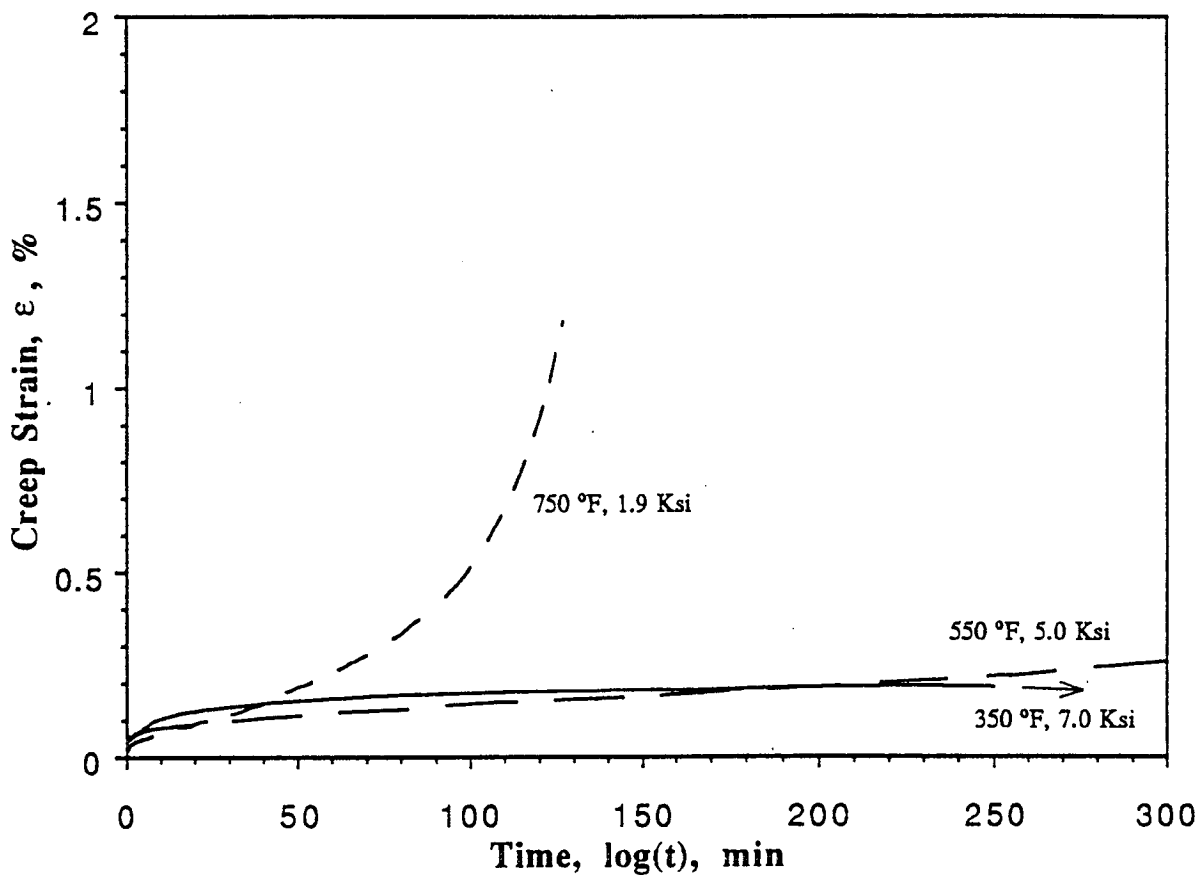

Fig. 5.22 Transverse Creep Curves of SiC/Al Composite at Three Different Temperatures

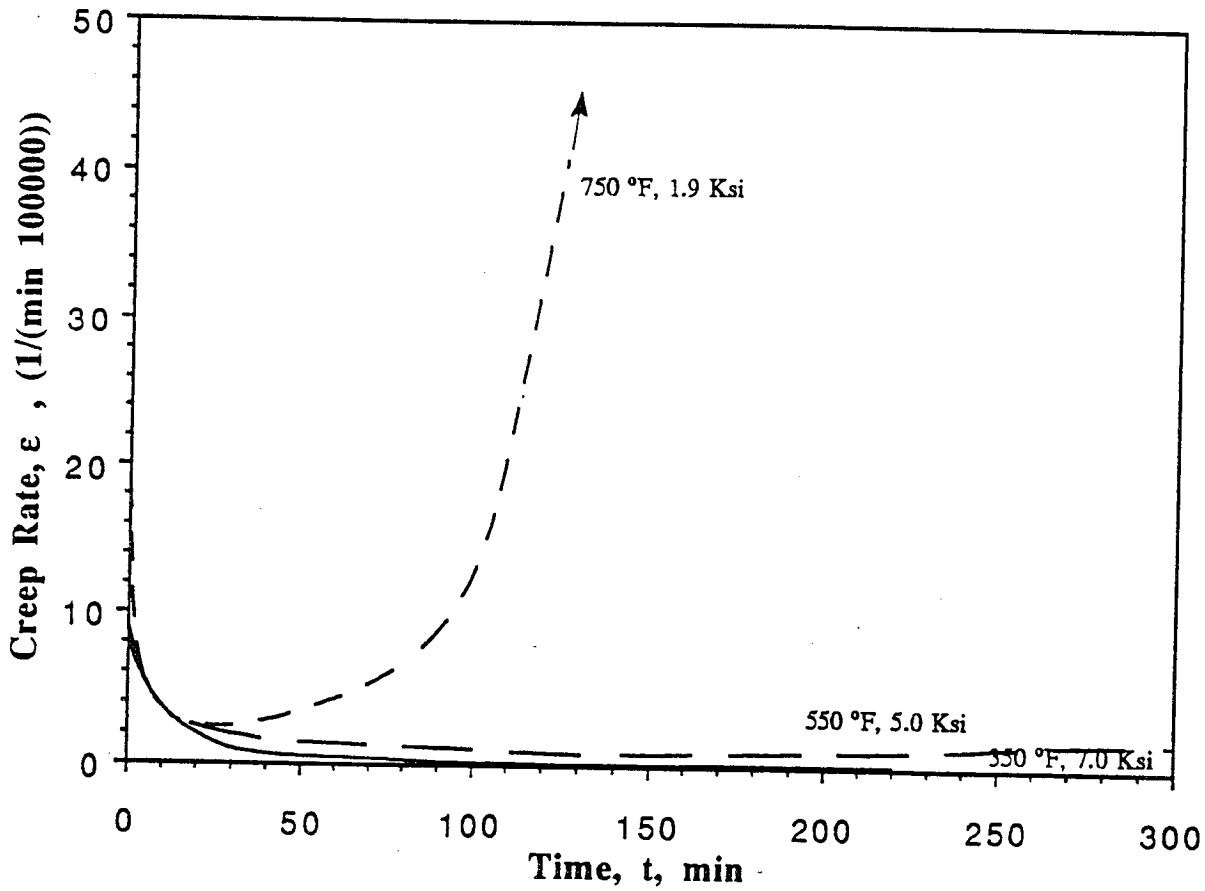

Fig. 5.23 Transverse Creep Rate Curves of SiC/Al Composite at Three Different Temperatures

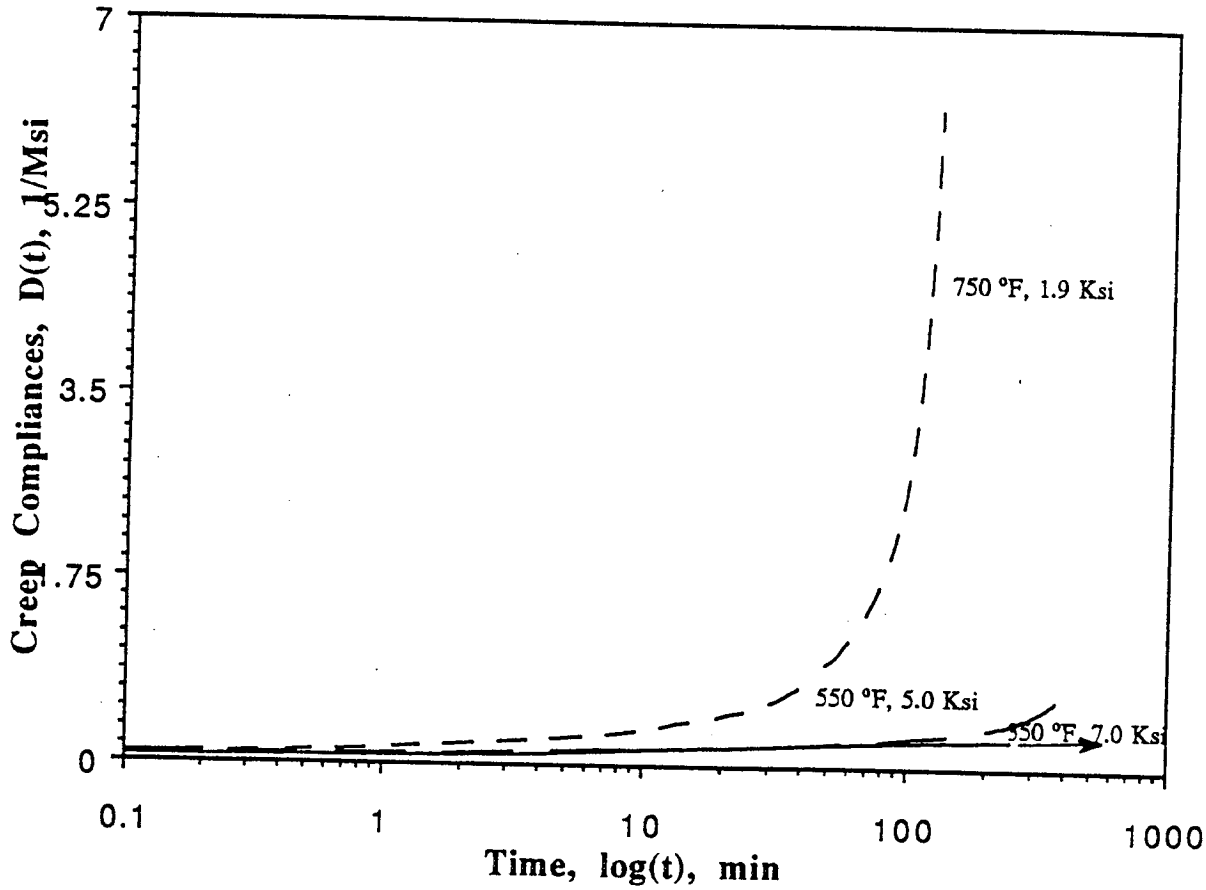

Fig. 5.24 Transverse Creep Compliances of SiC/Al Composite at Three Different Temperatures

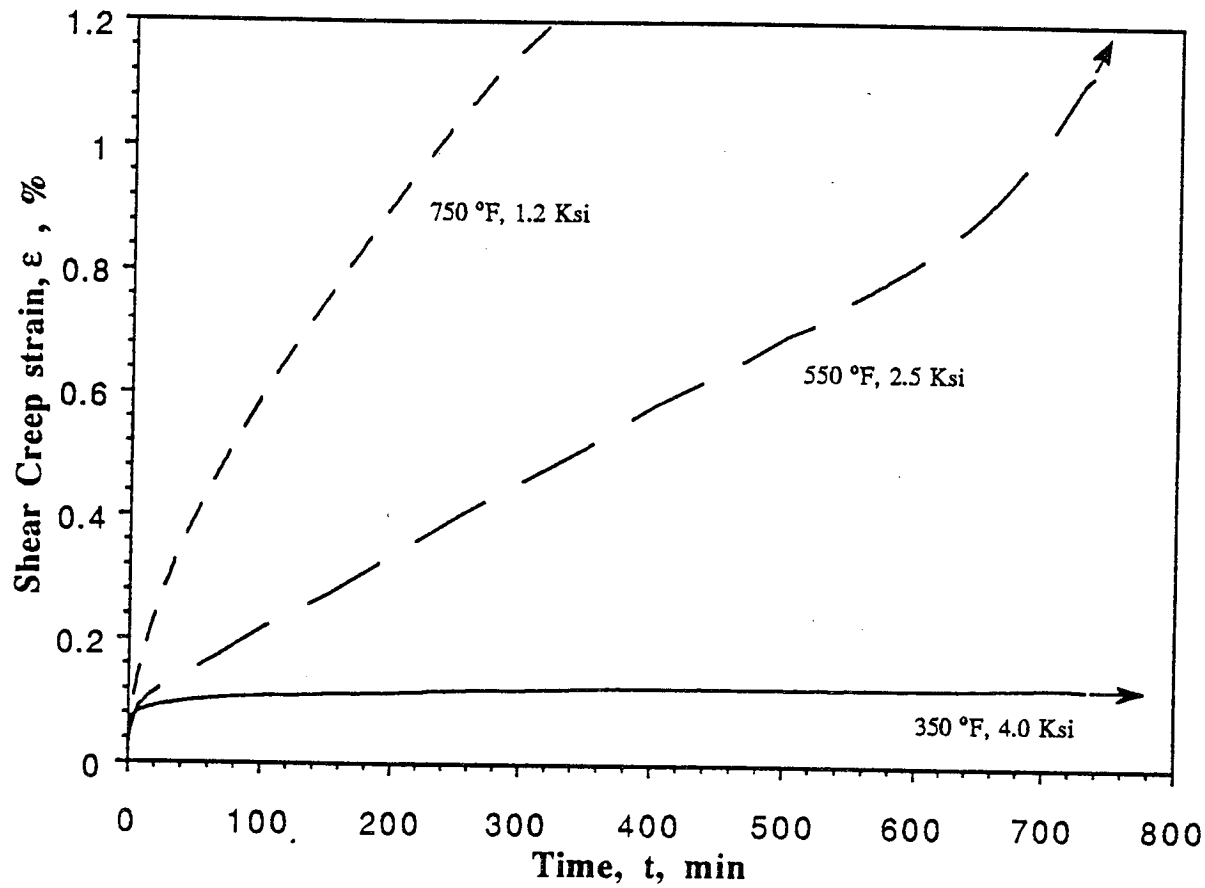

Fig. 5.25 Shear Creep Curves of SiC/Al Composite at Three Different Temperatures

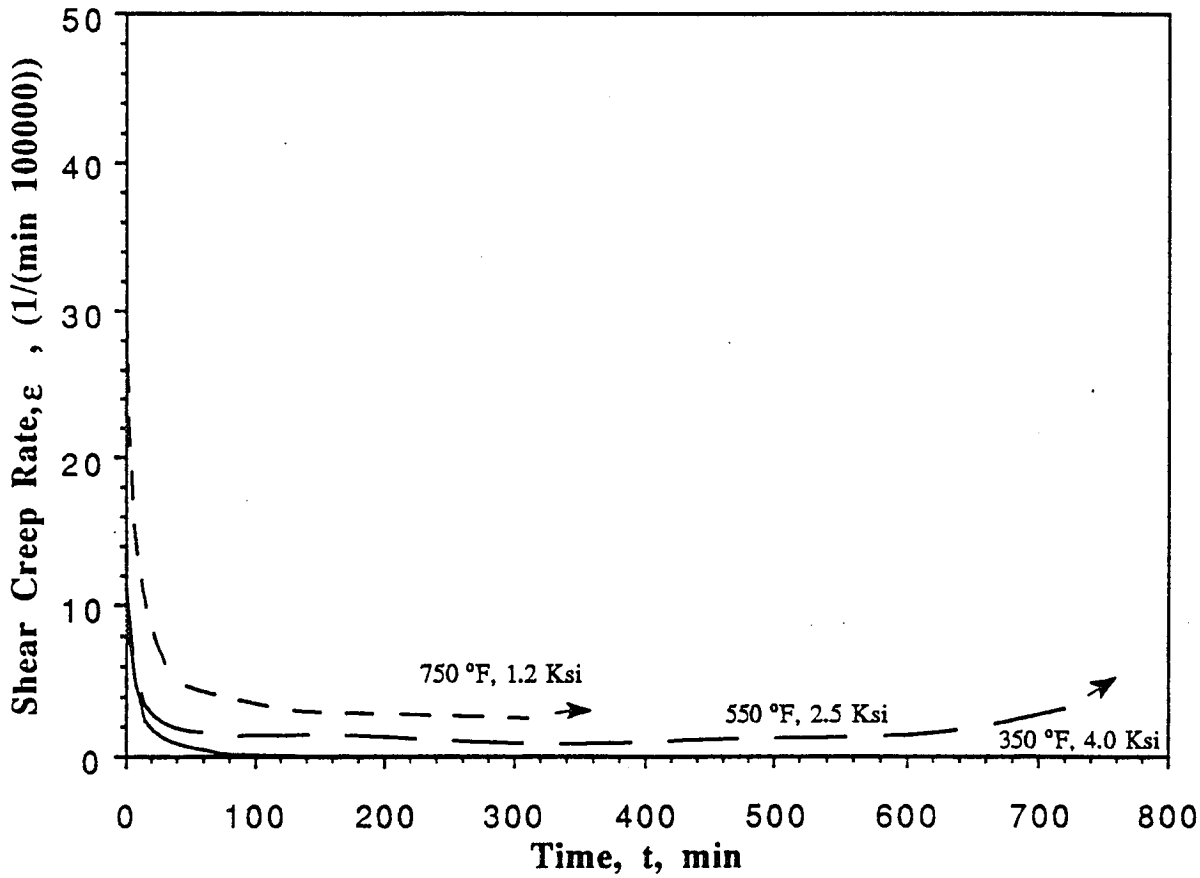

Fig. 5.26 Shear Creep rate Curves of SiC/Al Composite at Three Different Temperatures

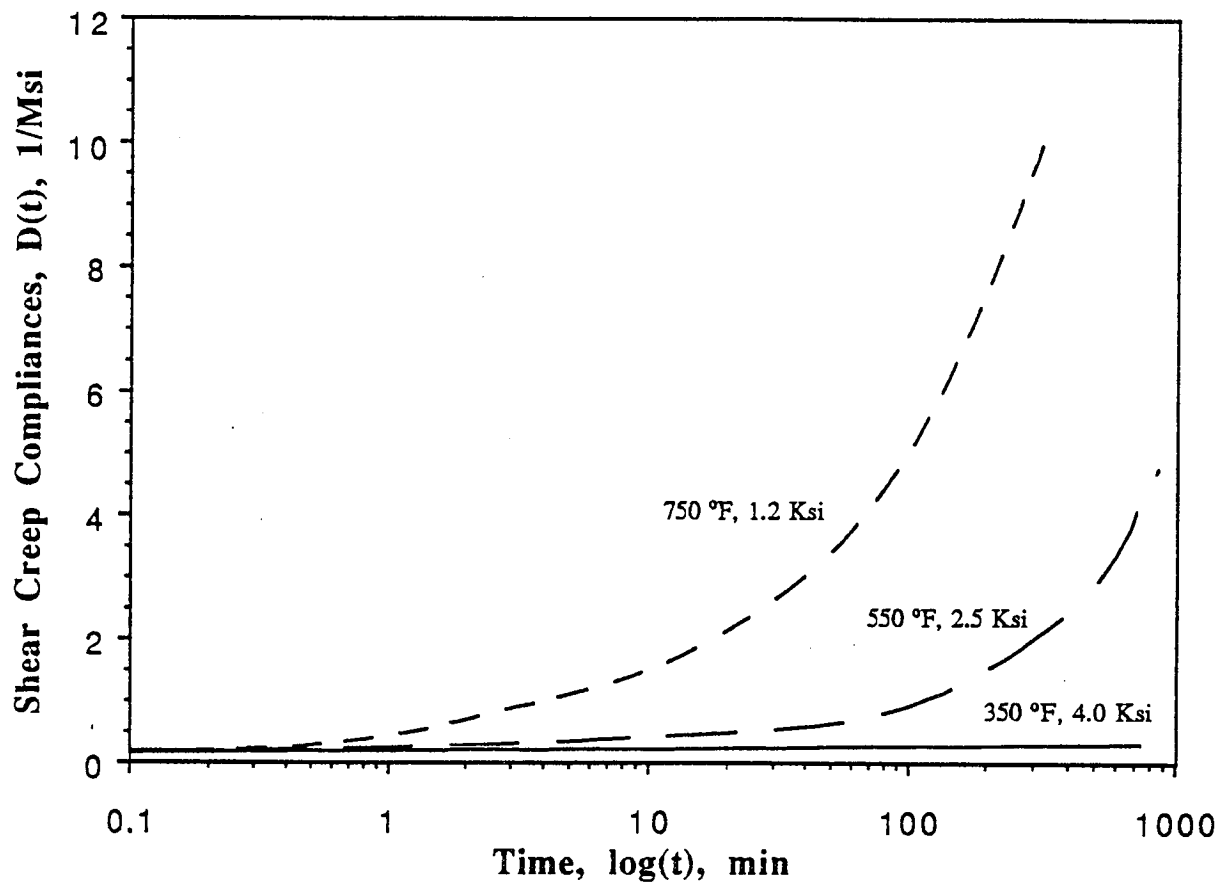

Fig. 5.27 Shear Creep Compliances of SiC/Al Composite at Three Different Temperatures

thermomechanical loading. It has been reported that composites creep and exhibit dimensional changes under very low stress levels when exposed to thermal cyclic conditions. Thus, it is very important to study how thermal cycling affects creep behavior in service. Such a study should take into consideration the local stresses and strains produced by thermal expansion mismatch between the constituents, on a microscopic level and between variously oriented plies on a macroscopic level.

Unidirectional SiC/A*l* specimens were tested under transverse and in-plane shear creep under thermal cyclic conditions. A small furnace was designed and built for the purpose in order to accelerate the thermal cycling. Temperature was measured by thermocouples welded to the specimen and heavily insulated with ceramic cement. A thin aluminum foil was used to cover the insulation and cut down the radiant heat that affects correct measurement of specimen temperature. The shielding of the thermocouples was found to be very important for correct measurement of specimen temperature when not embedded in the specimen. Thermal cycling was achieved by a system consisting of a controller with timers and relays. Specifically, the furnace operates until a preset high temperature is reached. At this point, the furnace switches off, and the specimen is cooled by forced air convection until the specimen temperature reaches a preset low temperature. Then, the timer resets, and the furnace is switched on again. Thus, the upper temperature of the cycle and the cycle period are controlled directly. Multilayer adhesive films were used to bond tabs to the specimens to cut down heat conduction from the specimen to the grips. This helped a great deal to reduce temperature gradients in the specimen.

A limited number of tests was conducted to study the effect of thermal cycling on creep strain in a transversely loaded composite for various applied stress levels. A thermal cycling range of 177 - 232° C (350 - 450° F) and a frequency of approximately 14 cycles per hour were selected. The creep strain for a specimen

loaded transversely under a constant stress of 17.2 MPa (2.5 ksi) and cycled over the temperature range above is shown in Fig. 5.28. The isothermal creep strain under the same load but at 232° C (450° F) is shown in Fig. 5.29. The upper envelopes of both records are compared in Fig. 5.30 where it is clearly shown that thermal cycling increases creep deformation significantly. Similar results were obtained for an increased stress level of 34.5 MPa (5.0 ksi) as shown in Figs. 5.31 and 5.32. All results for transverse creep are combined in Fig. 5.33 along with isothermal creep results at 399° C (550° F). It is seen that the creep strain obtained under thermal cycling betwen 177 and 232° C (350 and 450° F) is still higher than the isothermal creep obtained under the same stress at 399° C (550° F).

Similar creep tests wre conducted under in-plane shear using the 10° off-axis specimen. Figure 5.34 shows that the creep strain under cyclothermal conditions is larger than that under isothermal conditions as in the case of transverse loading. However, the difference between the two types of creep under shear loading is not as dramatic as under transverse loading. This could be attributed to the higher stress concentration around the fiber and the higher local stresses under transverse loading .

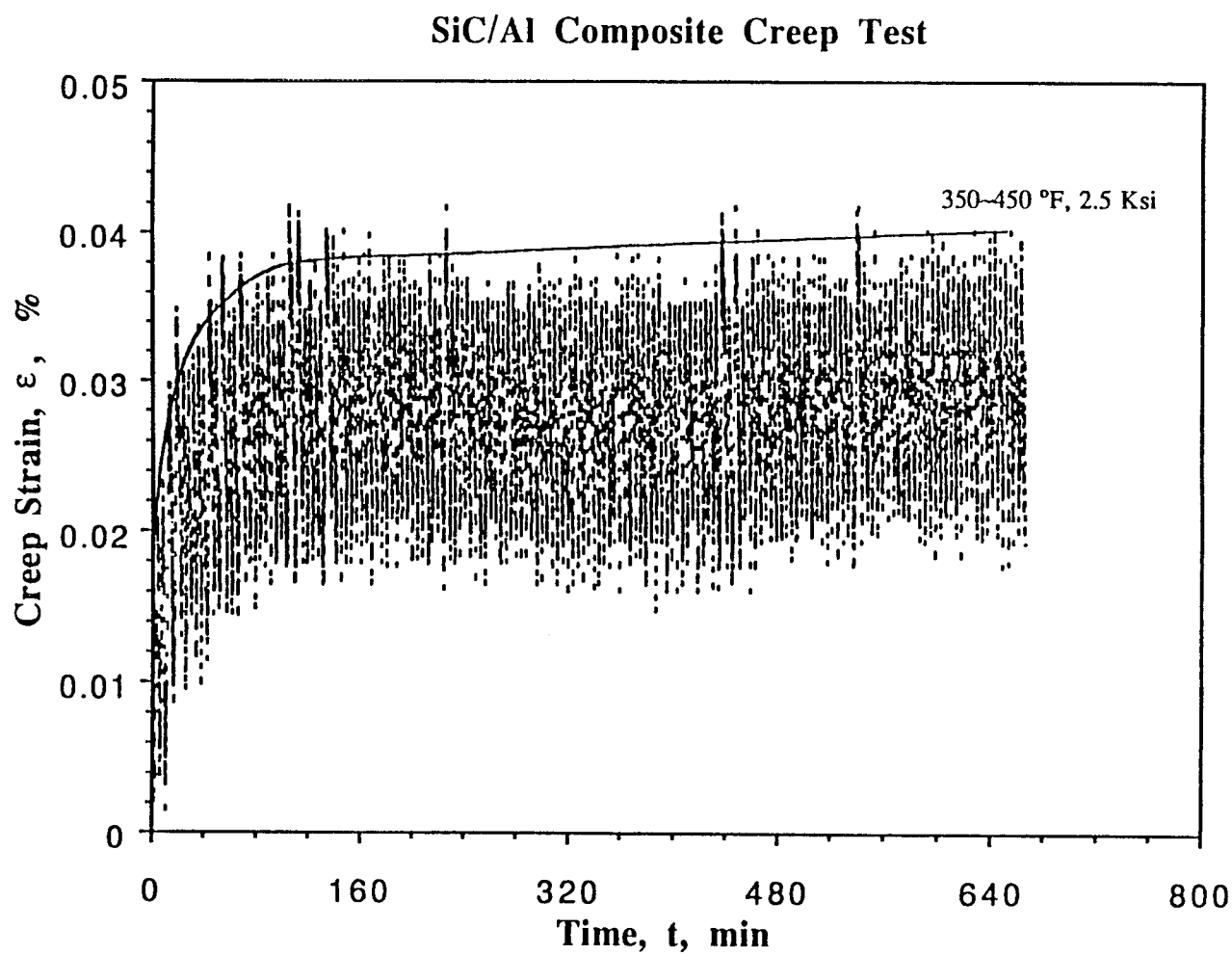

Fig. 5.28 Creep Strain in Transversely Loaded Unidirectional SiC/Al Composite under Cyclic Thermal Conditions

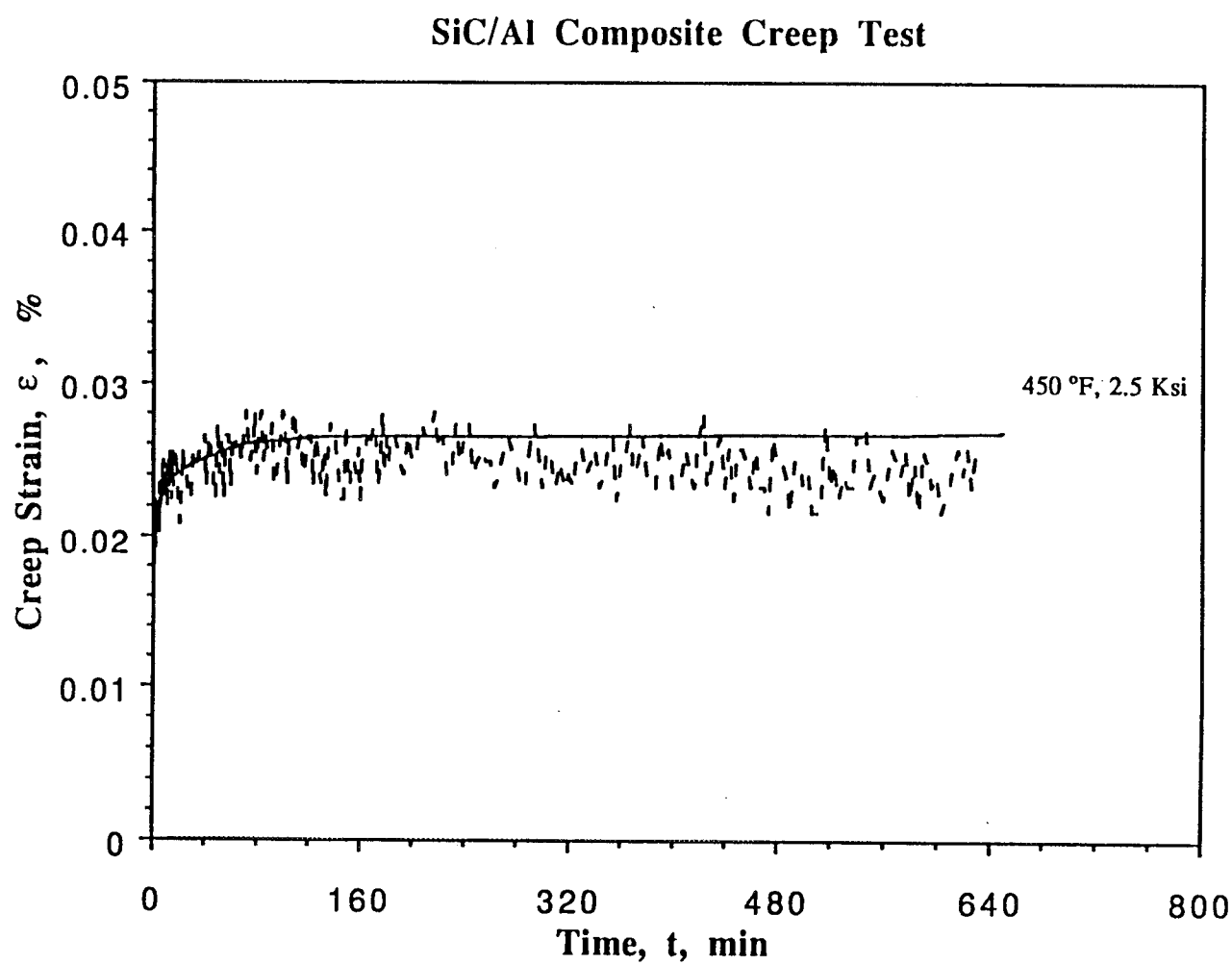

Fig. 5.29 Creep Strain in Transversely Loaded Unidirectional SiC/Al Composite under Isothermal Conditions

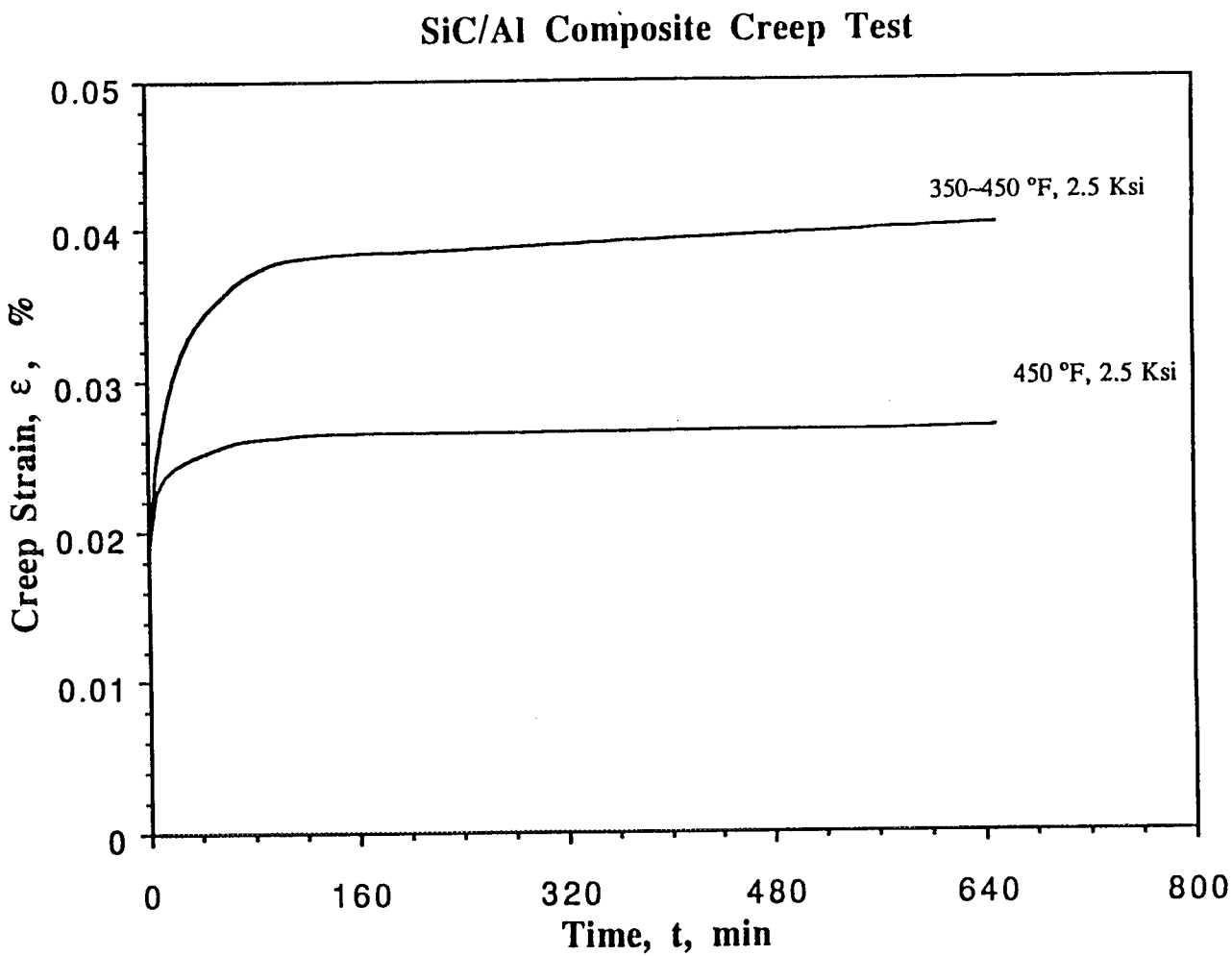

Fig. 5.30 Comparison of Transverse Creep in Unidirectional SiC/Al Composite under Isothermal and Thermal Cycling Conditions

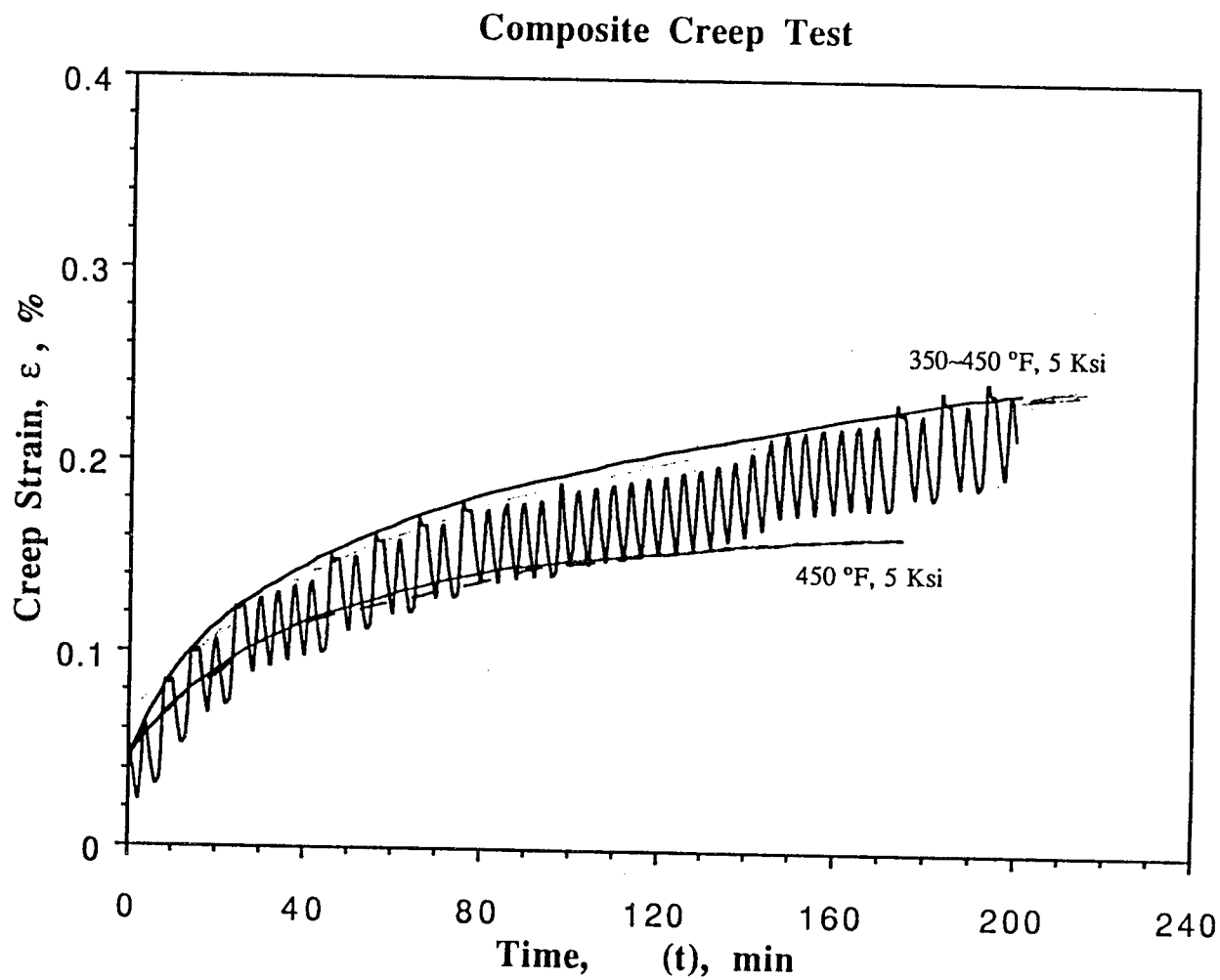

Fig. 5.31 Creep Strain in Transversely Loaded Unidirectional SiC/Al Composite under Isothermal and Cyclic Thermal Conditions

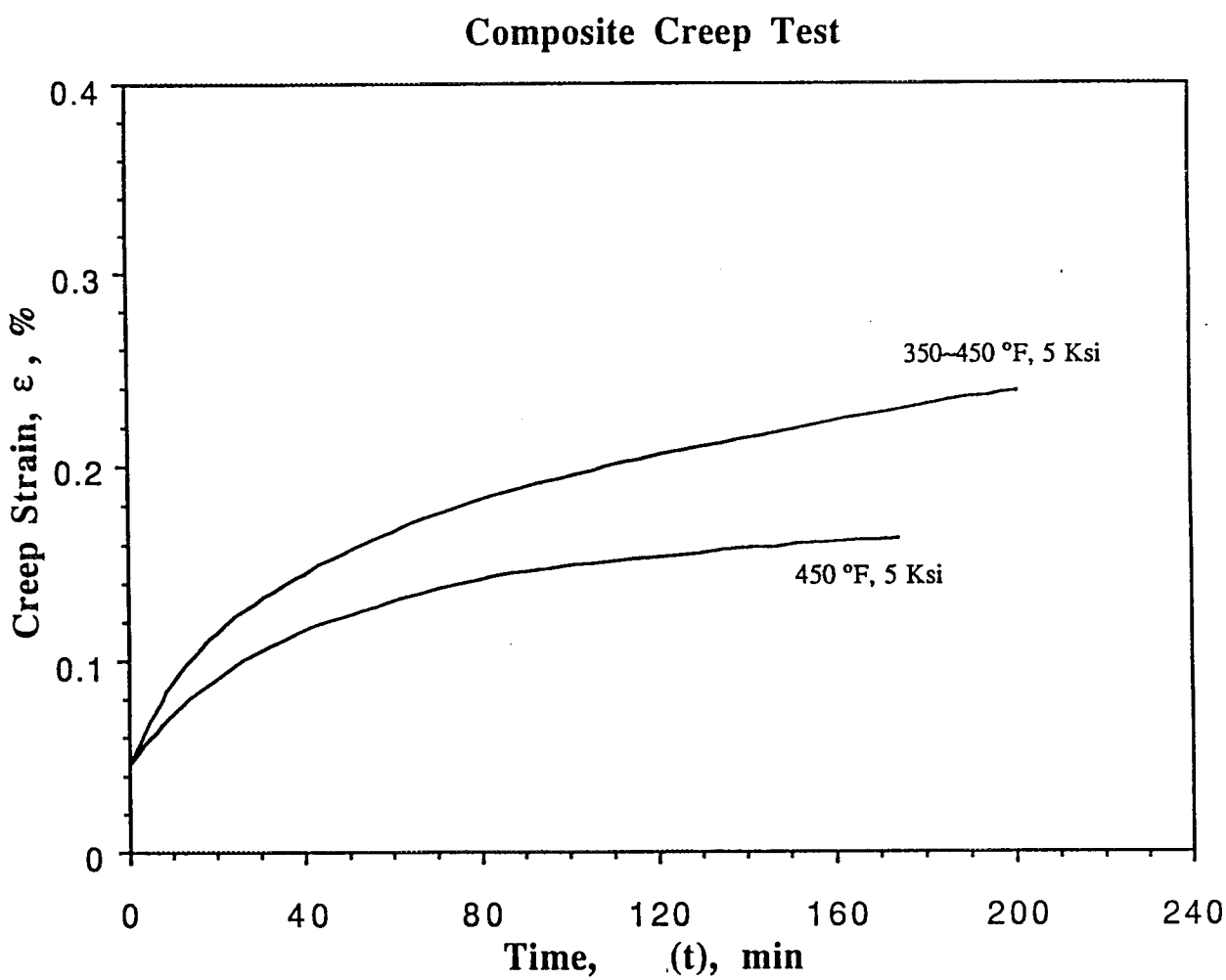

Fig. 5.32 Comparison of Creep Strains in Unidirectional SiC/Al Composite Obtained under Isothermal and Cyclic Thermal Conditions

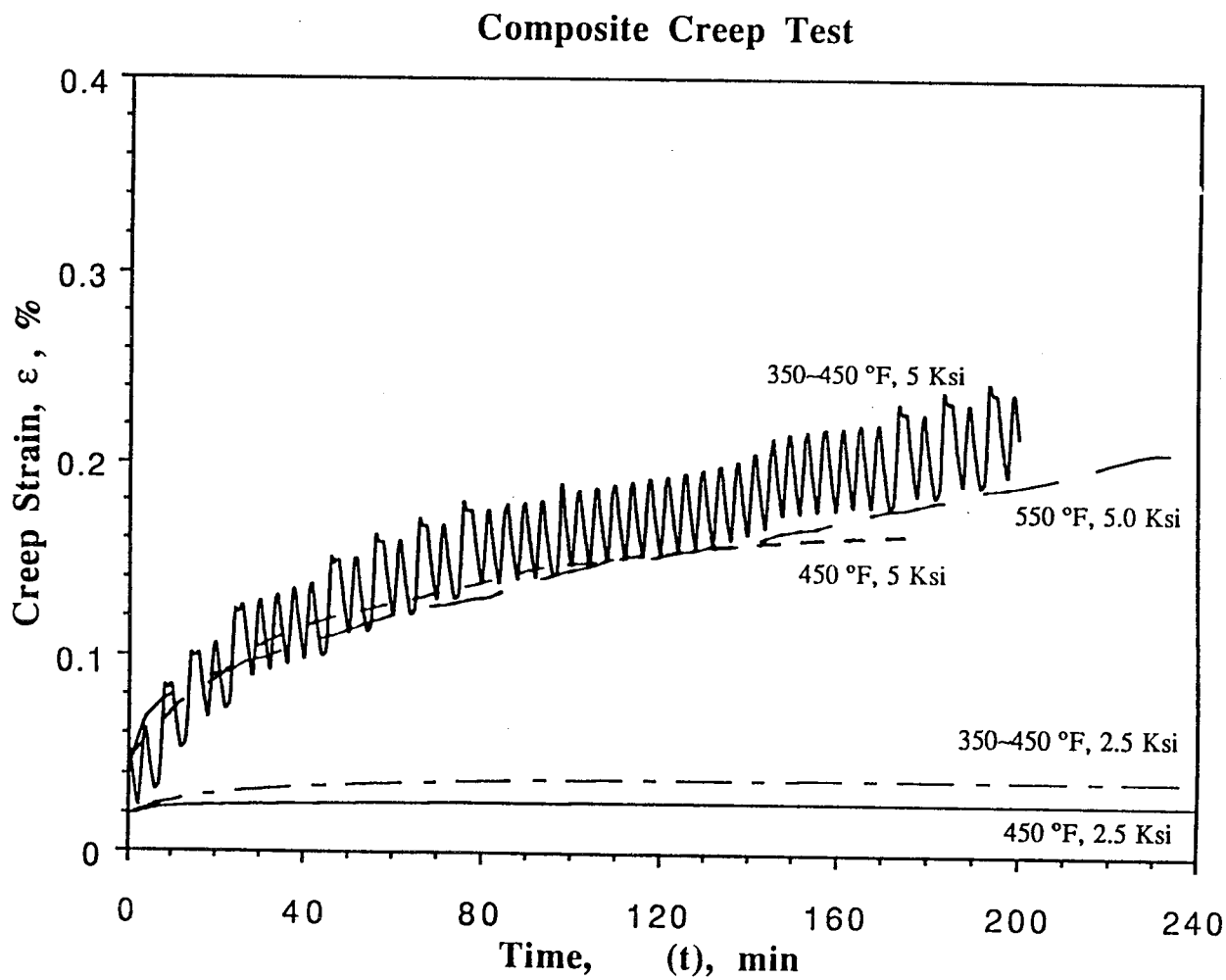

Fig. 5.33 Comparison of Isothermal and Cyclothermal Transverse Creep in Unidirectional SiC/Al Composite at Two Different Stress Levels

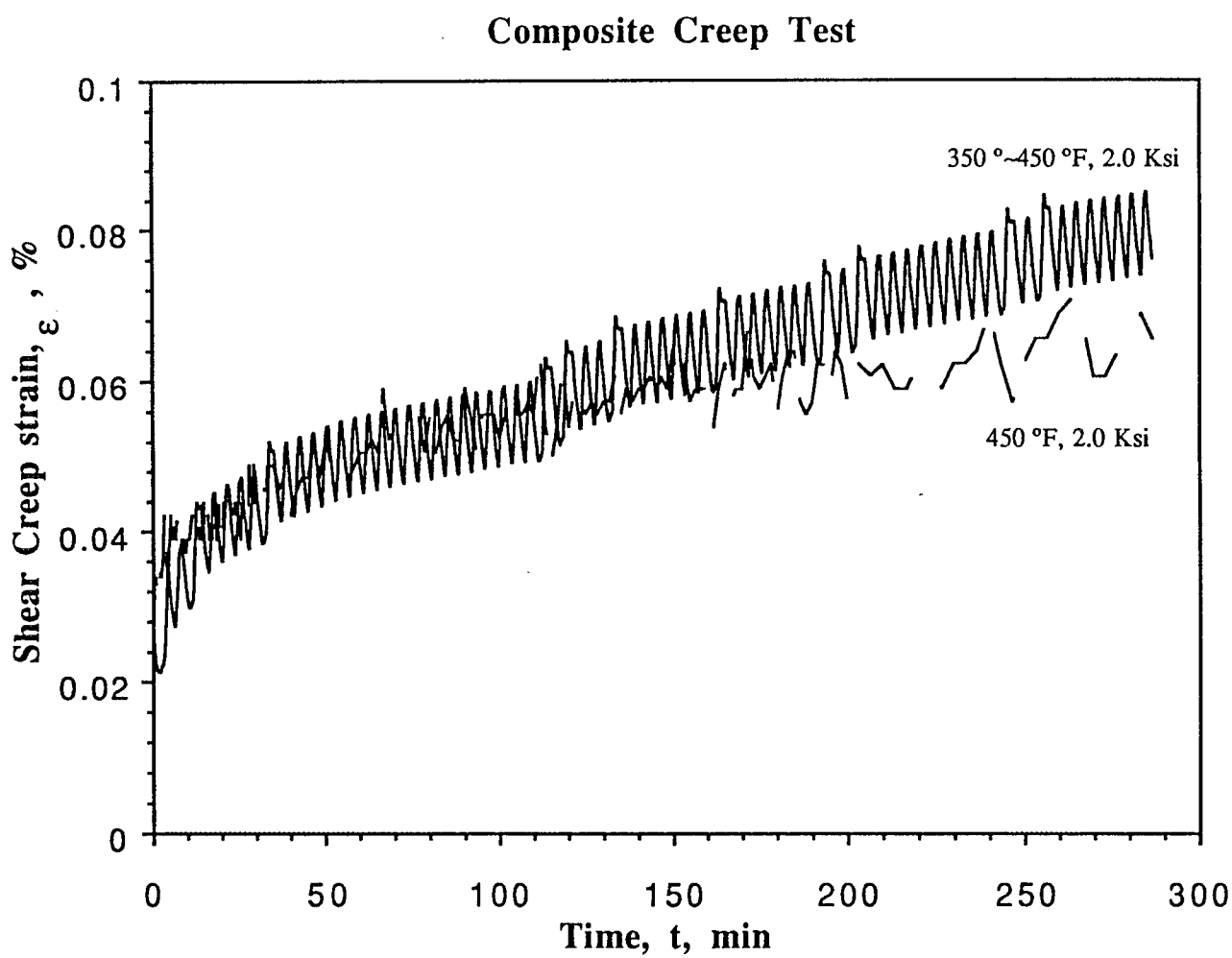

Fig. 5.34 In-Plane Shear Creep in Unidirectional SiC/Al Composite under Isothermal and Cyclothermal Conditions

6. APPLICATION OF THERMOVISCOPLASTIC NONLINEAR CONSTITUTIVE RELATIONSHIPS (TVP-NCR) AND METCAN COMPUTER CODE

The obtained experimental results (Sections 4 and 5) were used to determine the unknown exponents of the thermoviscoplastic nonlinear constitutive relationships (TVP-NCR) discussed in Section 3. In the present work only the temperature and stress dependence of the mechanical or thermal properties of the composite and its constituent matrix are considered. Therefore, the TVP-NCR expressed by equation (3.1) is reduced to only two terms on the right hand side as follows:

$$\frac{P}{P_o} = \left[\frac{T_u - T}{T_u - T_o}\right]^n \left[\frac{F_u - \sigma}{F_u - \sigma_o}\right]^m \tag{6.1}$$

where

P = current property of interest

P_o = corresponding property at reference conditions

T_u = ultimate temperature

T = current temperature

T_o = reference temperature at which P_o is determined

F = fracture stress determined at T_o

σ_o = reference stress at which P_o is determined

σ = current stress

At least squares method was used for the determination of the unknown exponents of equation (6.1) from the experimental data. From equation (6.1) we obtain

$$Q = \log\left[\frac{P}{P_o}\right] - n \log\left[\frac{T_u - T}{T_u - T_o}\right] - m \log\left[\frac{F - \sigma}{F - \sigma_o}\right] = 0 \tag{6.2}$$

Consider the variation of property P with stress, σ, for a number of temperatures, T. If N values of P are selected from these curves the least squares method requires that for a best fit

$$\sum_{j=1}^{N} Q_j^2 = \text{minimum} \tag{6.3}$$

The necessary conditions for the existence of this minimum are

$$\sum_{j=1}^{N} Q_j \frac{\partial Q_j}{\partial n} = 0 \tag{6.4a}$$

$$\sum_{j=1}^{N} Q_j \frac{\partial Q_j}{\partial m} = 0 \tag{6.4b}$$

Equations (6.4) yield

$$n \sum_{j=1}^{N} \overline{T}_j^2 + m \sum_{j=1}^{N} \overline{\sigma}_j \overline{T}_j = \sum_{j=1}^{N} \overline{P}_j \overline{T}_j \tag{6.5a}$$

$$n \sum_{j=1}^{N} \overline{\sigma}_j \overline{T}_j + m \sum_{j=1}^{N} \overline{\sigma}_j^2 = \sum_{j=1}^{N} \overline{P}_j \overline{\sigma}_j \tag{6.5b}$$

where

$$\overline{P}_j = \log\left[\frac{P_j}{P_o}\right] \tag{6.6}$$

$$\overline{T}_j = \log\left[\frac{T_u - T_j}{T_u - T_o}\right] \tag{6.7}$$

$$\overline{\sigma}_j = \log\left[\frac{F - \sigma_j}{F - \sigma_o}\right] \tag{6.8}$$

A repeating subscript in equations (6.5) does not imply summation of the respective terms over the values of the subscript. Equations (6.5) were incorporated into a computer program and were used for the determination of the values of exponents m and n for property P from the experimentally obtained data.

Using the previously developed procedure the coefficients m and n for a number of mechanical and thermal properties of the SiC/Al composite and 6061-T4

aluminum were determined. The properties investigated were

(a) For Aluminum 6061-T4

E = Modulus of Elasticity

ν = Poisson's Ratio

α = Coefficient of Thermal Expansion

σ_u = Ultimate Stress

(b) For SiC/Al metal matrix composite

E_1, E_2 = Longitudinal and transverse Young's moduli, respectively

α_1, α_2 = Longitudinal and transverse coefficients of thermal expansion

Values of the exponents m and n for the aluminum and the composite are given in Tables 6.1 and 6.2 for three different selected values of T_u. The first selected ultimate temperature of 593° C (1100° F) was taken to be the melting temperature of the aluminum matrix in the composite. The other two values of T_u equal to 1093° C (2000° F) and 1649° C (3000° F) were chosen to check the sensitivity of the exponent values to the selection of ultimate temperature. In the case of the SCS-2 fiber all properties were assumed to be independent of temperature and stress, therefore, the coefficients m and n were taken equal to zero.

Another method that can be used for determination of the unknown exponents is the graphical method. In equation (6.1), for example, if $T = T_o$, only properties at the reference temperature are considered and thus the temperature dependent term becomes unity. Then, the unknown exponent m is obtained as the slope of the log (P/P_o) versus log $(F - \sigma)$ $(F - \sigma_o)$ curve. A similar procedure is used for determination of exponent n.

The material properties under investigation can be expressed as follows:

Table 6.1 Values of the Exponents n and m of the TVP-NCR for Aluminum 6061-T4

Material Property, P	Temperature, T_u °C	°F	n	m
Tangent Modulus, E_t	593	1100	1.3046	3.1034
Coefficient of Thermal Expansion, α	593	1100	-0.2212	
	1093	2000	-0.5256	
	1649	3000	-0.8522	
Poisson's Ratio, ν	593	1100	-0.5045	-0.2251
	1093	2000	-1.0530	-0.2233
	1649	3000	-1.6583	-0.2227
Ultimate Stress, σ_u	593	1100	0.8252	
	1093	2000	1.8110	
	1649	3000	2.8857	

Table 6.2 Values of the Exponents n and m of the TVP-NCR for SiC/Al Composite

Material Property, P	Temperature, T_u		n	m
	^oC	^oF		
Longitudinal Tangent Modulus, E_{1t}	593	1100	-0.1226	0.0717
	1093	2000	-0.2693	0.0717
	1649	3000	-0.4306	0.0717
Transverse Tangent Modulus, E_{2t}	593	1100	0.4636	0.3792
	1093	2000	0.9761	0.3910
	1649	3000	1.2770	0.4120
Longitudinal Coefficient of Thermal Expansion, α_1	593	1100	0.9718	
	1093	2000	2.3094	
	1649	3000	3.7441	
Transverse Coefficient of Thermal Expansion, α_2	593	1100	-0.2827	
	1093	2000	-0.6718	
	1649	3000	-1.0892	

$$E = E_o \left[\frac{T_u - T}{T_u - T_o}\right]^n \left[\frac{F - \sigma}{F - \sigma_o}\right]^m \tag{6.9}$$

$$\nu = \nu_o \left[\frac{T_u - T}{T_u - T_o}\right]^n \left[\frac{F - \sigma}{F - \sigma_o}\right]^m \tag{6.10}$$

$$\alpha = \alpha_o \left[\frac{T_u - T}{T_u - T_o}\right]^n \tag{6.11}$$

$$\sigma_u = \sigma_o \left[\frac{T_u - T}{T_u - T_o}\right]^n \tag{6.12}$$

Equations (6.9 and (6.10 represent the temperature and stress dependence of the material modulus and Poisson's ratio while equations (6.11) and (6.12) represent only the temperature dependence of the coefficient of thermal expansion and ultimate stress.

The stress-strain curves of the SiC/A*l* composite and Aluminum 6061-T4 were obtained from the determined exponents (n, m) of the tangent modulus as follows:

$$d\sigma = E_t \, d\varepsilon$$

$$d\sigma = E_o \left[\frac{T_u - T}{T_u - T_o}\right]^n \left[\frac{F_u - \sigma}{F_u - \sigma_o}\right]^m d\varepsilon$$

$$\int \frac{1}{(F - \sigma)^m} d\sigma = E_o \left[\frac{T_u - T}{T_u - T_o}\right]^n \int \frac{1}{(F - \sigma)^m} d\varepsilon$$

$$\frac{F^{1-m} - (F - \sigma)^{1-m}}{1 - m} = \frac{E_o}{(F - \sigma_o)^m} \left(\frac{T_u - T}{T_u - T_o}\right)^n \varepsilon$$

$$\varepsilon = \frac{(F - \sigma_o)^m}{E_o} \left(\frac{T_u - T_o}{T_u - T}\right)^n \left(\frac{F^{1-m} - (F - \sigma)^{1-m}}{1 - m}\right) \tag{6.13}$$

By using equations (6.9) through (6.13) along with the calculated values of the exponents n and m (Tables 6.1 and 6.2) the material properties under investigation were obtained and compared with the experimentally measured ones in the following figures:

a. For unidirectional SiC/Al composite

(1) Longitudinal stress-strain curves for temperatures of 24° C (75° F) and 288° C (550° F) are shown in Figures 6.1 and 6.2, respectively.

(2) Transverse stress-strain curves for temperatures of 24° C (75° F) and 288° C (550° F) are shown in Figure 6.3.

(3) Longitudinal and transverse coefficients of thermal expansion as a function of temperature are shown in Figures 6.4 and 6.5.

b. For aluminum 6061-T4

(1) Stress-strain curves for temperatures of 24° C (75° F), 121° C (250° F), 149° C (300° F), 177° C (350° F) and 232° C (450° F) are shown in Figures 6.6 through 6.10.

(2) Coefficient of thermal expansion versus temperature curve is shown in Figure 6.11.

(3) Ultimate stress versus temperature curve is shown in Fig. 6.12.

From the above figures the following observations can be made:

(1) The exponents m and n take positive or negative values depending on the material property under investigation. No general rule assigning positive or negative values can be stated.

(2) Predictions of the thermomechanical behavior of composite and aluminum matrix by the TVP-NCR is generally good for most properties. Deviations, however, between experimental and predicted results appear in cases where the form of the experimental curve deviates from the generic form of the TVP-NCR expressed in terms of powers of dimensionless products.

(3) The exponent n for the coefficients of thermal expansion of the composite was found to be very sensitive to the selected value of the ultimate temperature, T_u. On the other hand, the exponent m for the mechanical properties was not affected by the selection of T_u.

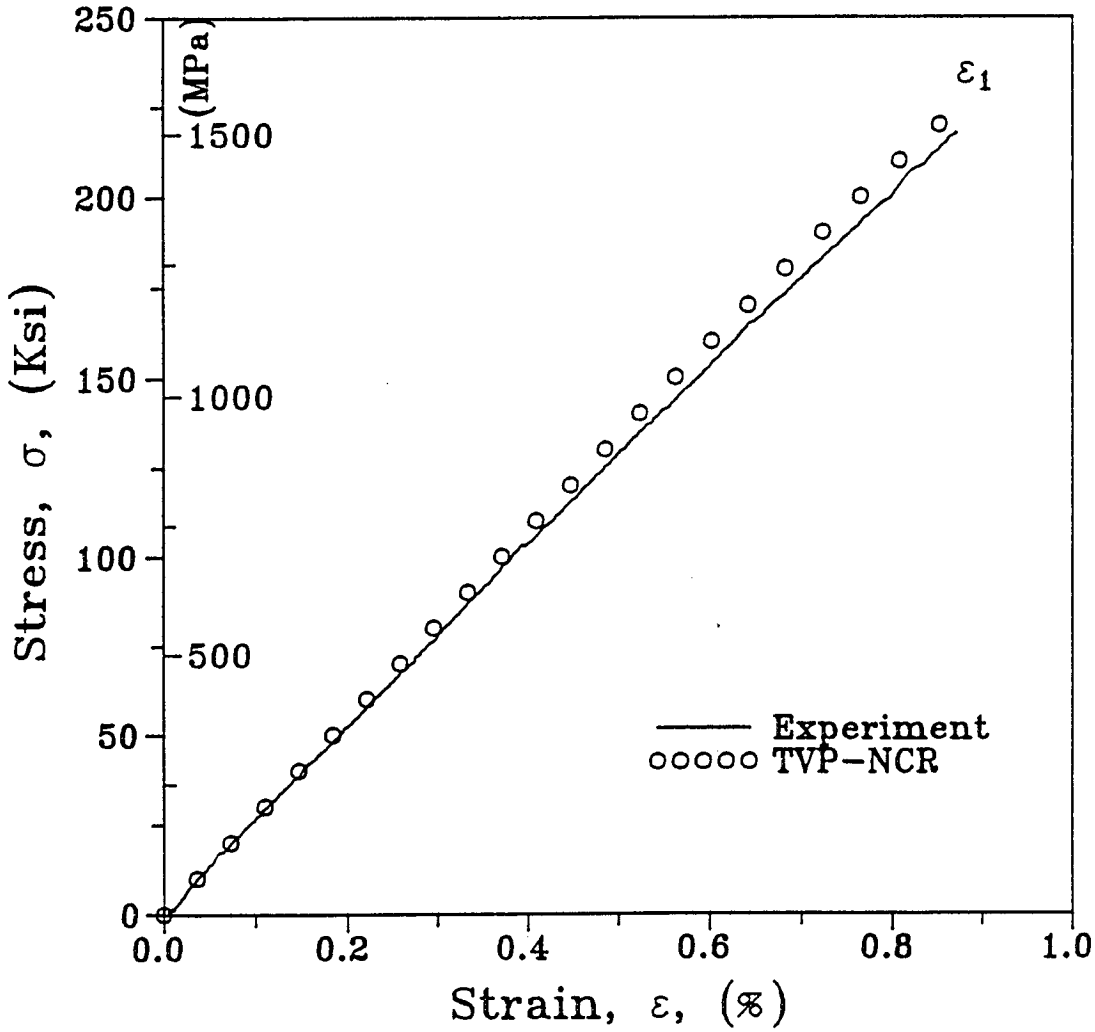

Fig. 6.1 Stress-Strain Curves for [0_8] SCS-2/6061 Aluminum Composite Specimen Under Uniaxial Tensile Loading at 24 °C (75 °F) as Obtained Experimentally and Predicted by the TVP-NCR.

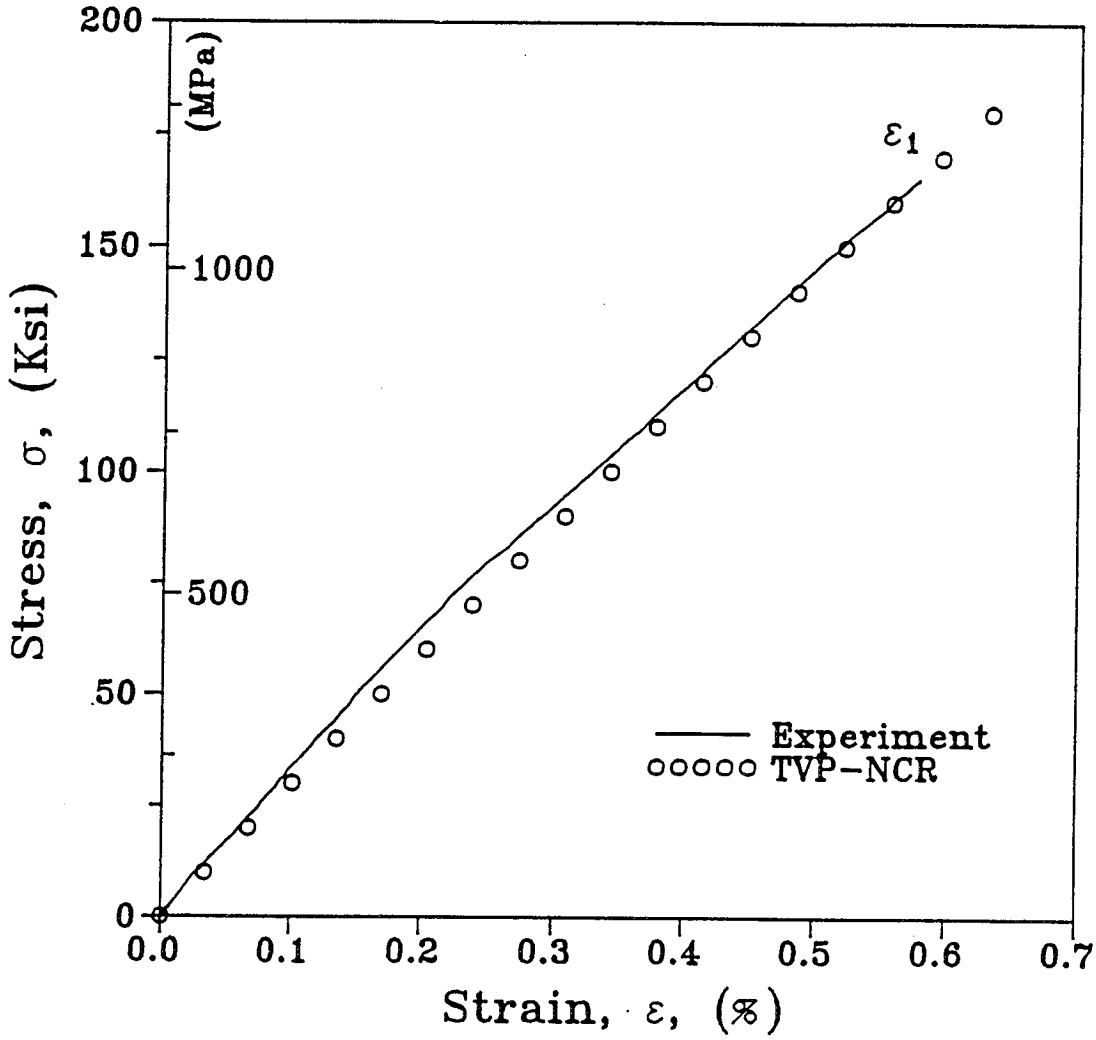

Fig. 6.2 Stress-Strain Curves for $[0_8]$ SCS-2/6061 Aluminum Composite Specimen Under Uniaxial Tensile Loading at 288 °C (550 °F) as Obtained Experimentally and Predicted by the TVP-NCR.

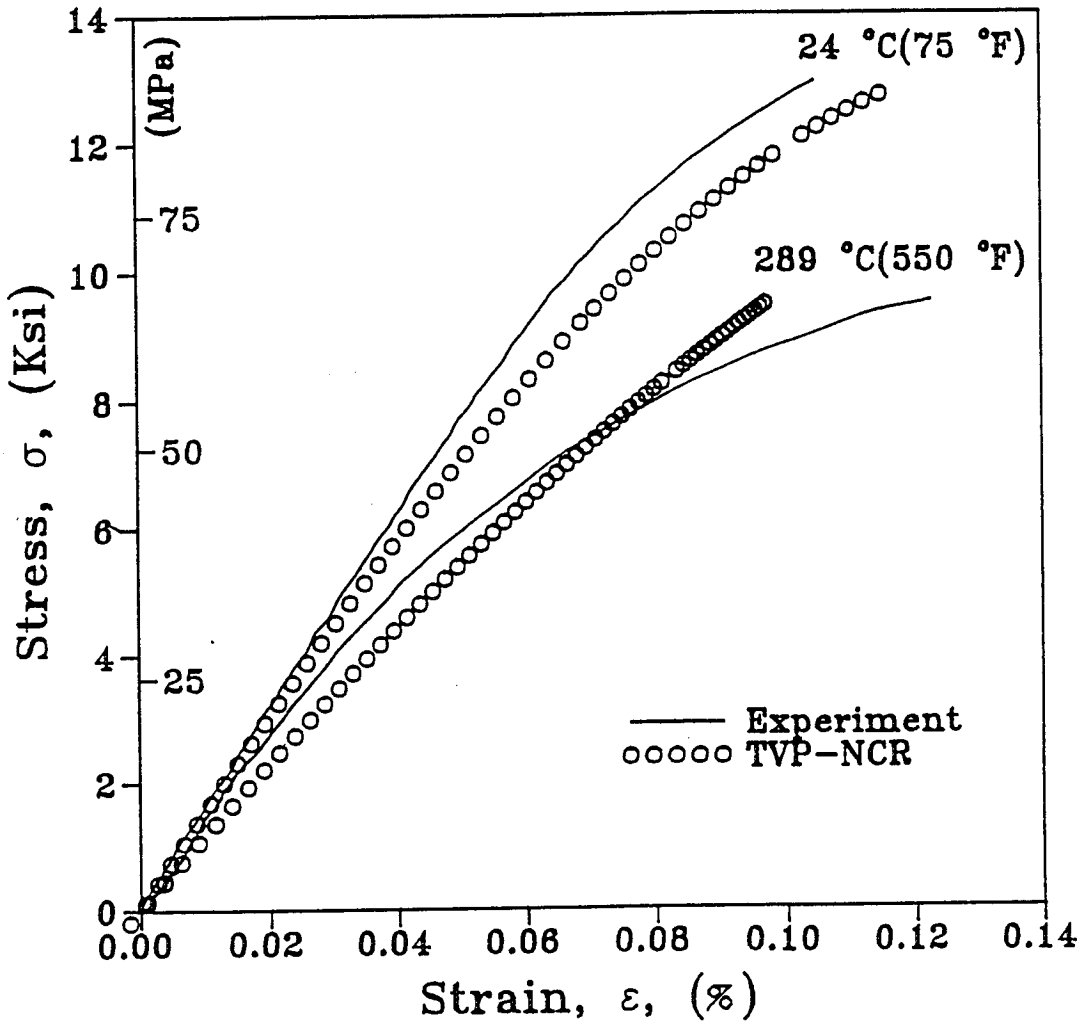

Fig. 6.3 Transverse Stress-Strain Curves for SCS-2/6061 Aluminum Composite Specimen Under Uniaxial Tensile Loading at 24° C (75° F) and 288° C (550° F) as Obtained Experimentally and Predicted by the TVP-NCR.

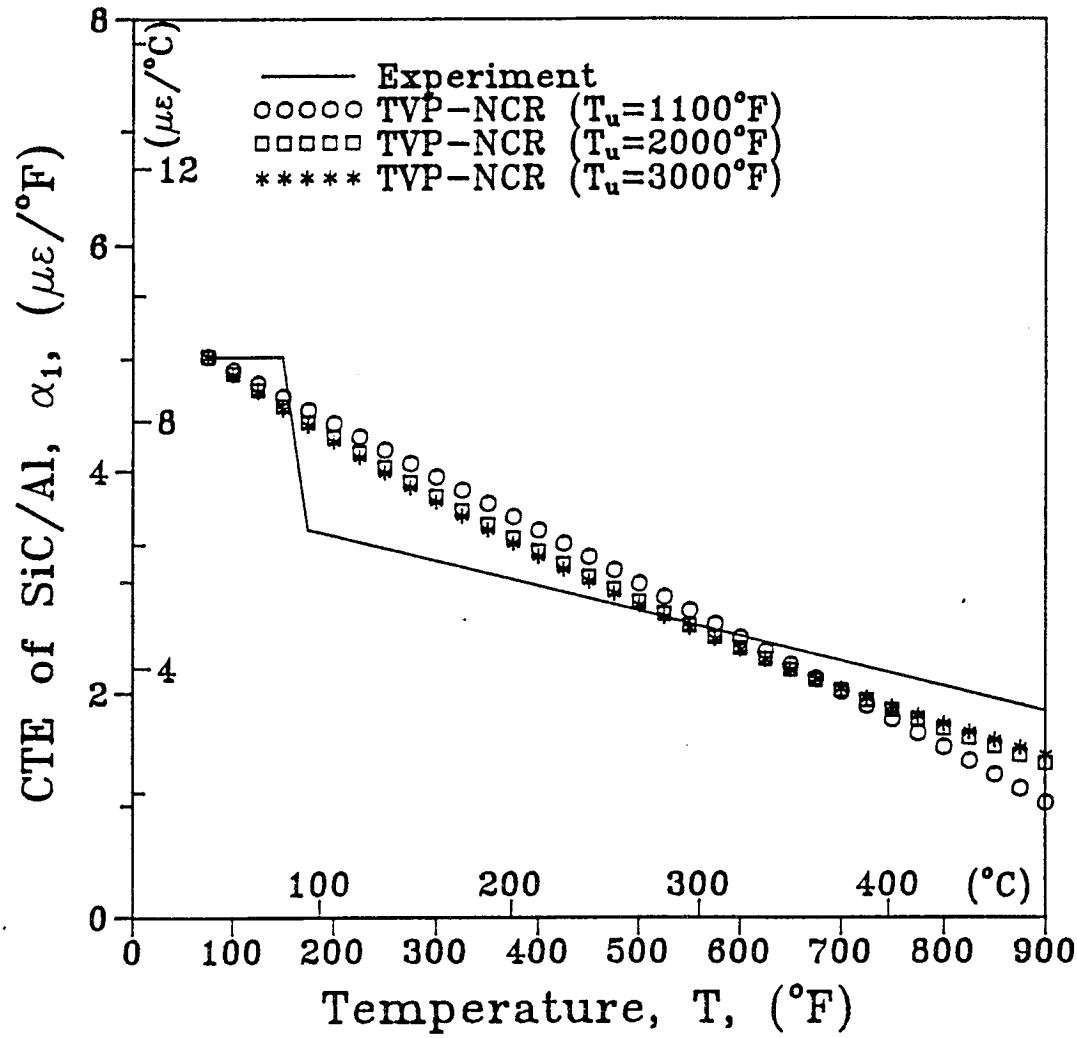

Fig. 6.4 Longitudinal Coefficient of Thermal Expansion (α_1) versus Temperature Curves for SCS-2/6061 Aluminum Composite Specimen as Obtained Experimentally and Predicted by the TVP-NCR.

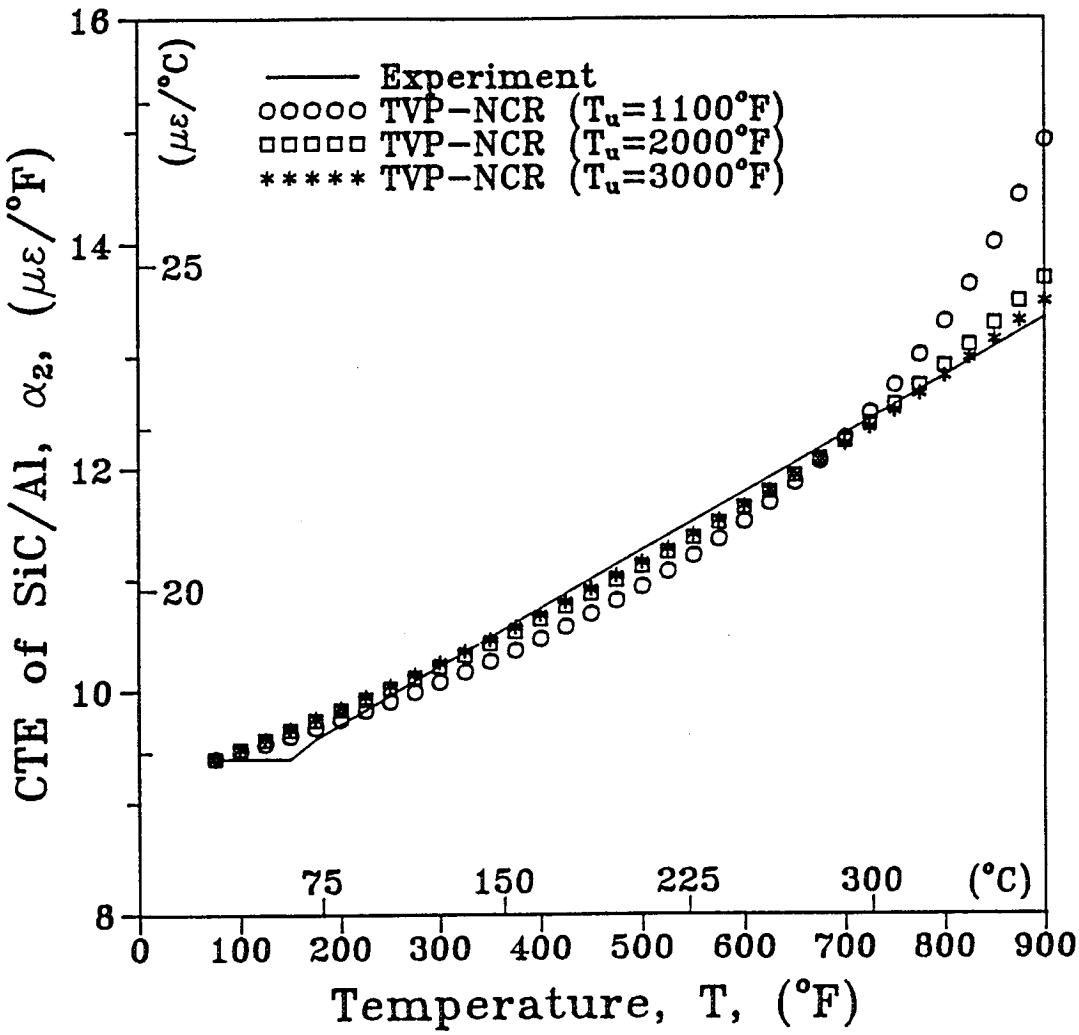

Fig. 6.5 Transverse Coefficient of Thermal Expansion (α_2) versus Temperature Curves for SCS-2/6061 Aluminum Composite Specimen as Obtained Experimentally and Predicted by the TVP-NCR.

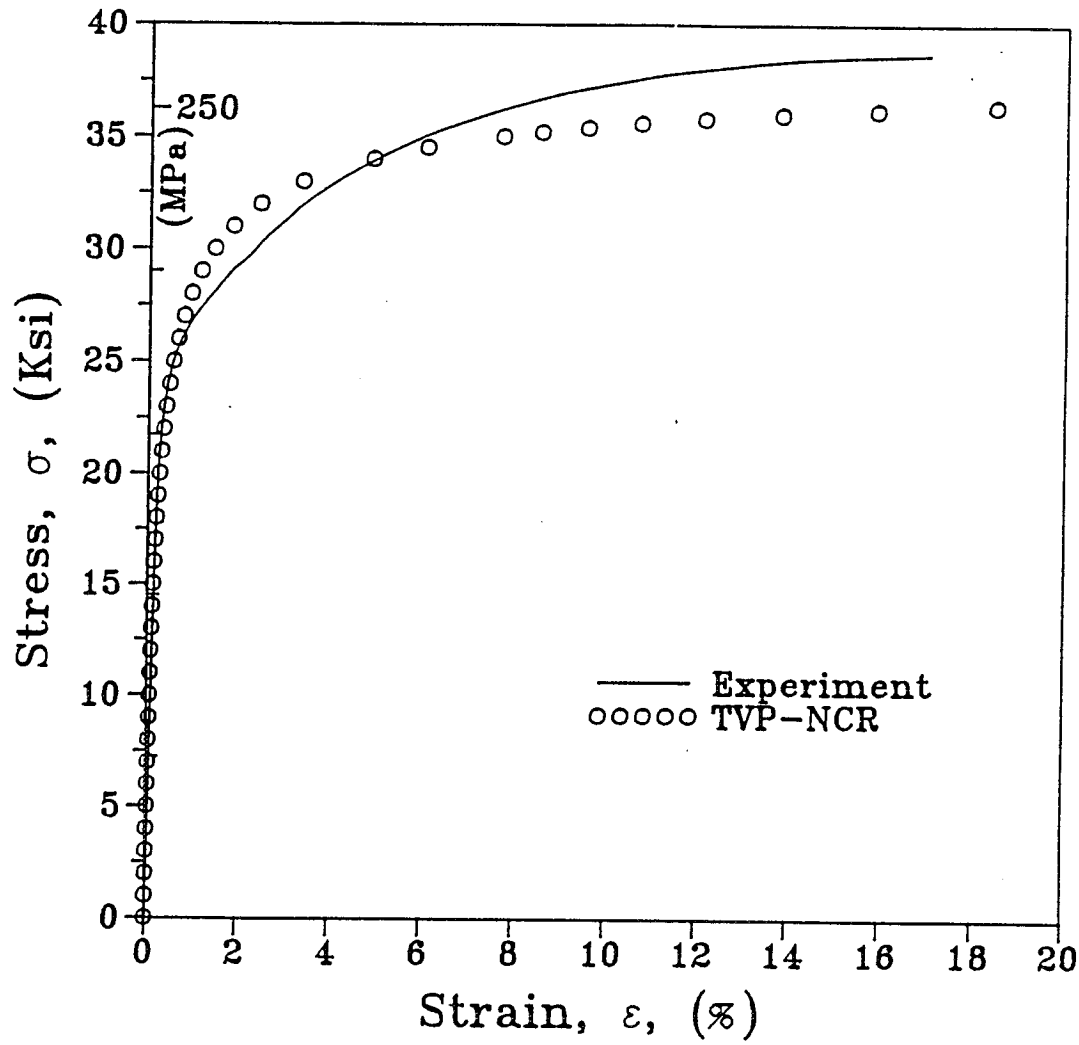

Fig. 6.6 Stress-Strain Curves for Aluminum 6061-T4 Specimen Under Uniaxial Tensile Loading at 24 °C (75 °F) as Obtained Experimentally and Predicted by the TVP-NCR.

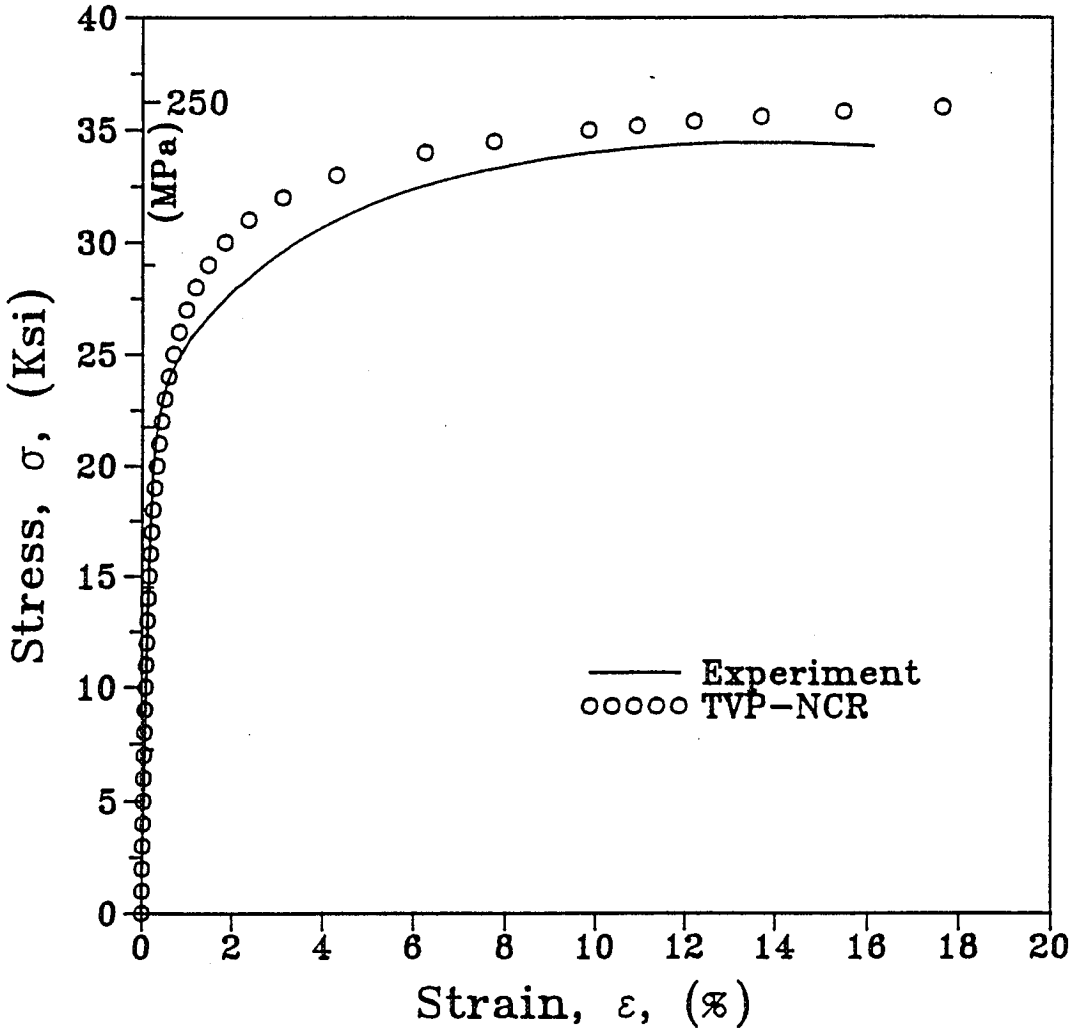

Fig. 6.7 Stress-Strain Curves for Aluminum 6061-T4 Specimen Under Uniaxial Tensile Loading at 121 °C (250 °F) as Obtained Experimentally and Predicted by the TVP-NCR.

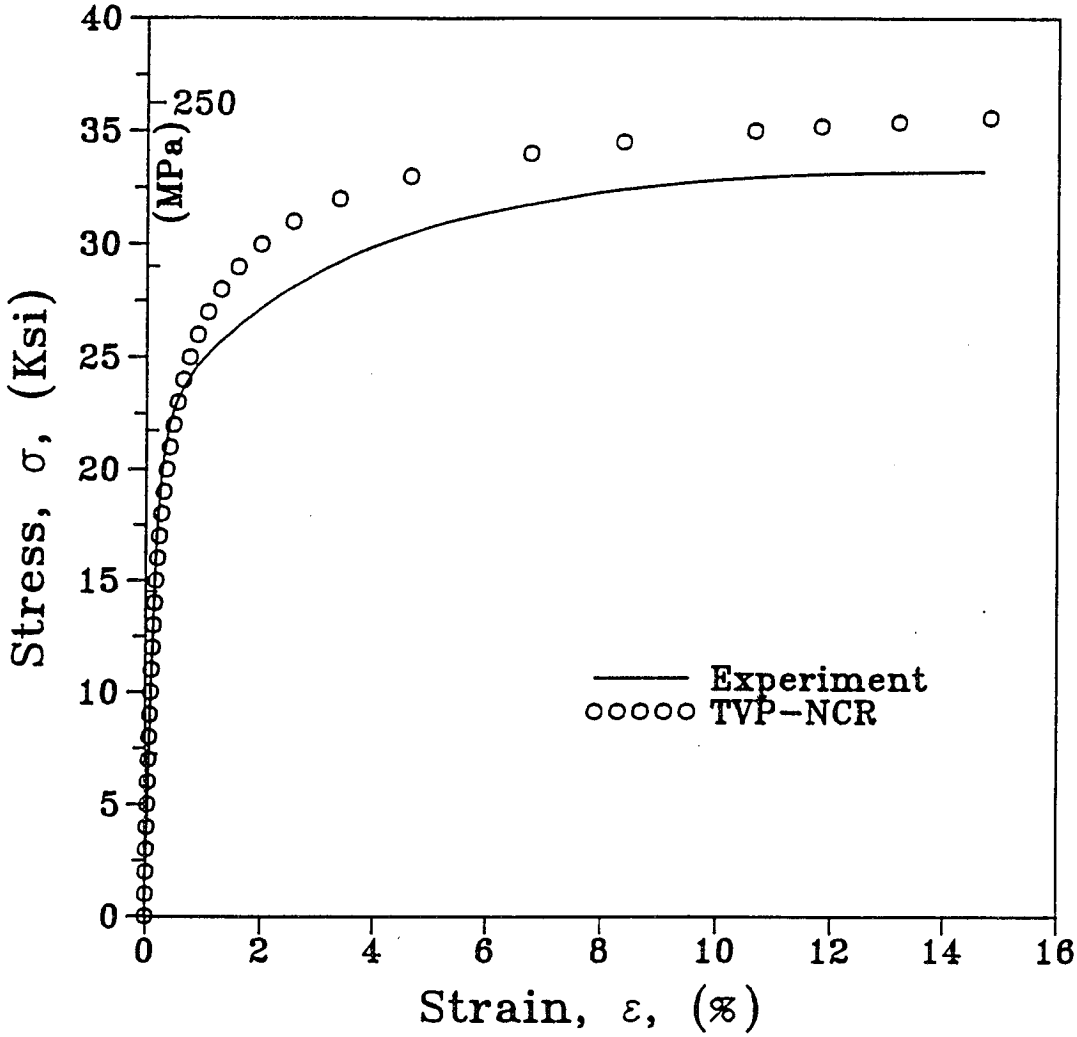

Fig. 6.8 Stress-Strain Curves for Aluminum 6061-T4 Specimen Under Uniaxial Tensile Loading at 149 °C (300 °F) as Obtained Experimentally and Predicted by the TVP-NCR.

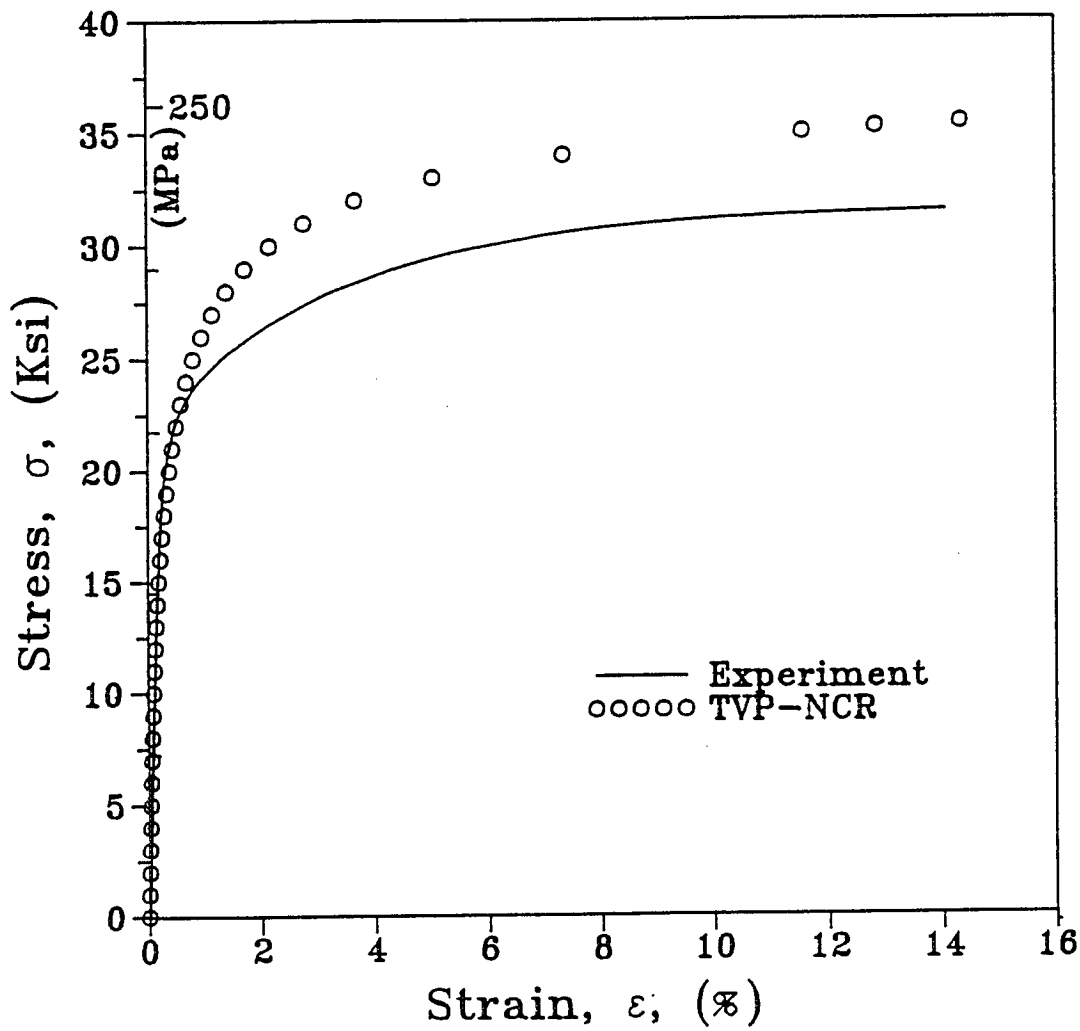

Fig. 6.9 Stress-Strain Curves for Aluminum 6061-T4 Specimen Under Uniaxial Tensile Loading at 177 °C (350 °F) as Obtained Experimentally and Predicted by the TVP-NCR.

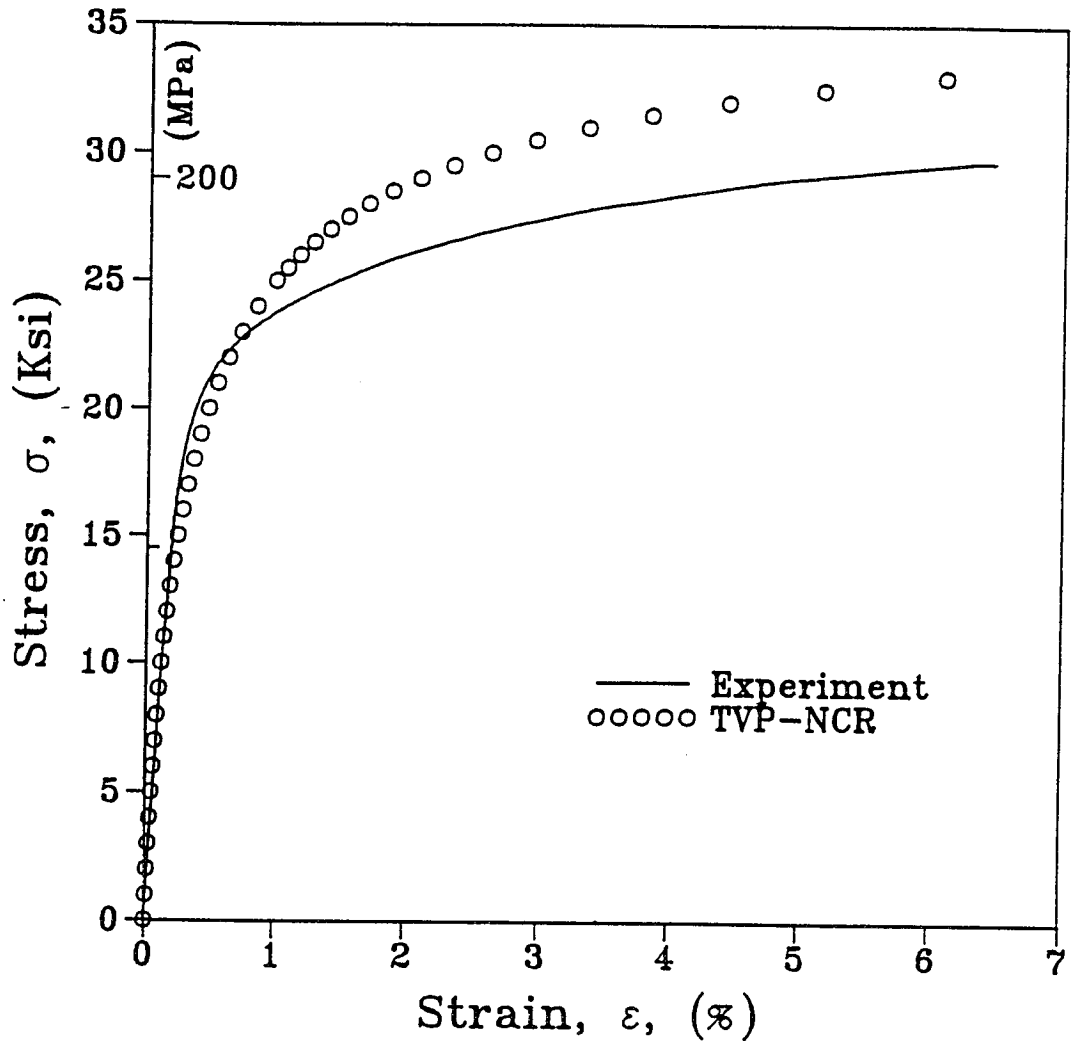

Fig. 6.10 Stress-Strain Curves for Aluminum 6061-T4 Specimen Under Uniaxial Tensile Loading at 232 °C (450 °F) as Obtained Experimentally and Predicted by the TVP-NCR.

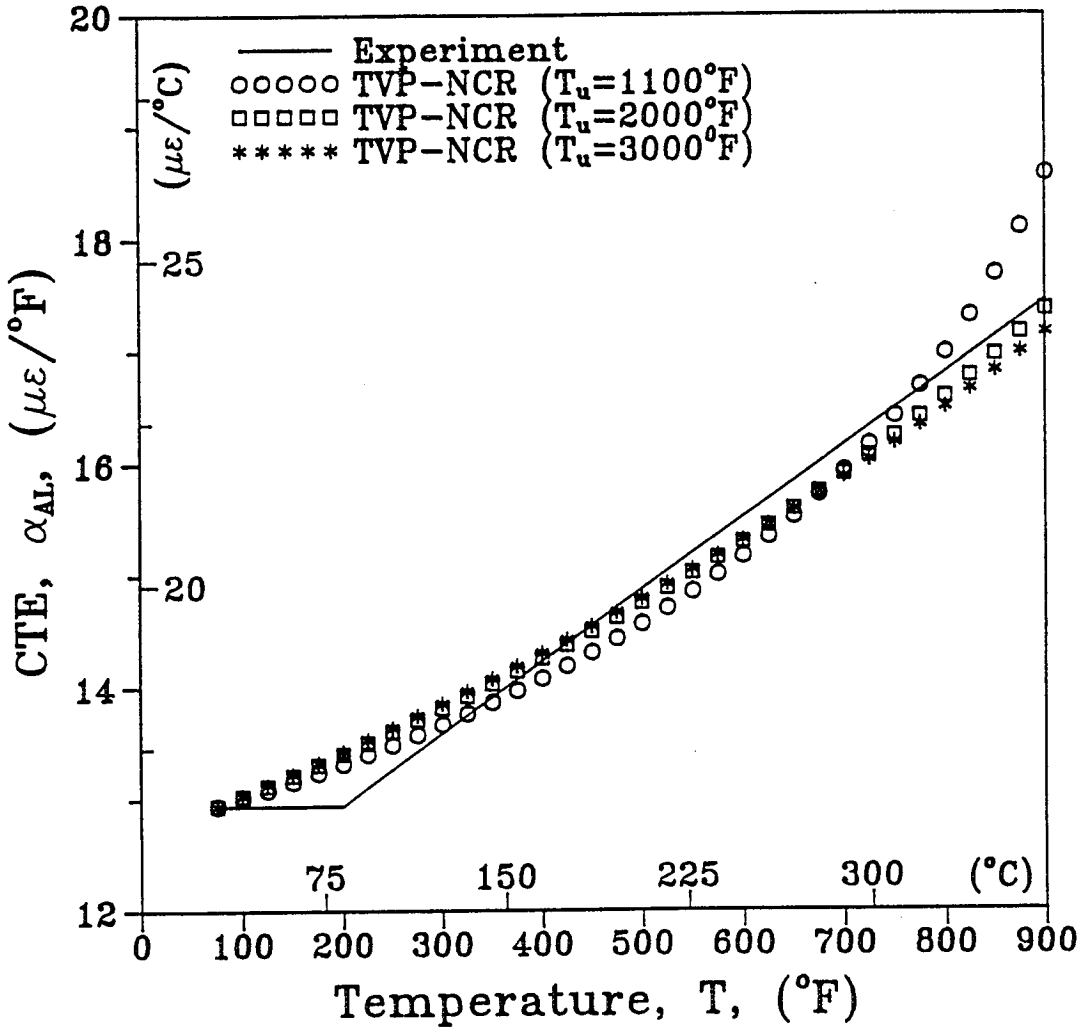

Fig. 6.11 Coefficient of Thermal Expansion versus Temperature Curves for Aluminum 6061-T4 Specimen as Obtained Experimentally and Predicted by the TVP-NCR.

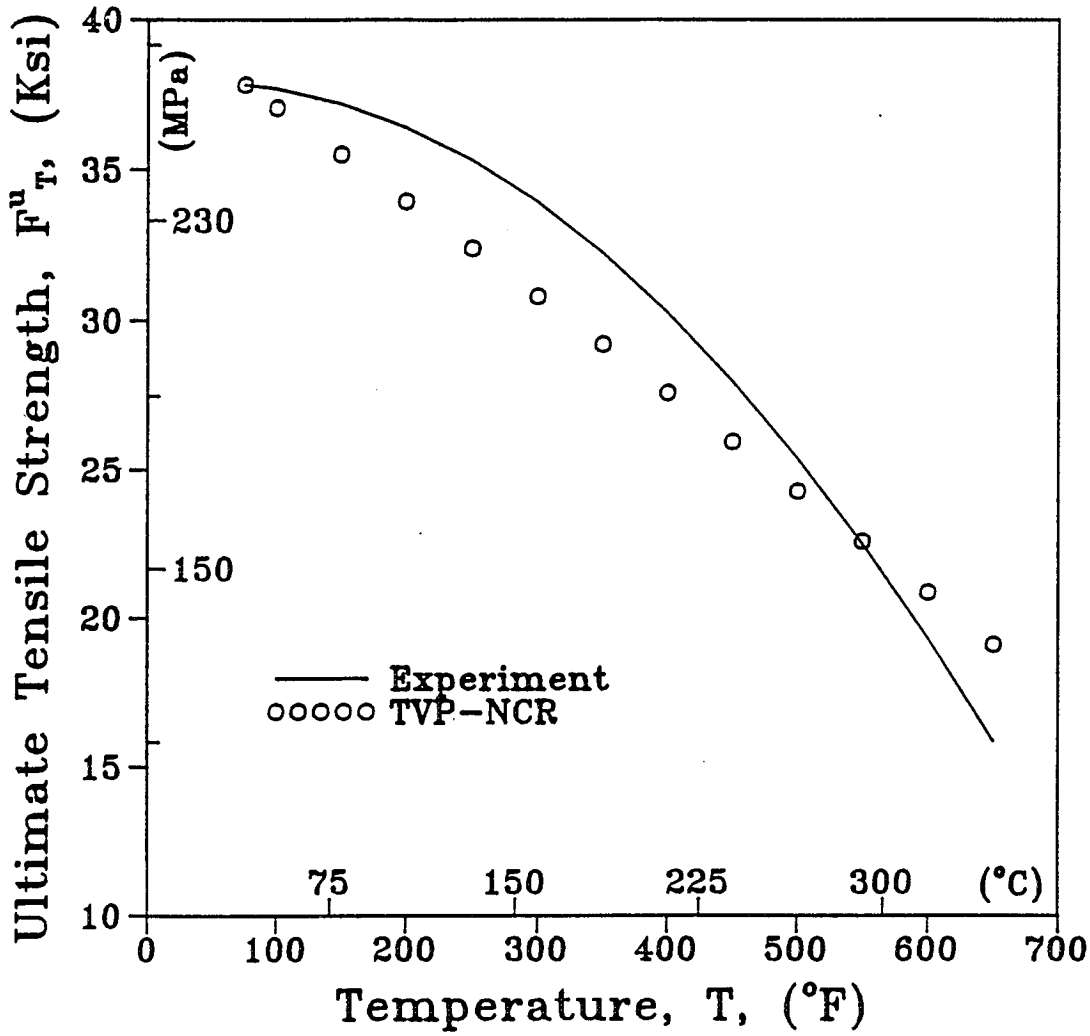

Fig. 6.12 Ultimate Stress versus Temperature Curve for Aluminum 6061-T4 Specimen as Obtained Experimentally and Predicted by the TVP-NCR.

(4) For material properties whose variation with a variable does not comply with the end conditions dictated by the TVP-NCR (the end value of a quantity should be zero or infinite) poor agreement between experimental and predicted results is obtained.

The modified TVP-NCR proposed in Section 3 were used to study two material properties (secant modulus and Poisson's ratio) which do not satisfy the end conditions of TVP-NCR developed by Chamis [17] at the ultimate value of a variable. The modified TVP-NCR used in the present analysis are of the following form:

$$\frac{\Delta P}{\Delta P_o} = \left[\frac{T_u - T}{T_u - T_o}\right]^n \left[\frac{F - \sigma}{F - \sigma_o}\right]^m \tag{6.14}$$

where,

$$\Delta P = P - P_u$$

$$\Delta P_o = P_o - P_u$$

The stress-strain curves for the SiC/A*l* $[0_8]$ and $[90_8]$ composite and Poisson's ratio versus stress curves for Aluminum 6061-T4 at two temperatures were obtained from the following equations

$$\varepsilon = \frac{\sigma}{(E_o - E_u)\left[\frac{T_u - T}{T_u - T_o}\right]^n \left[\frac{F - \sigma}{F - \sigma_o}\right]^m + E_u} \tag{6.15}$$

$$\nu = (\nu_o - 0.5)\left[\frac{T_u - T}{T_u - T_o}\right]^n \left[\frac{F - \sigma}{F - \sigma_o}\right]^m + 0.5 \tag{6.16}$$

By using equations (6.15) and (6.16) along with the recalculated values of the exponents n and m (Table 6.3) the material properties under investigation were obtained and are compared with the experimentally measured ones in Figures 6.13 through 6.17. It is seen from these figures that the predictions for the SiC/A*l* composite from the modified TVP-NCR are in very good agreement with the experimental results. In addition, it was found that the predictions from the

Table 6.3 Values of the Exponents n and m of the Modified TVP-NCR for SiC/Al Composite and Aluminum 6061-T4.

Material Property, P	Temperature, T_u °C	°F	n	m
SiC/Al Composite				
Longitudinal Secant Modulus, E_{1s}	593	1100	-0.9555	1.4698
	1093	2000	-2.0992	1.4698
	1649	3000	-3.5668	1.4698
Transverse Secant Modulus, E_{2s}	593	1100	-0.1685	0.4829
	1093	2000	-0.4487	0.4892
	1649	3000	-0.7487	0.4907
Aluminum 6061-T4				
Poisson's Ratio, ν	593	1100	3.1123	2.6180
	1093	2000	6.5084	2.6061
	1649	3000	10.2562	2.6024

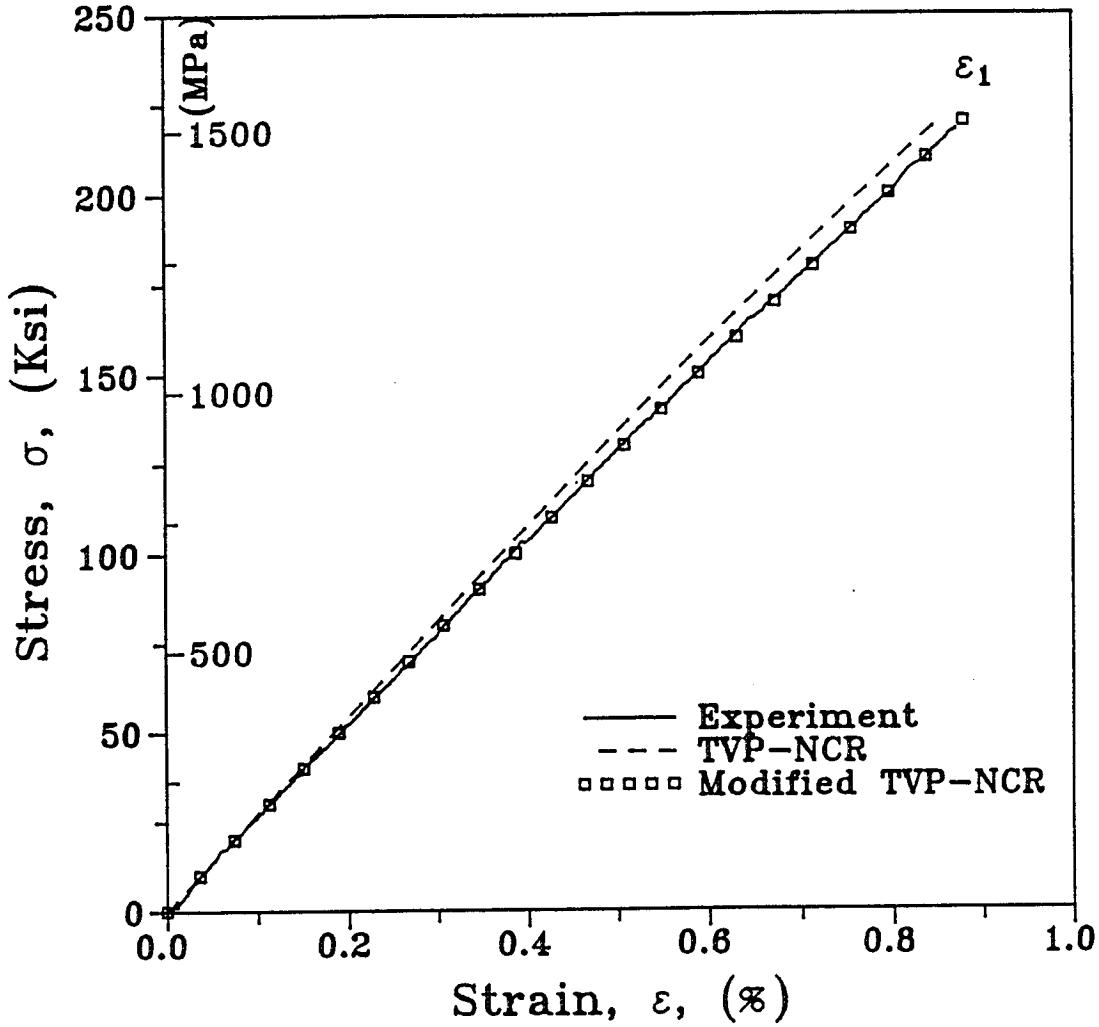

Fig. 6.13 Stress-Strain Curves for $[0_8]$ SCS-2/6061 Aluminum Composite Specimen Under Uniaxial Tensile Loading at 24 °C (75 °F) as Obtained Experimentally and Predicted by the Modified TVP-NCR.

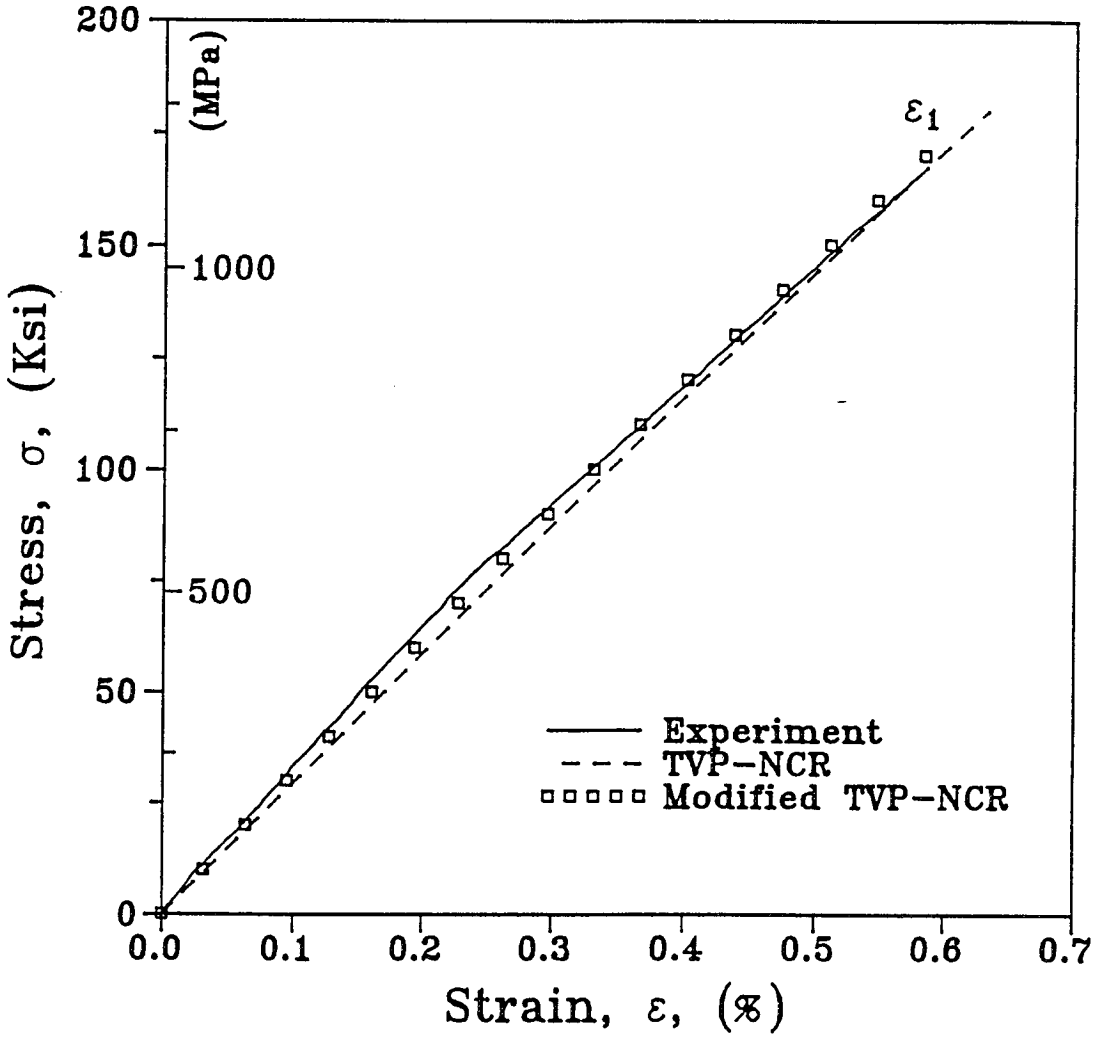

Fig. 6.14 Stress-Strain Curves for $[0_8]$ SCS-2/6061 Aluminum Composite Specimen Under Uniaxial Tensile Loading at 288 °C (550 °F) as Obtained Experimentally and Predicted by the Modified TVP-NCR.

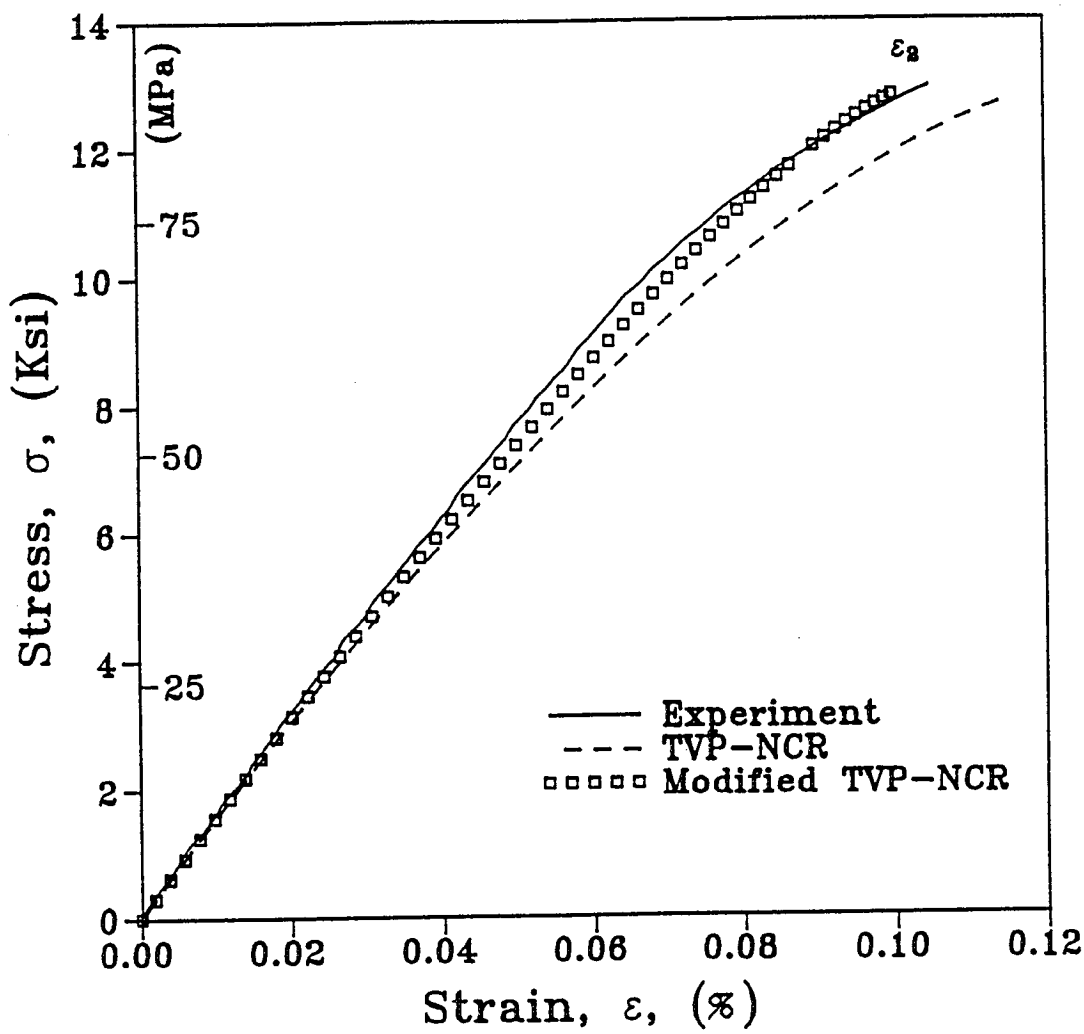

Fig. 6.15 Stress-Strain Curves for [90_8] SCS-2/6061 Aluminum Composite Specimen Under Uniaxial Tensile Loading at 24 °C (75 °F) as Obtained Experimentally and Predicted by the Modified TVP-NCR.

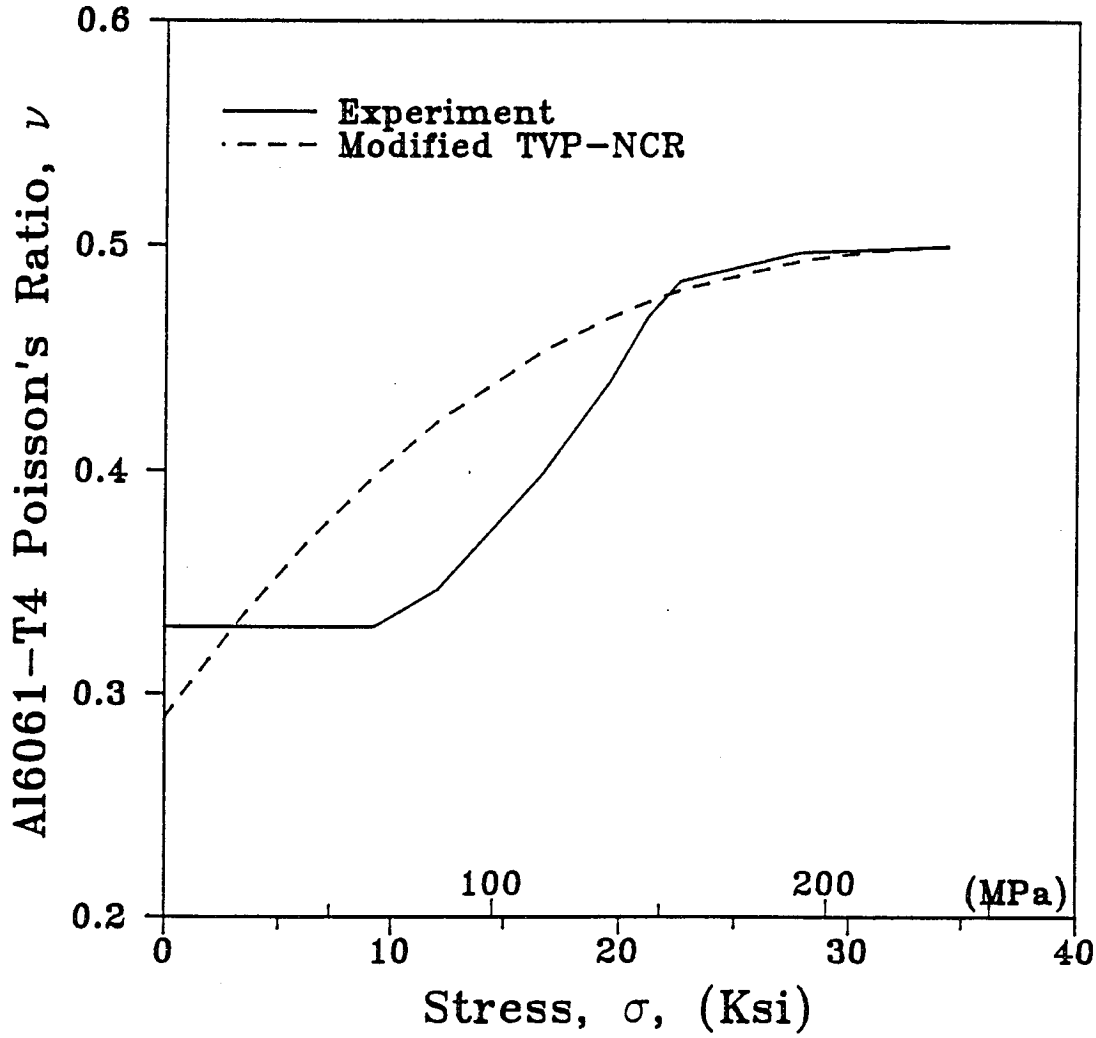

Fig. 6.16 Poisson's Ratio versus Stress Curves for Aluminum 6061-T4 Specimen at 121 °C (250 °F) as Obtained Experimentally and Predicted by the Modified TVP-NCR.

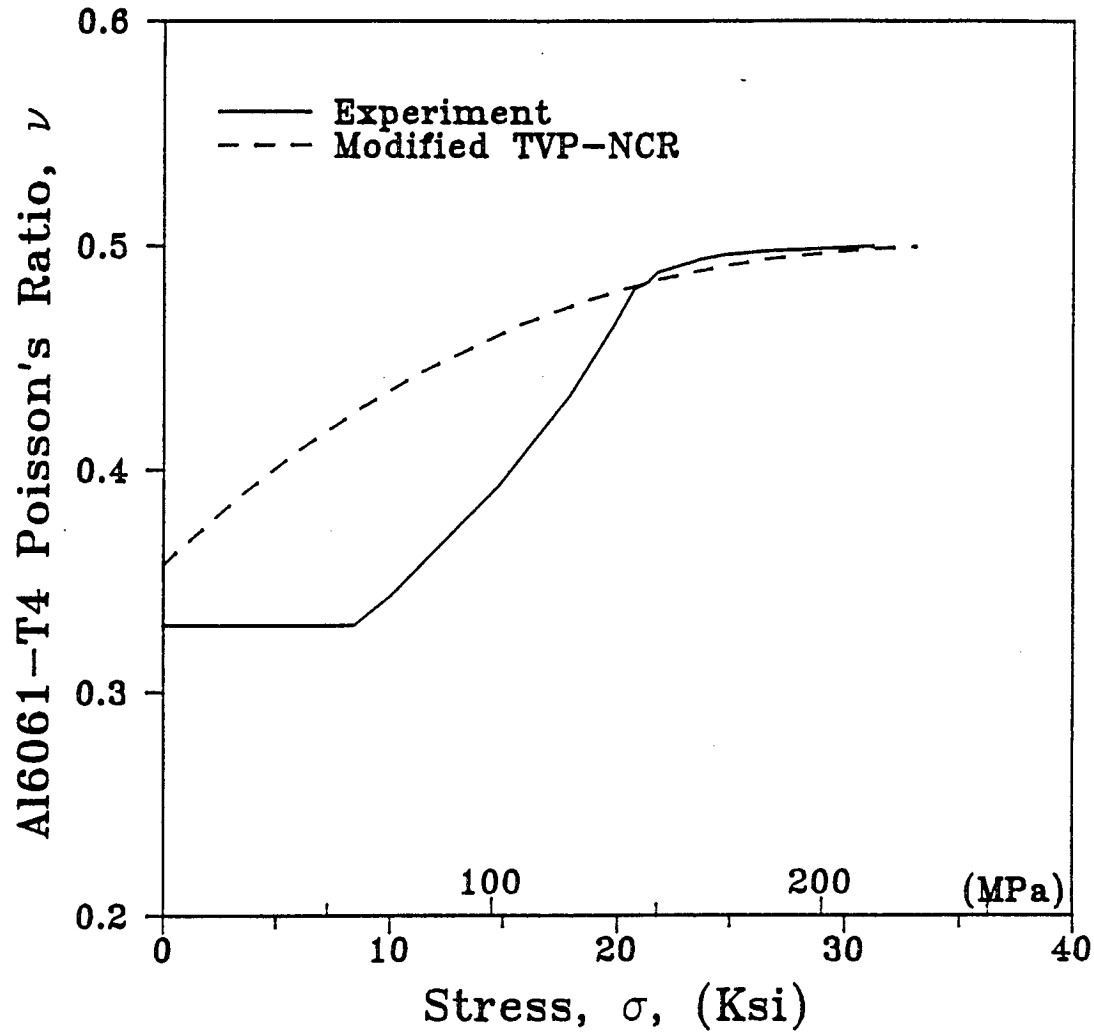

Fig. 6.17 Poisson's Ratio versus Stress Curves for Aluminum 6061-T4 Specimen at 177 °C (350 °F) as Obtained Experimentally and Predicted by the Modified TVP-NCR.

modified TVP-NCR were independent of the chosen value for ultimate temperature (T_u).

The computer code (METCAN) developed at NASA Lewis Research Center [18] to perform nonlinear analyses of fiber reinforced metal matrix composites was used for the prediction of the thermomechanical behavior of the SiC/A*l* composite under investigation. The METCAN code incorporates the TVP-NCR given by equation (6.1) Together with various levels of composite mechanics models [39] for the analysis of behavior of metal matrix composite materials and structures. Introducing the previously found values of the exponents n and m for the aluminum matrix into METCAN the longitudinal and transverse stress-strain curves of the unidirectional SiC/A*l* composite were predicted. The corresponding exponents n and m for the fiber were taken as zero in METCAN since the SiC fiber remains elastic up to failure and its thermomechanical behavior is independent of temperature. Results are shown in Figures 6.18 and 6.19 for temperatures 24° C (75° F) and 288° C (550° F), respectively. The experimental results are seen to be in good agreement with the theoretical predictions from METCAN.

Residual stresses are generated during cool-down from the fabrication temperature as a result of the large difference in thermal expansion coefficients of the silicon carbide fiber and aluminum matrix. These differences in expansion coefficient can result in compressive longitudinal and radial residual stresses in the filaments and corresponding tensile stresses in the matrix. The METCAN code was implemented to predict these stresses and to determine their influence on the behavior of the composite under subsequent loading. Results were obtained for two consolidation temperatures, 260° C (500° F) and 538 ° C (1000° F). Table 6.4 gives the axial residual stresses in the fiber and matrix as predicted by METCAN when the composite is cooled down to room temperature from these two fabrication temperatures.

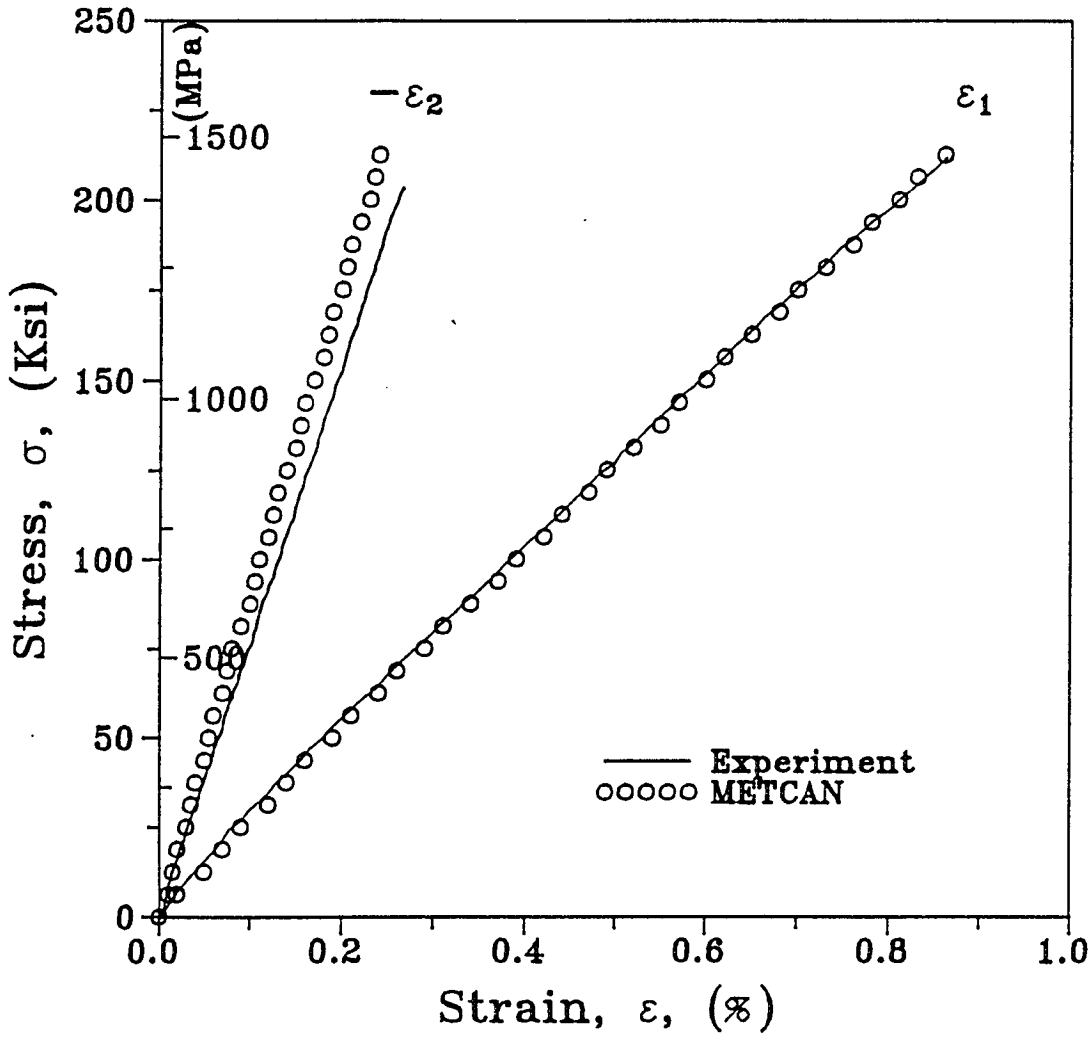

Fig. 6.18 Stress-Strain Curves for $[0_8]$ SCS-2/6061 Aluminum Composite Specimen Under Uniaxial Tensile Loading at 24 °C (75 °F) as Obtained Experimentally and Predicted by METCAN.

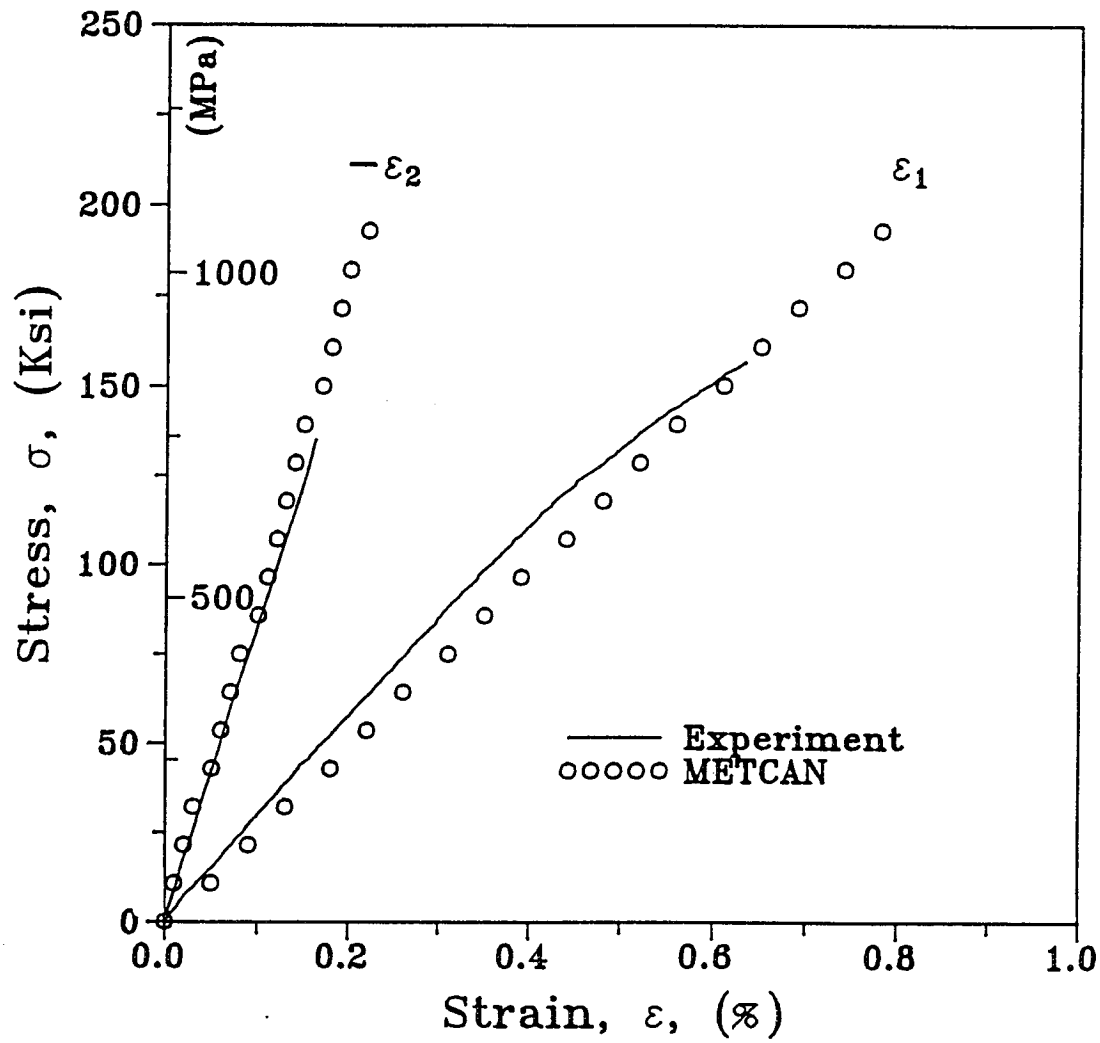

Fig. 6.19 Stress-Strain Curves for $[0_8]$ SCS-2/6061 Aluminum Composite Specimen Under Uniaxial Tensile Loading at 288 °C (550 °F) as Obtained Experimentally and Predicted by METCAN.

Table 6.4 Axial Residual Stresses in SCS-2 Fiber and Aluminum 6061-T4 Matrix as Predicted by METCAN Computer Code

Fabrication Temperature, T_f		Fiber $-\sigma^r_{zf}$		Matrix σ^r_{zm}	
°C	°F	MPa	ksi	MPa	ksi
260	500	105.24	15.26	82.76	12.00
538	1000	134.55	19.51	105.72	15.33

The influence of these residual stresses on the composite behavior is as follows. Since the filaments are initially loaded compressively, the composite failure strain in tension is higher than would be predicted if residual stresses were ignored. As the composite is loaded in tension, the filaments are initially unloaded from compression and subsequently loaded in tension. Therefore, the filament strain-to-failure is increased. In addition, since the filament tensile failure strain determines composite failure strain and consequently the tensile strength of the composite, this increased strain-to-failure will result in higher composite tensile strength. Furthermore, the initial load carrying capacity of the matrix is higher as a result of prior strain hardening. The strain hardening matrix can make a larger contribution to composite strength. These effects are shown schematically in Fig. 6.20 [54].

In Fig. 6.21 the experimentally obtained stress-strain curves of a unidirectional SiC/A*l* $[0_8]$ composite tested in tension at 24° C (75° F) are shown along with the predicted stress-strain curves from METCAN. The first predicted stress-strain curve was obtained by loading the composite without considering any previous processing history. Therefore, no residual stresses were taken into

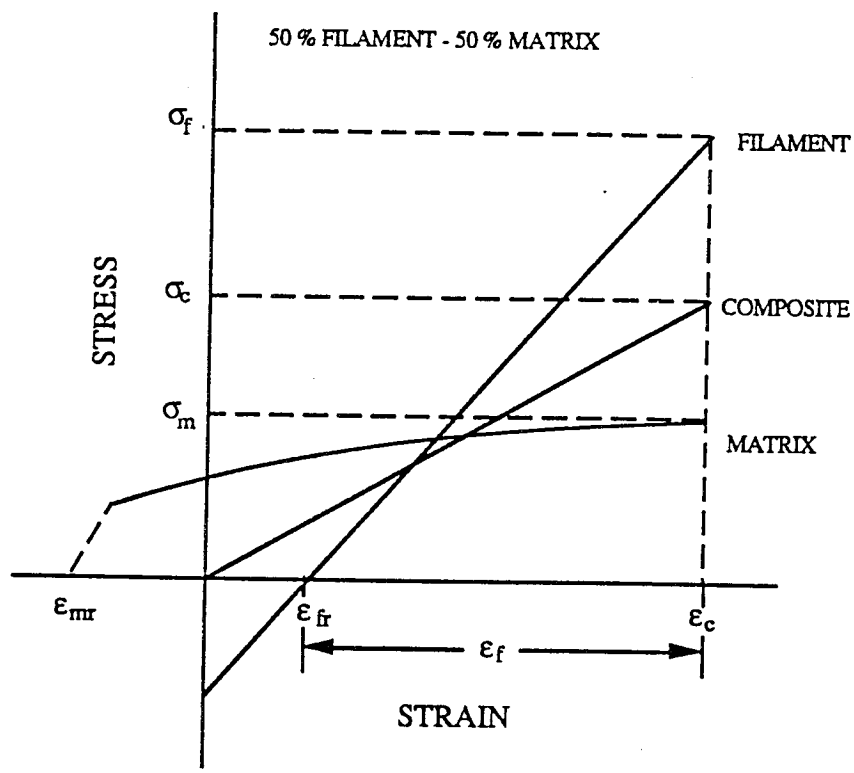

Fig. 6.20 Schematic Stress-Strain Curves for Matrix, Filament and Composite Demonstrating the Influence of Residual Stresses.

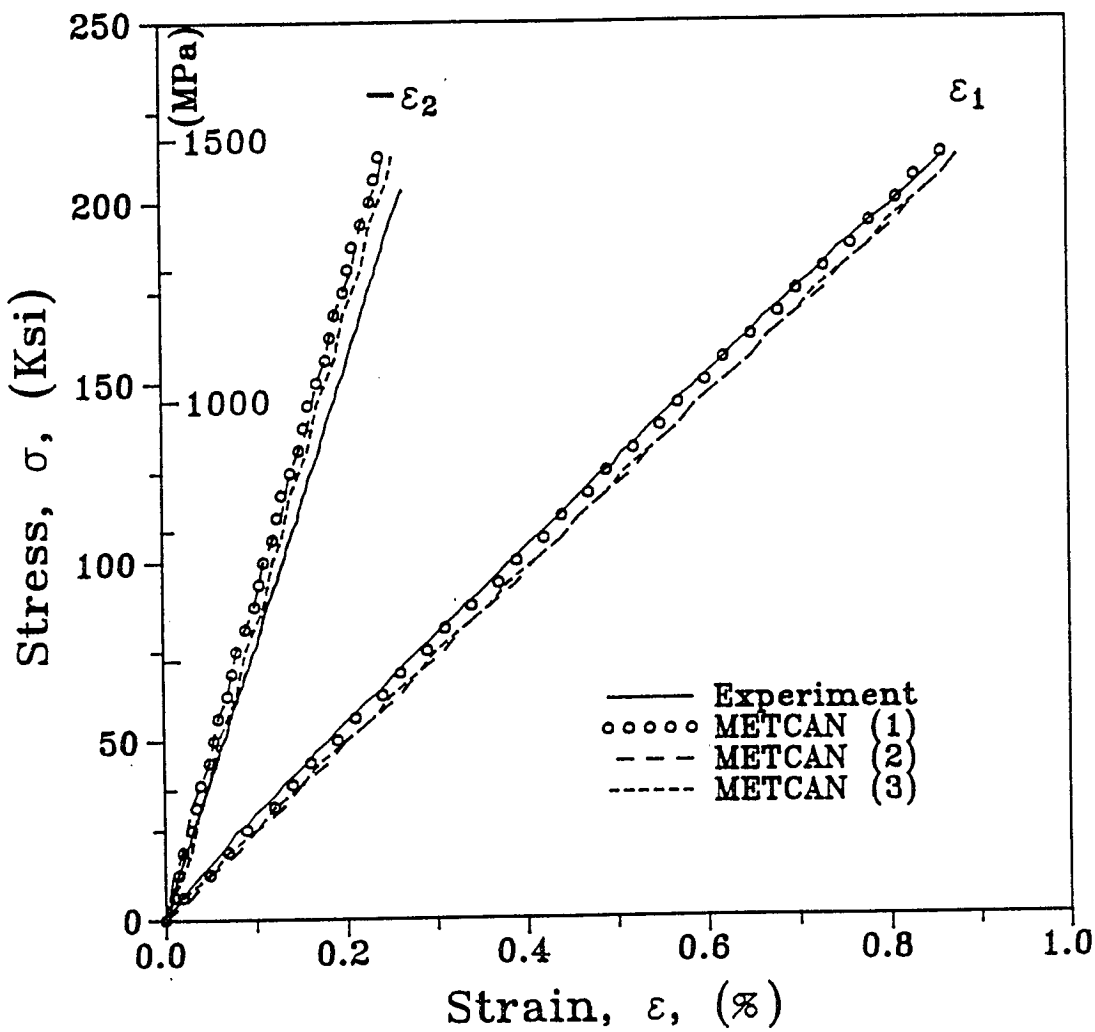

Fig. 6.21 Stress-Strain Curves for $[0_8]$ SCS-2/6061 Aluminum Composite Specimen Under Uniaxial Tensile Loading at 24 °C (75 °F) as Obtained Experimentally and Predicted by METCAN. METCAN Predictions were Made by (1) Considering No Processing History and by Accounting for Cool-Down from Fabrication Temperature of (2) 260 °C (500 °F) and (3) 538 °C (1000 °F), respectively.

account in this case. For the prediction of the second and third curves, the composite was first cooled to room temperature from fabrication temperatures of 260° C (500° F) and 538° C (1000° F) and subsequently loaded in tension to failure. It is observed in Figure 6.21 that when consolidation stresses are taken into account the predicted composite behavior exhibited no plastic deformation during subsequent loading in tension. In addition, better prediction of the composite actual behavior under tensile loading was obtained when no residual stresses were considered in METCAN. This prediction coupled with the aforementioned observation leads to the conclusion that matrix relaxation must take place in the actual composite system.

At higher temperatures the influence of residual stresses and matrix constrains are much less pronounced than at room temperature. It is seen in Figure 6.22 that both predictions (with and without residual stresses) by METCAN are in very good agreement because METCAN accounts for the relief of the fabrication-induced residual stresses when the composite is heated to its testing temperature of 288° C (550° F).

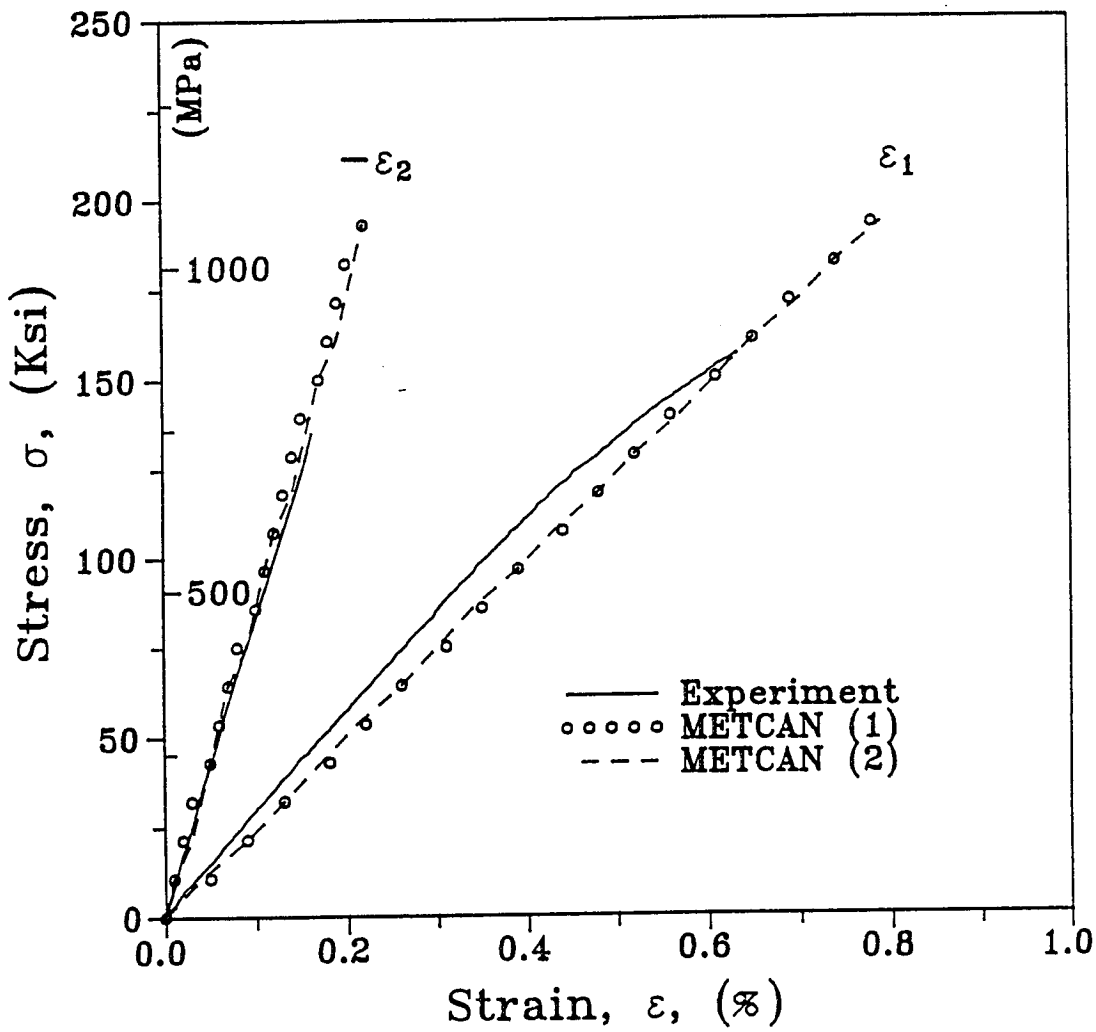

Fig. 6.22 Stress-Strain Curves for $[0_8]$ SCS-2/6061 Aluminum Composite Specimen Under Uniaxial Tensile Loading at 288 °C (550 °F) as Obtained Experimentally and Predicted by METCAN. METCAN Predictions were Made by (1) Considering No Processing History and by (2) Accounting for Cool-Down from Fabrication Temperature of 260 °C (500 °F).

7. THERMAL STRESS ANALYSIS OF SiC/Al COMPOSITE

7.1 Introduction

In the metal-matrix composite, the ceramic reinforcement and the metal matrix usually have large mismatch of thermal expansion coefficients in one or more directions. A change of temperature results in thermal constraint stresses which contribute significantly to the stress state of the constituents. For example, high residual thermal stresses are developed in the matrix during cooling from consolidation temperatures which may result in premature yielding even before application of external loading. The study of the thermal expansion behavior and the resulting thermal stresses is an important step in the characterization of the composite.

A number of studies have been devoted to the problem of thermal expansion behavior of MMC's. Levin [7] derived the macroscopic coefficients of thermal expansion (CTE's) of an elastic two-phase composite with perfectly bonded isotropic phases from the thermoelastic constants of the phases and the macroscopic elastic moduli of the composite. Bounds on the CTE's of fiber reinforced composites were given using bounds for the macroscopic elastic moduli of the composite. Expressions for CTE's of fiber reinforced composites with doubly periodic array of circular hollow or solid fibers were derived by Van Fo Fy [8,9] who performed a thorough stress analysis. Schapery [10] calculated upper and lower bounds of multiphase media by employing extremum principles of thermoelasticity. Levin's results were extended to two-phase composites with anisotropic constituents by Rosen and Hashin [11]. They also gave bounds for the CTE's of anisotropic composites with any number of anisotropic phases. Dvorak and Chen [12] presented exact expressions for the CTE's of a composite consisting of three cylindrical perfectly bonded phases having transverse isotropy and arbitrary transverse geometry.

The above works were concerned with the micromechanical prediction of the linear thermal expansion behavior of composites. However, when the composite is subjected to temperatures above a critical value, plastic stresses are developed in the matrix and the strain versus temperature curve of the composite becomes nonlinear. A relatively limited number of investigations has dealt with the problem of nonlinear thermal expansion behavior of composites. Hoffman [13] studied the elastic and elastoplastic stresses in tungsten fiber reinforced 80 Ni + 20 Cr matrix composites subjected to heating or cooling in the range of 27 to 1090° C (80 to 2000° F). Dvorak et al. [14] determined the initial yield surfaces of boron/aluminum composites for mechanical and thermal loading using a finite element analysis of a regular hexagonal array model. They found that small temperature changes in the range of 10 to 38° C (50 to 100° F) can introduce plastic strains in composites with a matrix tensile yield stress of the order of 10 ksi. These plastic strains were proportional to the yield stress. Flom and Arsenault [1] determined experimentally the plastic strains and the elastic-plastic boundaries produced in the aluminum matrix around a short SiC cylinder during a thermal cycle and developed a theoretical model for the prediction of the plastic zone. Kural and Min [15] presented an elastoplastic theoretical model for the study of plastic deformation in the matrix material of graphite fiber reinforced metal matrix composites caused by thermal cyclic loading and residual thermal stresses. Experimental results verified the elastoplastic stresses predicted by the theory. In another paper Min and Crossman [16] used the above theoretical model for the study of the thermomechanical behavior of Gr/A*l* composites. Gdoutos et al. [55] developed two elastoplastic micromechanical models for thermal stress analysis, one based on a one-dimensional rule of mixtures and the other on a composite cylinder. An elastoplastic analysis was also conducted by Chun et al. [56] based

on a successive approximation scheme with a Prandtl-Reuss plastic flow model and the von Mises criterion.

7.2 Rule of Mixtures Model (ROM) [55]

A one-dimensional rule-of-mixtures (ROM) model was used for the prediction of the thermal expansion behavior of the composite based on the constituent properties. Emphasis was placed on the prediction of the nonlinear part of the longitudinal and transverse strain-temperature curves.

The silicon carbide fiber is assumed to be isotropic and linear elastic up to failure. Its stress-strain-temperature behavior is given by

$$\varepsilon_f = \frac{\sigma_f}{E_f} + \alpha_f \, \Delta T \tag{7.1}$$

where ε_f and σ_f are the axial strain and stress, E_f the modulus of elasticity, α_f the CTE and ΔT the temperature change. It is assumed that α_f is constant.

The aluminum matrix has a yield point much lower than the fracture stress of the fiber and exhibits a pronounced plastic deformation prior to fracture. Its thermomechanical behavior is described by the Ramberg-Osgood equation:

$$\varepsilon_m = \frac{\sigma_m}{E_m} + \alpha_m \, \Delta T \qquad \sigma_m \le \sigma_{my} \tag{7.2a}$$

$$\varepsilon_m = \frac{1}{E_m}\left[\sigma_m + \beta\left[\left(\frac{\sigma_m}{\sigma_{my}}\right)^n - 1\right]\sigma_{my}\right] + \alpha_m \, \Delta T \qquad \sigma_m > \sigma_{my} \tag{7.2b}$$

where ε_m and σ_m are the strain and stress, E_m the modulus of elasticity, σ_{my} the proportionality limit of aluminum, β and n material parameters and α_m the coefficient of thermal expansion. The quantities σ_{my}, β, n and α_m are functions of temperature.

From the isostrain hypothesis and the equilibrium equation along the fiber direction the longitudinal stresses in the fiber, $\sigma^e{}_f$, and the matrix, $\sigma^e{}_m$, for linear elastic behavior are given by

$$\sigma_f^e = \frac{(\alpha_m - \alpha_f) E_f E_m V_m \Delta T}{E_m V_m + E_f V_f} \tag{7.3}$$

$$\sigma_m^e = -\frac{(\alpha_m - \alpha_f) E_f E_m V_f \Delta T}{E_m V_m + E_f V_f} \tag{7.4}$$

where V_f and V_m are the volume fractions of the fiber and matrix, respectively.

The temperature at which the matrix starts to deform plastically is determined from the relation

$$\sigma_m^e = \sigma_{my} \tag{7.5}$$

For higher temperature changes the matrix yields and the stress σ_m in the matrix is determined from the following equation

$$\left(\beta\, \sigma_{my}{}^{1-n}\right) \sigma_m^n + \left[1 + \left(\frac{E_m}{E_f}\right)\left(\frac{V_m}{V_f}\right)\right] \sigma_m + \left[(\alpha_m - \alpha_f) E_m \Delta T - \beta\, \sigma_{my}\right] = 0 \tag{7.6}$$

The stress in the fiber is given by

$$\sigma_f = -\sigma_m \left(\frac{V_m}{V_f}\right) \tag{7.7}$$

Having determined the stresses in the matrix and the fiber the longitudinal strain of the composite is determined from either equation (7.2a) or (7.2b). The transverse strain of the composite is calculated by

$$\varepsilon_t = \varepsilon_{tf} V_f + \varepsilon_{tm} V_m \tag{7.8}$$

where the transverse strains in the fiber, ε_{tf}, and the matrix, ε_{tm}, are given by

$$\varepsilon_{tf} = -\frac{\nu_f}{E_f} \sigma_f + \alpha_f \Delta T \tag{7.9a}$$

$$\varepsilon_{tm} = -\frac{\nu_m}{E_m} \sigma_m + \alpha_m \Delta T \tag{7.9b}$$

where ν_f and ν_m are Poisson's ratios of the fiber and matrix, respectively. While ν_f is constant, ν_m increases in the nonlinear range from its elastic value up to the limiting value of 0.5 for an incompressible material. In the transition region ν_m is determined as follows [57]:

$$\nu_m = 0.5 - (0.5 - \nu'_m)\frac{E_s}{E} \tag{7.10}$$

where ν'_m is the elastic value of Poisson's ratio and E and E_s are the elastic and secant moduli, respectively.

7.3 Composite Cylinder Model (CCM) [55]

In the two-material composite cylinder model (CCM), the representative volume element for the micro-mechanical analysis of low fiber volume composites consists of an inner solid cylinder, simulating the fiber, and an outer hollow cylinder, representing the matrix (Fig. 7.1). A fiber-reinforced composite is arbitrarily characterized as low fiber volume if the fiber volume ratio is less than 65 percent. It is assumed that the two components are perfectly bonded at the interface. The CCM has been proposed by Hill [58], Hashin and Rosen [59] and Whitney and Riley [60]. The model has been used for the study of the elastoplastic behavior of two- and three-material composite cylinders by Hecker et al. [61,62]. In the present study the CCM is used for the study of the thermal expansion behavior of a SiC/A*l* composite. The cases of elastic and elastoplastic deformation of the matrix cylinder are considered separately. The inner cylinder always remains linearly elastic.

When both components of the composite cylinder are linearly elastic, the following equations for the radial displacement u, the radial and circumferential stresses σ_r and σ_θ and the axial stress σ_z are obtained from the thermoelastic solution [61].

$$\begin{aligned} u &= Ar + \frac{B}{r} \\ \sigma_r &= K\left[A - (1 - 2\nu)\frac{B}{r^2} + \nu\,\varepsilon_z - (1 + \nu)\,\alpha\Delta T\right] \\ \sigma_\theta &= K\left[A + (1 - 2\nu)\frac{B}{r^2} + \nu\,\varepsilon_z - (1 + \nu)\,\alpha\Delta T\right] \end{aligned} \tag{7.11}$$

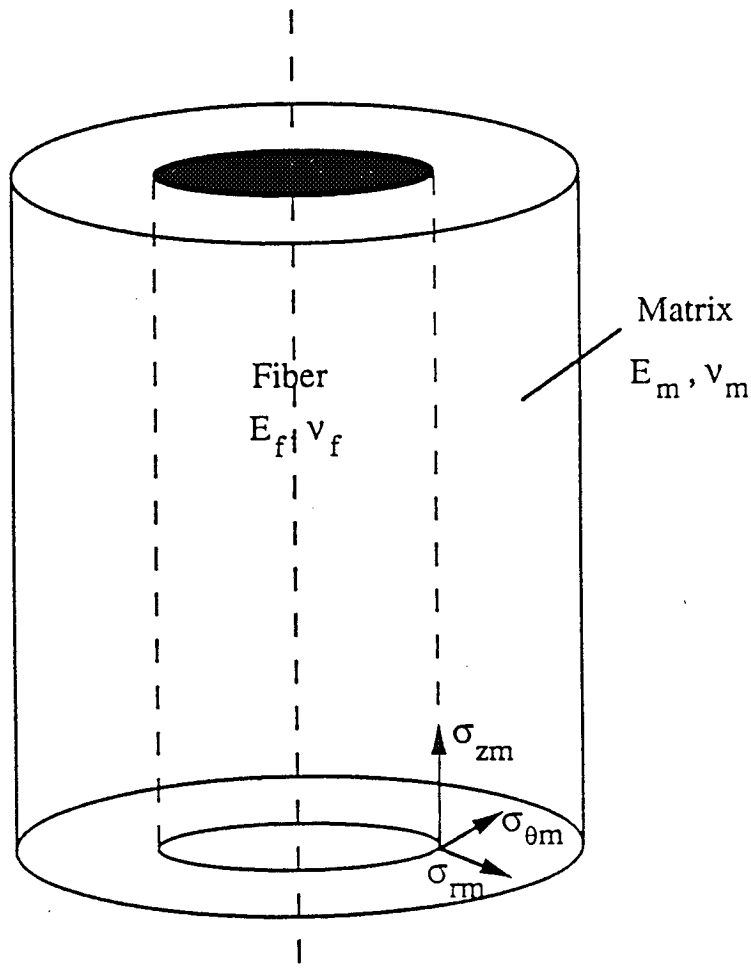

Fig. 7.1 A Single Fiber Surrounded by its Matrix Shell.

$$\sigma_z = K\left[2\nu A + (1 - \nu)\ )\ \varepsilon_z - (1 + \nu)\,\alpha\Delta T\right]$$

In these equations r is the radial distance from the center of the cylinder, ε_z is the axial strain, A and B are constants to be determined from the boundary conditions of the problem and K is the bulk modulus.

The boundary conditions of the problem imply continuity of the radial displacement u and the radial stress σ_r along the boundary of the two materials. Furthermore, they should be finite at r = 0. Finally, on the outer surface the radial stress σ_r is assumed to be zero.

For a temperature change ΔT, the constants A_j, B_j (j = 1,2 refer to the inner and outer cylinder, respectively) and the axial strain ε_z are determined from the following matrix equation:

$$\begin{bmatrix} R_1 & -R_1 & -R_1^{-1} & 0 \\ K_1 & -K_2 & (1 - 2\nu_2)\,K_2R_1^2 & K_1\nu_1 - K_2\nu_2 \\ 0 & K_2 & -(1 - 2\nu_2)\,K_2R_2^{-2} & K_2\nu_2 \\ 2\nu_1K_1R_1^2 & 2\nu_2K_2(R_2^2-R_1^2) & 0 & K_1(1 - \nu_1)R_1^2 + K_2(1 - \nu_2)(R_2^2 - R_1^2) \end{bmatrix} \begin{bmatrix} A_1 \\ A_2 \\ B_2 \\ \varepsilon_z \end{bmatrix}$$

$$\begin{bmatrix} 0 \\ K_1(1 + \nu_1)\,\alpha_1 - K_2(1 + \nu_2)\,\alpha_2 \\ (1 + \nu_2)\,\alpha_2 K_2 \\ K_1(1 + \nu_1)\,\alpha_1 R_1^2 + K_2(1 + \nu_2)\,\alpha_2(R_2^2 - R_1^2) \end{bmatrix} \Delta T \qquad (7.12)$$

with $B_1 = 0$. R_1 and R_2 denote the radii of the inner and outer cylinders, respectively.

After determination of A_j, B_j and ε_z, the stresses and radial displacement in the two materials are calculated by equations (7.11).

The elasticity solution of the problem is used in conjunction with the von Mises yield criterion for the determination of the critical temperature at which the most stressed elements of the matrix along the fiber-matrix interface enter into the plastic domain of deformation. This temperature is determined from equation

$$\sigma_{eff} = \sigma_{my} \tag{7.13}$$

where σ_{eff} is given by

$$\sigma_{eff} = \frac{1}{\sqrt{2}}\left[(\sigma_z - \sigma_r)^2 + (\sigma_r - \sigma_\theta)^2 + (\sigma_\theta - \sigma_z)^2\right]^{1/2} \tag{7.14}$$

The stress σ_{my}, the proportional limit of aluminum, is a function of temperature.

When the temperature is increased beyond a critical value, plastic zones in the form of concentric cylindrical layers starting from the fiber-matrix interface are developed in the aluminum cylinder. The deformation in the aluminum becomes inhomogeneous and an elastic-plastic analysis is required for the determination of the stress components and the extent of the elastic-plastic boundary.

The deformation theory of plasticity is used in conjunction with the von-Mises yield criterion and the isotropic hardening rule for the solution of the elastic-plastic problem. The fundamental assumption made is that the effective stress-strain curve $\sigma_{eff} = f\,(d\varepsilon_{eff})$ for an element in a triaxial state of stress coincides with the stress-strain curve in uniaxial tension. The effective strain is defined as

$$d\varepsilon_{eff} = \frac{1}{\sqrt{2}(1 + \nu_m)}\left[(d\varepsilon_z - d\varepsilon_r)^2 + (d\varepsilon_r - d\varepsilon_\theta)^2 + (d\varepsilon_\theta - d\varepsilon_z)^2\right]^{1/2} \tag{7.15}$$

where the value of Poisson's ratio ν_m is determined from equation (7.10).

The stress-strain relations take the form

$$d\varepsilon_z = \frac{1}{E_t}[d\sigma_z - \nu(d\sigma_r + d\sigma_\theta)]$$

$$d\varepsilon_r = \frac{1}{E_t}[d\sigma_r - \nu(d\sigma_\theta + d\sigma_z)] \qquad (7.16)$$

$$d\varepsilon_\theta = \frac{1}{E_t}[d\sigma_\theta - \nu(d\sigma_z + d\sigma_r)]$$

where $d\varepsilon_z$, $d\varepsilon_r$ and $d\varepsilon_\theta$ are the total, elastic plus plastic, strain increments and $d\sigma_z$, $d\sigma_r$ and $d\sigma_\theta$ are the stress increments. E_t is the tangent modulus of the uniaxial stress-strain curve of the material in tension after the proportional limit . In the elastic region E_t is equal to the modulus of elasticity. For a work-hardening material beyond the proportional limit, E_t decreases gradually as plastic deformation advances.

Equations (7.16) along with the equations of equilibrium and compatibility are used for the solution of the elastic-plastic problem. It is thus evident that the deformation theory of plasticity is actually a nonlinear elasticity theory with changing values of modulus of elasticity and Poisson's ratio depending on the amount of plastic deformation. This observation led to the following solution of the elastic-plastic problem of the composite cylinder: The aluminum ring was divided into N concentric layers with each layer having different elastic modulus and Poisson's ratio. An elasticity analysis of an N+1 material composite cylinder was then performed following an analogous procedure as in the case of the two-material cylinder. This solution served as a subroutine to a computer program written for the elastoplastic solution of the problem [63]. Having determined the critical temperature at which the first layer at the fiber-matrix interface yields, the temperature is increased in small steps. For each step, the tangent modulus and Poisson's ratio of each layer are determined from the value of the equivalent strain

in conjunction with the uniaxial stress-strain curve of the material in tension. For each layer, stresses and strains are determined at a representative point at the middle of its thickness. An iterative analysis was performed for each temperature step until convergence was achieved. For each temperature, the values of tangent modulus and Poisson's ratio for each layer were updated according to the value of the equivalent strain. In this way the complete history of stress and strain along the radius of the composite cylinder was determined as the temperature was increased incrementally. The flow chart for the computational procedure used is shown in Fig. 7.2.

7.4 Results and Discussion (ROM and CCM)

The analyses made use of the constituent properties described in Section 3.

The post yield stress-strain curve of aluminum was represented by a polynomial of the form

$$\sigma = \sum_{n=0}^{5} C_n \varepsilon^n$$

where the coefficients C_n are temperature-dependent. They were determined at various temperatures and then a least squares regression analysis was performed to obtain the functions $C_n = C_n(T)$.

Both the ROM and CCM micromechanical models discussed before were used. For the two-material composite cylinder model, the outer radius R_2 was taken equal to 1.51 R_1 which corresponds to a fiber volume ratio of 0.44. For the elastoplastic analysis the matrix cylinder was divided into eight layers each of thickness equal to 0.064 R_1. The critical temperature at which the aluminum matrix starts to deform plastically was first determined by the two micromechanical models. It was found that $(\Delta T)_{cr}$ = 74°C and 66°C (165°F and 150°F) for the ROM and CCM models, respectively.

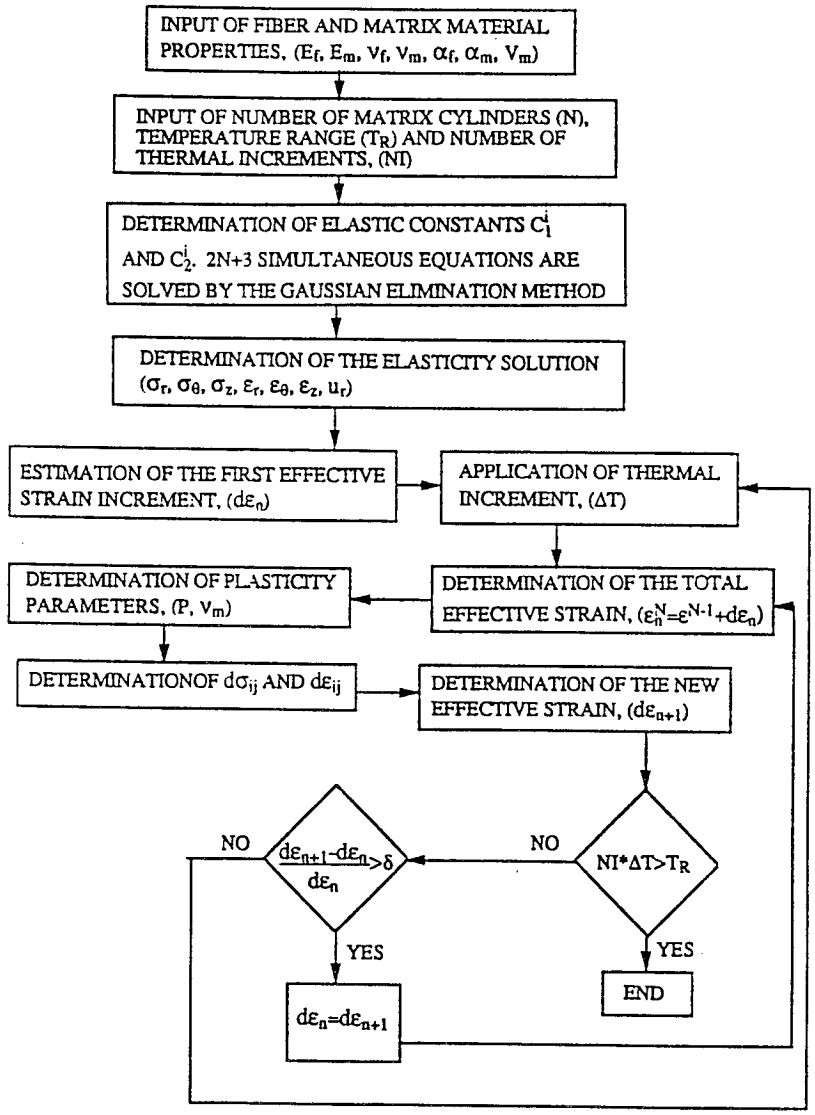

Fig. 7.2 Flow Chart of the Composite Cylinder Thermal Loading Program.

In the CCM an incremental stress-strain analysis based on the deformation theory of plasticity as described previously was performed. The temperature was increased in steps of 13.89°C (25° F) and the complete three-dimensional stress distribution at the midpoint of the thickness of each layer of the aluminum ring was determined.

Predictions of the longitudinal and transverse thermal strain of the composite by the ROM and the CCM are shown in Fig. 7.3 by circles and asterisks, respectively, together with the experimental results. The variation of the two CTE's α_1 and α_2 with temperature as it was determined experimentally and predicted by the two models is shown in Fig. 7.4. From Figs.7.3 and 7.4 it is observed that the theoretical predictions are in good agreement with the experimental results for both the longitudinal and transverse strains. Furthermore, it can be seen that the predictions based on the CCM are closer to experimental results than those of the ROM. This result is attributed to the fact that, in the CCM, the complete three-dimensional stress distribution is considered, while in the ROM, the effect of transverse stresses is omitted and only the longitudinal stresses are accounted for.

Figure 7.5 shows the variation of the axial, σ_z, radial, σ_r, and circumferential, σ_θ, stresses along half the radius of the CCM for ΔT = 79°C (175°F). All three stress components are constant in the fiber, while they vary along the thickness of the ring. The axial stress is tensile in the fiber and compressive in the matrix with increasing magnitude from the fiber/matrix interface to the outer radius of the composite cylinder. The radial stress is tensile in both the fiber and matrix, while the circumferential stress is tensile in the fiber and compressive in the matrix. In the fiber it is equal to the radial stress, while in the matrix it takes its maximum value at the fiber/matrix interface. Note that high transverse stresses of the same order of magnitude as the axial stress are developed

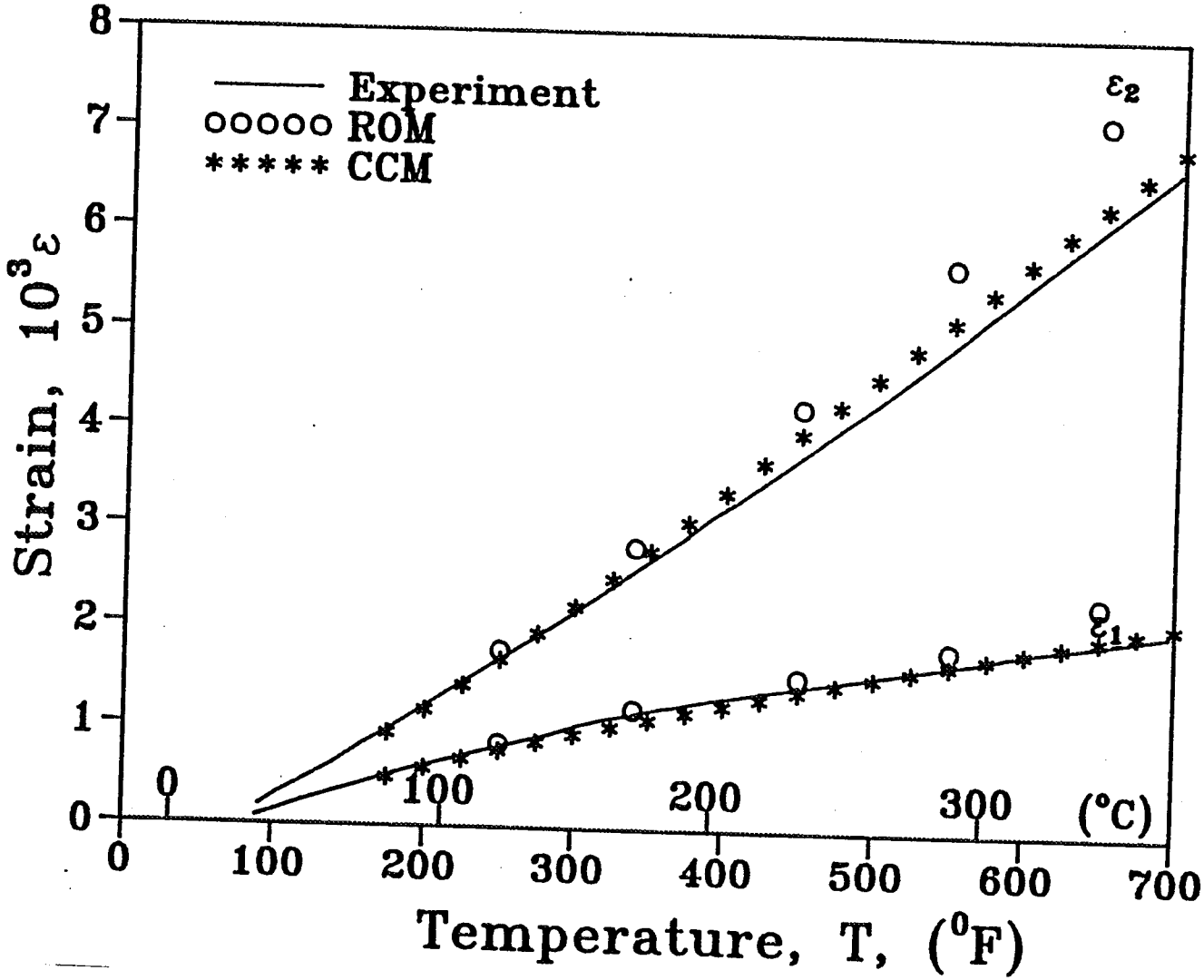

Fig. 7.3 Longitudinal, ε_1, and transverse, ε_2, strain versus temperature curves as obtained by experiment and predicted by the rule of mixtures and the composite cylinder models.

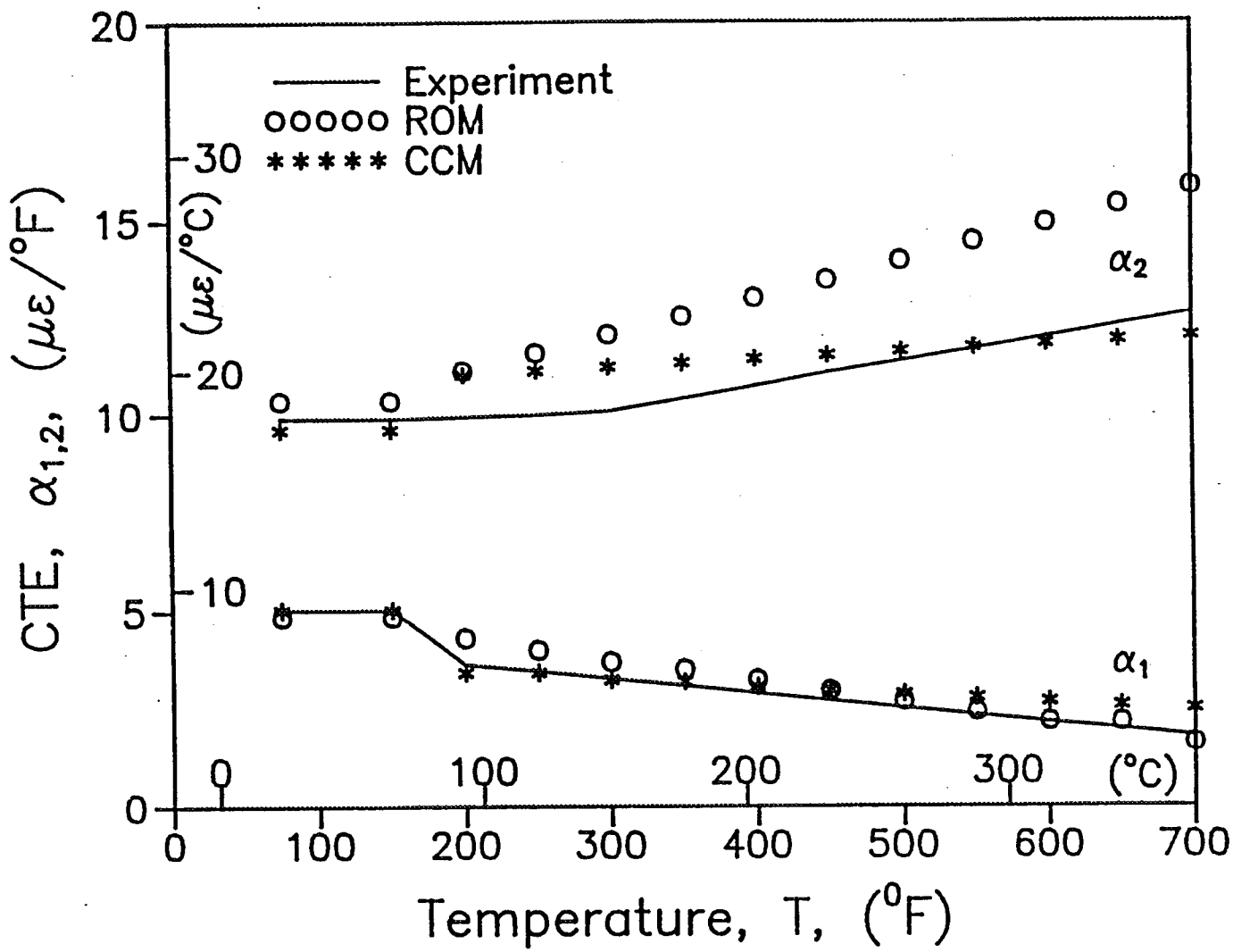

Fig. 7.4 Variation of the two CTE's α_1 and α_2 with temperature according to experiment and theoretical predictions by the ROM and CCM models.

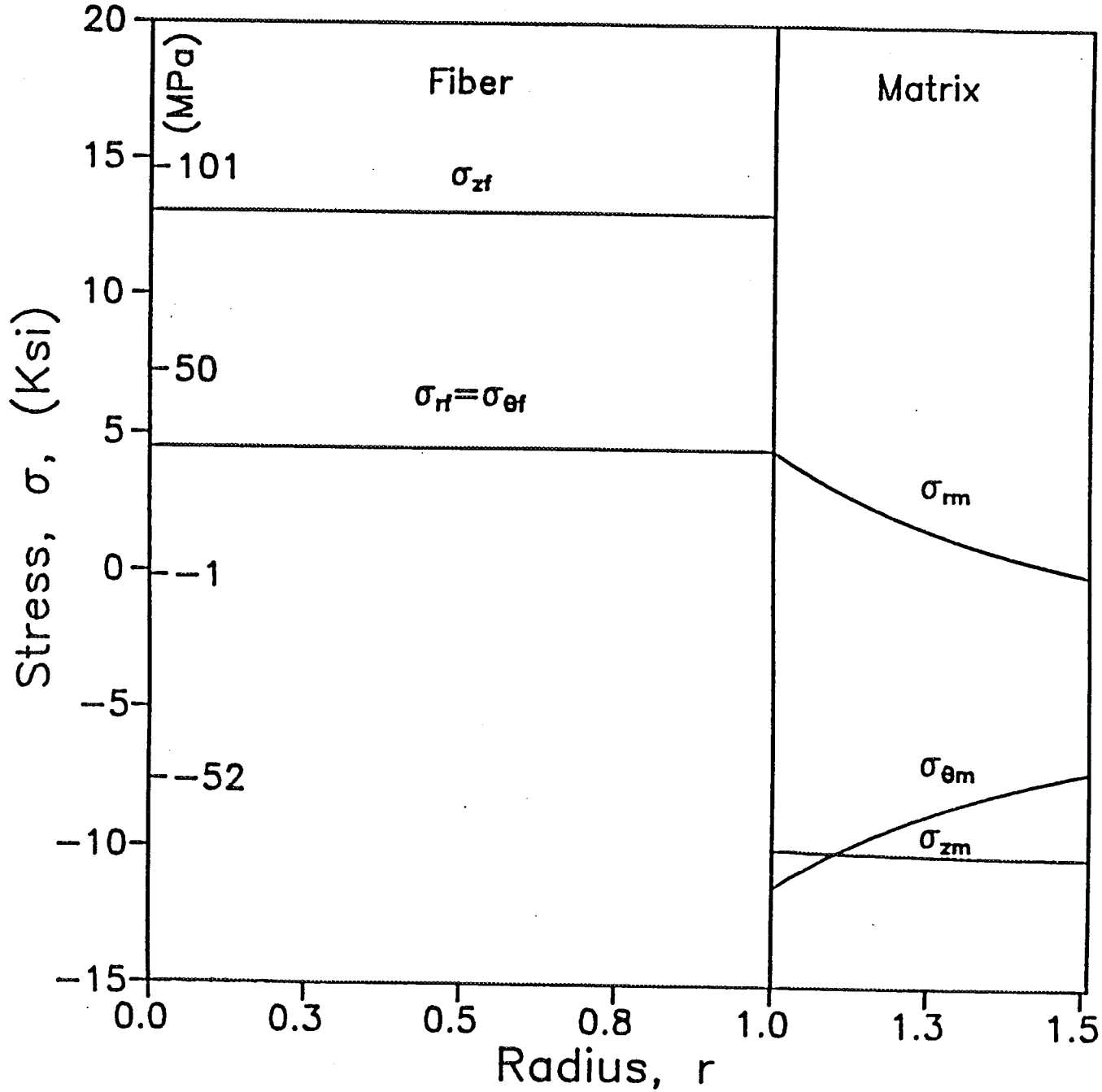

Fig. 7.5 Variation of the axial, $\sigma_{zf,m}$, radial $\sigma_{rf,m}$ and circumerential $\sigma_{\theta f,m}$ stresses in the fiber and matrix along half the fiber/matrix cross section for a temperature difference $\Delta T = 79°$ C (175° F)

in the matrix and the fiber. These stresses are ignored in the ROM model. The variation of the σ_r, σ_θ and σ_z stresses along the thickness of the aluminum matrix for various temperatures is shown in Figs. 7.6 to 7.8. In Fig. 7.8 the variation of σ_z stress is shown in a piecewise form, as it was determined in the eight layers of the matrix along which it is constant. Observe from Figs. 7.6 to 7.8 that all stresses increase with temperature but with a decreasing rate. The variation with temperature of the stress components σ_z in the fiber and the matrix (σ_{zf} and σ_{zm}) according to the CCM and the ROM models and the stress $\sigma_{rf} = \sigma_{\theta f}$ in the fiber according to the CCM is shown in Fig. 7.9. Note that the stresses approach a plateau as the temperature approaches 370°C (700°F). The axial stress predicted by the two models differs by approximately 15 percent at high temperatures. Finally, Fig. 7.10 shows the variation of the effective strain ε_{eff} along the thickness of the matrix for different temperatures. This strain decreases from the fiber/matrix interface toward the outer radius of the composite cylinder and increases with temperature.

The main results of the present investigation may be summarized as follows:

1. Above a critical temperature of 66°C (150°F) the longitudinal and transverse thermal strains become nonlinear resulting in decreasing longitudinal and increasing transverse CTE's with temperature.

2. The beginning of nonlinearity of the strain-temperature curves coincides with the development of plastic deformation in the aluminum matrix.

3. Elastic-plastic micromechanical analyses based on the rule of mixtures and the composite cylinder model were developed. In the analysis the changing material properties of the aluminum matrix, including the stress-strain curve and the CTE, were taken into consideration.

4. The complete three-dimensional stress distribution in both the fiber and

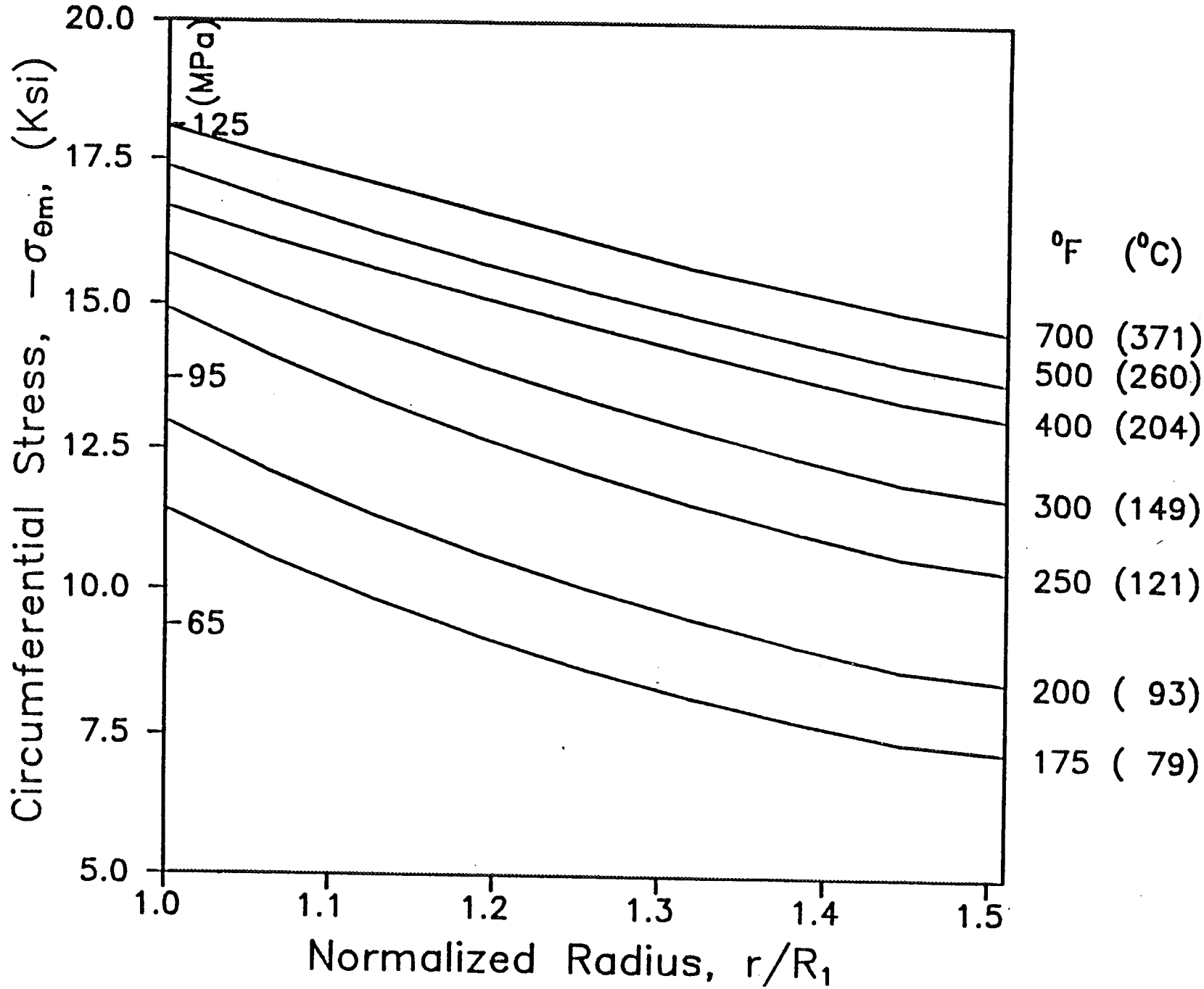

Fig. 7.6 Variation of the circumferential stress $-\sigma_{\theta m}$ along the thickness of the matrix at different

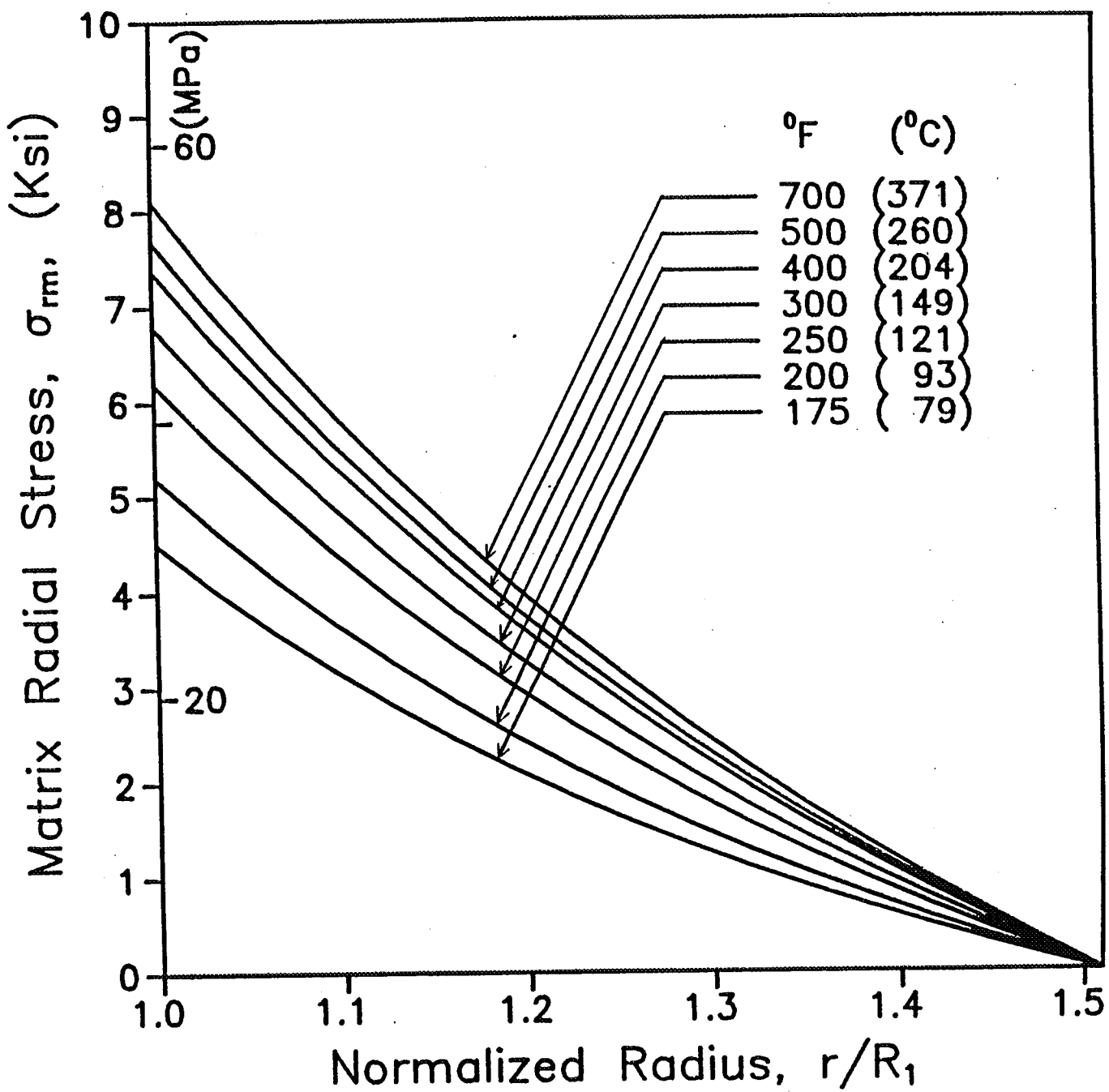

Fig. 7.7 Variation of the radial stress σ_{rm} along the thickness of the matrix at different temperatures as predicted by the CCM.

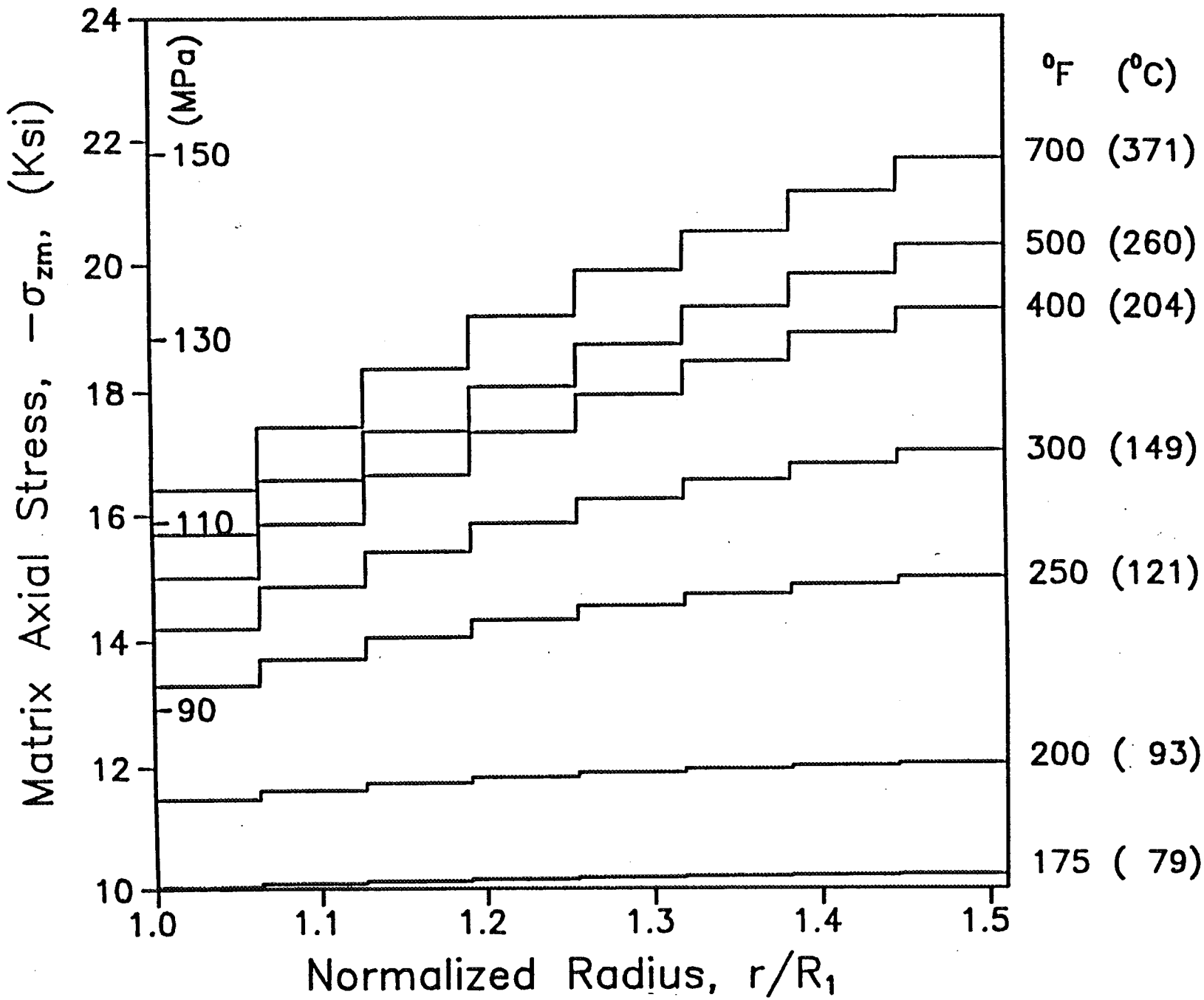

Fig. 7.8 Variation of the axial stress - σ_{zm} along the thickness of the matrix at different temperatures as predicted by the CCM.

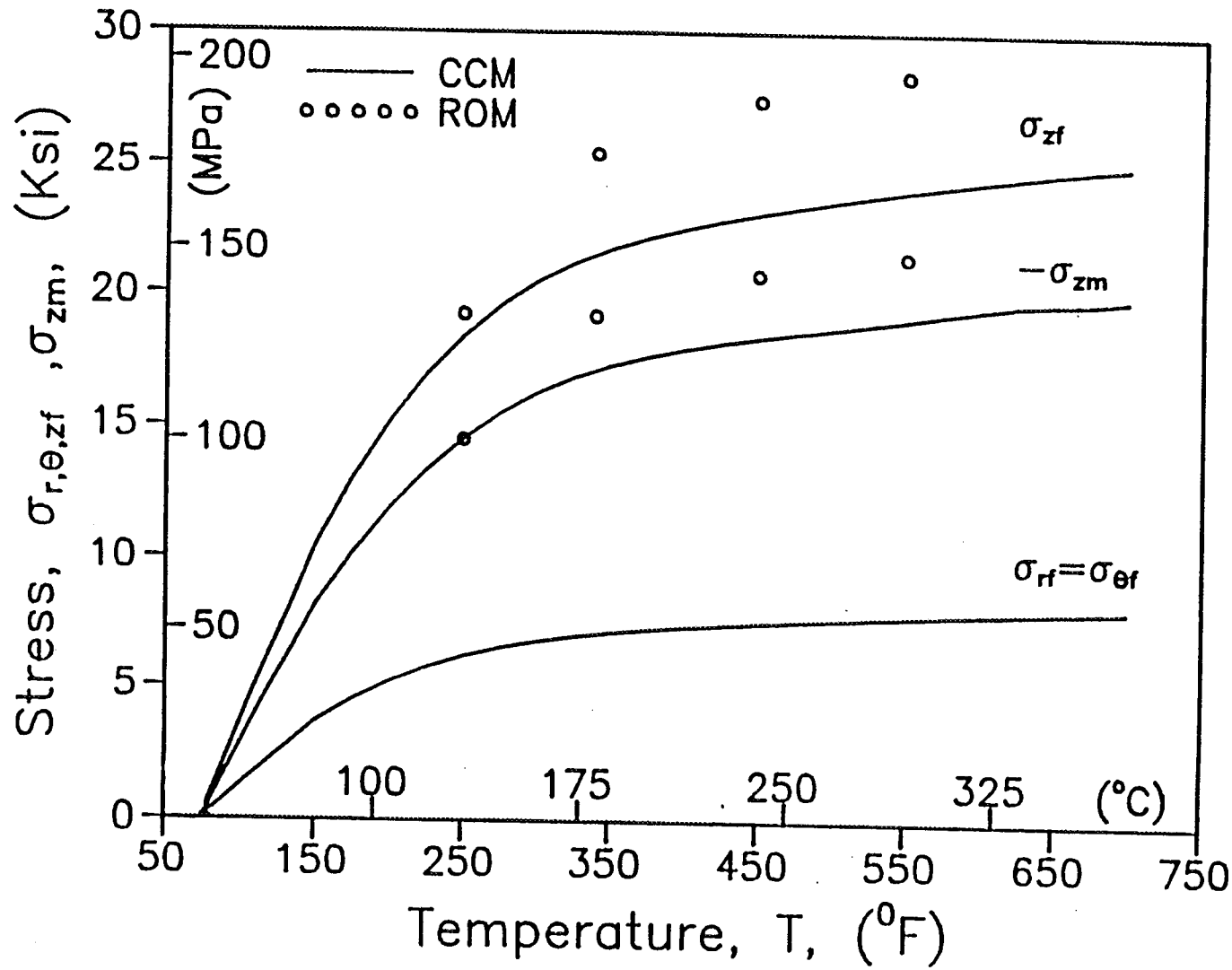

Fig. 7.9 Variation of the axial stress in the fiber, σ_{zf}, and the matrix, σ_{zm}, predicted by the CCM and the ROM models and the radial, σ_{rf}, and circumferential, $\sigma_{\theta f}$, stresses in the fiber versus temperature. σ_{zm} for the CCM is the axial stress at the mid point of the thickness of the aluminum phase.

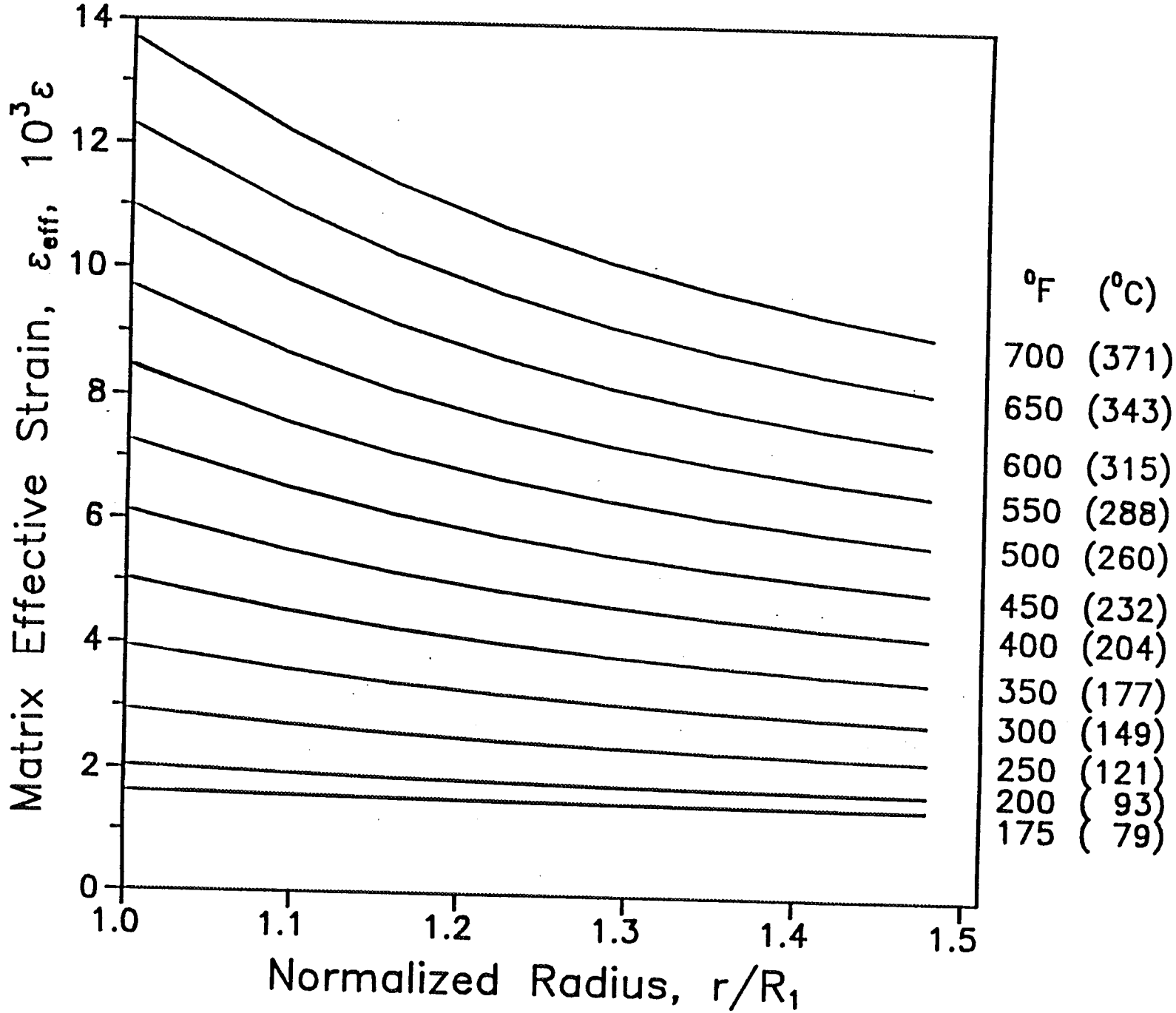

Fig. 7.10 Variation of the matrix effective strain ε_{eff} along the thickness of the matrix at different temperatures as predicted by the CCM

the matrix was determined from the micromechanical analysis.

5. High triaxial stresses above the critical temperature resulting in plastic deformation of the matrix were developed. Plastic stresses are higher at the fiber/matrix interface and decrease away from it.

6. The transverse radial and circumferential stresses in the fiber and the matrix predicted by the CCM are of the same order of magnitude as the axial stresses and should not be ignored. These stresses are responsible for the development of excessive plastic yielding in the matrix. The ROM model does not take into account the transverse stresses.

7. The axial and transverse stresses developed in the fiber and matrix increase with temperature and approach limiting values.

8. Theoretical predictions by both models and the experimental results for the longitudinal CTE were in satisfactory agreement. However, for the transverse CTE the predictions of the CCM are much closer to the experimental values than those of the ROM model. Deviations between the predictions of the ROM model and experimental results are large at higher temperatures.

7.5 Thermo-elastoplastic Analysis Model [56]

A thermo-elastoplastic analytical model was developed for prediction of the three-dimensional state of residual stress in the SiC/A*l* composite. The full development and description of the analytical model is included in Appendix A. The analysis was based on the coaxial cylinder model with perfect interfacial bonding. It was assumed that the fiber is linear elastic and temperature-independent and the matrix is elastoplastic following the power law strain hardening model. The residual stress-free temperature was assumed to be 288° C (550° F), i.e., 0.6 of the absolute melting temperature of aluminum, because above this temperature stress relaxation relieves the residual stress buildup.

Figure 7.11 shows the distribution of thermal residual stresses in the fiber and matrix at various temperatures. All residual stress components in the fiber are constant with radial distance and compressive. In the matrix, the radial stress is compressive whereas the circumferential and axial stresses are tensile. Matrix plastic flow reduces the residual stress buildup significantly. Figure 7.12 shows the variation with temperature of the longitudinal and transverse thermal strains compared with experimental measurements.

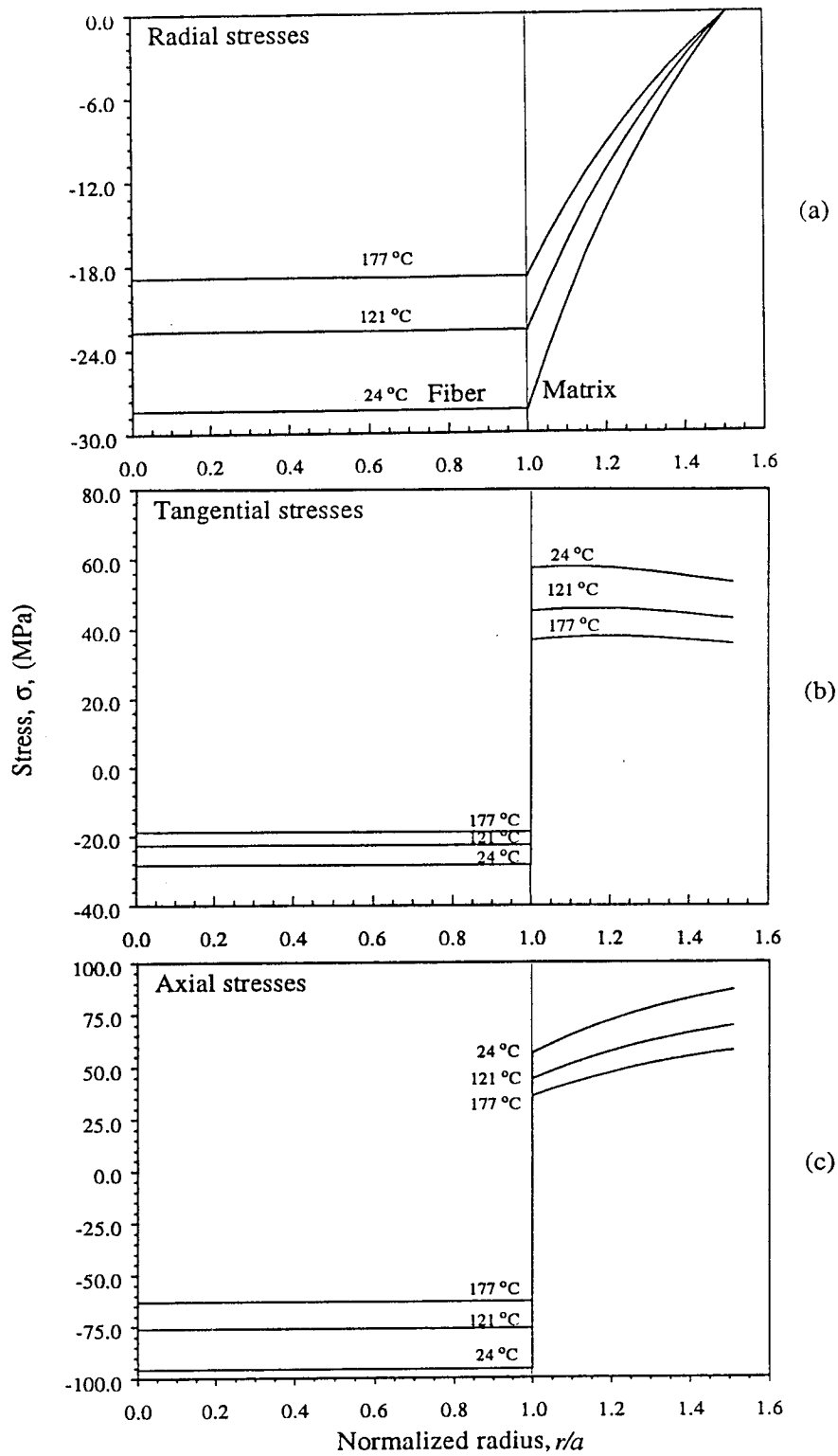

Fig. 7.11 Thermal Residual Stress Distributions in the Fiber and Matrix as a Function of Normalized Radius at Various Temperatures.
(a) Radial, (b) Tangential, (c) Axial Stresses

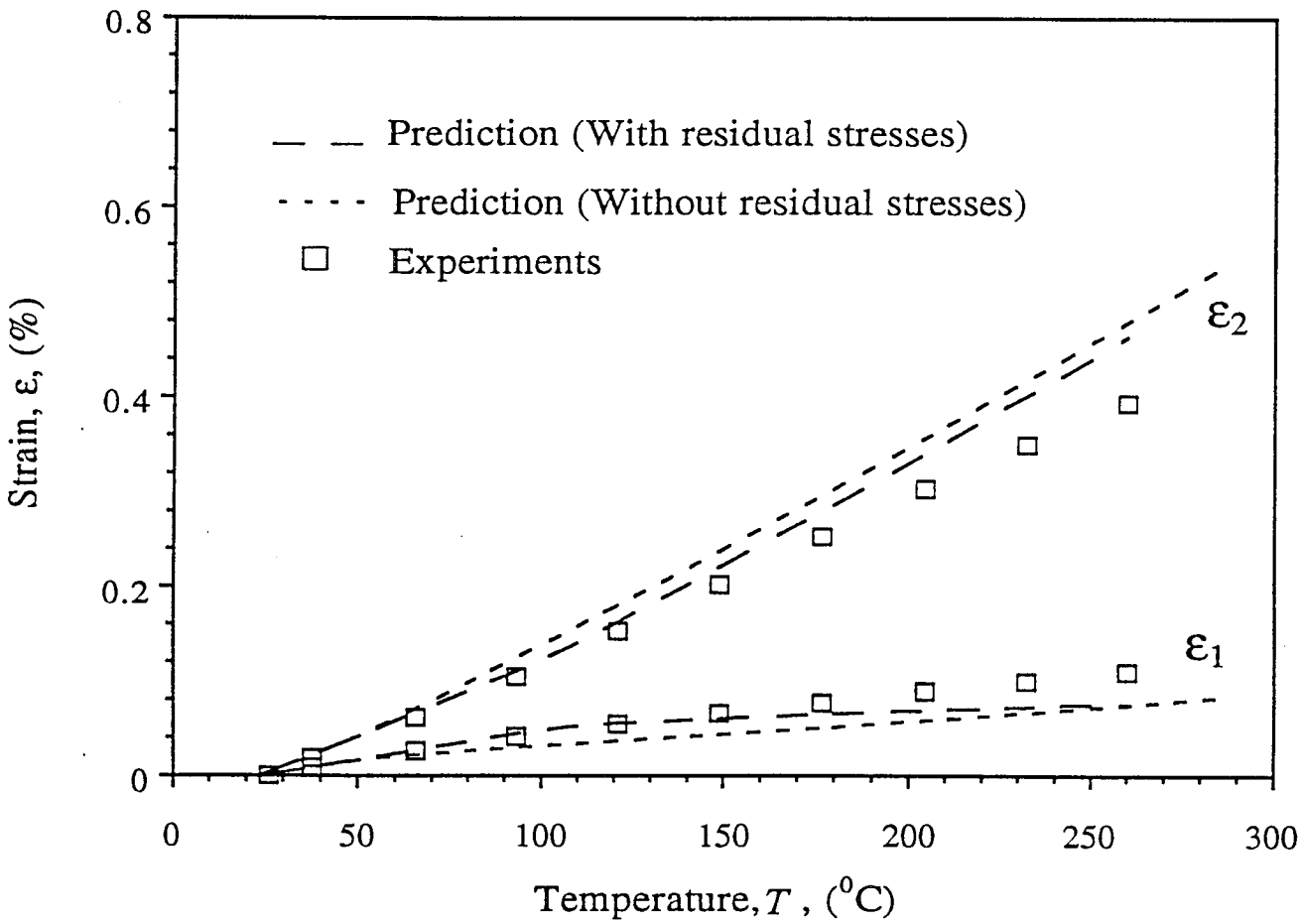

Fig. 7.12 Longitudinal and Transverse Thermals Strains versus Temperature for Unidirectional SiC/Al Composite

8. THERMOMECHANICAL ANALYSIS OF SiC/Al COMPOSITE

8.1 Introduction

Metal matrix composites reinforced with continuous elastic fibers may experience a pronounced degree of inelastic deformation when subjected to thermomechanical loading. This inelastic behavior is indicative of the overall nonlinear stress-strain or strain-temperature response of the composite. The state of stress in the matrix is no longer homogeneous and it depends on the history of deformation and the strain rate. A number of different micromechanical approaches which give not only the overall behavior of the composite but also the detailed stress state in the constituent materials have been proposed.

Shaffer [64, 65] developed a simple strength of materials analysis to predict the longitudinal and transverse stress-strain curves of a unidirectional composite containing elastic fibers in a nonlinear matrix material. Hill [66] studied the average moduli of fiber composites in which the matrix exhibits elastoplastic behavior. The finite element method has been applied extensively to analyze micromechanical models of fibrous composites exhibiting elastoplastic deformation. Lin et al. [67] performed an elastic-plastic analysis using finite elements in conjunction with the Prandtl-Reuss incremental plasticity equation to analyze filamentary composites subjected to longitudinal loading. Adams [68] studied the response to transverse loading of a unidirectional composite with nonlinear matrix using a finite element program. A nonlinear finite element analysis of a composite under shear and transverse loading based on triangular elements and regularly-spaced inclusion arrays has been performed by Foye [36]. Finite element studies for the investigation of the behavior of unidirectional composites with matrix material exhibiting inelastic behavior have been conducted by Adams and Miller [69]. A three-dimensional finite element code for the elastoplastic analysis of fiber-reinforced composite materials and structures has been developed by Bahei-El-Din

et al. [70]. This code uses a continuum material model for elastic-plastic analysis developed by Bahei-El-Din and Dvorak [71, 72]. A finite element analysis of a regular hexagonal array model was used by Dvorak et al. [14] for the construction of initial yield surfaces of boron/aluminum composites subjected to arbitrary combinations of applied stress and temperature.

A class of micromechanical models for the study of elastoplastic fibrous, particulate and hybrid composite systems based on a hexagonal array geometry have been presented by Dvorak and Teply [73]. Upper and lower bounds of the instantaneous stiffnesses of the composite were obtained. A two-material composite cylinder model has been proposed by Hill [74], Hashin and Rosen [59] and Whitney and Riley [60] for micromechanical analysis. The model was used for the study of the elastoplastic behavior of two- and three-material composite cylinders by Hecker et al. [61,62]. A mechanics of materials elastoplastic model for the investigation of the thermomechanical behavior of metal matrix composites has been proposed by Min and Crossman [16]. The matrix was considered as an elastic-perfectly plastic material. A continuum model for the prediction of the overall behavior of filamentary composites with elastoplastic constituents has been proposed by Aboudi [75,76]. The model is based on the assumption that the continuous fibers are arranged in a doubly periodic array and employs the unified theory of Bodner and Partom for the description of the inelastic behavior of the matrix. Explicit constitutive relations between the average stresses and elastic and inelastic strains were given. This model was also used by Pindera et al [77,78] for the prediction of the elastoplastic response of boron/aluminum and graphite/aluminum composites under combined loading. A review of several elastoplastic models for fibrous composites was given by Bahei-El-Din and Dvorak [79]. Sun and co-workers [80,81] presented an orthotropic plasticity model to describe the elastoplastic behavior of metal matrix composites. The model is

derived from a plastic potential function of the stress components which has a quadratic form. Gdoutos et al. [82] used an elastoplastic analysis of the composite cylinder model (CCM) described before to determine the mechanical behavior of the SiC/A*l* composite at different temperatures. Chun et al. [83,84] conducted two different thermoelastoplastic analyses, one based on an approximation scheme with the Prandtl-Reuss plastic flow model and the von Mises criterion and the other based on an average field theory.

8.2 Composite Cylinder Model [82]

The description and assumptions of the CCM were given before (Section 7.3). The application of this model to the study of mechanical behavior of the SiC/A*l* composite is described in detail in Appendix B. An elastoplastic micromechanical analysis of the model was performed in which the fiber was assumed to be linear elastic and the matrix elastoplastic with work hardening. The analysis was based on the deformation theory of plasticity in conjunction with the von Mises yield criterion.

Figures 8.1 and 8.2 show how the predicted longitudinal stress-strain curves at 24° C (75° F) and 288° C (550° F) are in good agreement with the experimental ones. The analysis also yielded the complete three-dimensional stress distributions in the composite. Typical stress distributions in the fiber and matrix for a given applied strain of $\varepsilon_z = 0.175\%$ at room temperature are shown in Fig. 8.3. Similar stress distributions were calculated for various levels of applied strain up to $\varepsilon_z = 0.833\%$. It is seen that in addition to longitudinal stresses transverse stresses in both the fiber and matrix were developed as a result of the difference in Poisson's ratios of the two materials. The transverse stresses, although much smaller than the longitudinal stresses, contributed to the plastic deformation of the matrix.

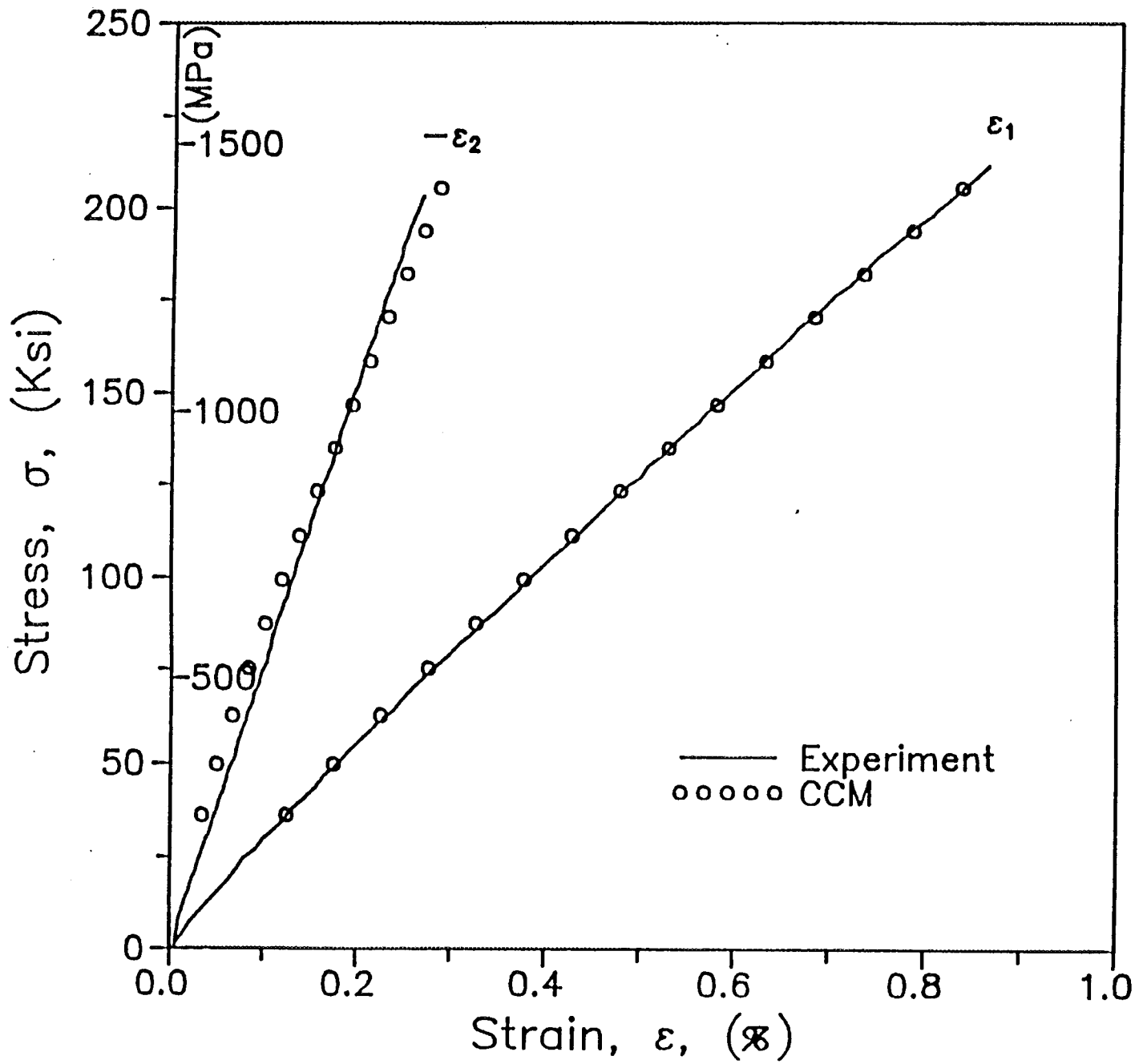

Fig. 8.1 Longitudinal Tensile Stress-Strain Curves of SiC/Al Composite at T = 24°C (75°F) Obtained Experimentally and Predicted by the Composite Cylinder Model (ε_1 and ε_2 are longitudinal and transverse strains in composite, respectively)

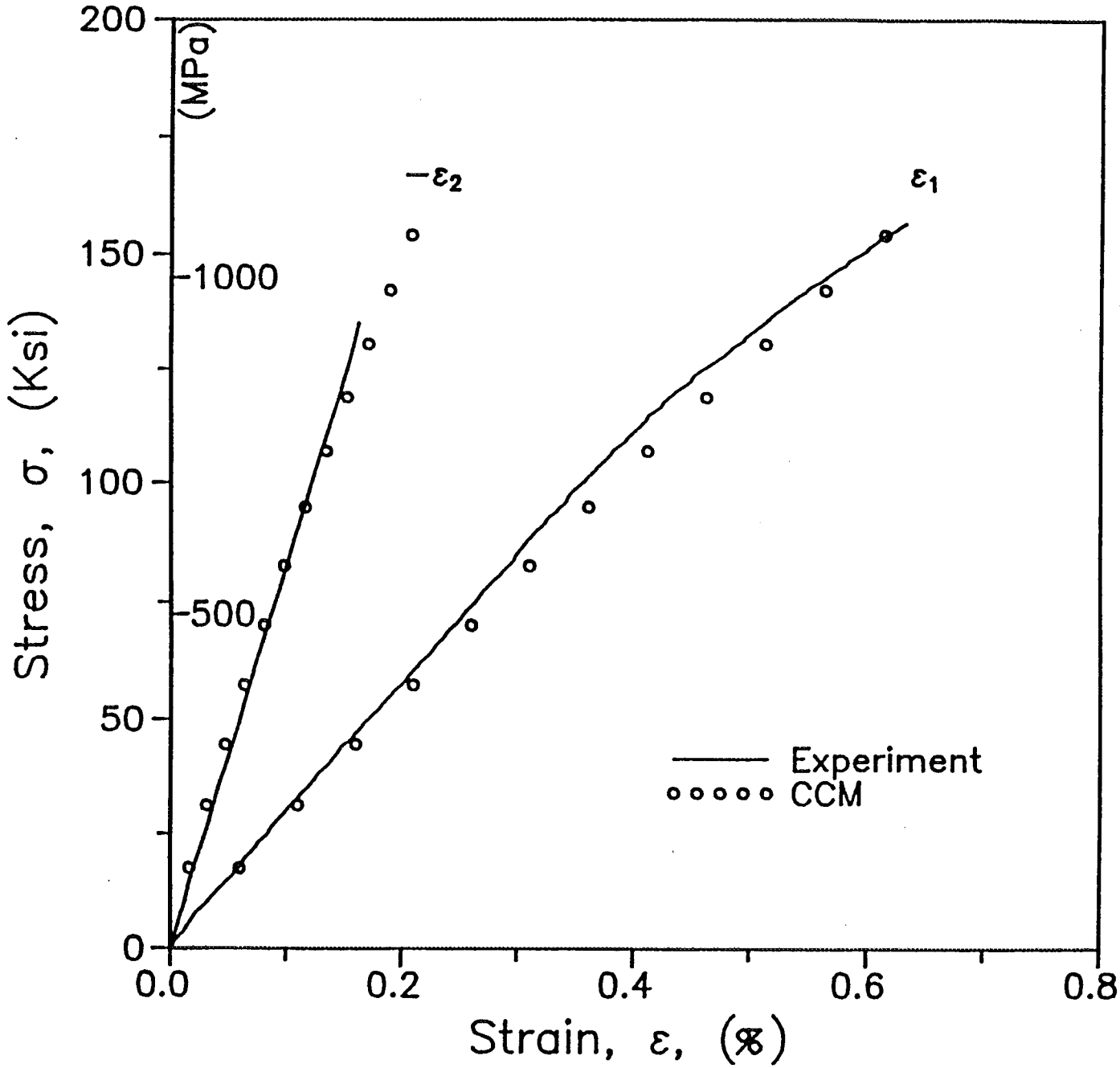

Fig. 8.2 Longitudinal Tensile Stress-Strain Curves of SiC/Al Composite at T = 288°C (550°F) Obtained Experimentally and Predicted by the Composite Cylinder Model (ε_1 and ε_2 are longitudinal and transverse strains in composite, respectively).

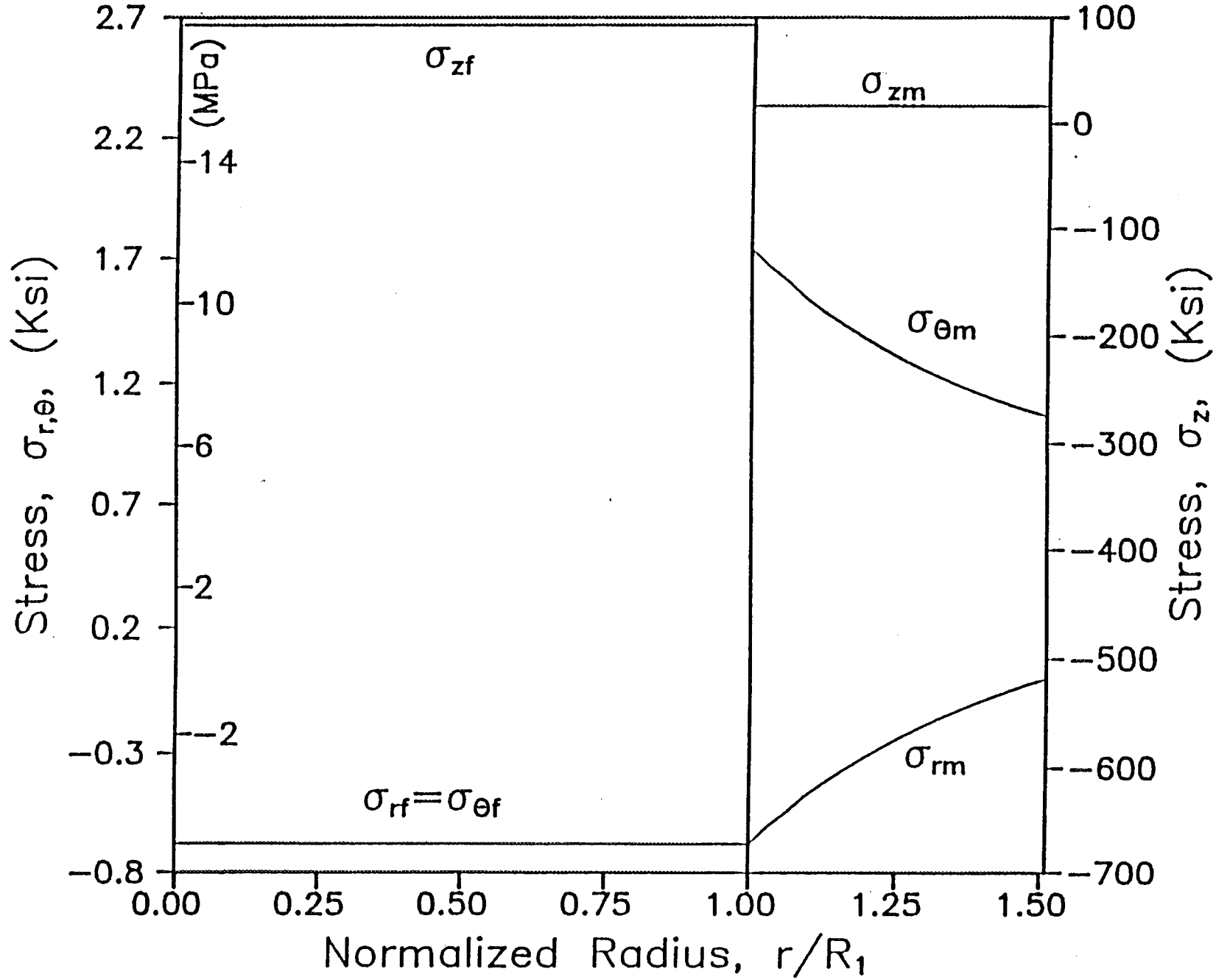

Fig. 8.3 Variation of Axial (σ_z), Radial (σ_r) and Circumferential (σ_θ) Stresses Along Half the Fiber/Matrix Cross Section for an Applied Strain $\varepsilon_z = 0.175$ percent and T = 24° (75°F).

The main results of the CCM analysis may be summarized as follows:

1. Slight nonlinearity in the stress-strain behavior of SiC/A*l* appears beyond a critical value of applied strain. This is attributed to the fact that most of the applied load is taken by the fibers due to their much higher elastic modulus. The deviation from linearity is more pronounced at higher temperatures.

2. The beginning of nonlinearity in the stress-strain curves coincides with the development of plastic deformation in the aluminum matrix.

3. The transverse stresses developed due to the difference in Poisson's ratios of the fiber and matrix are small for linear elastic behavior, but they increase as plastic deformation is advanced. However, the transverse stresses are an order of magnitude smaller than the axial stresses. These stresses are ignored in the micromechanical analysis based on the rule of mixtures.

4. The radial stresses in the matrix are compressive, while the circumferential stresses are tensile. This results in an increase of the equivalent stress and the accelerated plastic distortion of the matrix when compared with the case when the transverse stresses are ignored.

5. Very good agreement between the experimental results and the predictions of the composite cylinder model was achieved.

8.3 Thermo-elastoplastic Analysis Model - Successive Approximation Scheme [83]

A thermo-elastoplastic analytical model was developed for prediction of the three-dimensional state of stress in the fiber and matrix of the SiC/A*l* composite under longitudinal tensile loading. The full development and application of the model is included in Appendix C. The same approach described in Section 7.5 was followed.

Stress distributions in the fiber and matrix were obtained for various levels of applied stress and at various temperatures. Figure 8.4 shows such stress

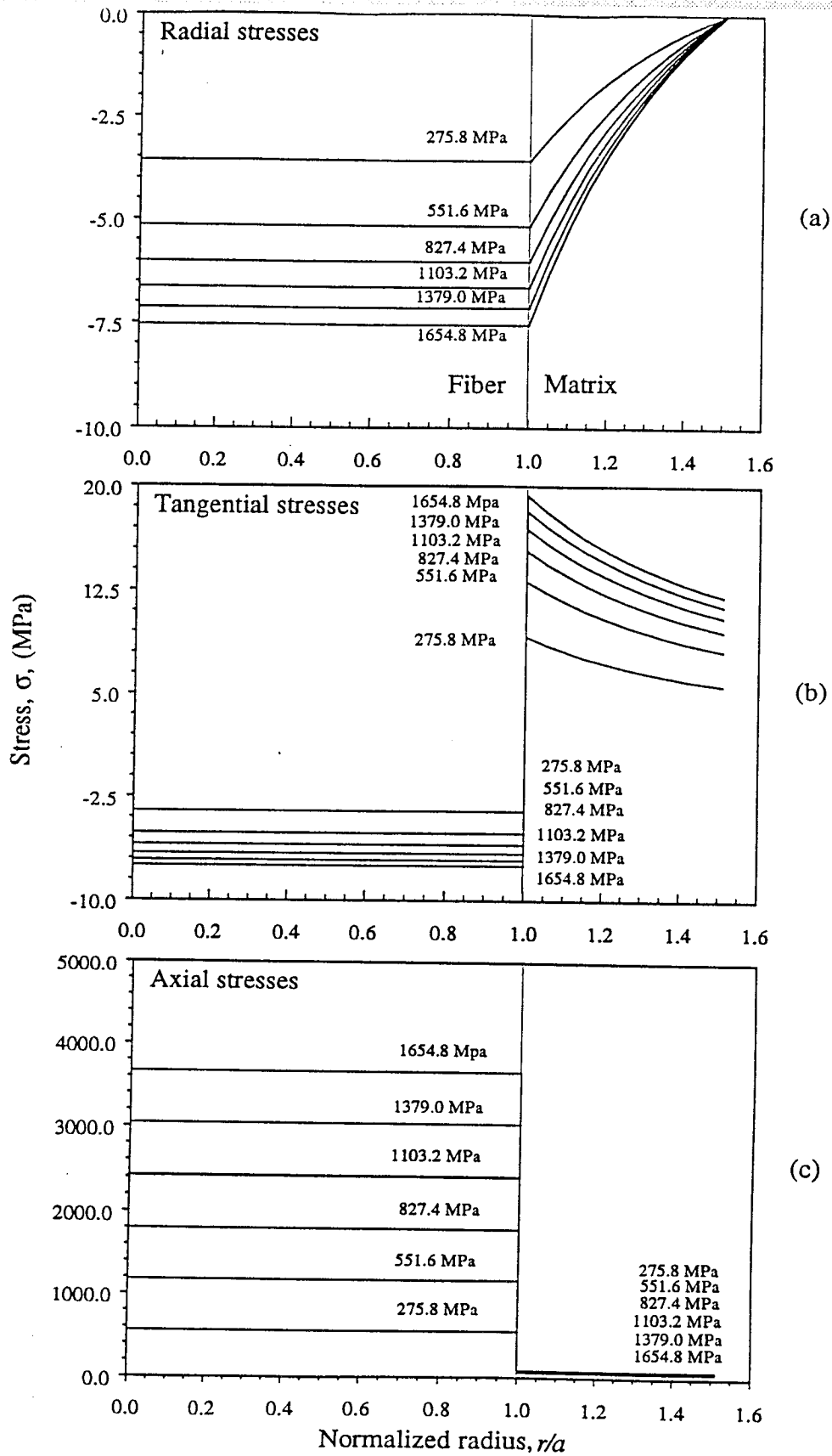

Fig. 8.4 Stress distributions in the fiber and matrix as a function of radial distance for various levels of longitudinal loading (a) radial, (b) tangential, (c) axial stresses.

distributions for various levels of applied longitudinal stress from $\sigma_a = 275$ MPa to $\sigma_a = 1654.8$ MPa. The radial and circumferential stresses are approximately an order of magnitude lower than the axial stress. The stresses in the matrix show large variations while the stresses in the fiber are uniform.

Figure 8.5 shows how the predicted stress-strain curves under longitudinal loading at 24° C (75° F) and 288° C (550° F) agree well with the experimental ones.

The successive approximation method was found to be a useful tool in solving problems where the boundary conditions are not explicitly prescribed. The best advantage of this approach is that the strain and stress fields are computed for any given load without incrementing the load. However, the method should be refined by considering additional effects such as residual stresses and creep, particularly for studying the composite behavior in the transverse direction.

8.4 Thermo-elastoplastic Analysis - Average Field Theory Model [84]

The thermo-elastoplastic behavior of a unidirectional SiC/A*l* composite was studied with a micromechanical model based on the average field theory proposed by Mori and Tanaka [85]. The full development and application of the model is included in Appendix D.

The effective strain response of the composite under thermomnechanical loading was obtained by an average field theory. The fiber is assumed to be elastic and temperature independent and the matrix is assumed to be a thermoelastoplastic material that is fitted into a series of power law strain hardening models. The thermoelastoplastic analysis was carried out by introducing the concept of secant properties to the average field theory.

Under transverse tensile loading the secant properties of the matrix and the average stresses in the matrix and fiber at room temperature were obtained as a function of applied stress. It is noticed that the larger portion of the load is

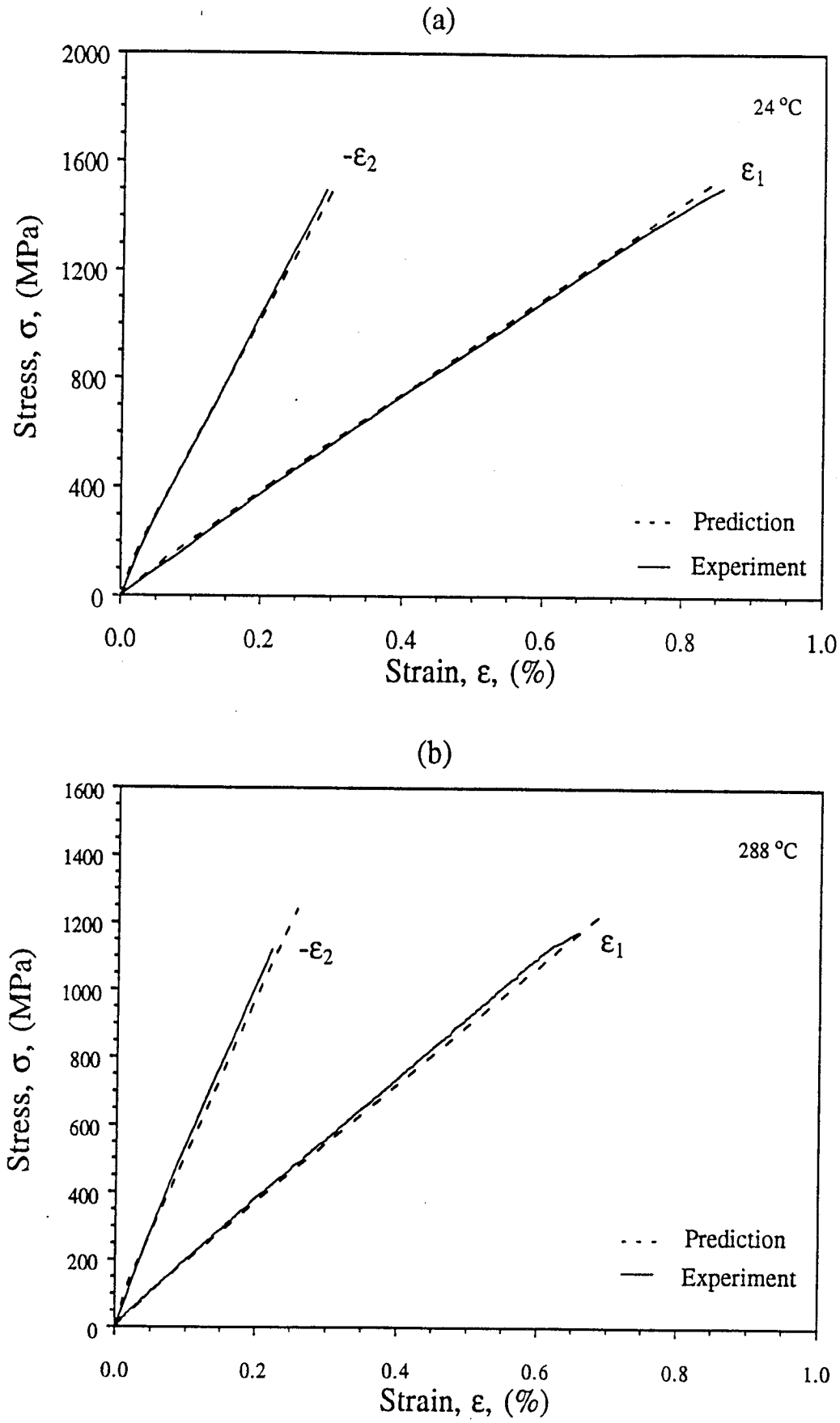

Fig. 8.5 Stress-strain curves of unidirectional SiC/Al composite under longitudinal loading (a) 24° C (75° F) and (b) 288° C (550° F)

transferred to the fibers due to their high stiffness. Figure 8.6 shows predicted and experimental stress-strain curves under transverse tensile loading at three different temperatures. At room temperature the agreement between predicted and experimental results is good. At higher temperatures the agreement is generally good, but some deviations occur in the transition regions between elastic and fully plastic behavior. This can be attributed to inelastic deformation other than plastic flow (creep), higher heterogeneous local deformation of matrix and degradation of interfacial properties with temperature.

The predicted stress-strain curves under longitudinal tensile loading at different temperatures are also compared with the experimental ones (Figs. 8.7 - 8.9). Favorable agreement is observed at all three temperatures, because, under longitudinal loading, the behavior of the composite is dominated by the fibers and any complex behavior of the matrix has a small influence.

The model was found to be a useful tool for predicting thermomechanical behavior of unidirectional metal matrix composites. However, the model should be improved by considering additional inelastic effects such as creep, particularly for transverse loading above the homologous temperature of the matrix.

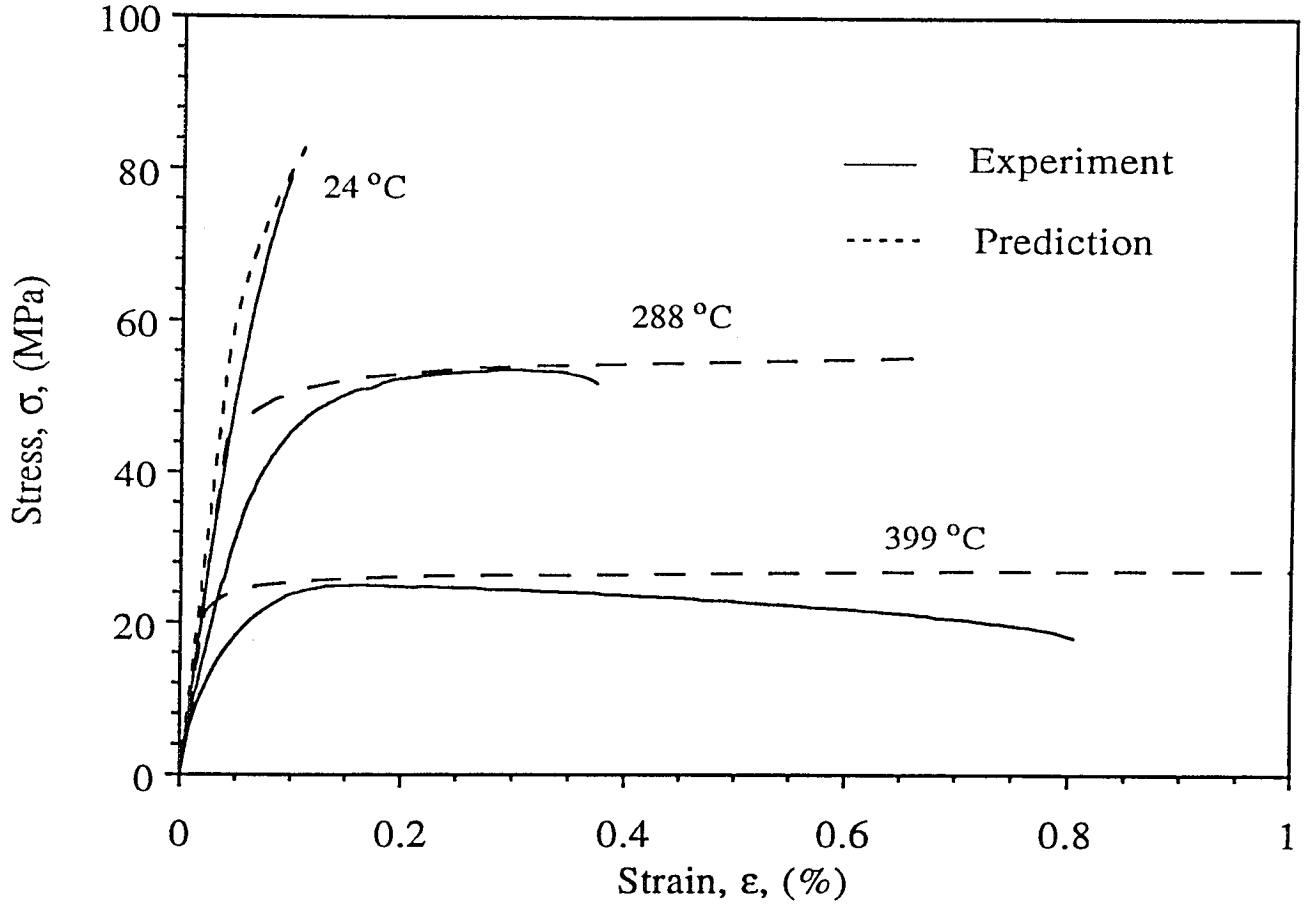

Fig. 8.6 Predicted and Experimental Stress-Strain Curves for Unidirectional SiC/Al Composite under Transverse Tensile Loading at Different Temperatures.

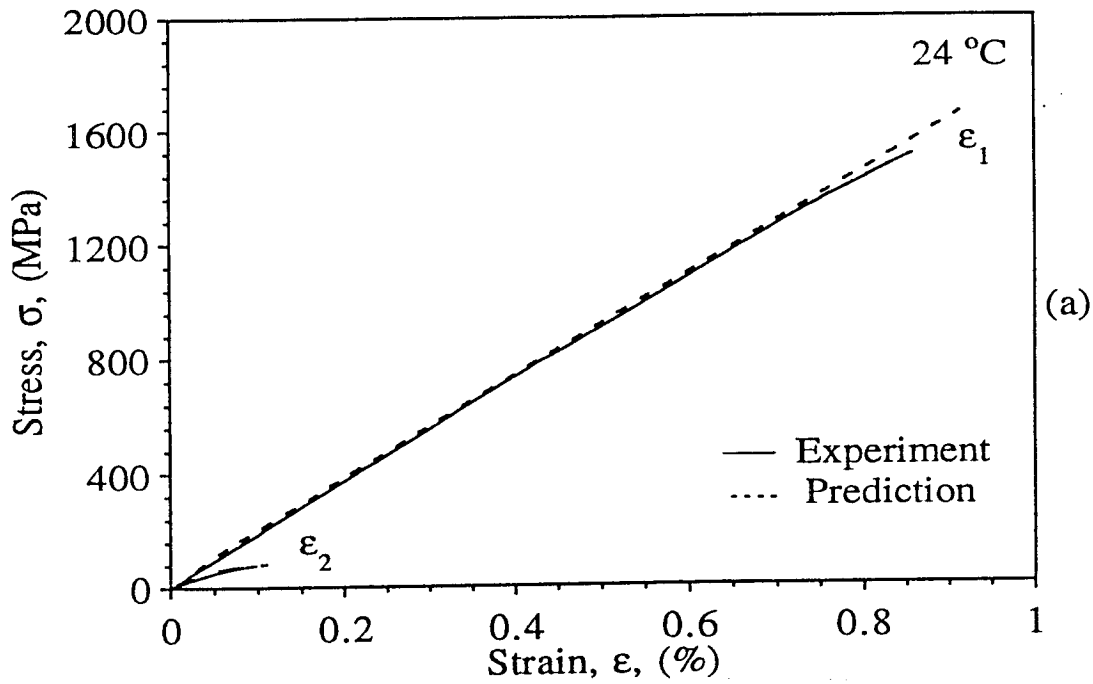

Fig. 8.7 Stress-Strain Curves for Unidirectional SiC/Al Composite under Longitudinal and Transverse Tensile Loading at T = 24° C (75° F).

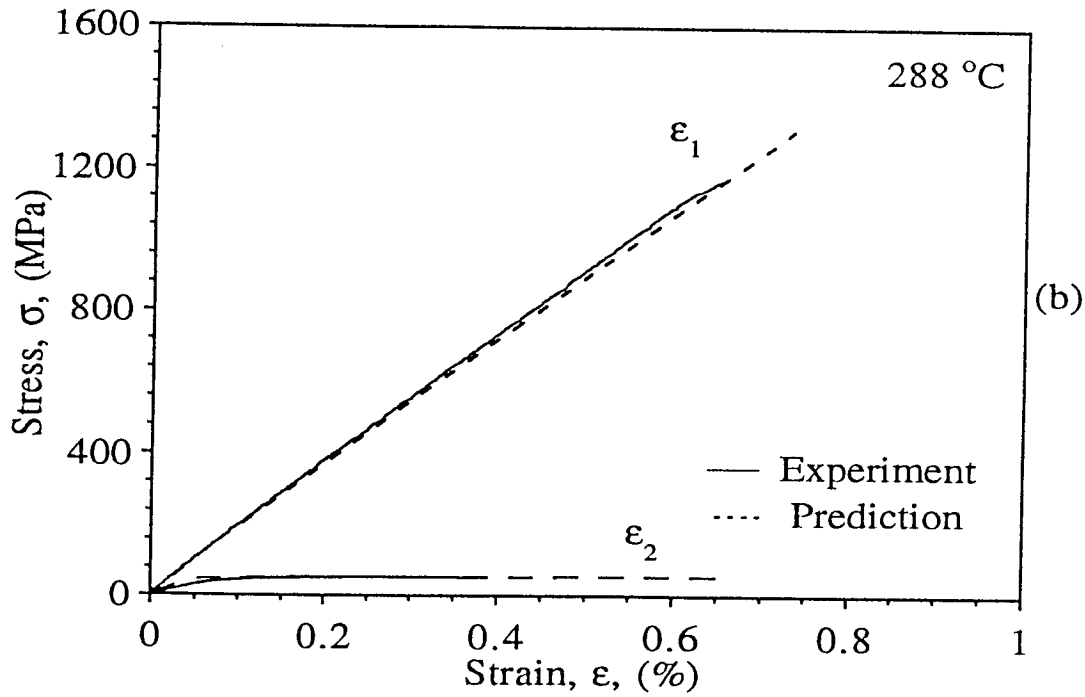

Fig. 8.8 Stress-Strain Curves for Unidirectional SiC/A*l* Composite under Longitudinal and Transverse Tensile Loading at T = 288° C (550° F).

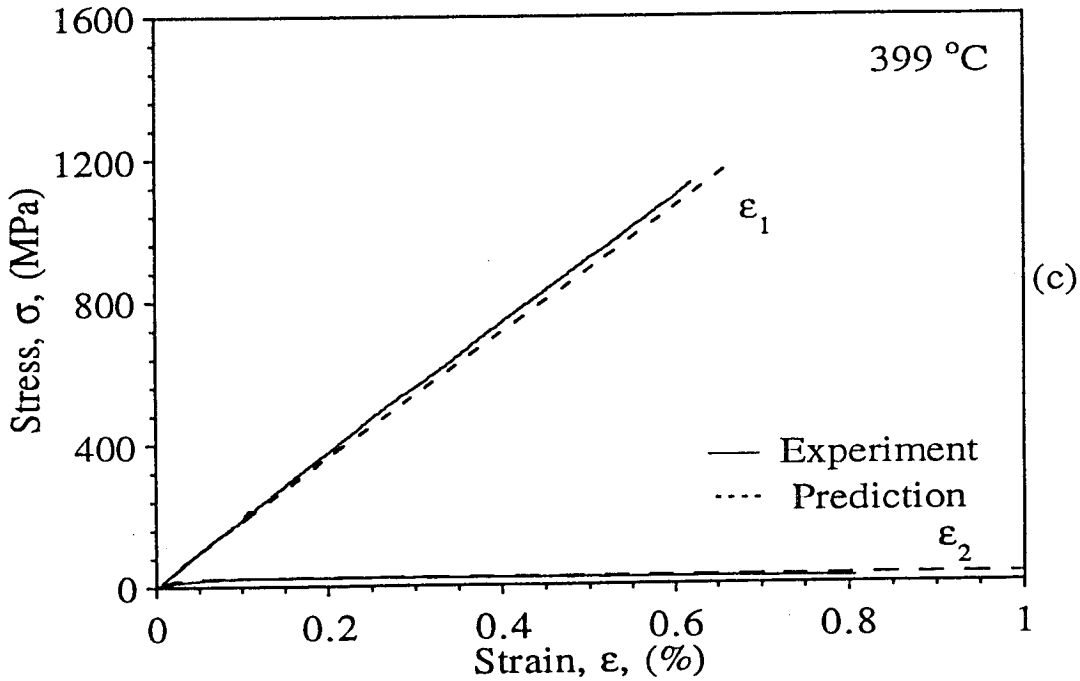

Fig. 8.9 Stress-Strain Curves for Unidirectional SiC/Al Composite under Longitudinal and Transverse Tensile Loading at T = 399° C (750° F).

9. SUMMARY, CONCLUSIONS AND RECOMMENDATIONS FOR FUTURE WORK

Experimental methods were developed, adapted and applied to the characterization of a metal matrix composite system and its constituents. The material investigated was unidirectional silicon carbide/aluminum (SCS-2/6061 *Al*).

The silicon carbide fiber (SCS-2) was characterized by determining its modulus, strength and coefficient of thermal expansion. A new method was developed for the latter determination. The aluminum matrix was characterized in two forms, the T4 and the fully annealed conditions. Stress-strain curves were obtained at several temperatures between 24° C (75° F) and 399 ° C (750° F) and at two strain rates, 0.02% and 115% per second. Thermal expansion behavior was measured up to 482° C (900° F). Creep behavior was also measured at three different temperatures.

The unidirectional composite obtained in the form of 8-ply 1.422 mm (0.56 in.) thick plates was characterized physically and thermomechanically at three temperatures 24° C (75° F), 288° C (550° F) and 399° C (750° F). Stress-strain curves to failure were obtained under longitudinal, transverse and in-plane shear loading at the three temperatures above. The longitudinal tensile strength decreases moderately with temperature whereas the transverse tensile and in-plane shear strengths decrease sharply with increasing temperature. The longitudinal and in-plane shear moduli do not change with temperature whereas the transverse modulus shows a gradual reduction. Creep rates increase sharply near and above 288° C (550° F) under isothermal conditions. Thermal cycling increases creep rates much above the corresponding rates under isothermal conditions at the upper limit of the thermal cycling.

The applicability of a proposed set of multifactor thermoviscoplastic nonlinear constitutive relationships (TVP-NCR) and a computer code (METCAN) was investigated. A procedure was developed for determining the unknown

exponents in the TVP-NCR equations by fitting them to experimental data. In the present work only the temperature and stress dependence of the mechanical and thermal properties of the composite and its constituent matrix were considered. Predictions of the thermomechanical behavior of the composite and aluminum matrix by the TVP-NCR was generally good for most properties. A modification of the TVP-NCR was proposed in the present work to accommodate for material properties whose variation with a variable does not comply with the end conditions dictated by the TVP-NCR. Theoretical predictions from the modified TVP-NCR were found to be in good agreement with the experimental results. Deviations, however, between experimental and predicted results appeared in cases where the form of the experimental curve deviates from the generic form of the TVP-NCR.

The computer code (METCAN) developed at NASA Lewis Research Center [18] to perform nonlinear analysis of fiber reinforced composites was used for the prediction of the thermomechanical behavior of the SiC/A*l* composite under investigation. Introducing the previously determined values of the exponents for the aluminum matrix into METCAN, the longitudinal and transverse stress-strain curves of the unidirectional composite were predicted at two temperatures. The experimental results were found to be in good agreement with the theoretical predictions from METCAN . Furthermore, the METCAN code was used to predict the magnitude of the residual stresses and strains generated in the composite and its constituent materials during cool-down from the fabrication temperature. These residual stresses were high enough to cause strain hardening of the matrix during cool-down. The composite residual strains as predicted by METCAN and the two-material composite cylinder were found to be in very good agreement.

Thermal deformations and stresses were studied in the silicon-carbide/aluminum filamentary composite at temperatures up to 370° C (700° F). An elastoplastic micromechanical analysis based on a one-dimensional rule-of-

mixtures model and a two material composite cylinder model was performed. It was established that beyond a critical temperature of 66° C (150° F) thermal strains become nonlinear with decreasing longitudinal and increasing transverse thermal expansion coefficients. This behavior was attributed to the plastic stresses in the aluminum matrix above the critical temperature. An elastoplastic analysis of both micromechanical models was performed to determine the stress distributions in both the fiber and matrix of the composite. A thermo-elastoplastic analysis was also conducted based on a successive approximation scheme with a Prandtl-Reuss plastic flow model. Theoretical predictions by all models and the experimental results for the coefficients of thermal expansion were in satisfactory agreement.

The behavior of the unidirectional SiC/A*l* composite under thermomechanical loading was also analyzed by three different approaches, the composite cylinder model, the thermo-elastoplastic analysis with the successive approximation scheme, and a similar analysis based on the average field theory. The first two models gave results for the longitudinal stress-strain behavior of the composite which were in good agreement with experiment plus the three-dimensional state of stress in the matrix and fiber. However, these two models are not applicable to the case of transverse loading. The third model, based on the average field theory did not yield detailed stress distributions in the matrix and fiber, however, predicted stress-strain behavior under longitudinal and transverse loading at different temperatures. The agreement with experimental results was very good for the case of longitudinal loading and reasonable for the case of transverse loading.

The following recommendations are made for future work.

(1) Investigate other MMC systems, especially those with better potential for high-temperature applications. Attention should be directed towards developing MMC systems that are more easily processable, more readily

available in various forms and less expensive.

(2) Investigate further time and temperature effects by conducting creep tests at different temperatures and at different stress amplitudes.

(3) Perform thermomechanical cyclic testing of the selected MMC systems and investigate failure mechanisms.

(4) Investigate the accelerated creep phenomenon under thermal cycling and develop analysis for its description and prediction. The subject of nonisothermal creep in general is very important and deserves deeper investigation.

(5) Extend characterization and analyses to crossply and multi-directional laminates.

(6) Investigate the effects of flexural, torsional and combined loading on the behavior of MMC's.

(7) Investigate dynamic effects, such as high-rate properties, impact response and wave propagation characteristics.

(8) Develop nondestructive evaluation methods for detection and characterization of flaws and damage in MMC's resulting from a variety of loading conditions.

(9) Evaluate METCAN for different materials, loading and environmental conditions. There is evidence that much better agreement between experimental results and METCAN can be obtained if the proper in-situ matrix properties are used. In the case of aluminum, properties in the fully annealed state would give a much better agreement with experiments. This should be verified.

REFERENCES

1. Flom, Y. and Arsenault, R. J., "Deformation in Al-SiC Composites Due to Thermal Stresses," *Mat. Sci. Engng.,* Vol. 75, 1985, pp. 151-167.

2. Flom, Y. and Arsenault, R. J., "Interfacial Bond Strength in an Aluminum Alloy 6061-SiC Composite," *Mat. Sci. Engng.,* Vol. 77, 1986, pp. 191-197.

3. McDanels, D. L., "Analysis of Stress-Strain, Fracture, and Ductility Behavior of Aluminum Matrix Composites Containing Discontinuous Silicon Carbide Reinforcement," *Metal. Trans.,* Vol. 16A, 1985, pp. 1105-1115.

4. Divecha, A. P., Fishman, S. G. and Karmarkar, S.D., "Silicon Carbide Reinforced Aluminum. A Formable Composite," *J. Metals,* Vol. 9, 1981, pp. 12-17.

5. Arsenault, R. J., "The Strengthening of Aluminum Alloy 6061 by Fiber and Platelet Silicon Carbide," *Mat Sci. Engng.,* Vol. 64, 1984, pp. 171-181.

6. Tsangarakis, N., Andrews, B.O. and Cavallaro, C., "Mechanical Properties of Some Silicon Carbide Reinforced Aluminum Composites," *J. Comp. Mat.,* Vol. 21, 1987, pp. 481-492.

7. Levin, V. M.,"On the Coefficients of Thermal Expansion of Heterogeneous Materials," (in Russian) *Mekhanika Tverdogo Tela,* Vol. 2, 1967, pp. 88-94.

8. Van Fo Fy, G. A., "Elastic Constants and Thermal Expansion of Certain Bodies with Inhomogeneous Regular Structure," *Soviet Physics, Doklady,* Vol. 11, 1966, p. 176.

9. Van Fo Fy, G. A., "Basic Relations of the Theory of Oriented Glass-Reinforced Plastics with Hollow Fibers," (in Russian), *Mekhanika Tverdogo Tela,* Vol. 2, 1966, p. 763.

10. Schapery, R. A., "Thermal Expansion Coefficients of Composite Materials Based on Energy Principles," *J. Comp. Mat.,* Vol. 2, 1968, pp. 380-404.

11. Rosen, B. W. and Hashin, Z., "Effective Thermal Expansion Coefficients and Specific Heats of Composite Materials," *Int. J. Engng. Sci.,* Vol. 8, 1970, pp. 157-173.

12. Dvorak, G. J. and Chen, T., "Thermal Expansion of Three-Phase Composite Materials," *J. Appl. Mech.,* Vol. 56, 1989, pp. 418-422.

13. Hoffman, C. A., "Effects of Thermal Loading on Fiber-Reinforced Composites with Constituents of Differing Thermal Expansivities," *J. Engng. Mat. Tech.,* Vol. 95, 1973, pp. 55-62.

14. Dvorak, G. J., Rao, M. S. M. and Tarn, J. Q., "Yielding in Unidirectional Composites under External Load and Temperature Changes," *J. Comp. Mat.,* Vol. 7, 1973, pp. 194-216.

15. Kural, M. H. and Min, B. K., "The Effects of Matrix Plasticity on the Thermal Deformation of Continuous Fiber Graphite/Metal Composites," *J. Comp. Mat.,* Vol. 18, 1984, pp. 519-535.

16. Min., B. K. and Crossman, F. W., "History-Dependent Thermomechanical Properties of Graphite/Aluminum Unidirectional Composites," *Composite Materials: Testing and Design (Sixth Conference),* ASTM STP 787, edited by I. M. Daniel, *American Society for Testing and Materials,* Philadelphia, 1982, pp. 371-392.

17. Chamis, C. C. and Hopkins, D. A., "Thermoviscoplastic Nonlinear Constitutive Relationships for Structural Analysis of High-Temperature Metal Matrix Composites," in *Testing Technology of Metal Matrix Composites,* ASTM STP 964, edited by DiGiovanni, P. R. and Adsit, N. R., American Society for Testing and Materials, Philadelphia, 1988, pp. 177-196.

18. Hopkins, D. A. and Pappu, L. M., *"METCAN-The Metal Matrix Composite Analyzer,"* NASA-Lewis Research Center, 1988.

19. Palazotto, A. N., Ruh, R. and Watt, G., "Introduction to Metal Matrix Composites in Aerospace Application," *Journal of Aerospace Engineering,* Vol. 1, No. 1, January 1988, pp. 3-17.

20. Strong, A. B., *"Fundamentals of Composite Manufacturing: Materials, Methods, and Applications,"* SME, 1989.

21. Schwartz, M. M., *"Composite Materials Handbook,"* McGraw-Hill, 1984.

22. Vinson, J. J. and Chou, T.-W., *"Composite Materials and Their Use in Structures,"* John Wiley & Sons, 1975.

23. McConnell, V. P., "Metal-Matrix Composites: Materials in Transition-Part I," *Advanced Composites,* May/June 1990, pp. 29-38.

24. Hunt, M., "Aluminum Composites Come of Age," *Materials Engineering,* January 1989, pp. 37-40.

25. Lynch, C. T., Kershaw, J. P. and Collins, B. R., "Mechanical Properties of Metal-Matrix Composites," *CRC Crit. Rev. Solid State Sci.,* Vol. 1, Issue 4, November 1970, pp. 481-573.

26. Hill, R., "Elastic Properties of Reinforced Solids: Some Theoretical Principles," *J. Mech. Phys. Solids,* Vol. 11, 1963, pp. 357-372.

27. Daniel, I. M. and Ishai, O.,*Engineering Mechanics of Composite Materials,* Oxford University Press, New York, 1994, pp. 85-90.

28. Lynch, C. T. and Kershaw, J. P., "Metal Matrix Composites," *CRC Press,* 1972, p. 135.

29. Hashin, Z., "Analysis of Composite Materials-A Survey," *J. Applied Mechanics,* Vol. 50, 1983, pp. 481-505.

30. Hashin Z. and Rosen, B. W., "The Elastic Moduli of Fiber-Reinforced Materials," *J. Appl. Mechanics,* Vol. 21, 1964, pp. 233-242.

31. Halpin, J. C. and Tsai, S. W., "Effects of Environmental Factors on Composite Materials," Air Force Technical Report AFML-TR-67-423, Wright Aeronautical Labs, Dayton, OH, 1967.

32. Hashin, "Analysis of Composites with Anisotropic Constituents," *J. Appl. Mech.,* Vol. 46, 1979, pp. 543-550.

33. Rogers, K. F., Phillips, L. N., Kingston-Lee, D. M., Yates, B., Overy, M. J., Sargent, J. P. and McCalla, B. A., "The Thermal Expansion of Carbon Fibre-Reinforced Plastics, Part I - The Influence of Fibre Type and Orientation," *Journal of Material Science,* Vol. 12, 1977, pp. 718-734.

34. Chamis, C. C., "Simplified Composite Micromechanics Equations for Hygral, Thermal and Mechanical Properties," *SAMPE Quarterly,* Vol. 15, April 1984, pp. 14-23.

35. Adams, D. F., "Combined Loading Micromechanical Analysis of a Unidirectional Composite," *Composites,* Vol. 15, July 1984, pp. 181-192.

36. Foye, R. L., "Theoretical Post-Yielding Behavior of Composite Laminates. Part I - Inelastic Micromechanics," *J. Comp. Mat..,* Vol. 7, 1973, pp. 178-193.

37. Caruso, J. J. and Chamis, C. C., "Assessment of Amplified Composite Micromechanics Using Three-Dimensional-Finite Elements Analysis," *Journal Composites Technology and Research,* Vol. 8, Fall 1986, pp. 77-83.

38. Bowles, D. E., "Finite Element Composite Analysis Program (FECAP) for a Microcomputer," *NASA TM-100670*, JULY 1988.

39. Hopkins, D. A. and Chamis, C. C., "A Unique Set of Micromechanics Equations for High-Temperature Metal Matrix Composites," in *Testing Technology of Metal Matrix Composites,* ASTM STP 964, edited by DiGiovanni, P. R. and Adsit, N. R., American Society for Testing and Materials, Philadelphia, 1988, pp. 159-176.

40. Nutt, S. and F. E. Wawner, "Silicon Carbide Filament: Microstructure," *J. Mat. Scie.*, Vol 20, 1985, pp. 1953-60.

41. DiCarlo, J. A., "Creep of CVD Silicon Carbide Fibers," *J. Mat. Scie.*, Vol. 21, 1986, pp. 217-24.

42. ASTM D3379-75, *American Society for Testing Materials,* Philadelphia, U.S.A.

43. Whitney, J. M., Daniel, I. M. and Pipes, R. B., *"Experimental Mechanics of Fiber Reinforced Composite Materials,"* Revised Edition, Prentice-Hall, New Jersey, 1984.

44. Nunes, J., "Tensile Behavior of Silicon Carbide Filaments and Silicon Carbide Fiber-Reinforced 6061 Aluminum," in *Failure Mechanisms in High Performance Materials*, edited by Early, J. G., Shives, T. R. and Smith, J. H., Cambridge University Press, 1985, pp. 138-146.

45. Skinner, A., Koczak, M. J. and Lawley, A., "Tensile Properties of SiC/Aluminum Filamentary Composites: Thermal Degradation Effects," *Powder Metallurgy International,* Vol. 14, No. 3, 1982, pp. 144-147.

46. Crane, R. L. and Krukonis, V. J., *Ceramic Bulletin,* Vol. 54, 1975, pp. 184-188.

47. Hilmmer, N. J., "Thermal Expansion of Chemically Vapor Deposited Silicon Carbide Fibers," Symposium on High Temperature Composites, *Proceedings of the American Society for Composites,* Dayton, OH, June 13-15, 1989, pp. 206-213.

48. Tsai, C.-L. and Daniel, I. M., "Method for Thermo-Mechanical Characterization of Single Fibers," *Composites Scie. and Tech.,* Vol. 50, 1994, pp. 7-12.

49. Daniel, I.M., Liber, T. and Chamis, C.C., "Measurement of Residual Strains in Boron/Epoxy and Glass/Epoxy Laminates," *Composite Reliability*, ASTM STP 580, Amer. Soc. for Testing and Materials, Philadelphia, 1975, pp. 340-51.

50. Daniel, I. M. and Ishai, O., *Engineering Mechanics of Composite Materials*, Oxford University Press, New York, 1994, pp.309-11; pp. 323-4.

51. Pindera, M. J. and Lin, M. W., "Micromechanical Analysis of the Elastoplastic Response of Metal Matrix Composites," *J. Pressure Vessel Technology*, Vol. 111, 1989, pp. 183-90.

52. Fedor, R. J. and Ebert, L. J., "A Study of the Effects of Prestrain on the Tensile Properties of Filamentary Composites," *Journal of Engineering Materials and Technology, Trans. ASME,* April 1973, pp. 69-75.

53. Lynch, C. T. and Kershaw, J. P., *"Metal Matrix Composites"* CRC Press, 1972, p. 107.

54. Ibid, p. 85.

55. Gdoutos, E. E., Karalekas, D. and Daniel, I. M., "Thermal Stress Analysis of a Silicon Carbide/Aluminum Composite," *Exper. Mechanics,* Vol. 31, No. 3, 1991, pp. 202-08.

56. Chun, H.-J., Daniel, I.M. and Wooh, S.-C., "Residual Thermal Stresses in a Filamentary SiC/Al Composite," to be submitted for publication.

57. Nadai, A., *"Theory of Flow and Fracture of Solids,"* McGraw-Hill, 2nd Edition, 1950, p. 387.

58. Hill, R., "Theory of Mechanical Properties of Fibre-Strengthened Materials: I. Elastic Behavior, II. Inelastic Behavior," *J. Mech. Phys. Solids,* Vol. 12, 1964, pp. 199-218.

59. Hashin, Z. and Rosen, B.W., "The Elastic Moduli of Fiber-Reinforced Materials," *J. Appl. Mech.,* Vol. 31, 1964, pp. 223-232.

60. Whitney, J. M. and Riley, M. B., "Elastic Properties of Fiber Reinforced Composite Materials," *AIAA J.,* Vol. 4, 1966, pp. 1537-1542.

61. Hecker, S. S., Hamilton, C. H. and Ebert, L. J., "Elastoplastic Analysis of Residual Stresses and Axial Loading in Composite Cylinders," *J. Mater.,* Vol. 5, 1970, pp. 868-900.

62. Hamilton, C. H., Hecker, S. S. and Ebert, L. J., "Mechanical Behavior of Uniaxially Loaded Multilayered Cylindrical Composites," *J. Basic Engng.,* Trans. ASME, Ser. D, Vol. 93, 1971, pp. 661-670.

63. Karalekas, D., Gdoutos, E. E. and Daniel, I. M., "Micromechanical Analysis of Nonlinear Thermal Deformation of Filamentary Metal Matrix Composites," *Computational Mechanics*, Vol. 9, 1991, pp. 17-26.

64. Shaffer, B.W., "Stress-Strain Relations of Reinforced Plastics Parallel and Normal to Their Internal Filaments," *AIAA, J.,* Vol. 2, 1964, pp. 348-352.

65. Shaffer, B. W., "Elastic-Plastic Stress Distribution Within Reinforced Plastics Loaded Normal to its Internal Filaments," *AIAA J.,* Vol. 6, 1968, pp. 2316-2324.

66. Hill, R., "Theory of Mechanical Properties of Fibre-Strengthened Materials: II. Inelastic Behavior," *J. Mech. Phys. Sol.,* Vol. 12, 1964, pp. 213-218.

67. Lin, T. H., Salinas, D. and Ito, Y. M., "Elastic-Plastic Analysis of Unidirectional Composites," *J. Comp. Mat.,* Vol. 6, 1972, pp. 48-60.

68. Adams, D. F., "Inelastic Analysis of a Unidirectional Composite Subjected to Transverse Normal Loading," *J. Comp. Mat.*, Vol. 4, 1970, pp. 310-328.

69. Adams, D. F. and Miller, A. K., "Hygrothermal Microstresses in a Unidirectional Composite Exhibiting Inelastic Material Behavior," *J. Comp. Mat.,* Vol. 11, 1977, pp. 285-299.

70. Bahei-El-Din, Y. A., Dvorak, G. J. and Utku, S., "Finite Element Analysis of Elastic-Plastic Fibrous Composite Structures," *Comp. and Struct.,* Vol. 13, 1981, pp. 321-330.

71. Bahei-El-Din, Y. A. and Dvorak, G. J., "Plasticity of Composite Laminates," *Proc. Research Workshop on Mechanics of Composite Materials*, edited by G. J. Dvorak, Duke University, 1978, pp. 32-54.

72. Bahei-El-Din, Y. A. and Dvorak, . J., "Plastic Yielding at a Circular Hole in a Laminated FP-Al Plate," *Modern Developments in Composite Materials and Structures,* edited by J. R. Vinson, 1979, pp. 123-147.

73. Dvorak, G. J. and Teply, J. L., "Periodic Hexagonal Array Models for Plasticity Analysis of Composite Materials," in *Plasticity Today* . Modelling, Methods and Applications, edited by A. Sawczuk and G. Bianchi, Elsevier Appl. Sci. Publ., 1985, pp. 623-642.

74. Hill, R., "Theory of Mechanical Properties of Fibre-Strengthened Materials: I, Elastic Behavior," *J. Mech. Phys. Solids,* Vol. 12, 1964, pp. 199-212.

75. Aboudi, J. "Elastoplasticity Theory for Composite Materials," *Sol. Mech. Arch.,* Vol. 11, 1986, pp. 141-183.

76. Aboudi, J., "Closed Form Constitutive Equations for Metal Matrix Composites," *Int. J. Engng. Sci.,* Vol. 25. 1987, pp. 1229-1240.

77. Pindera, M-J. and Lin, M. W., "Micromechanical Analysis of the Elastoplastic Response of Metal Matrix Composites," *J. Pressure Vessel Tech.,* Vol. 111, 1989, pp. 183-190.

78. Pindera, M.-J., Herakovich, C. T., Becker, W. and Aboudi, J., "Nonlinear Response of Unidirectional Boron/Aluminum," *J. Comp. Mat.,* Vol. 24, 1990, pp. 2-21.

79. Bahei-El-Din, Y. A. and Dvorak, G. J., "A Review of Plasticity Theory of Fibrous Composite Materials," in *Metal Matrix Composites: Testing, Analysis, and Failure Modes,* ASTM STP 1032, edited by W. S. Johnson, American Society for Testing and Materials, 1989, pp. 103-129.

80. Rizzi, S. A., Leewood, A. R., Doyle, J. F. and Sun, C. T., "Elastic-Plastic Analysis of Boron/Aluminum Composite Under Constrained Plasticity Conditions," *J. Comp. Mat.,* Vol. 21, 1987, pp. 734-749.

81. Sun, C. T., "Modeling Continuous Fiber Metal Matrix Composite as an Orthotropic Elastic-Plastic Material," in *Metal Matrix Composites: Testing, Analysis and Failure Modes,* ASTM STP 1032, edited by W. S. Johnson, American Society for Testing and Materials, 1989, pp. 148-160.

82. Gdoutos, E. E., Karalekas, D. and Daniel, I. M., "Micromechanical Analysis of Filamentary Metal Matrix Composites under Longitudinal Loading," *J. Comp. Tech. and Research,* Vol. 13, No. 3, 1991, pp. 168-74.

83. Chun, H. J., Wooh, S. C. and Daniel, I. M., "Thermoelastoplastic Analysis of Filamentary Metal Matrix Composites," submitted to J. of Applied Mechanics, 1994.

84. Chun, H. J., Daniel, I. M. and Wooh, S. C., "Unidirectional SiC/A*l* Composite Behavior under Thermomechanical Loading," to be submitted.

85. Mori, T. and Tanaka, K., "Average Stresses in Matrix and Average Energy of Materials with Misfitting Inclusions," *Acta Metallurgica,* Vol. 21, pp. 571-74.

APPENDIX A

Residual Thermal Stresses in a Filamentary SiC/Al Composite

Heoung-Jae Chun, Research Assistant

Isaac M. Daniel, professor

Shi-Chang Wooh, Research Assistant Professor

Robert R. McCormick School of Engineering and Applied Science

Nothwestern University,

Evanston, Illinois 60208

Abstract

Residual stresses introduced by the cooling process were investigated. The large mismatch of the coefficients of thermal expansion (CTE) between the SCS-2 fiber and 6061 aluminum matrix tends to produce high residual stresses so that plastic flow of the matrix is inevitable during cool down.

The elastoplastic behavior of a metal matrix composite material was studied. The analysis is based on the successive approximation scheme with the Prandtl-Reuss plastic flow model and von Mises criterion. The three-dimensional state of residual stress was computed. It was found from the study that the plastic flow of the matrix relieves the residual stresses in both fiber and matrix. In addition, the longitudinal stress-strain curve at room temperature under uniaxial tension and the thermal strain-temperature relationship of the composite were predicted and compared with experimental results.

Introduction

Application of metal matrix composites (MMC's) are in demand for the use of many structural components in intermediate to high temperature ranges. The MMC's have higher fracture toughness and ductility than ceramic matrix composites (CMC's) among the high temperature materials. The MMC's have additional advantages including high strength, elastic modulus, toughness, impact resistance, resistivity to temperature change or thermal shock and surface durability, low sensitivity to surface flaws, and high electrical and thermal conductivity.

When a MMC is cooled down from the high fabrication temperature to room temperature, high residual stresses may develop due to the mismatch of the coefficients of thermal expansion between fiber and matrix. The residual stresses are also dependent on the fiber and matrix properties and the matrix plasticity behavior which are all functions of temperature. It is reasonable that the matrix may experience plastic flow since the relief of residual stresses in the composite at room temperature is not possible other than through plastic flow. This may cause initial yielding of the matrix prior to any application of loading. Thus, it is desirable to study the composite behavior by considering the plastic flow and residual stresses.

Residual stresses were investigated by many authors. For example, Haener and Ashbaugh (1967), Uemura *et al.* (1979) and Arsenault and Taya (1987) studied the case of elastic constituents, while Hill (1964), Piggott (1966), Hecker *et al.* (1970), Gayda and Ebert (1979) and Vedula *et al.* (1988) considered plastic flow in determining residual stresses.

According to Vedula *et al.* (1988) the matrix experiences three stages during cool down. Stage I is at high temperature where the stress relaxation is dominant. Residual stresses in the matrix are negligibly small in this stage. The temperature range or the lower bound of this stage dependents on the cooling rate. For slow cooling, aluminum remains in stage I for temperatures down to 200°C (392°F). Stage II occurs at an intermediate temperature where the stress relaxation is no longer significant and elastic stresses build up in the constituents. Stage III is at the lower temperature where plastic flow of matrix begins. In this paper, the lower bound temperature of stage II used is

288°C (550°F) that is 0.6 of absolute melting temperature and slightly above the homologous temperature.

In this study, a continuous fiber composite is modeled by two concentric cylinders representing the elastic fiber and elastoplastic matrix respectively. The effects of residual stresses and plastic flow on thermomechanical behavior were studied by applying a successive approximation method since the exact solution is not available. The buildup of triaxial stresses in the cooling process is observed. A more realistic prediction of thermomechanical behavior is obtained by considering plastic deformation of the matrix along with residual stresses.

Theoretical Background

The representative volume element used in the analysis is a coaxial cylindrical model (CCM). It has been used in micromechanical studies of the axisymmetry problems by Ishikawa *et al.* (1978), Iesan (1980), Mikata and Taya (1985), Warwick and Clyne, (1991) and Hsueh and Becher (1988). The model was used for the study of elastoplastic analysis under thermomechanical loading by the successive approximation method by Chun *et al.* (1994). The same analysis was used in this paper to study the residual stresses and their effects. Figure 1 illustrates the continuous fiber model of MMC used in the analysis.

The following assumptions were made during derivation of the model. The constituent materials are isotropic and the bonding between fiber and matrix is perfect. Fibers are linearly elastic up to failure and the matrix is elastoplastic. There is no

temperature gradient in the material and the axial plane remains always plane. The fiber volume fraction is reasonably low.

For an axisymmetric problem, the force equilibrium equation in the radial direction and the compatibility conditions give

$$\frac{d\sigma_r}{dr} + \frac{\sigma_r - \sigma_\theta}{r} = 0 \tag{1}$$

$$\frac{d\varepsilon_\theta}{dr} + \frac{\varepsilon_\theta - \varepsilon_r}{r} = 0 \tag{2}$$

Furthermore, the elastoplastic stress-strain relationships are formulated by considering additional plastic strains (ε_r^p, ε_θ^p, ε_z^p), i.e.,

$$\sigma_r = \frac{E}{(1-2\nu)(\nu+1)}[(1-\nu)(\varepsilon_r - \varepsilon_r^p) + \nu(\varepsilon_\theta - \varepsilon_\theta^p) + \nu(\varepsilon_z - \varepsilon_z^p) - (\nu+1)\alpha\Delta T] \tag{3.a}$$

$$\sigma_\theta = \frac{E}{(1-2\nu)(\nu+1)}[(1-\nu)(\varepsilon_\theta - \varepsilon_\theta^p) + \nu(\varepsilon_r - \varepsilon_r^p) + \nu(\varepsilon_z - \varepsilon_z^p) - (\nu+1)\alpha\Delta T] \tag{3.b}$$

$$\sigma_z = \frac{E}{(1-2\nu)(\nu+1)}[(1-\nu)(\varepsilon_z - \varepsilon_z^p) + \nu(\varepsilon_r - \varepsilon_r^p) + \nu(\varepsilon_\theta - \varepsilon_\theta^p) - (\nu+1)\alpha\Delta T] \tag{3.c}$$

where E is the elastic modulus, ν Poisson's ratio and α the coefficient of thermal expansion. From eqs. (1), (2) and (3), the following differential equation is obtained

$$\frac{d^2\varepsilon_\theta}{dr^2} + \frac{3}{r}\frac{d\varepsilon_\theta}{dr} = \frac{(1-2\nu)}{(1-\nu)r}\frac{d\varepsilon_r^p}{dr} + \frac{(1-2\nu)(\varepsilon_r^p - \varepsilon_\theta^p)}{(1-\nu)r^2} + \frac{(\nu+1)}{(1-\nu)r}\frac{d(\alpha\Delta T)}{dr} \tag{4}$$

For the case of uniform temperature distribution, this differential equation is solved in the form

$$\varepsilon_\theta = \frac{(1-2\nu)}{(1-\nu)r^2}\int r\varepsilon_r^p dr - \frac{(1-2\nu)}{2(1-\nu)r^2}\int r(\varepsilon_r^p - \varepsilon_\theta^p)dr + \frac{(1-2\nu)}{2(1-\nu)}\int\frac{(\varepsilon_r^p - \varepsilon_\theta^p)}{r}dr - \frac{C_1}{2r^2} + C_2 \tag{5.a}$$

the radial strain is obtained from eqs. (2) and (5.a) as

$$\varepsilon_r = \frac{(1-2\nu)}{(\nu-1)}\varepsilon_r^p - \frac{(1-2\nu)}{(1-\nu)r^2}\int r\varepsilon_r^p dr + \frac{(1-2\nu)}{2(1-\nu)r^2}\int r(\varepsilon_r^p - \varepsilon_\theta^p)dr$$
$$+\frac{(1-2\nu)}{2(1-\nu)}\int\frac{(\varepsilon_r^p - \varepsilon_\theta^p)}{r}dr + \frac{C_1}{2r^2} + C_2 \tag{5.b}$$

and the displacement

$$u = \frac{(1-2\nu)}{(1-\nu)r}\int r\varepsilon_r^p dr - \frac{(1-2\nu)}{2(1-\nu)r}\int r(\varepsilon_r^p - \varepsilon_\theta^p)dr + \frac{(1-2\nu)r}{2(1-\nu)}\int\frac{(\varepsilon_r^p - \varepsilon_\theta^p)}{r}dr$$
$$-\frac{C_1}{2r} + C_2 r \tag{6}$$

is obtained from the strain-displacement relationship. Note that the solutions have the same form to those of the elastic case if the plastic strains become zero.

Elastic and Elastoplastc Solutions

Elastic and elastoplastic solutions are obtained from the previously derived elastoplastic relations. The elastic solution is used for the fiber while the elastoplastic solution is applied to the matrix. The prescribed boundary conditions for the elastoplastic problems are not given in explicit form so that it is difficult to obtain the exact solutions. However, approximate solutions were found numerically by introducing the successive approximation scheme, that was used to solve various similar problems by many investigators; Mendelson and Spero (1962), Davis (1963), and Tuba (1965).

There are altogether six unknowns: two constants C_{1f} and C_{2f} in the elastic solution, two constants C_{1m}, C_{2m} and the plastic strains ε_r^p and ε_θ^p fin the elastoplastic

solution. These unknowns are determined by satisfying the following six boundary conditions:

1. The axial strains in the fiber and matrix are equal and constant:

$$\varepsilon_{zf} = \varepsilon_{zm} = \varepsilon_z \tag{7}$$

where subscripts f and m denote fiber and matrix, respectively.

2. There exits no singularity in the displacement field at the center of the cylinder, i. e. :

$$C_{1f} = 0 \tag{8}$$

3. Displacements are continuous at the boundary between fiber and matrix:

$$u_f(a) = u_m(a) \tag{9}$$

4. Radial stresses are continuous at the boundary between fiber and matrix:

$$\sigma_{rf}(a) = \sigma_{rm}(a) \tag{10}$$

5. The radial stress vanishes at $r = b$:

$$\sigma_{rm}(b) = 0 \tag{11}$$

6. Force equilibrium in the fiber direction yields

$$\int_0^a \sigma_{zf} r dr + \int_a^b \sigma_{zm} r dr = \frac{\sigma_0 b^2}{2} \tag{12}$$

where σ_0 is the applied stress.

Nonlinear stress-strain behavior of the matrix is expressed by the power-law strain hardening formula for the theoretical prediction as an input for constituent properties. Figure 2 shows the model, in which the stress-strain curve of a station is expressed as:

$$\sigma = \sigma_Y + kE_m \varepsilon_p'^n \tag{13}$$

where k, and n, are material constants, and σ_Y the elastic limit stress or the yield stress.

If the station is unloaded before yielding, the unloading path traces the loading path. On the other hand, if the station is unloaded after yielding, the path follows the line parallel to that of the elastic region as shown in Fig. 2. During unloading, if there is no reversal yielding, the reversal stresses are purely elastic. But if reversal yielding occurs, then the successive approximation method is used to calculate reversal elastoplastic stresses. The Bauschinger effect may be considered since it is not required that yield stresses in tension and compression be the same. However, the Bauschinger effect is neglected in this paper.

The step-by-step procedure of the successive approximation scheme is the following:

1. Assign number of equidistant stations (N) along the radial direction from the center of the cylinder as illustrated in Fig. 1.
2. Assume that ε_r^p and ε_θ^p are zero at every station, as a first approximation.
3. Determine four unknowns C_{2f}, C_{1m}, C_{2m} and ε_z from the boundary conditions.
4. Compute strains for fiber and matrix and obtain the corresponding stresses.
5. Calculate effective stresses in the matrix ($\bar{\sigma}_m$) at each station from

$$\bar{\sigma}_m = \sqrt{\frac{3}{2} S_{ij} S_{ij}} \tag{14}$$

where S_{ij} is the deviatoric stress tensor of the matrix.

6. For all stations at which the effective stress exceeds the elastic limit, calculate the effective total strain in the matrix from

$$\bar{\varepsilon}_m = \sqrt{\frac{2}{3} e_{ij} e_{ij}} \tag{15}$$

where e_{ij} is the deviatoric strain tensor of the matrix.

7. The effective plastic strain $\bar{\varepsilon}_m^p$ is calculated from the stress-strain curves and the following relationships:

$$\bar{\varepsilon}_m^p = \bar{\varepsilon}_m - \frac{2(1+\nu_m)\bar{\sigma}_m}{3E_m} \tag{16}$$

8. Obtain the next approximate plastic strains from the plastic flow rule expressed in terms of strains:

$$\varepsilon_{ij}^p = \frac{\bar{\varepsilon}_m^p}{\bar{\varepsilon}_m} e_{ij} \tag{17}$$

Use these computed plastic strains in the second approximation for the yielded stations and zero for the remaining stations.

9. Repeat from step 3 until the strains at all stations converge.

Experimental Procedure

To implement the predictive model above, it is necessary to know the thermomechanical properties of the constituent materials and the fiber volume ratio of the composite. The fiber (SCS-2) has an average diameter of 140 μm (0.00551 in.) and its measured elastic modulus is 400 GPa (58 Msi). The fiber behaves elasticly up to failure and is assumed isotropic and temperature independent. The thermal expansion of the fiber shows significant nonlinearity in the range between room temperature and 449°C (840°F), but it is linear up to 1299°C (2370°F), as discussed by Hillmer (1989). The CTE of SCS-

2 measured by Tsai and Daniel (1994) was used in this study. The stress-strain curves of Al 6061-O (annealed state) are obtained for various temperatures. The thermal expansion of the matrix was also measured. The experimental results show that the matrix behaves thermoelastoplastically. The measured constituent properties are shown in Table 1.

The material investigated is an eight-ply unidirectional silicon carbide/aluminum (SiC/Al) composite (SCS-2/6061Al, Textron Specialty Materials). The composite was fabricated by the diffusion bonding consolidation process.

The as-obtained 1.42mm (0.056in.) thick composite plate was cut into 12.7mm (0.5in.) wide 152.4mm (6.0in.) long coupons and tabbed with high strength adhesive for use at elevated temperatures. Two types of adhesive were used for different temperature ranges. For the temperature range between 24°C (75°F) and 288°C (550°F), a polyimide adhesive film (FM36, American Cyanamid) was used; while an aluminum filled condensation type polyimide adhesive film (FM680, American Cyanamid) was used for the temperature range of 288°C (550°F) to 399°C (750°F). Both types are supported by a glass cloth carrier for better shear and peel-off strengths. These adhesives provide sufficiently high strength for testing if the bonded tabs are sufficiently long (38.1mm, 1.5in.).

High temperature tests were conducted in a thermal chamber. For strain measurement, the specimens were instrumented with commercially available strain gages for high temperature applications (WK-gages from Micro Measurements and RKO-gages from J. P. Technology). The strain readings from the gages were compensated for temperature by using a dummy gage technique and were verified by measuring the axial

strain with a water-cooled clip-on extensometer. The specimen surface temperature was monitored by a K-type thermocouple bonded on the surface with ceramic adhesive. The temperature signal was also used as a feedback to the temperature controller.

The thermal strains of the composite were measured with strain gages. Unidirectional specimens were instrumented with WK-00 (Micro Measurements) gages for measuring longitudinal and transverse thermal strains. At least three thermocouples were attached to the specimen to monitor temperature. A programmable hot press (MTP-14, Tetahedron) was used for controlling temperature change step by step. The specimens were heated up to 260°C (500°F) with the gages at increments of 14°C (25°F) with half hour dwell intervals to stabilize the temperature and expansivity of the specimen. A strain gage bridge conditioner (BC-8SSG, KAYE Instruments) and data logger (Digistrip, KAYE) were used to record time, temperature and strain.

The obtained apparent strains were corrected to obtain true thermal strains. Similar gages were attached to a titanium silicate reference specimen that has a known stable coefficient of thermal expansion of 0.0306×10^{-6} /° C (0.017×10^{-6} /° F). The reference specimen was included in the test together with the test specimens. The true thermal strain ε_t was obtained by correcting the apparent strain ε_a by the reference strains as follows

$$\varepsilon_t = \varepsilon_a - (\varepsilon_r - \varepsilon_{tr}) \tag{18}$$

where ε_r is the measured gage output from the reference specimen and ε_{tr} is the known thermal expansion of titanium silicate.

Results and Discussion

The equivalent ratio of outer to inner cylinder radius is determined by measuring the fiber volume ratio of the composite by photomicrographic examination. The measured fiber volume ratio was 0.44 so that the equivalent ratio of outer to inner cylinder radius is 1.51.

The stress-strain curves of 6061-O aluminum at different temperatures are fitted into a power law strain hardening model from eq. (13). The temperature dependent parameters, k, n, and σ_Y are tabulated in Table 2. As seen from Fig. 3, the mechanical properties of 6061-O aluminum decrease with increasing temperature. Above 288°C (550°F), the yield stress, ultimate strength and the effect of strain-hardening of the matrix decrease significantly so that the stress-strain behavior becomes close to that of an elastic perfectly-plastic solid.

The theoretical model described here was applied to study the residual stress buildup in SiC/Al composites In the analysis, 26 stations were assigned along the radial direction in the composite cylinder model as seen in Fig. 1. The residual stress-free temperature is assumed to be 288°C (550°F), that is 0.6 of absolute melting temperature of aluminum. Above this temperature stress relaxation plays a large role and only low residual stresses are expected to be built up. The assumption of this residual stress-free temperature is not considered a very significant factor once the matrix has yielded under cooling. Further increase in differential thermal strains is taken up by plastic flow in the matrix with small increase in residual stresses. The important factor that is likely to affect residual stresses is the yield stress of the matrix when the residual stresses are generated

during cool down. The residual stress buildup in the composite and the behavior under mechanical and thermal loading were also studied. The calculation of residual stresses in the composite due to cool down from the residual stress-free temperature was carried out with the elastoplastic formulation and a successive approximation method.

Figures 4 and 5 show the residual stresses of the composite as a function of the radial distance normalized by the fiber radius without and with consideration of plastic flow of the matrix. Note that all components of residual stresses in the fiber are compressive and constant. The radial and tangential stresses in the fiber are equal. The residual radial stress is compressive and the tangential and axial stresses are tensile in the matrix. By comparing Figs. 4 and 5, one can observe that the plastic flow in the matrix greatly influences the residual stresses in both matrix and fiber. The stresses computed by considering the plastic flow in the matrix are an order of magnitude less than the ones without consideration of plastic flow. It is also noted that the residual stresses in the axial and tangential direction decrease relatively more toward the interface than the outer cylinder of matrix when plastic flow is considered.

Figure 6 shows the residual stress components at different temperatures. Residual stresses increase in absolute terms with cooling. Figure 7 shows the computed stresses in the fiber and matrix at the interface plotted as a function of temperature. The stresses at the interface increase linearly in absolute terms in the initial stage of cooling. However, the rate of increase slowed down below a certain temperature when the matrix yields. The residual stresses may further increase due to the increase of yield stress and strain

hardening rate of the matrix with decreasing temperature. The plastic flow of the matrix starts at the interface and moves outward in the matrix cylinder.

The axial and transverse strains of the composite were computed under axial loading without or with consideration of residual stresses. The stress-strain curves show the change of slope due to matrix yielding but the change is relatively small. The predicted stress-strain curves were not sensitive to residual stresses because the behavior of the composite under longitudinal loading is dominated by the fiber properties so that yielding of matrix does not contribute much. The predicted stress-strain curves of the composite for both cases at room temperature show favorable agreement with experimental measurements as shown Fig. 8.

Figure 9 shows the longitudinal and transverse thermal strains as a function of temperature. It shows that the residual stresses tend to delay yielding of the matrix. The predicted results show a better agreement with experimental results when the residual stresses are considered in the analysis. The thermal strain curves show nonlinear behavior. Near room temperature, both fiber and matrix expand linearly as the temperature increases. At the critical temperature of initial yielding the fiber properties influence more the longitudinal strains than the matrix properties. On the other hand, the transverse strains are more influenced by the matrix properties. This is shown in the figure where the slope of the transverse strain versus temperature curve increases while that of the longitudinal strain decreases in the temperature range above the yield point. These predictions are in good agreement with experimental results.

Summary and Conclusions

The state of residual stresses induced in the composite by the cool down from the fabrication temperature were calculated. The large difference in CTE's between the fiber and matrix causes high residual stresses but the matrix may experience plastic flow reducing the residual stresses in the composite. An attempt was made to predict the residual stresses in the composite by considering the plastic flow of the matrix.

A thermoelastoplastic analysis was developed and applied to the prediction of the residual stresses in a metal matrix composite The model was based on the coaxial cylindrical model with the perfect bonding at the fiber-matrix interface. It was assumed that the fiber is elastic and the matrix is elastoplastic following the power law strain hardening model.

The residual stress-free temperature was assumed to be 0.6 of the absolute melting temperature, because above this temperature the stress relaxation relieves the residual stress buildup. Below this residual stress-free temperature the elastic residual stress buildup starts followed shortly thereafter by plastic flow of the matrix. The triaxial state of residual stress was then computed. Residual stresses in all directions in the fiber are constant and compressive. The radial residual stress is compressive while the tangential and axial residual stresses are tensile in the matrix. It is observed that the plastic flow of the matrix reduces significantly the amount of residual stress buildup.

The stress-strain behavior under axial loading is not affected by the presence of residual stresses while the thermal strain-temperature curves show a better agreement with the experimental results when the effect of residual stresses is considered. The stress-

strain curves and thermal strain-temperature curves of the composite from the elastoplastic analysis are in good agreement with experimental results

Acknowledgment

This work was supported by NASA-Lewis Research Center, Cleveland, OH. We are grateful to Dr. C. C. Chamis of NASA for his encouragement and cooperation.

References

Alloy Digest Al-3, 1952, Engineering Alloys Digest, Inc., Upper Montclare, New Jersey

Alloy Digest Al-205, 1973, Engineering Alloys Digest, Inc., Upper Montclare, New Jersey

Alsenault, R. J. and Taya, M., 1987, "Thermal Residual Stress in Metal Matrix Composite," *Acta Metallurgica*, Vol. 35, No. 3, pp. 651-659.

ASTM D3379-75, American Society for Testing and Materials, Philadelphia., U.S.A.

Chun, H. J., Wooh, S. C., and Daniel, I. M., 1994, "Thermoelastoplastic Behavior of Unidirectional Composite Materials: Succesive Approximation Method," *ASME Journal of Applied Mechanics*, To be submitted.

Davis, E. A., 1963, "Extension of Iteration Method for Determining Strain Distributions to the Uniformly Stressed Plate with a Hole," *ASME Journal of Applied Mechanics*, June, pp. 210-214.

Gayda, J. and Ebert, L. J., 1979, "The Effect of Cryogenic Cooling on the Tensile Properties of Metal-Matrix Composites ," *Metallurgical Transactions A*, Vol. 10.A, Mar., pp. 349-353.

Haener, J. and Ashbaugh, N., 1967, "Three-Dimensional Stress Distribution in a Unidirectional Composite ," *Journal of Composite Materials*, Vol. 1, pp. 54-63.

Hecker, S. S., Hamilton, C. H., and Ebert, L. J., 1970, "Elastoplastic Analysis of Residual Stresses and Axial Loading in Composite Cylinders," *Journal of Materials*, JMLSA, Vol. 5, No. 4, pp. 868-900.

Hill, R., 1964, "Theory of Mechanical Properties of Fiber Strengthened Materials; II Inelastic Behavior ," *Journal of the Mechanics and Physics of Solids*, JMPSA, Vol. 12, pp. 213-218.

Hillmer, N. J., 1989, "Thermal Expansion of Chemically Vapor Deposited Silicone Carbide Fibers, " *Proceeding of the American Society for Composite*, Dayton, OH, pp. 206-213.

Hsueh, C. and Becher, P. F., 1988, "Thermal Expansion Coefficients of Unidirectional Fiber Reinforced Ceramics," *Journal of the American Ceramic Society*, Vol. 71, pp. 438-441.

Iesan, D., 1980, "Thermal Stresses in Composite Cylinders," *Journal of Thermal Stress*, Vol. 3, pp. 495-508.

Ishikawa, T., Koyama, K. and Kobayash, S., 1978, "Thermal Expansion Coefficients of Unidirectional Composites," *Journal of Composite Materials.*, Vol. 12, pp. 153-168.

Mendelson, A. and Spero, S. W., 1962, "A general Solution for the Elastoplastic Thermal Stresses in a Strain-Hardening Plate with Arbitrary Material Properties," *ASME Journal of Applied Mechanics*, March, pp. 151-158.

Mikata, Y. and Taya, M., 1985, "Stress Field in a Coated Continuous Fiber Composite Subject to Thermo-Mechanical Loadings," *Journal of Composite Materials*, Vol. 19, pp. 554-578.

Piggott, M. R., 1966, "A Theory of Fiber Strengthening," *Acta Metallurgica*, Vol. 14, Nov., pp. 1429-1436.

Pindera, M.-J. and Lin, M. W., 1989, "Micromechanical Analysis of the Elastoplastic Response of Metal Matrix Composites," *Journal of Pressure Vessel Technology*, Vol. 111, pp. 183-190.

Tsai, C-L., and Daniel, I. M., 1994, "Method for Thermo-mechanical Characterization of Single fibers, " *Composite Science and Technology*, Vol. 50, pp. 7-12.

Tuba, S., 1965, "Elastic-Plastic Stress and Strain Concentration Factors at a Circular Hole in a Uniformly Stressed Infinite Plate," *ASME Journal of Applied Mechanics*, September, pp. 170-171.

Uemura, M., Iyama, H. and Yamaguchi, Y., 1979, "Thermal Residual Stresses in Filament Wound Carbon Fiber-reinforced Composites," *Journal of Thermal Stresses*, Vol. 2, pp. 393-412.

Vendula, M., Pangborn, R. N., and Queeney, R. A., 1988, "Fiber Anisotropic Thermal Expansion and Residual Thermal Stress in a Graphite/Aluminum Composite," *Composite*, Vol. 19, No. 1, pp. 55-60.

Warwick, C. M. and Clyne, T. W., 1991, "Development of Composite Coaxial Cylinder Stress Analysis Model and Its Application to SiC Monofilament Systems," *Journal of Material Science*, Vol. 26, pp. 3817-3827.

Whitney, J. M., Daniel, I. M., and Pipes, R. B., 1985, *Experimental Mechanics of Fiber Reinforced Composite Materials*, SEM Monograph 4, Second Ed., Bethel, CT.

Figure Captions

Fig. 1 Coaxial cylindrical composite model.

Fig. 2 Schematic stress-strain curves of power law strain hardening models..

Fig. 3 Tensile stress-strain curves of 6061-O aluminum at various temperatures.

Fig. 4 Thermal residual stresses distribution in the fiber and matrix at room temperature as a function of normalized radial distance without considering plastic flow in the matrix.

Fig. 5 Thermal residual stresses distribution in the fiber and matrix at room temperature as a function of normalized radial distance with considering plastic flow in the matrix.

Fig. 6 Thermal residual stress distributions in the fiber and matrix as a function of normalized radius due to cool down from residual stress free temperature. (a) radial, (b) tangential, (c) axial stresses.

Fig. 7 Radial, tangential and axial residual stresses in the matrix at $r=a$ and in the fiber as a function of temperature.

Fig. 8 Stress-strain curves of unidirectional SiC/Al composite at room temperature.

Fig. 9 Longitudinal and transverse thermals strains versus temperature curves of unidirectional SiC/Al composite.

Table 1 Properties of aluminum 6061-O and SCS-2 fiber at room temperature

Property	6061-O Aluminum	SCS-2 Fiber
Elastic modulus, E, GPa (Msi)	69.0 (10)	399.9 (58)
Poisson's ratio, ν	0.33	0.22
Yield stress, , MPa (ksi)	55.2 (8)	---
Tensile strength, , MPa (ksi)	124.1 (18)	3461 - 5309 (502 - 770)
Coefficient of thermal expansion, α, $\mu\varepsilon/°C$ ($\mu\varepsilon/°F$)		
24 (75)	23.4(13)	2.25(1.25)
121 (250)	23.6(13.1)	2.34(1.30)
177 (350)	23.9(13.3)	2.81(1.56)
288 (550)	24.8(13.5)	---
450-1300 (842-2372)	---	4.86(2.70)

Table 2 Values of material dependent parameters

Temperature	Modulus E, GPa (Msi)	Elastic limit stress σ_Y, MPa (ksi)	Material constant k ($\times 10^{-5}$)	Material constant n ($\times 10^{-2}$)
24°C (75°F)	68.6 (10)	41.4 (6)	510	45.3
121°C (250°F)	63.8 (9.25)	39.3 (5.7)	450	45.5
177°C (350°F)	60.7 (8.8)	37.4 (5.35)	380	45.6
288°C (550°F)	55.2 (8)	33.1 (4.8)	6.62	45.8
399°C (750°F)	48.3 (7)	15.9 (2.3)	6.12	46.0

Table 3 Properties of SiC/Al composite at room temperature

Property	SiC/Al Composite
Longitudinal modulus, E_1, GPa (Msi)	206.9 (30.0)
Major Poisson's ratio, ν_{12}	0.27
Longitudinal tensile strength, F_t, MPa (ksi)	1620.0 (235.0)
Longitudinal coefficient of thermal expansion, α_1, $\mu\varepsilon/°C$ ($\mu\varepsilon/°F$)	5.94 (3.3)
Transverse coefficient of thermal expansion, α_2, $\mu\varepsilon/°C$ ($\mu\varepsilon/°F$)	16.0 (8.9)
Fiber volume ratio, V_f	0.44

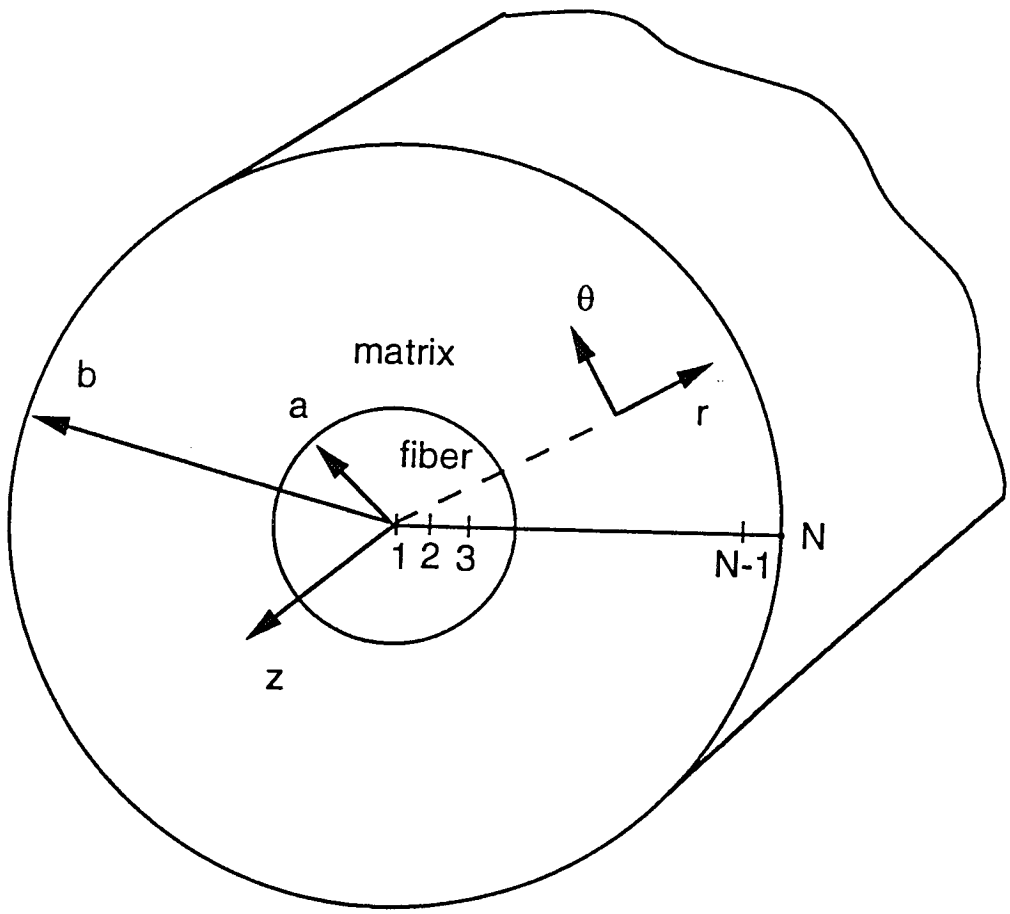
θ
matrix
b
a
r
fiber
1 2 3
N
N-1
z

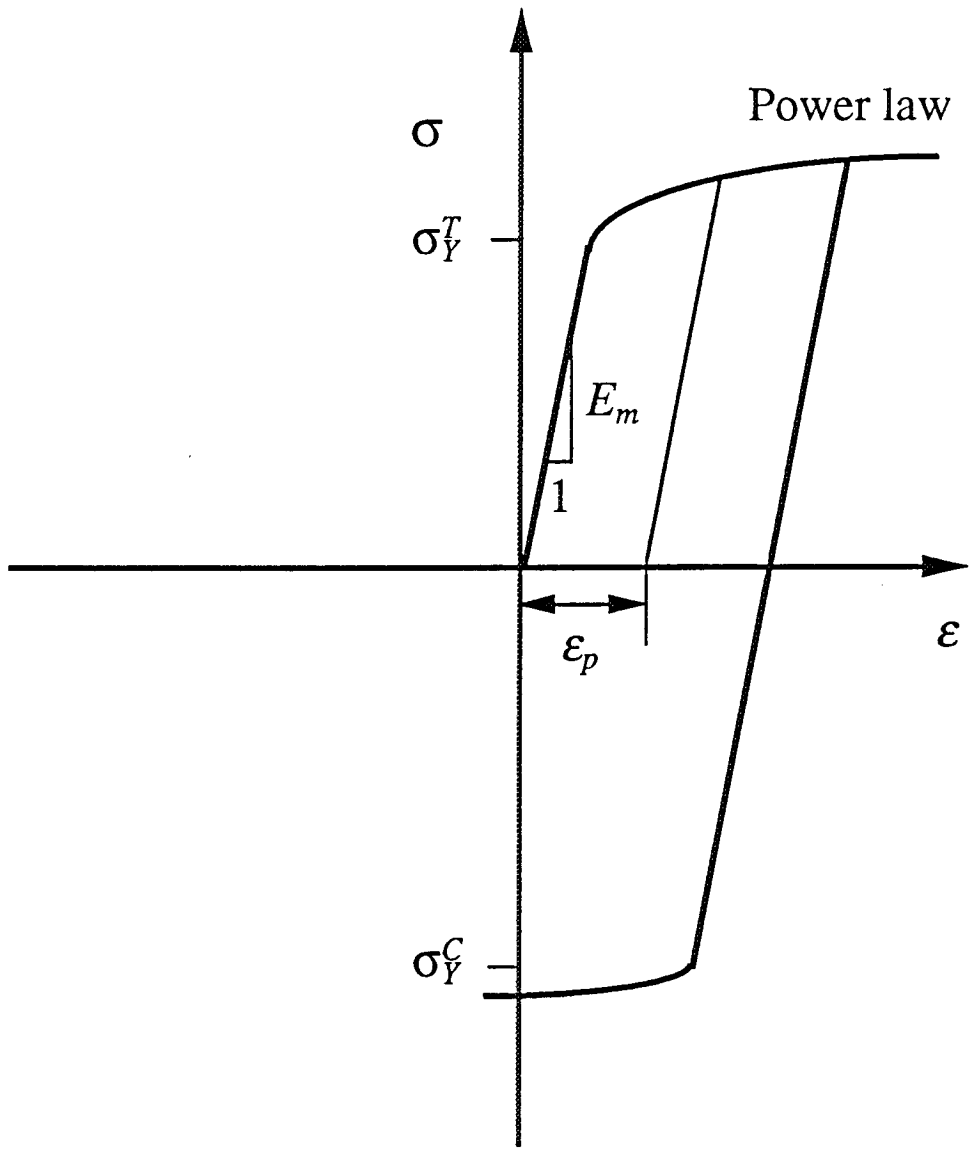
Power law
σ
σ_Y^T
E_m
1
ε_p
ε
σ_Y^C

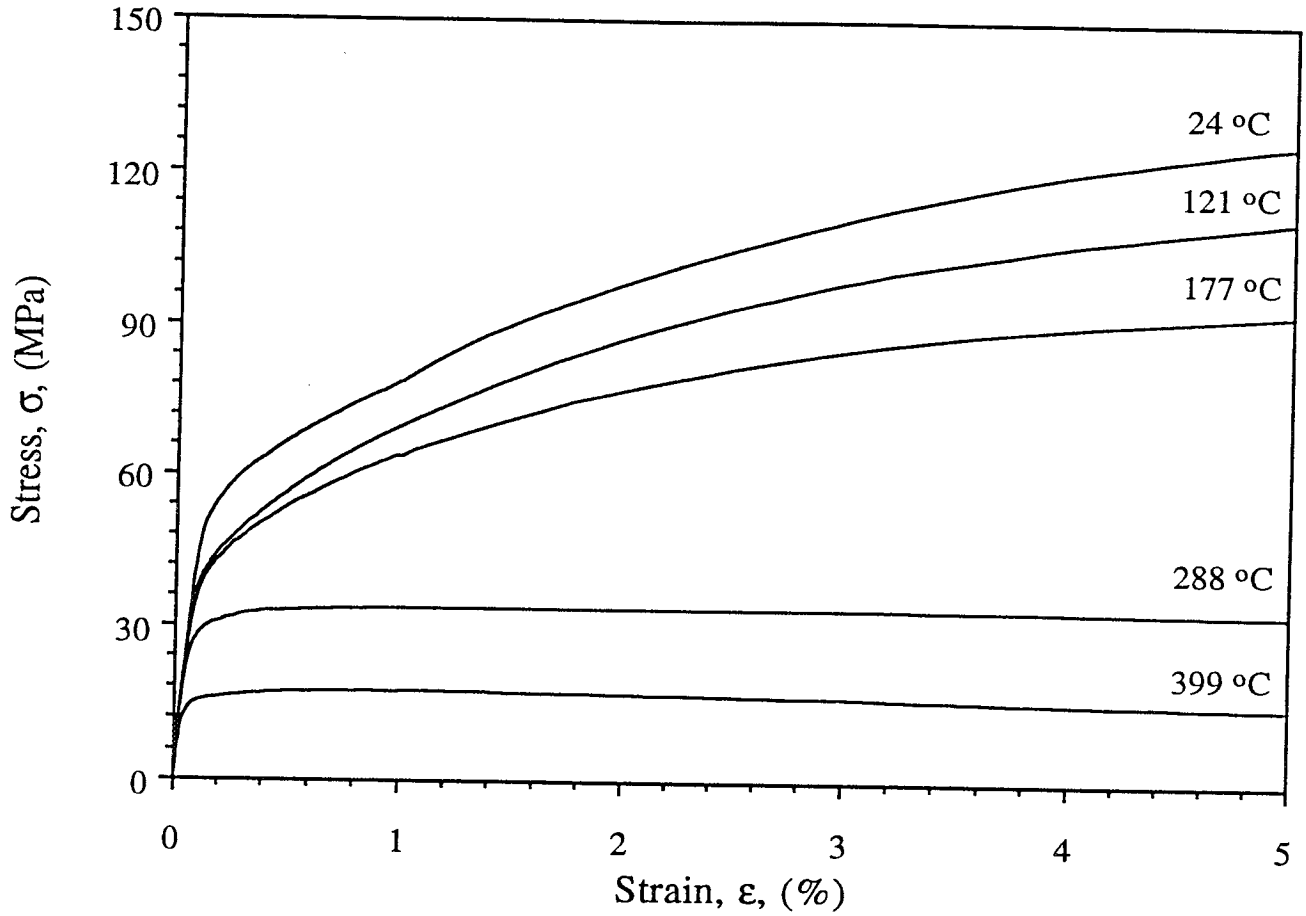
150
120
90
60
30
0
Stress, σ, (MPa)
24 °C
121 °C
177 °C
288 °C
399 °C
0
1
2
3
4
5
Strain, ε, (%)

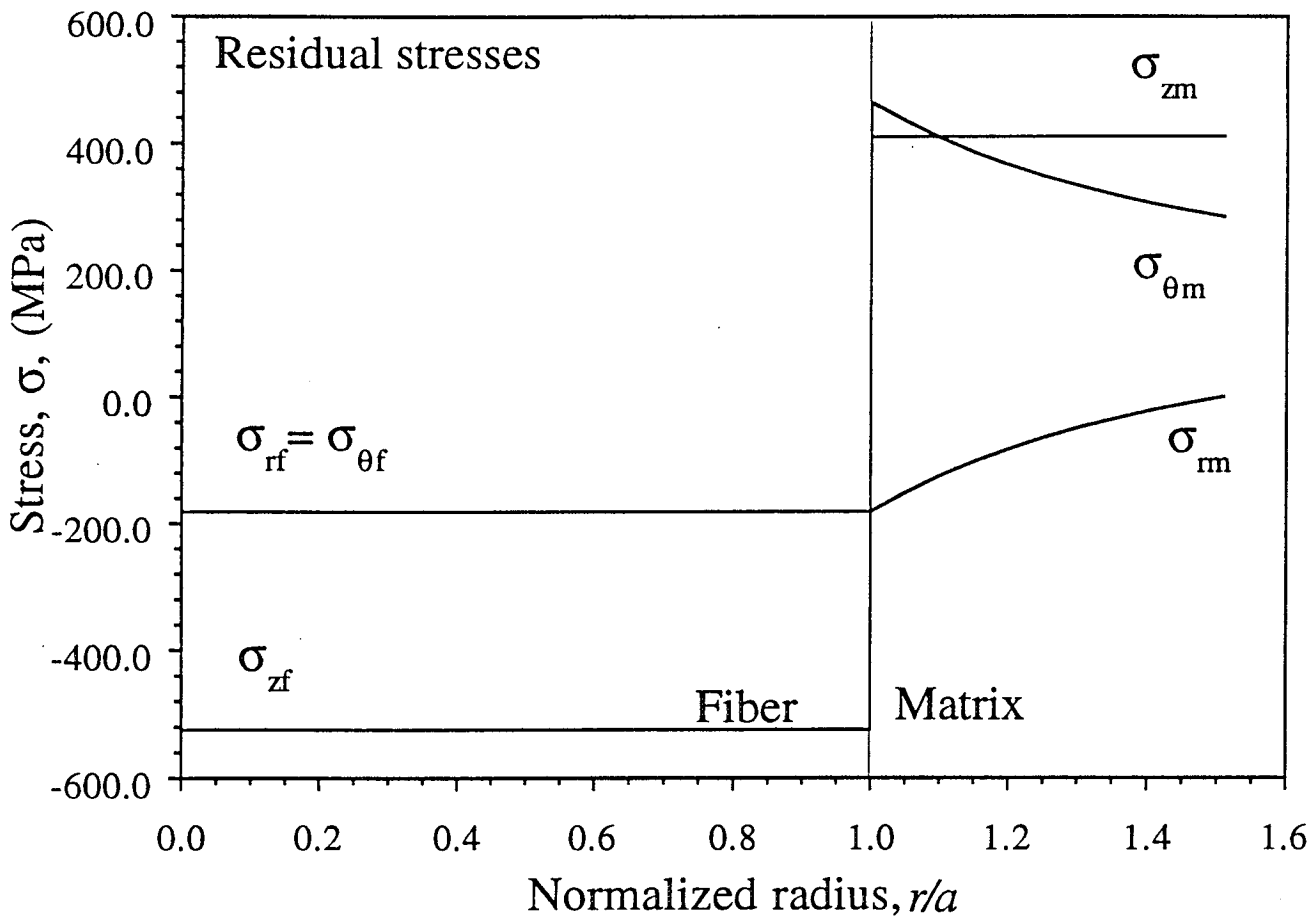
Residual stresses
σ_{zm}
$\sigma_{\theta m}$
σ_{rm}
$\sigma_{rf} = \sigma_{\theta f}$
σ_{zf}
Fiber
Matrix
600.0
400.0
200.0
0.0
-200.0
-400.0
-600.0
Stress, σ, (MPa)
0.0
0.2
0.4
0.6
0.8
1.0
1.2
1.4
1.6
Normalized radius, r/a

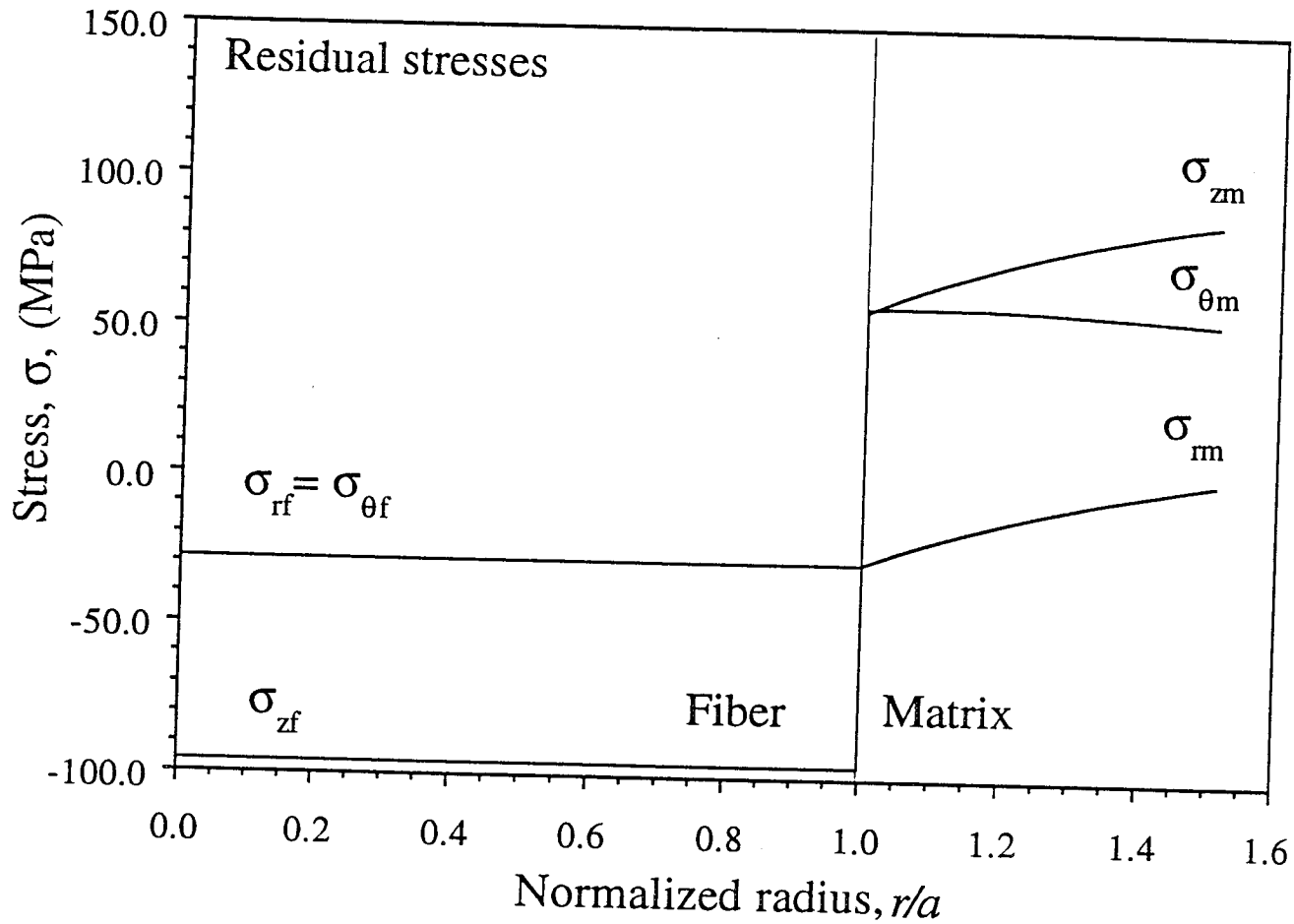
Residual stresses
150.0
100.0
50.0
0.0
-50.0
-100.0
Stress, σ, (MPa)
σzm
σθm
σrm
σrf= σθf
σzf
Fiber
Matrix
0.0
0.2
0.4
0.6
0.8
1.0
1.2
1.4
1.6
Normalized radius, r/a

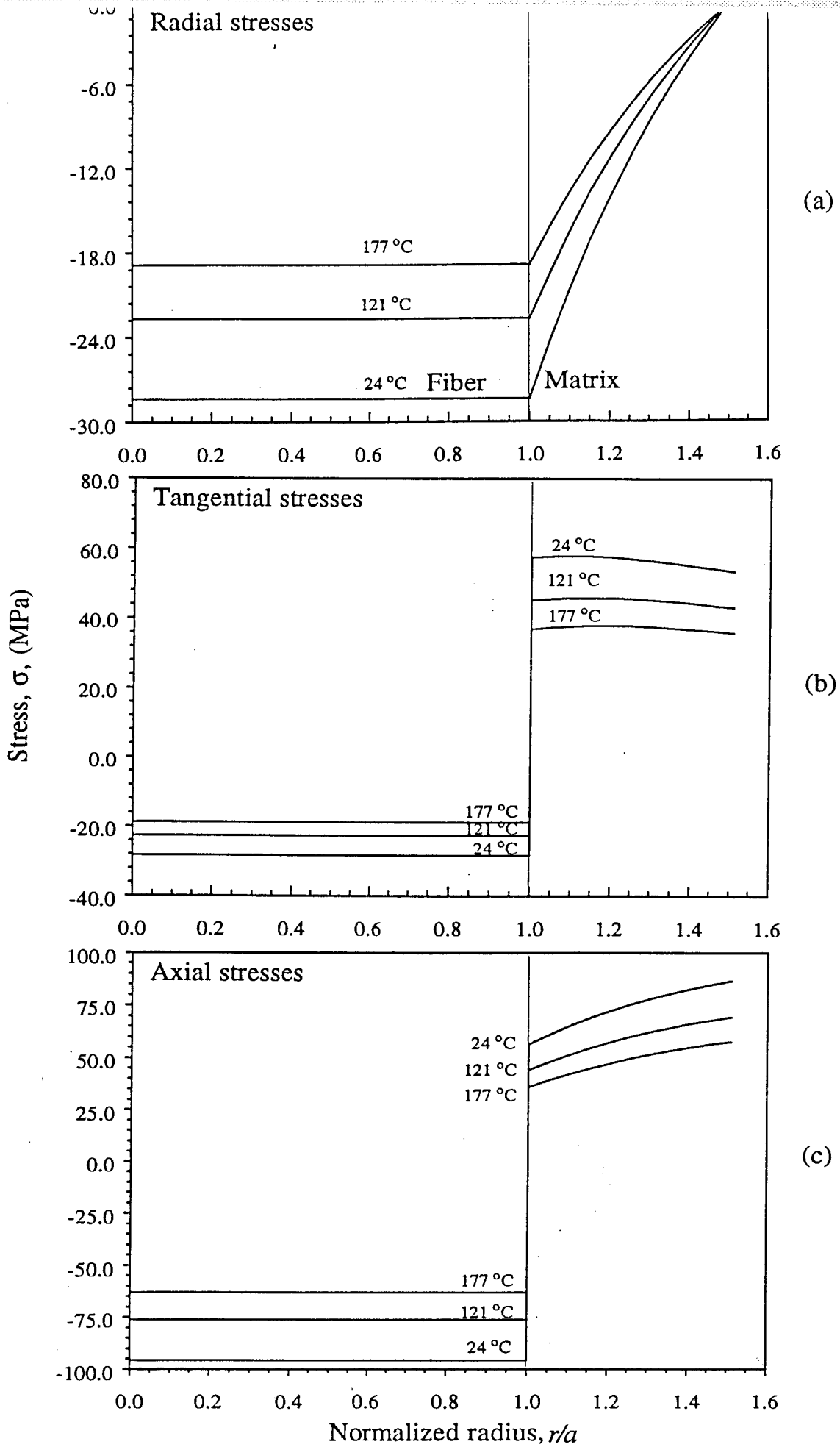
Radial stresses
-6.0
-12.0
-18.0
-24.0
-30.0
177 °C
121 °C
24 °C
Fiber
Matrix
(a)
0.0
0.2
0.4
0.6
0.8
1.0
1.2
1.4
1.6
Tangential stresses
80.0
60.0
40.0
20.0
0.0
-20.0
-40.0
24 °C
121 °C
177 °C
(b)
Axial stresses
100.0
75.0
50.0
25.0
0.0
-25.0
-50.0
-75.0
-100.0
(c)
Stress, σ, (MPa)
Normalized radius, r/a

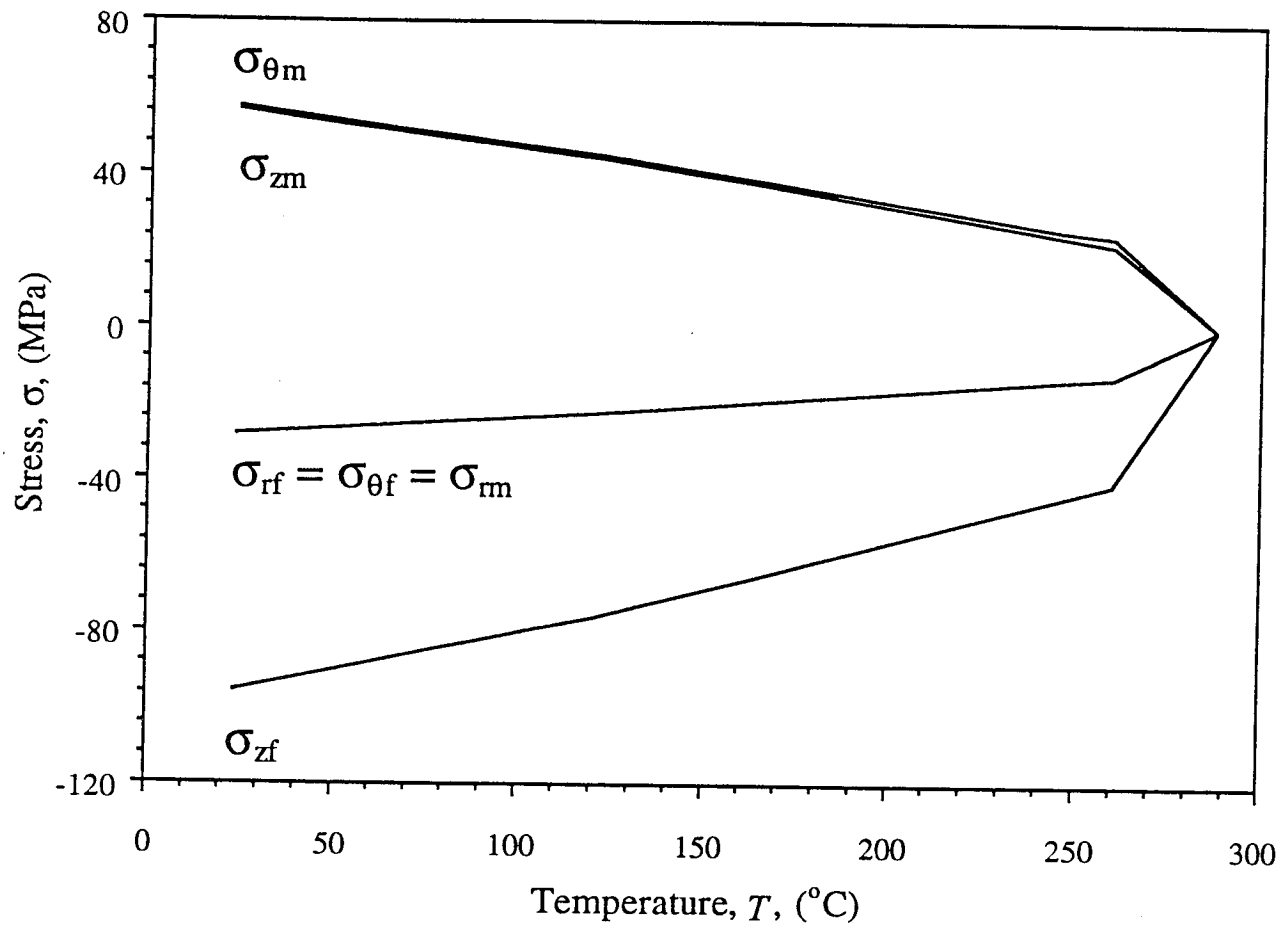
80
40
0
-40
-80
-120
Stress, σ, (MPa)
σθm
σzm
σrf = σθf = σrm
σzf
0
50
100
150
200
250
300
Temperature, T, (°C)

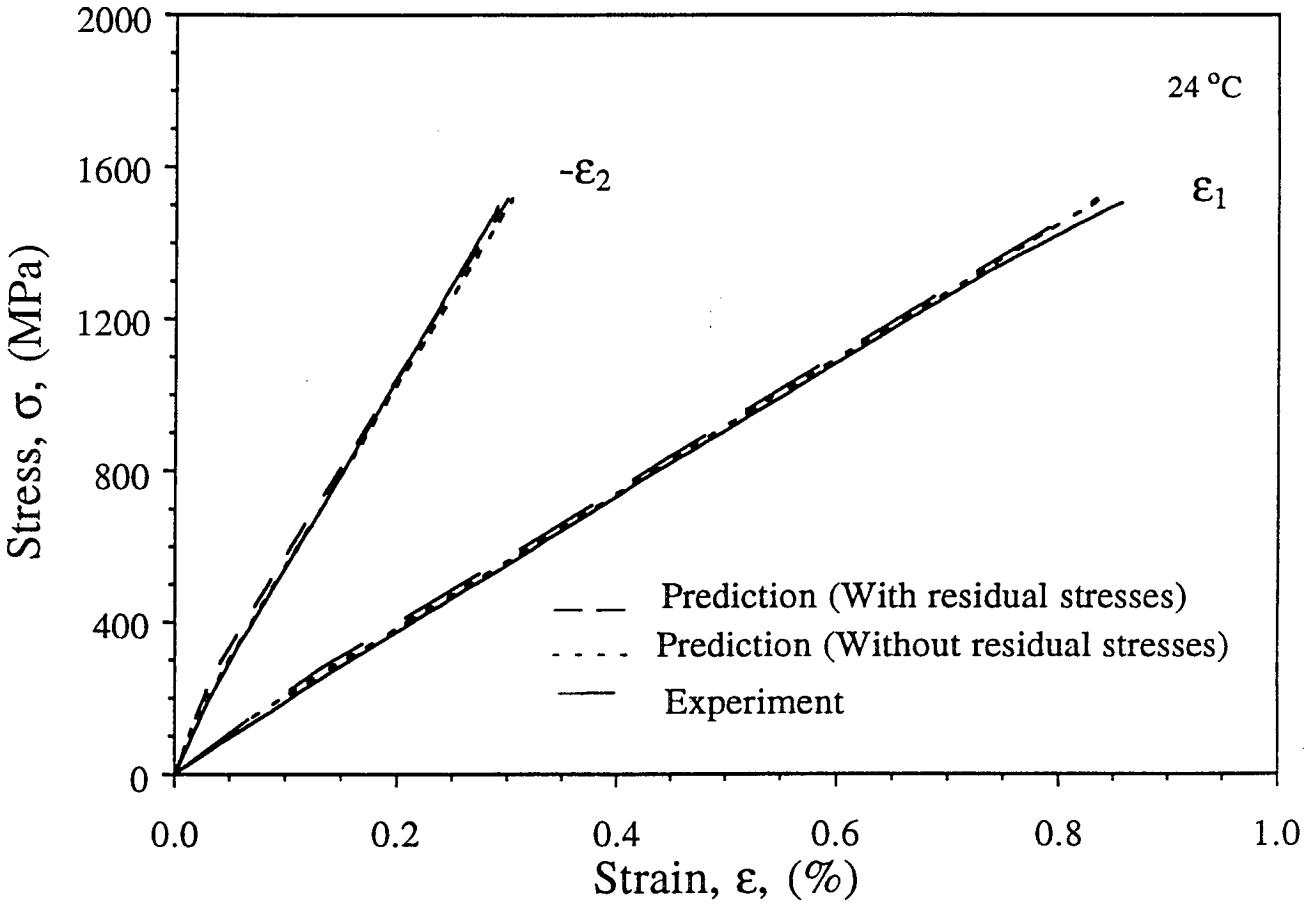
2000
1600
1200
800
400
0
Stress, σ, (MPa)
0.0
0.2
0.4
0.6
0.8
1.0
Strain, ε, (%)
24 °C
-ε2
ε1
Prediction (With residual stresses)
Prediction (Without residual stresses)
Experiment

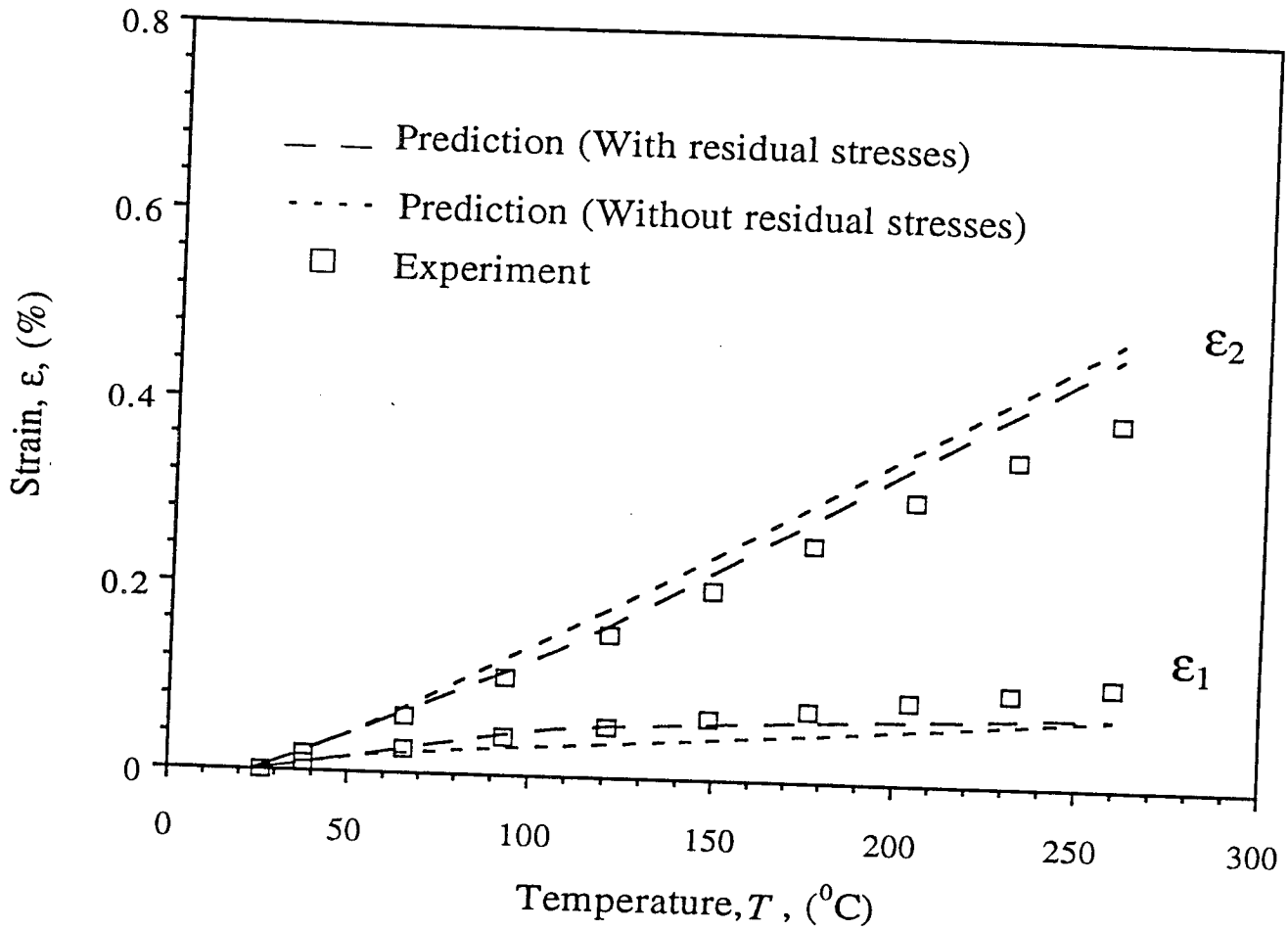
0.8
0.6
0.4
0.2
0
Strain, ε, (%)
Prediction (With residual stresses)
Prediction (Without residual stresses)
Experiment
ε2
ε1
0
50
100
150
200
250
300
Temperature, T , (°C)

APPENDIX B

MICROMECHANICAL ANALYSIS OF FILAMENTARY METAL MATRIX COMPOSITES UNDER LONGITUDINAL LOADING

by

Emmanuel E. Gdoutos,[1] Dimitrios Karalekas[2] and Isaac M. Daniel[3]

1 Professor, Democritus University of Thrace, GR-67100 Xanthi, Greece

2 Manager, R & D, European Center of Advanced Technologies, Athens, Greece

3 Professor, Robert R. McCormick School of Engineering and Applied Science, Northwestern University, Evanston, IL 60208

MICROMECHANICAL ANALYSIS OF FILAMENTARY METAL MATRIX COMPOSITES

ABSTRACT

A two-material composite cylinder model (CCM) was considered for the study of the mechanical behavior at different temperatures of a fiber reinforced silicon carbide/aluminum (SiC/Al) composite. An elastoplastic analysis of the model was performed in which the fiber was assumed to be linear elastic and the matrix elastoplastic with work-hardening. The analysis was based on the deformation theory of plasticity in conjunction with the von-Mises yield criterion. Experimental stress-strain curves of a SiC/Al composite were obtained at 24°C (75°F) and 288°C (550°F). The complete three-dimensional stress distribution in the composite using the CCM was determined. It was found that in addition to longitudinal stresses, transverse stresses in both the fiber and the matrix were developed as a result of the different Poisson's ratios of the two materials. The transverse stresses, although much smaller than the longitudinal stresses, contributed to the plastic deformation of the matrix. The experimental stress-strain curves were favorably compared with the theoretical predictions.

KEYWORDS: Metal-Matrix Composites; Micromechanics; Silicon Carbide/Aluminum; Elasto-plastic Analysis; High-temperature behavior.

INTRODUCTION

Metal matrix composites reinforced with continuous elastic fibers may experience a pronounced degree of inelastic deformation when subjected to thermomechanical loading. This inelastic behavior is indicative of the overall nonlinear stress-strain or strain-temperature response of the composite. The state of stress in the matrix is no longer homogeneous and it depends on the history of deformation and the strain rate. A number of different micromechanical models which give not only the overall behavior of the composite but also the detailed stress state in the constituent materials have been proposed.

These models for the study of linear and nonlinear behavior of fibrous composites in which the matrix exhibits elastoplastic deformation were based on mechanics of materials analysis [1-3],

bounding methods of plasticity [4,5] and finite elements [6-13]. Further studies on modeling the thermomechanical response of metal matrix composites are listed in references [14-20]. A two-material composite cylinder model has been proposed in [21-23] for micromechanical analysis. This model was used in the study of the elastoplastic behavior of two and three-material composite cylinders in [24,25].

In the present paper an elastoplastic analysis of the composite cylinder model based on the deformation theory of plasticity in conjunction with the von-Mises yield criterion was performed. Complete three-dimensional stress distributions in the cylinder were obtained. The model was successfully used for the prediction of the longitudinal stress-strain behavior of a SiC/A*l* composite at two temperatures.

THE COMPOSITE CYLINDER MODEL

The representative volume element in the two-material composite cylinder model (CCM) consists of an inner cylinder simulating the fiber and a shell included between the inner and outer radii of the cylinder simulating the matrix (Fig. 1). This representation is characteristic of low fiber volume composites in which the fiber volume ratio is usually taken arbitrarily less than 65 percent. For high fiber volume composites the inner cylinder simulates the matrix and the shell the fiber. The composite material used in this study, silicon carbide/aluminum, has a relatively low fiber volume ratio.

The fiber (SiC) is considered linear elastic up to fracture, while the aluminum matrix exhibits elastoplastic behavior and its thermomechanical properties are temperature-dependent. The CCM is first analyzed for the case when both components remain linear elastic and then when the matrix shell is deformed elastoplastically.

Elastic Behavior

For linear elastic behavior of both materials of the composite cylinder the non-zero displacement and stress fields for axisymmetric mechanical deformation are given by the following equations [16]

$$u = Ar + \frac{B}{r} \tag{1a}$$

$$\sigma_r = K\left[A - (1 - 2\nu)\frac{B}{r^2} + \nu\,\varepsilon_z\right] \tag{1b}$$

$$\sigma_\theta = K\left[A + (1 - 2\nu)\frac{B}{r^2} + \nu\,\varepsilon_z\right] \tag{1c}$$

$$\sigma_z = K\left[2\nu A + (1 - \nu)\,\varepsilon_z\right] \tag{1d}$$

In the above equations u is the radial displacement, σ_r, σ_θ and σ_z the radial, circumferential and axial stresses, r the radial distance from the center of the cylinder, ε_z the axial strain and A and B constants to be determined from the boundary conditions of the problem. The bulk modulus K is given by

$$K = \frac{E}{(1 + \nu)(1 - 2\nu)} \tag{2}$$

where E is the modulus of elasticity and ν Poisson's ratio.

Since the inner cylinder and the shell are perfectly bonded, continuity of the radial displacement u and the radial stress σ_r at the interface between the two components is implied. Furthermore, u should be finite at r = 0 and σ_r is zero at the outer boundary of the cylinder.

For an applied constant strain ε_z across the composite cylinder cross section the constants A_j, B_j (j = 1,2) are determined from the solution of the following matrix equation

$$\begin{bmatrix} R_1 & -R_1 & -R_1^{-1} \\ K_1 & -K_2 & (1-2\nu_2)\,K_2\,R_1^{-2} \\ 0 & 1 & -(1-2\nu_2)\,R_2^{-2} \end{bmatrix} \begin{bmatrix} A_1 \\ A_2 \\ B_2 \end{bmatrix} = \begin{bmatrix} 0 \\ -K_1\nu_1 + K_2\nu_2 \\ -\nu_2 \end{bmatrix} \varepsilon_z \tag{3a}$$

$$B_1 = 0 \tag{3b}$$

where the subscripts 1 and 2 refer to the inner (fiber) and outer (matrix) components and R_1 and R_2 are the inner and outer radii of the composite cylinder.

After determining the constants A_j, B_j (j = 1,2) the stresses σ_r, σ_θ and σ_z and the

displacement u are computed from equations (1). From equation (1d) it is observed that the axial stresses σ_{z1} and σ_{z2} are constant along the axis of the composite cylinder. The average axial stress σ on the cylinder is determined by

$$\sigma = \frac{\sigma_{z1} R_1^2 + \sigma_{z2}\left(R_2^2 - R_1^2\right)}{R_2^2} \tag{4}$$

The critical strain $(\varepsilon_z)_{cr}$ for which the most stressed elements of the matrix along the fiber-matrix interface start to yield is determined by

$$\sigma_{eff} = \sigma_{my} \tag{5}$$

where the effective stress σ_{eff} is given by

$$\sigma_{eff} = \frac{1}{\sqrt{2}}\left[(\sigma_z - \sigma_r)^2 + (\sigma_r - \sigma_\theta)^2 + (\sigma_\theta - \sigma_z)^2\right]^{1/2} \tag{6}$$

Equation (5) expresses the von-Mises criterion for initial yielding. The yield stress σ_{my} of the aluminum is a function of temperature.

Elastoplastic Behavior

When the applied axial strain ε_z is increased beyond its critical value $(\varepsilon_z)_{cr}$ plastic deformation occurs in the aluminum phase. It takes the form of concentric cylindrical layers starting from the fiber-matrix interface and spreads progressively towards the outer radius as ε_z is increased. The deformation in the aluminum becomes inhomogeneous and an elastic-plastic analysis is required for the determination of the stress field and the elastic-plastic boundary.

The deformation theory of plasticity in conjunction with the von-Mises yield criterion and the isotropic hardening rule are employed. The results obtained by this theory coincide with those of the flow theory for proportional loading, while for non-proportional monotonic loading without unloading reasonably accurate predictions are obtained. [26] The basic assumption made in the elastoplastic analysis is that the effective stress-strain relation $\sigma_{eff} = f(d\varepsilon_{ff})$ for a triaxial state of stress coincides with the stress-strain curve in uniaxial tension. The effective strain is defined by

$$d\varepsilon_{ff} = \frac{1}{\sqrt{2}\,(1+\nu)}\left[(d\varepsilon_z - d\varepsilon_r)^2 + (d\varepsilon_r - d\varepsilon_\theta)^2 + (d\varepsilon_\theta - d\varepsilon_z)^2\right]^{1/2} \tag{7}$$

The value of Poisson's ratio ν beyond the yield point can be determined by

$$\nu = 0.5 - (0.5 - \nu')\,\frac{E_s}{E} \tag{8}$$

where E and E_s are the elastic and secant moduli of the material in tension and ν' the Poisson's ratio in the elastic region.

The incremental stress-strain relations in the deformation theory of plasticity take the form

$$d\varepsilon_z = \frac{1}{E_t}\left[d\sigma_z - \nu\,(d\sigma_r + d\sigma_\theta)\right] \tag{9a}$$

$$d\varepsilon_r = \frac{1}{E_t}\left[d\sigma_r - \nu\,(d\sigma_\theta + d\sigma_z)\right] \tag{9b}$$

$$d\varepsilon_\theta = \frac{1}{E_t}\left[d\sigma_\theta - \nu\,(d\sigma_z + d\sigma_r)\right] \tag{9c}$$

where $d\varepsilon_z$, $d\varepsilon_r$ and $d\varepsilon_\theta$ are the total, elastic plus plastic, strain increments and $d\sigma_z$, $d\sigma_r$ and $d\sigma_\theta$ are the stress increments. E_t represents the tangent modulus ($E = d\sigma/d\varepsilon$) of the uniaxial stress-strain curve of the material in tension.

Equations (9) are used in conjunction with the equations of equilibrium and compatibility. The deformation theory of plasticity is actually a nonlinear elasticity theory with changing values of modulus of elasticity and Poisson's ratio depending on the amount of plastic deformation. Thus, for the solution of the elastic-plastic problem the aluminum shell was divided into a number (N) of concentric layers, each layer having a different modulus and Poisson's ratio. The following procedure was followed:

1. An elasticity solution of the (N+1) material composite cylinder was obtained following a procedure analogous to that used in the previous case of the two-material composite

cylinder. This solution served as a subroutine to a computer program written for the elastoplastic solution of the problem.

2. The applied critical strain $(\varepsilon_z)_{cr}$ for which the first layer at the fiber-matrix interface yields was determined, using the stress solution obtained by the subroutine in conjunction with equation (5).

3. A strain increment $\Delta\varepsilon$ above the critical strain $(\varepsilon_z)_{cr}$ was applied. The effective total (cumulative) strain is given by $\varepsilon_n^N = \varepsilon_n^{N-1} + d\varepsilon_n$, where N denotes the number of the loading step, and n the iteration number. $d\varepsilon_n$ is the first effective strain increment.

4. The tangent modulus was determined for each layer from the value of the equivalent strain obtained from the uniaxial stress-strain curve of the material and Poisson's ratio v from equation (8).

5. Stress and strain increments $d\sigma_{ij}$ and $d\varepsilon_{ij}$ (using equations (9)) were determined for all cylinders with the new values of modulus and Poisson's ratio, as determined in step 4.

6. The new effective strain increment $d\varepsilon_{n+1}$ was determined from equation (7).

7. Strain increments $d\varepsilon_{n+1}$ and $d\varepsilon_n$ were compared. If $(d\varepsilon_{n+1}-d\varepsilon_n)/d\varepsilon_n > \delta$ for all cylinders (δ is a predetermined cutoff value), the program returned to step 3 with the value $d\varepsilon_{n+1}$ substituting the value $d\varepsilon_n$. The entire process from step 3 to step 6 was repeated. If $(d\varepsilon_{n+1}-d\varepsilon_n)/d\varepsilon_n < \delta$ for all cylinders, then, the correct states of stress and strain for the load increment used are given by those obtained with the values of $d\varepsilon_n$. The program was then returned to step 3 and the entire procedure was repeated.

Using this procedure the complete history of stress and strain along the radius of the composite cylinder was determined as the strain was increased incrementally.

EXPERIMENTAL RESULTS

The composite material consisted of a 6061-T6 aluminum matrix reinforced with 140 μm (5.6×10^{-3} in.) diameter silicon carbide fibers (SCS-2, Textron Specialty Material, Inc.). The

fiber volume ratio was measured as 0.44. The material was produced by a diffusion bonding consolidation, during which the temper of the aluminum is changed to one approaching T-4 temper. For this reason 6061-T4 aluminum was obtained and tested to determine its mechanical and thermal response.

The composite material was obtained in the form of unidirectional 8-ply plates, 0.178 mm (7×10^{-3} in.) thick. Specimens 15.2 cm (6 in.) long and 1.27 cm (0.5 in.) wide with the long dimension parallel to the fibers were machined with a water-cooled diamond saw. Aluminum tabs were bonded to the specimen ends with a high strength adhesive. The tab length was long enough (5.1 cm. (2 in.)) to provide an area which is large enough to transfer the load to the specimen through shear. Great care was exercised in cutting the specimens so that the fibers do not experience any significant damage and the tabs were precisely aligned on the specimens.

Tensile tests were carried out in a servo-hydraulic Instron testing machine. The specimens were loaded at a crosshead rate of 0.06 in/min. up to failure. Particular care was taken in aligning the coupons in the grips. Tests at ambient and elevated temperatures were performed. Special grips were used for testing at elevated temperatures. A water-cooling system was installed to lower the grip temperature. Special high-temperature strain gages (Micromeasurements gage type WK-06-125 TM-350) were used to record the strains along the axial (ε_1) and transverse (ε_2) directions. Axial strains were also monitored with an extensometer of 1 in. gage length (0.1 in. range). The application of the extensometer as a second means of measuring strain was considered essential because the strain obtained from the gage output could then be double-checked. A data acquisition system (Metrabyte Corp.) was used to acquire, process and plot data in reportable form.

Figures 2 and 3 show longitudinal stress-strain curves for the SiC/A*l* composite at 24 °C (75°F) and 288 °C (550°F). Both curves exhibit a linear elastic portion that extends up to strains ε = 0.12 percent and 0.07 percent, for temperatures 24°C and 288°C, respectively. Note that the stress-strain curves up to failure deviate little from linearity which is attributed to the fact that most of the applied load is carried by the fibers due to their much higher elastic modulus. The deviation

from linearity is more pronounced at 288°C. The stress vs. transverse strain curve for 24°C and 288°C (Figures 2 and 3) are almost linear up to fracture.

For the micromechanical prediction of the stress-strain behavior of the composite the stress-strain curves of the aluminum matrix at 24°C and 288°C are needed. Prismatic 6061-T4 aluminum specimens of dimensions 20.32 cm (8.0 in.) long, 1.27 cm (0.5 in.) wide and 0.16 cm (0.062 in.) thick were prepared. For testing at elevated temperatures steel tabs were bonded onto the specimen ends with a high strength adhesive (FM-36). The stress-strain curves of 6061-T4 aluminum at various temperatures ranging from 24°C to 288°C are shown in Fig. 4. Only the portion of the curves up to 1 percent strain is shown. As temperature increases the stress at which the curves deviate from linearity decreases. Values of the proportional limit of aluminum at 24°C and 288°C are shown in Table 1. The modulus of elasticity for all stress-strain curves at various temperatures is the same and equal to 69 GPa (10 Msi). In the nonlinear portion of the curves the stresses corresponding to the same strain decrease with increasing temperature.

THEORETICAL PREDICTIONS

Prediction of the stress-strain behavior of the composite by the composite cylinder model necessitates the values of the various material parameters entering into the previously described micromechanical equations. The fiber (SiC) remains almost linear elastic up to fracture. Its mechanical parameters are independent of temperature and they are given in Table 2. Unlike the fiber, aluminum exhibits pronounced plastic deformation and its thermomechanical parameters are temperature dependent. The post yield stress-strain curve of aluminum was represented by a fifth-order polynomial of the form

$$\sigma = \sum_{n=1}^{5} C_n \varepsilon^n$$

The coefficients C_n are temperature dependent. They were determined from the stress-strain curves of aluminum in uniaxial tension at different temperatures. Values of C_n for temperatures of 24°C and 288°C (75° and 550°F) are given in Table 1.

For a fiber volume ratio of the SiC/A*l* composite studied in this investigation (0.44) the outer radius R_2 of the composite cylinder model (CCM) is equal to 1.51 R_1, where R_1 is the inner radius. In order to perform an elastoplastic analysis of the composite cylinder the matrix shell was divided into eight layers each of thickness 0.064 R_1. The critical value of the applied average uniaxial strain $(\varepsilon_z)_{cr}$ for which the aluminum matrix starts to deform plastically was first determined from equation (5). It was found to be $(\varepsilon_z)_{cr} = 0.125$ percent for T = 24°C and $(\varepsilon_z)_{cr} = 0.060$ percent for T = 288°C. These strains are very close to the critical ones at which aluminum deviates from linearity. For applied strains ε_z below these values the stress-strain curve of the composite is linear and the triaxial stress field developed in the fiber and matrix is directly proportional to ε_z. The stresses in the fiber are

$$\sigma_{zf} = 364.3\ \varepsilon_z \text{ GPa } (52.8\ \varepsilon_z \text{ Msi})$$

$$\sigma_{rf} = \sigma_{\theta f} = -\ 2.7\ \varepsilon_z \text{ GPa } (-0.386\ \varepsilon_z \text{ Msi})$$

and the stresses in the matrix at $r = R_1$ are

$$\sigma_{zm} = 70.4\ \varepsilon_z \text{ GPa } (10.2\ \varepsilon_z \text{ Msi})$$

$$\sigma_{rm} = -\ 2.7\ \varepsilon_z \text{ GPa } (-\ 0.386\ \varepsilon_z \text{ Msi})$$

$$\sigma_{\theta m} = 6.8\ \varepsilon_z \text{ GPa } (0.989\ \varepsilon_z \text{ Msi})$$

Note that the transverse stresses are an order of magnitude lower than the axial stresses. It is also worthwhile to observe that the axial stresses in the fiber and the matrix are very close to those predicted by the rule of mixtures which yields the values $\sigma_{zf} = 359$ GPa (52 ε_z Msi) and $\sigma_{zm} = 69$ GPa (10 ε_z Msi), respectively. For linear elastic behavior the longitudinal elastic modulus and major Poisson's ratio take the values of 199.8 GPa (28.96 Msi) and 0.276 which are very close to the values of 199.6 GPa (28.92 Msi) and 0.282 predicted by the rule of mixtures. The experimental values for the elastic modulus and Poisson's ratio are 176 GPa (25.5 Msi) and 0.29, respectively.

When the applied strain ε_z is increased beyond its critical value $(\varepsilon_z)_{cr}$, plastic deformation takes place in the aluminum matrix. An incremental elastoplastic stress/strain analysis as described

before was performed. The strain ε_z was increased at intervals of 0.05 percent and the three-dimensional stress distributions at the midsurface of each layer of the aluminum shell was determined. The predicted longitudinal stress-strain curves of the composite at temperatures of 24°C and 288°C are shown in Figs. 2 and 3, respectively. They agree well with the experimental results.

According to the elastoplastic analysis of the composite cylinder based on the deformation theory of plasticity, each layer of the aluminum shell is considered as an elastic material with varying modulus of elasticity, E_m, and Poisson's ratio, ν_m, depending on the amount of plastic deformation. The variation of E_m and ν_m across the thickness of the aluminum shell ($1.00 < r/R_1 < 1.51$) is shown in Figs. 5 and 6 for various values of the applied strain ε_z at T = 288 °C (550°F). Observe that E_m decreases from its elastic value of 69 GPa (10 Msi) while ν_m increases from its elastic value of 0.33 up to the limiting value of 0.50 as ε_z increases. The variation of both E_m and ν_m along the radius of the shell is small with E_m increasing and ν_m decreasing from the fiber/matrix interface to the outer radius of the composite cylinder. The variation of E_m and ν_m at the midsurface of the aluminum shell with the applied strain ε_z is shown in Fig. 7 for T = 24 °C.

Figure 8 shows the variation of the axial, σ_z, radial, σ_r, and circumferential, σ_θ, stresses along half the diameter of the composite cylinder for ε_z = 0.175 percent and T = 24°C. All three stress components are constant in the fiber, while the stresses vary along the thickness of the shell. A slight variation of the axial stress σ_z with increasing values from the fiber/matrix interface to the outer radius of the composite cylinder is observed. Note that the radial stress is compressive in both the fiber and matrix, while the circumferential stress is compressive in the fiber and tensile in the matrix. Both radial and circumferential stresses have equal values in the fiber, while a large variation of these stresses is observed in the matrix. The transverse stresses are ignored in the micromechanical analysis of the composite based on the rule of mixtures. The variation of the stresses σ_r, σ_θ and σ_z along the thickness of the aluminum matrix for various values of the applied strain ε_z is shown in Figs. 9 to 11 for T = 24°C (75°F). In Fig. 11 the variation of stress σ_z is shown in a stepwise form, as it was determined at the midsurface of each of the eight layers of the

matrix. Note from Figs. 9 to 11 that all stresses increase with applied strain ε_z and that the rate of increase decreases as the strain is increased.

CONCLUSIONS

A study of the stress-strain behavior of a SiC/Al filamentary composite was performed. Experimental longitudinal stress-strain curves at temperatures 24°C (75°F) and 288°C (550°F) were obtained. An elastoplastic micromechanical analysis based on the composite cylinder model was performed and yielded complete three-dimensional stress distributions in both the fiber and the matrix. The main results of the present study may be summarized as follows:

1. Slight nonlinearity in the stress-strain behavior of SiC/Al appears beyond a critical value of applied strain. This is attributed to the fact that most of the applied load is taken by the fiber due to their much higher elastic modulus. The deviation from linearity is more pronounced at higher temperatures.

2. The beginning of nonlinearity in the stress-strain curves coincides with the development of plastic deformation in the aluminum matrix.

3. The transverse stresses developed due to the difference in Poisson's ratios of the fiber and matrix are small for linear elastic behavior, but they increase as plastic deformation is advanced. However, the transverse stresses are an order of magnitude smaller than the axial stresses. These stresses are ignored in the micromechanical analysis based on the rule of mixtures.

4. The radial stresses in the matrix are compressive, while the circumferential stresses are tensile. This results in an increase of the equivalent stress and the accelerated plastic distortion of the matrix when compared with the case when the transverse stresses are ignored.

5. Very good agreement between the experimental results and the predictions of the composite cylinder model was achieved.

ACKNOWLEDGEMENT

The work described here was sponsored by the NASA-Lewis Research Center, Cleveland, OH. We are grateful to Dr. C. C. Chamis of NASA for his encouragement and cooperation and to Mrs. Yolande Mallian for typing the manuscript.

REFERENCES

1. Shaffer, B. W., "Stress-Strain Relations of Reinforced Plastics Parallel and Normal to their Internal Filaments," AIAA J., Vol 2, 1964, pp. 348-352.

2. Shaffer, B. W., "Elastic-Plastic Stress Distribution within Reinforced Plastics Loaded Normal to its Internal Filaments," AIAA J., Vol 6, 1968, pp. 2316-2324.

3. Min, B. K. and Crossman, F. W., "History-Dependent Thermomechanical Properties of Graphite/Aluminum Unidirectional Composites," in Composite Materials, Testing and Design (Sixth Conference), ASTM STP 787, edited by I. M. Daniel, American Society for Testing and Materials, 1982, pp. 371-392.

4. Hill, R., "Theory of Mechanical Properties of Fibre-Strengthened Materials: II. Inelastic Behavior," J. Mech. Phys. Sol., Vol. 12, 1964, pp. 213-218.

5. Dvorak, G. J. and Teply, J. L., "Periodic Hexagonal Array Models for Plasticity Analysis of Composite Materials," in Plasticity Today, Modeling, Methods and Applications, edited by A. Sawczuk and G. Bianchi, Elsevier Appl. Sci. Publ., 1985, pp. 623-642.

6. Lin, T. H., Salinas, D. and Ito, Y. M., "Elastic-Plastic Analysis of Unidirectional Composites," J. Comp. Mat., Vol 6, 1972, pp. 48-60 .

7. Adams, D. F., "Inelastic Analysis of a Unidirectional Composite Subjected to Transverse Normal Loading," J. Comp. Mat., Vol. 4, 1970, pp. 310-328.

8. Foye, R. L., "Theoretical Post-Yielding Behavior of Composite Laminates. Part I - Inelastic Micromechanics," J. Comp. Mat., Vol. 7, 1973, pp. 178-193.

9. Adams, D. F. and Miller, A. K., "Hygrothermal Microstresses in a Unidirectional Composite Exhibiting Inelastic Material Behavior," J. Comp. Mat., Vol. 11, 1977, pp. 285-299.

10. Bahei-El-Din, Y. A., Dvorak, G. J. and Utku, S., "Finite Element Analysis of Elastic-Plastic Fibrous Composite Structures," Comp. and Struct., Vol. 13, 1981, pp. 321-330.

11. Bahei-El-Din, Y. A. and Dvorak, G. J., "Plasticity of Composite Laminates," Proc. Research Workshop on Mechanics of Composite Materials, edited by G. J. Dvorak, Duke University, 1978, pp. 32-54.

12. Bahei-El-Din, Y. A. and Dvorak, G. J., "Plastic Yielding at a Circular Hole in a Laminated FP-Al Plate," Modern Developments in Composite Materials and Structures, edited by J. R. Vinson, 1979, pp. 123-147.

13. Dvorak, G. J., Rao, M. S. M. and Tarn, J. Q., "Yielding in Unidirectional Composites Under External Loads and Temperature Changes," J. Comp. Mat., Vol. 7, 1973, pp. 194-216.

14. Aboudi, J., "Elastoplasticity Theory for Composite Materials," Sol. Mech. Arch., Vol. 11, 1986, pp. 141-183.

15. Aboudi, J., "Closed Form Constitutive Equations for Metal Matrix Composites," Int. J. Engng. Sci., Vol. 25, 1987, pp. 1229-1240.

16. Pindera, M. J. and Lin, M. W., "Micromechanical Analysis of the Elastoplastic Response of Metal Matrix Composites," J. Pressure Vessel Tech., Vol. 111, 1989, pp. 183-190.

17. Pindera, M. J., Herakovich, C. T., Becker, W. and Aboudi, J., "Nonlinear Response of Unidirectional Boron/Aluminum," J. Comp. Mat., Vol. 24, 1990, pp. 2-21.

18. Bahei-El-Din, Y. A. and Dvorak, G. J., "A Review of Plasticity Theory of Fibrous Composite Materials," in Metal Matrix Composites: Testing, Analysis, and Failure Modes, ASTM STP 1032, edited by W. S. Johnson, American Society for Testing and Materials, 1989, pp. 103-129.

19. Rizzi, S. A., Leewood, A. R., Doyle, J. F. and Sun, C. T., "Elastic-Plastic Analysis of Boron/Aluminum Composite Under Constrained Plasticity Conditions," J. Comp. Mat., Vol. 21, 1987, pp. 734-749.

20. Sun, C. T., "Modeling Continuous Fiber Metal Matrix Composite as an Orthotropic Elastic-Plastic Material," in Metal Matrix Composites: Testing, Analysis and Failure Modes, ASTM STP 1032, edited by W. S. Johnson, American Society for Testing and Materials, 1989, pp. 148-160.

21. Hill, R., "Theory of Mechanical Properties of Fibre-Strengthened Materials: I. Elastic Behavior," J. Mech. Phys. Solids, Vol. 12, 19 64, pp. 199-212.

22. Hashin, Z. and Rosen, B. W., "The Elastic Moduli of Fiber-Reinforced Materials," J. Appl. Mech., Vol. 31, 1964, pp. 223-232.

23. Whitney, J. M. and Riley, M. B., "Elastic Properties of Fiber Reinforced Composite Materials," AIAA J., Vol. 4, 1966, pp. 1537-1542.

24. Hecker, S. S., Hamilton, C. H. and Ebert, L. J., "Elastoplastic Analysis of Residual Stresses and Axial Loading in Composite Cylinders," J. Mater., Vol. 5, 1970, pp. 868-900.

25. Hamilton, C. H., Hecker, S. S. and Ebert, L. J., "Mechanical Behavior of Uniaxially Loaded Multilayered Cylindrical Composites," J. Basic Engng., Trans. ASME, Ser. D, Vol. 93, 1971, pp. 661-670.

26. Kachanov, L. M., Foundations of the Theory of Plasticity, North Holland, 1971.

Table 1. Values of the quantities σ_{my} and C_j (j=0,1,2,3,4,5) of aluminum Al 6061-T4 at T=24 °C (75 °F) and 288 °C (550 °F)

T		σ_{my}		C_0		C_1		C_2		C_3		C_4		C_5	
°C	°F	MPa	Ksi	MPa	Ksi	10^{-2} MPa	10^{-2} Ksi	10^{-4} MPa	10^{-4} Ksi	10^{-6} MPa	10^{-6} Ksi	10^{-8} MPa	10^{-8} Ksi	10^{-10} MPa	10^{-10} Ksi
24	75	86.2	12.5	-44.8	-6.5	1490.3	216.1	-4479.3	-649.5	6932.4	1005.2	-5318.6	-771.2	1601.4	232.2
288	550	41.4	6.0	13.1	-1.9	835.9	121.2	-1621.4	-235.1	1359.3	197.1	-306.9	-44.5	-91.7	-13.3

Table 2. Mechanical properties of silicon carbide SCS-2 fiber at room temperature

Material	E		ν	σ_u		ε_u
	GPa	Msi	-	MPa	Ksi	%
SCS-2	365	53	0.22	3195	463	0.87

FIGURE CAPTIONS

Fig. 1 Composite Cylinder Model.

Fig. 2 Longitudinal Tensile Stress-Strain Curves of SiC/Al Composite at T = 24°C (75°F) Obtained Experimentally and Predicted by the Composite Cylinder Model (ε_1 and ε_2 are longitudinal and transverse strains in composite, respectively).

Fig. 3 Longitudinal Tensile Stress-Strain Curves of SiC/Al Composite at T = 288°C (550°F) Obtained Experimentally and Predicted by the Composite Cylinder Model (ε_1 and ε_2 are longitudinal and transverse strains in composite, respectively).

Fig. 4 Tensile Stress-Strain Curves of 6061-T4 Aluminum Up to 1 Percent Strain at Different Temperatures.

Fig. 5 Variation of Tangent Modulus Along the Thickness of the Aluminum Matrix Shell in the CCM for Different Values of the Applied Strain ε_z at T = 288°C (550°F).

Fig. 6 Variation of Poisson's Ratio Along the Thickness of the Aluminum Matrix Shell in the CCM for Different Values of the Applied Strain ε_z at T = 288°C (550°F).

Fig. 7 Variation of Tangent Modulus and Poisson's Ratio at the Midsurface of the Aluminum Matrix Shell of the Composite Cylinder Versus the Applied Strain ε_z at T = 24°C (75°F).

Fig. 8 Variation of Axial (σ_z), Radial (σ_r) and Circumferential (σ_θ) Stresses Along Half the Fiber/Matrix Cross Section for an Applied Strain ε_z = 0.175 percent and T = 24° (75°F).

Fig. 9 Variation of the Radial Stress σ_{rm} Along the Thickness of Aluminum Matrix Shell in the CCM for Different Values of the Applied Strain ε_z at T = 24°C (75°F).

Fig.10 Variation of the Circumferential Stress $\sigma_{\theta m}$ Along the Thickness of the Aluminum Matrix Shell in the CCM for Different Values of the Applied Strain ε_z at T = 24°C (75°F).

Fig.11 Variation of the Axial Stress σ_{zm} Along the Thickness of the Aluminum Matrix Shell in the CCM for Different Values of the Applied Strain ε_z at T = 24°C (75°F).

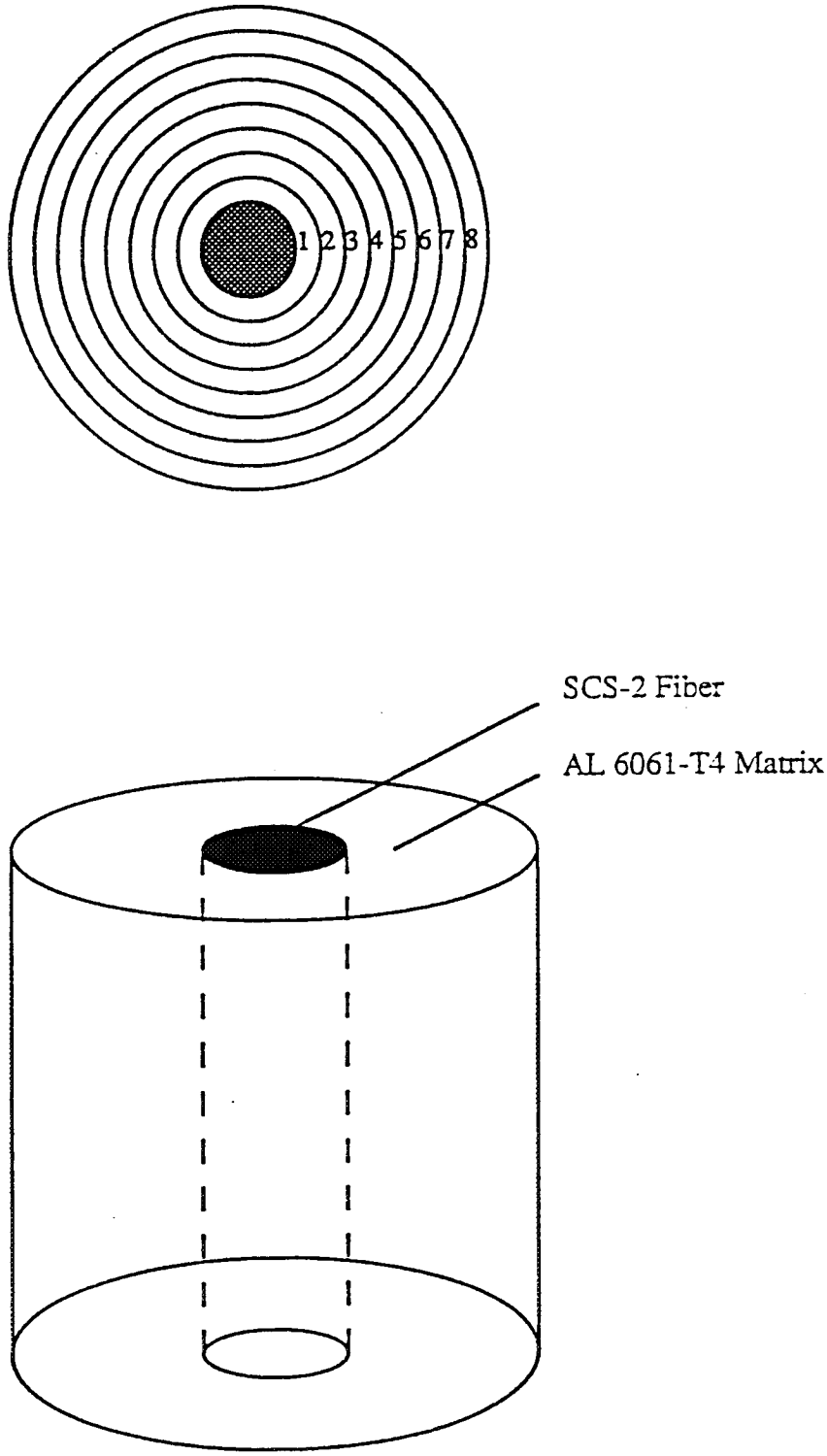

Fig. 1 Composite Cylinder Model.

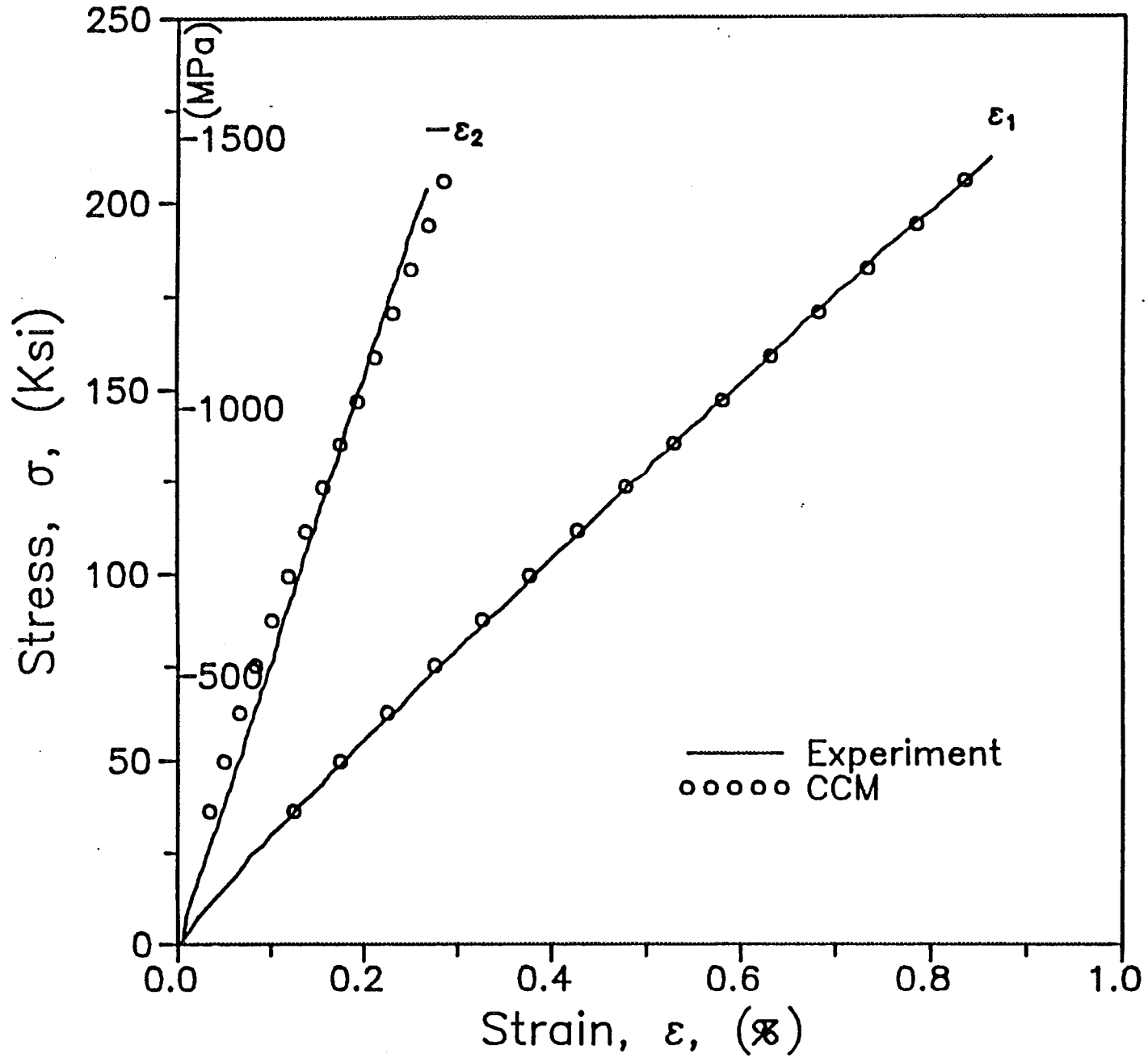

Fig. 2 Longitudinal Tensile Stress-Strain Curves of SiC/Al Composite at T = 24°C (75°F) Obtained Experimentally and Predicted by the Composite Cylinder Model (ε_1 and ε_2 are longitudinal and transverse strains in composite, respectively).

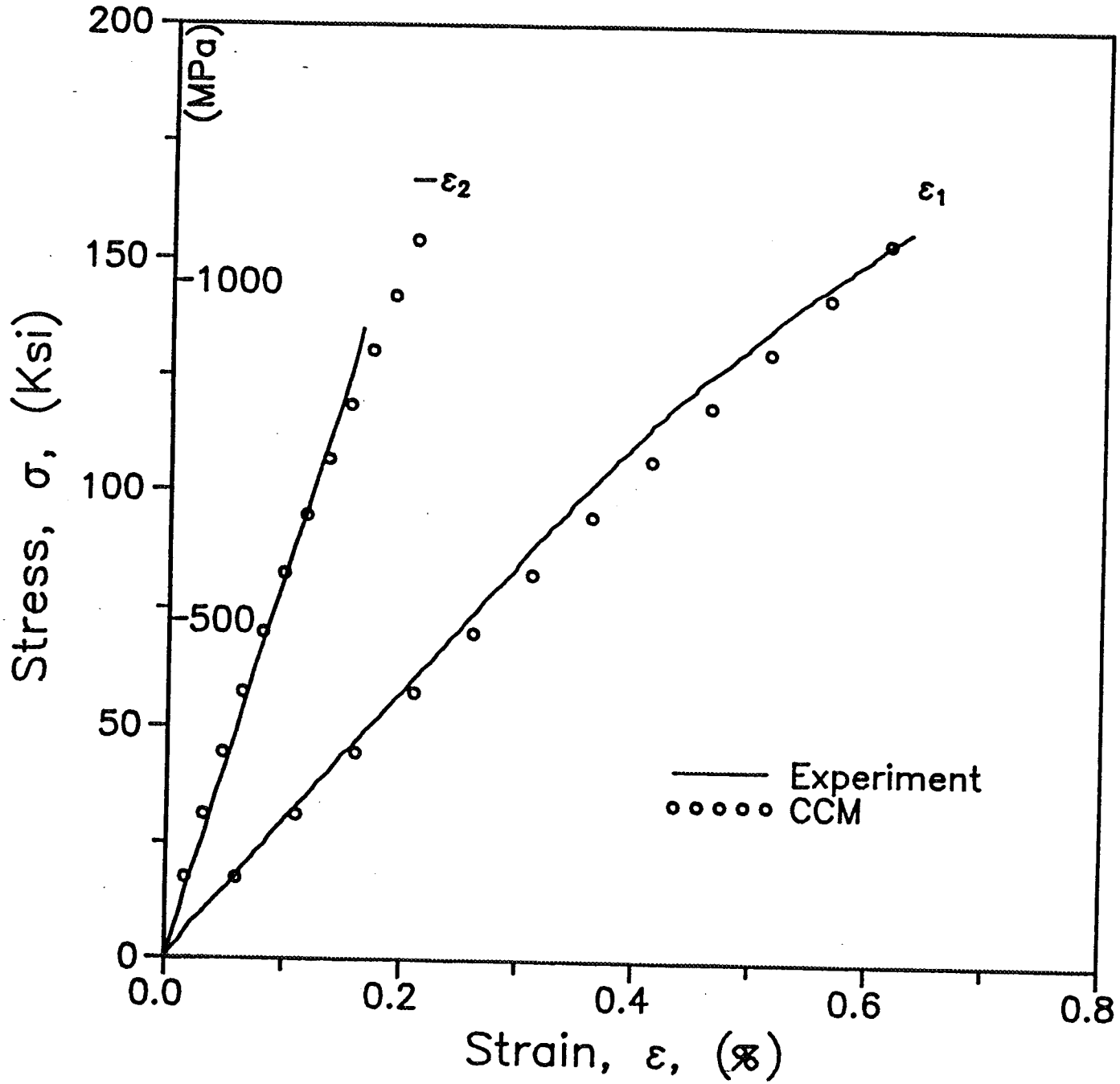

Fig. 3. Longitudinal Tensile Stress-Strain Curves of SiC/Al Composite at T = 288°C (550°F) Obtained Experimentally and Predicted by the Composite Cylinder Model (ε_1 and ε_2 are longitudinal and transverse strains)

ORIGINAL PAGE IS OF POOR QUALITY

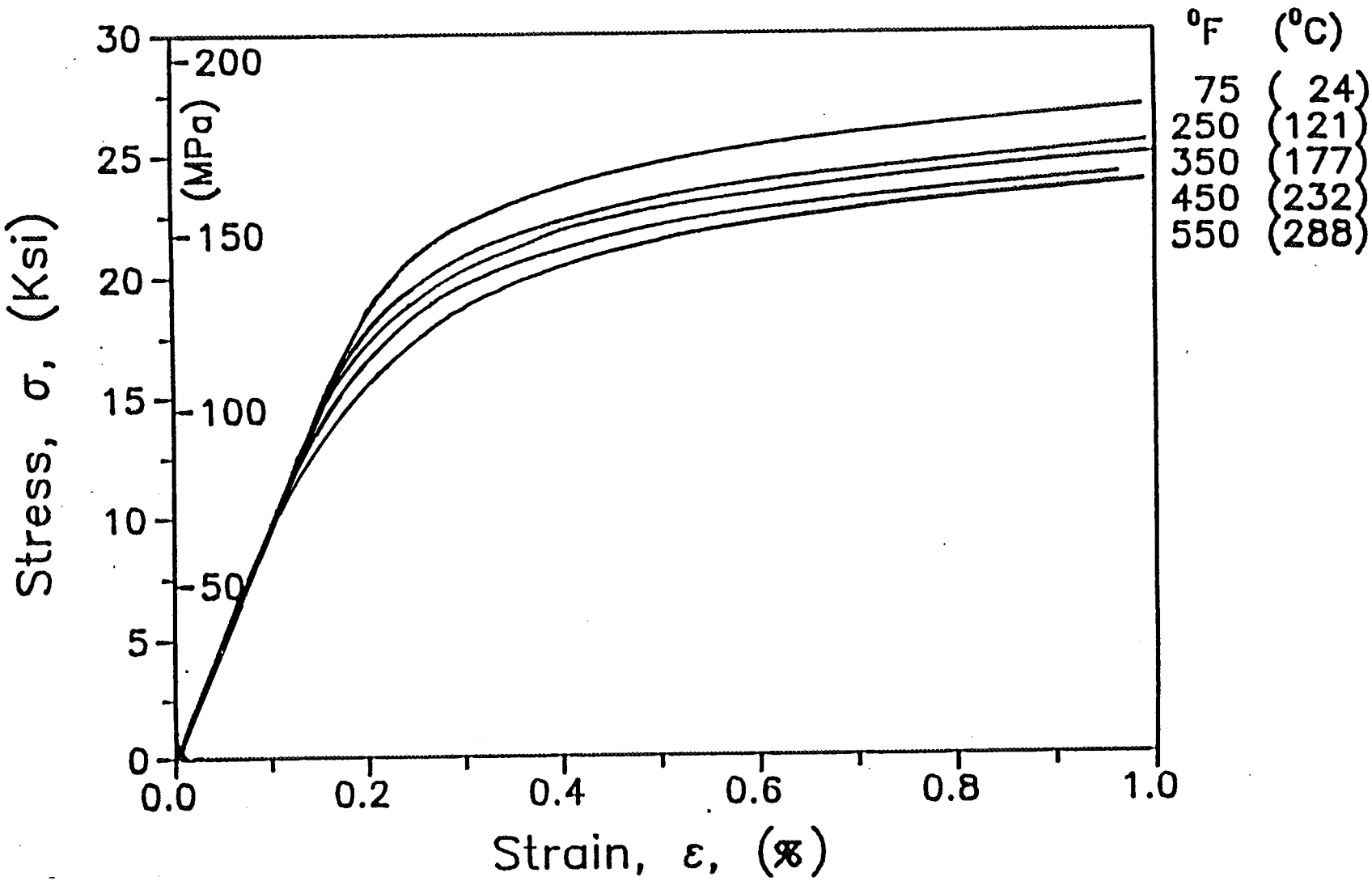

Fig. 4 Tensile Stress-Strain Curves of 6061-T4 Aluminum Up to 1 Percent Strain at Different Temperatures.

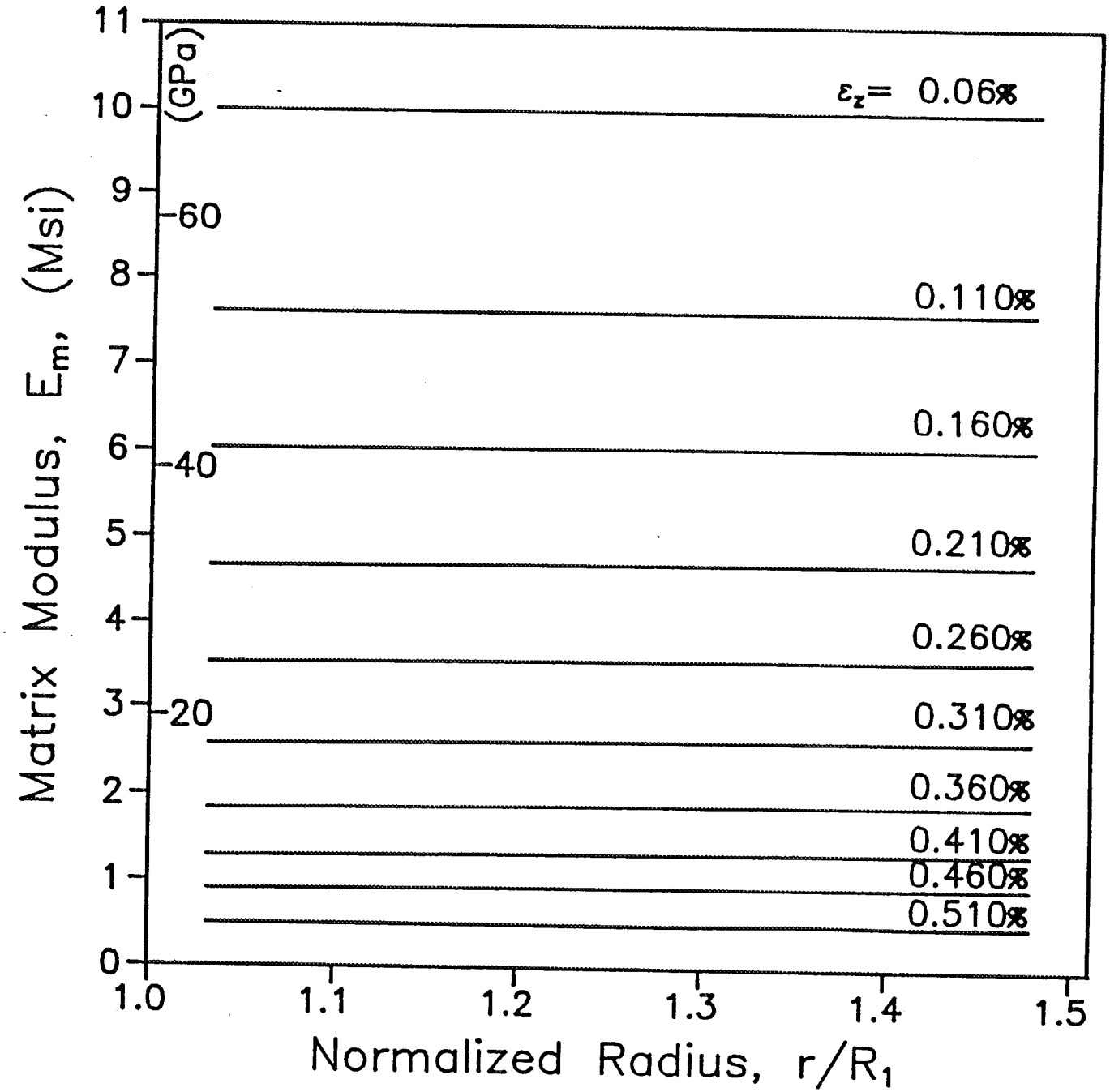

Fig. 5 Variation of Tangent Modulus Along the Thickness of the Aluminum Matrix Shell in the CCM for Different Values of the Applied Strain ε_z at T = 288°C (550°F)

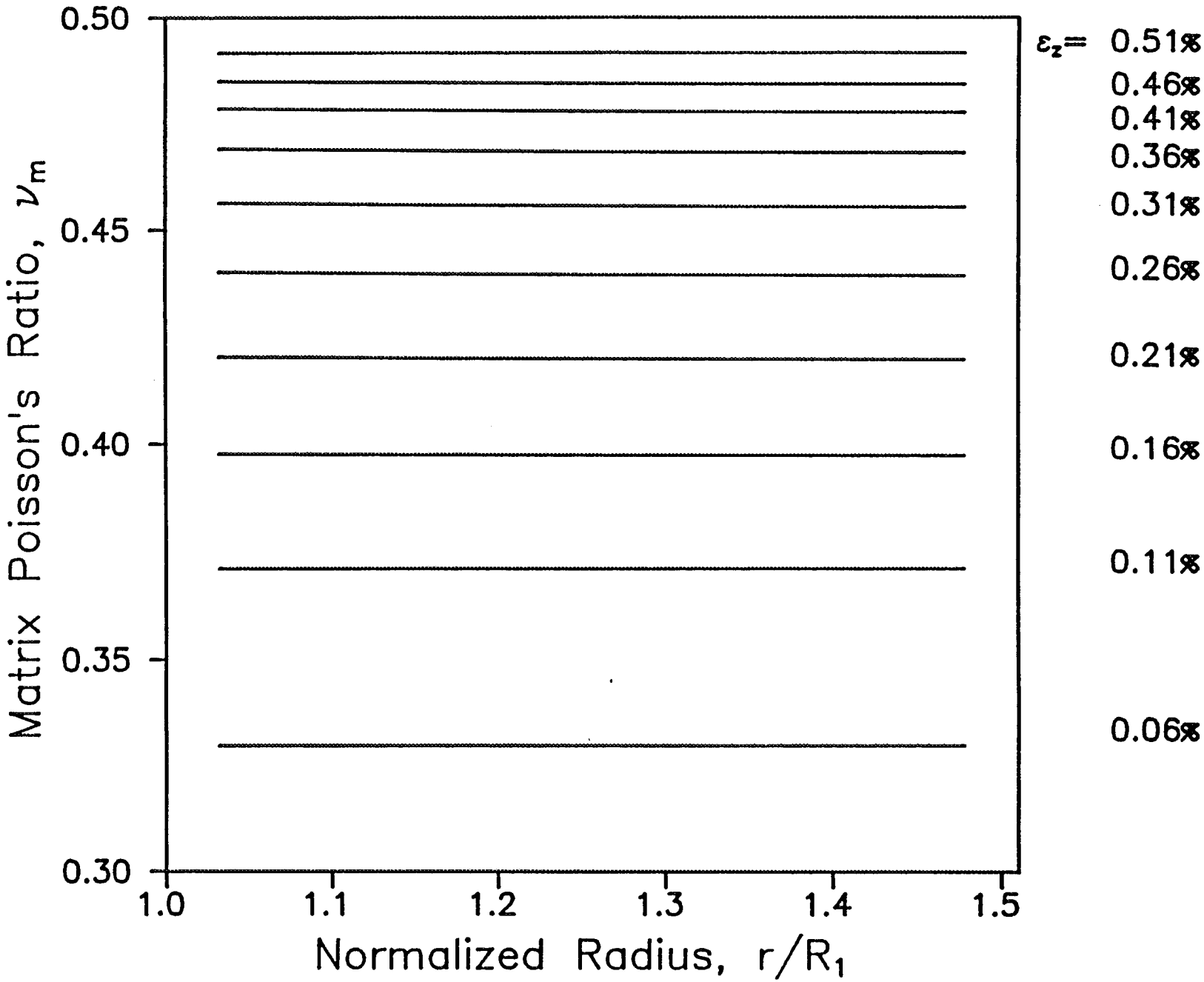

Fig. 6. Variation of Poisson's Ratio Along the Thickness of the Aluminum Matrix Shell in the CCM for Different Values of the Applied Strain ε_z at T = 288°C (550°F).

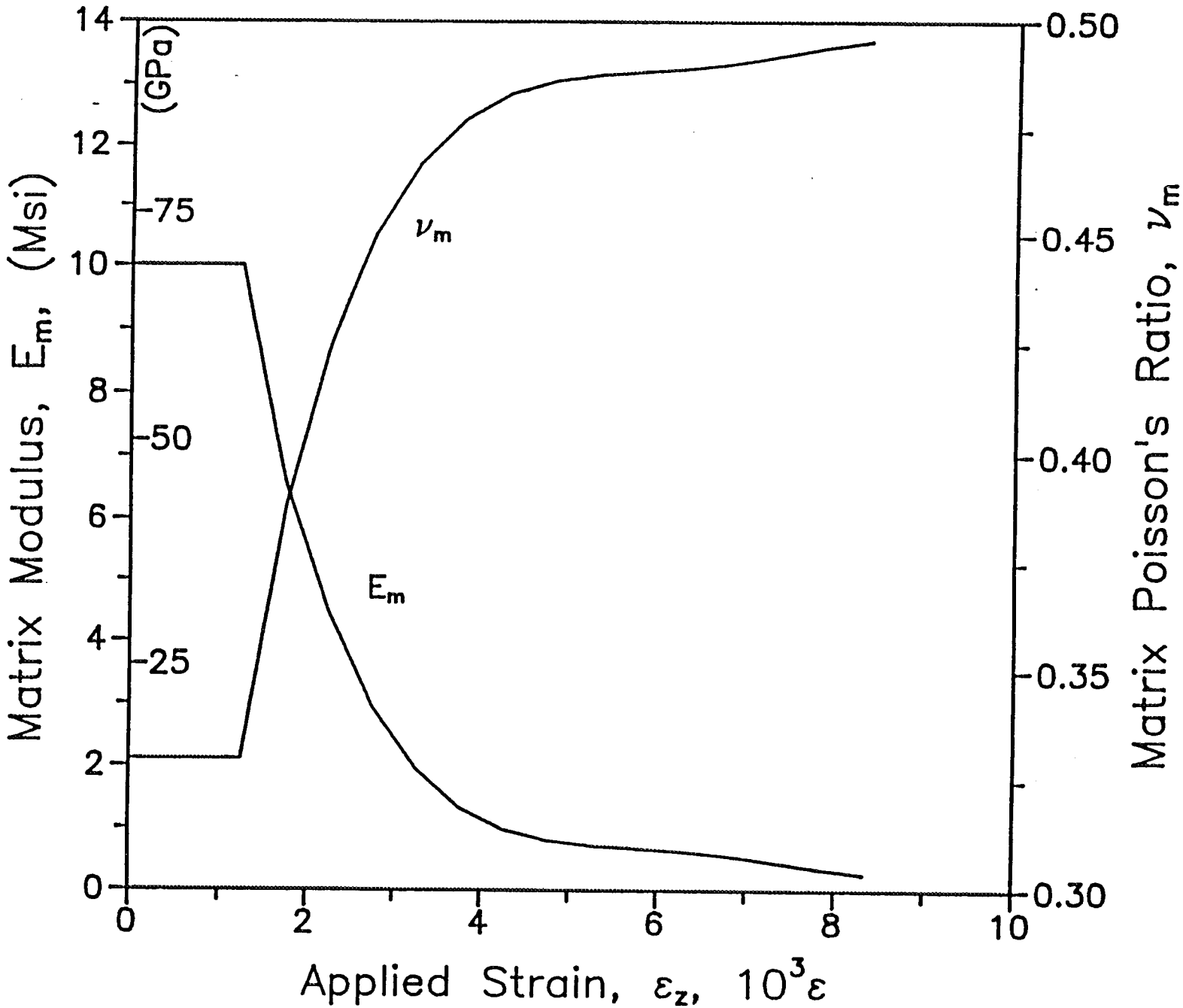

Fig. 7 Variation of Tangent Modulus and Poisson's Ratio at the Midsurface of the Aluminum Matrix Shell of the Composite Cylinder Versus the Applied Strain ε_z at T = 24°C (75°F).

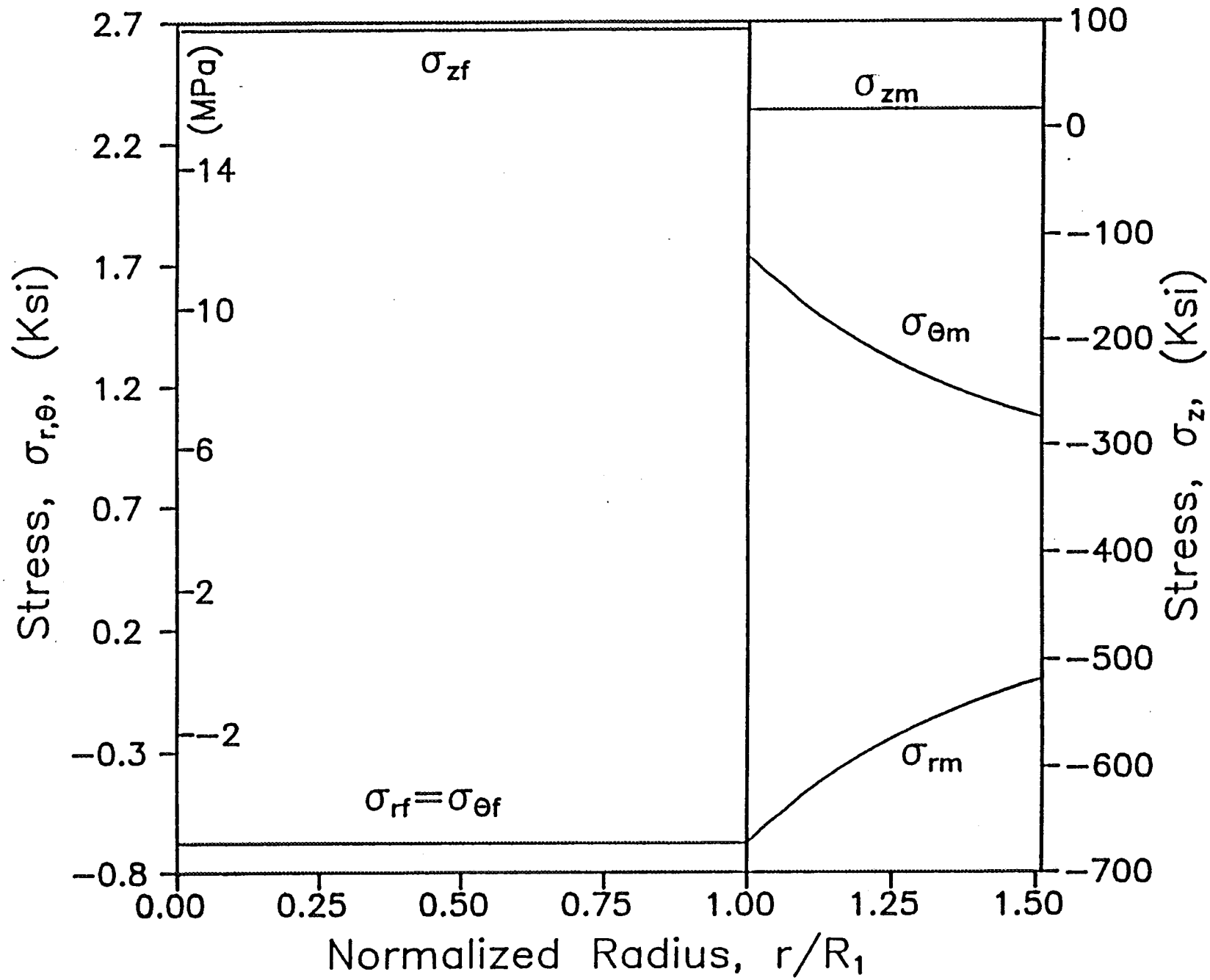

Fig. 8 Variation of Axial (σ_z), Radial (σ_r) and Circumferential (σ_θ) Stresses Along Half the Fiber/Matrix Cross Section for an Applied Strain $\varepsilon_z = 0.175$ percent and T = 24° (75°F).

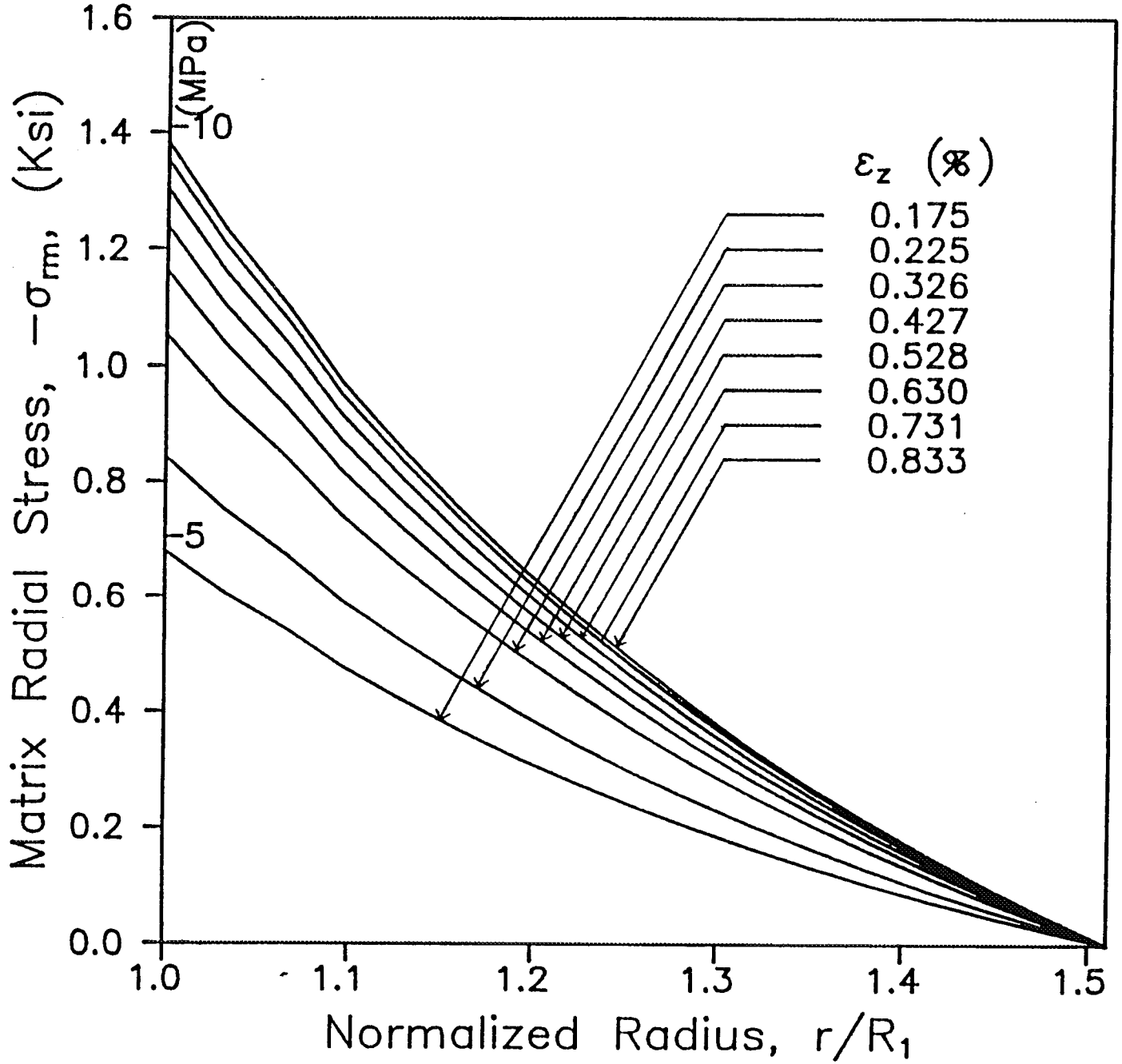

Fig. 9. Variation of the Radial Stress σ_{rm} Along the Thickness of Aluminum Matrix Shell in the CCM for Different Values of the Applied Strain ε_z at T = 24°C (75°F).

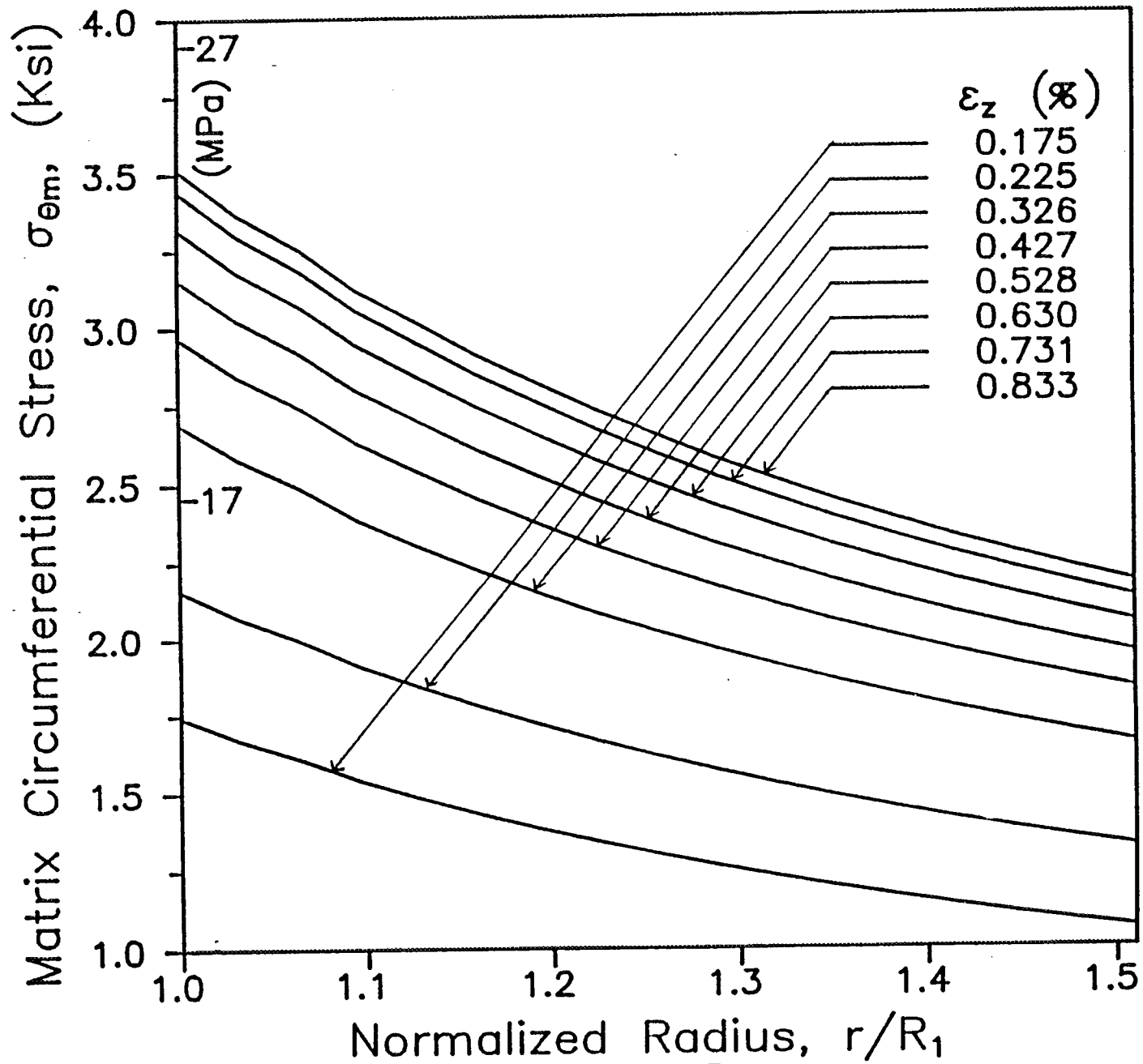

Fig.10 Variation of the Circumferential Stress $\sigma_{\theta m}$ Along the Thickness of the Aluminum Matrix Shell in the CCM for Different Values of the Applied Strain ε_z at T = 24°C (75°F).

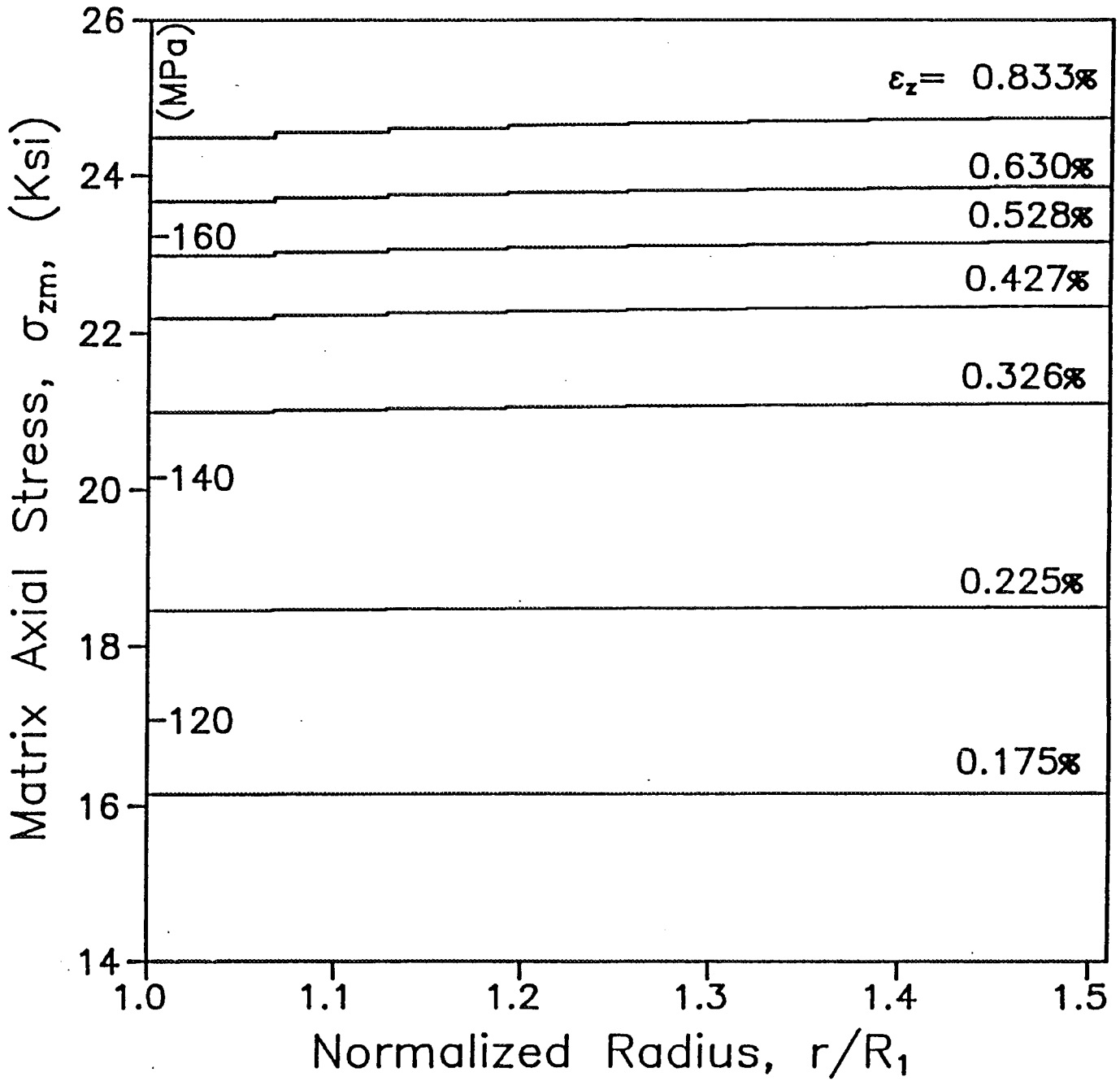

Fig.11 Variation of the Axial Stress σ_{zm} Along the Thickness of the Aluminum Matrix Shell in the CCM for Different Values of the Applied Strain ε_z at T = 24°C (75°F).

APPENDIX C

Thermoelastoplastic Analysis of Filamentary Metal Matrix Composites

Heoung-Jae Chun, Research Assistant

Shi-Chang Wooh, Research Assistant Professor

Isaac M. Daniel, Professor, Mem. ASME

Robert R. McCormick School of Engineering and Applied Science

Northwestern University,

Evanston, Illinois 60208

Abstract

The elastoplastic behavior of a metal matrix composite material was analyzed based on a successive approximation scheme with the Prandtl-Reuss plastic flow model and von Mises criterion. Results obtained were applied to a unidirectional silicon carbide/aluminum composite. The three-dimensional state of internal stress was computed for mechanical and thermal loading conditions. In addition, the stress-strain curves under uniaxial tension at different temperatures and the thermal strain-temperature relation of the composite were predicted and compared with experimental results. The method is particularly useful in the case when the boundary conditions are not explicitly prescribed and it has the advantage that the strains and stresses are computed for any given loading conditions without step-incrementing the load.

1 Introduction

Composite materials are ever finding many structural applications because of their superior performance to conventional metal counterparts. Due to the simple and cost-effective fabrication process, polymer based composites are most widely used. However, these materials, in general, are not adequate for the use in structures operating at an elevated temperature. On the other hand, ceramic matrix composites (CMC) and metal matrix composites (MMC) are more suitable for such applications. The maximum operating temperature range of the CMC's are generally much higher than that of the MMC's, but the CMC's fail in a brittle fashion so that these materials usually have lower fracture toughness. By contrast, the MMC's are used over intermediate temperature

ranges and have advantages such as high strength, high stiffness, high toughness, high impact resistance, high resistivity to temperature change or thermal shock, high surface durability, low sensitivity to surface flaws, and high electrical and thermal conductivity.

Unidirectional composites subjected to thermomechanical loading have been investigated by many authors, for example, Ishikawa *et al.* (1978), Unemura *et al.* (1979), Iesan (1980), Mikata and Taya (1985), and Warwick and Clyne (1991), by considering a coaxial cylinder model. These models assume elastic constituents, particularly on elastic matrix. In the case of MMC, the matrix undergoes plastic flow and is sensitive to the environmental temperature. Thus, it is desirable to study the composite behavior taking into consideration the elastoplastic properties.

In the case of longitudinal tension, the composite behavior is dominated by the properties of the fiber. In addition to the axial stresses, transverse stresses are also developed. These radial and tangential stresses, although small in magnitude, contribute to the plastic deformation of the matrix and should not be overlooked.

Dimensional stability over a broad temperature range is one of the important factors that should be taken into consideration. Due to the coefficient of thermal expansion (CTE) mismatch between fiber and matrix, thermal stresses are introduced when the material experiences a temperature change. Also, when the composite is consolidated from the fabrication temperature, thermal residual stresses develop. When such stresses are sufficiently high, the matrix yields and affects the composite behavior. Thus, the study of the thermal behavior is an important aspect in understanding composite behavior. Hsueh and Becher (1988) made an attempt to predict the coefficient of thermal

expansion of a ceramic composite using the coaxial cylinder model. Their result agrees well with other predictions such as those by Schapery (1968), Takao and Taya (1985, 1987), Rosen (1970), and Hoffman (1973). In this study, the method was extended for an elastoplastic matrix in the model.

A continuous fiber composite was modeled by two concentric cylinders representing the elastic fiber and elastoplastic matrix. The proposed model not only predicts the overall behavior of the composite but also gives detailed stress and strain distributions in the constituent materials under thermomechanical loading.

2 Materials

The material investigated was an eight-ply unidirectional silicon carbide/aluminum (SiC/Al) composite. The specimens were obtained from the manufacturer (Textron Specialty Materials) in composite plate form and characterized by standard tensile tests (See Whitney *et al.* (1985)). Tables 1 and 2 show the measured elastic properties of the composite and the constituents, respectively.

Continuous SiC filament (SCS-2) was produced by chemical vapor deposition (CVD) around a carbon monofilament core, according to the manufacturer. The measured average diameter of the fiber is 140 μm (0.00551 in.). To the authors' knowledge, there is no available method for direct measurement of the in-situ matrix properties. The properties of 6061-0 aluminum (annealed state) were used in the analysis for various reasons including agreement with experimental results as will be discussed later.

The composite was fabricated by the manufacturer by a diffusion bonding consolidation process. The producibility of SiC reinforced metals is attributed to the SiC fiber characteristics, because the SiC fibers are well bonded to metals and are resistant to strength degradation during the elevated temperature process. Such characteristics of the SiC fiber and the light weight of aluminum made the SiC/Al composite a widely used material.

3 Theoretical Background

Figure 1 illustrates the continuous fiber model of the MMC used in the analysis. The inner cylinder (fiber) of radius a is surrounded by the outer cylinder (matrix) of outer radius b. The following assumptions were made in the development of the model:

1. The constituent materials are isotropic.
2. Bonding between fiber and matrix is perfect.
3. The fiber is linearly elastic up to failure and the matrix is elastoplastic.
4. There is no temperature gradient in the material. In other words, the temperature distribution is uniform for the entire material.
5. Residual stresses are ignored.
6. The fiber volume ratio is reasonably low.

For an axisymmetric problem, the displacements in the radial, tangential, and axial directions are respectively assumed to be of the form:

$$u_r = u(r)$$

$$u_\theta = 0 \tag{1}$$

$$u_z = w(z)$$

and the linear elastic strain-displacement relations are:

$$\varepsilon_{rr} = \frac{\partial u}{\partial r} \tag{2.a}$$

$$\varepsilon_{\theta\theta} = \frac{u}{r} \tag{2.b}$$

$$\varepsilon_{zz} = \frac{\partial w}{\partial z} \tag{2.c}$$

$$\varepsilon_{rz} = \varepsilon_{\theta z} = \varepsilon_{r\theta} = 0 \tag{2.d}$$

The equilibrium conditions are expressed as

$$\frac{d\sigma_r}{dr} + \frac{\sigma_r - \sigma_\theta}{r} = 0 \tag{3.a}$$

$$\frac{d\sigma_\theta}{d\theta} = 0 \tag{3.b}$$

$$\frac{d\sigma_z}{dz} = 0 \tag{3.c}$$

and the compatibility conditions yield the following relationship:

$$\frac{d\varepsilon_\theta}{dr} + \frac{\varepsilon_\theta - \varepsilon_r}{r} = 0 \tag{4}$$

3.1 Elastic Solution

The thermoelastic stress-strain relations are thus obtained as

$$\sigma_r = \frac{E}{(1-2\nu)(\nu+1)}[(1-\nu)\varepsilon_r + \nu(\varepsilon_\theta + \varepsilon_z) - (\nu+1)\alpha\Delta T]$$

$$\sigma_\theta = \frac{E}{(1-2\nu)(\nu+1)}[(1-\nu)\varepsilon_\theta + \nu(\varepsilon_r + \varepsilon_z) - (\nu+1)\alpha\Delta T] \qquad (5)$$

$$\sigma_z = \frac{E}{(1-2\nu)(\nu+1)}[(1-\nu)\varepsilon_z + \nu(\varepsilon_r + \varepsilon_\theta) - (\nu+1)\alpha\Delta T]$$

where E is the elastic modulus, ν Poisson's ratio and α the coefficient of thermal expansion. From eqs. (2) through (5), the following differential equations are obtained.

$$\frac{d^2u}{dr^2} + \frac{1}{r}\frac{du}{dr} - \frac{u}{r^2} = \frac{(1+\nu)}{(1-\nu)}\frac{d(\alpha\Delta T)}{dr} \qquad (6.a)$$

$$\frac{d^2w}{dz^2} = 0 \qquad (6.b)$$

For the case of uniform temperature distribution, eq. (6.a) becomes homogeneous because

$$\frac{d(\alpha\Delta T)}{dr} = 0 \qquad (7)$$

Thus the following general solutions are obtained:

$$u = \frac{A_1}{r} + A_2 r \qquad (8.a)$$

$$w = D_1 + D_2 z \qquad (8.b)$$

and the strain field is obtained from the strain-displacement relations as

$$\varepsilon_r = -\frac{A_1}{r^2} + A_2$$

$$\varepsilon_\theta = \frac{A_1}{r^2} + A_2 \qquad (9)$$

$$\varepsilon_z = D_2$$

where A_1, A_2, D_1, and D_2 are constants which are determined from the boundary conditions.

3.2 Elastoplastic Solution

The elastoplastic stress-strain relationships are formulated by considering additional plastic strains (ε_r^p, ε_θ^p, ε_z^p) in eqs. (5).

$$\sigma_r = \frac{E}{(1-2\nu)(\nu+1)}[(1-\nu)(\varepsilon_r - \varepsilon_r^p) + \nu(\varepsilon_\theta - \varepsilon_\theta^p) + \nu(\varepsilon_z - \varepsilon_z^p) - (\nu+1)\alpha\Delta T] \qquad (10.a)$$

$$\sigma_\theta = \frac{E}{(1-2\nu)(\nu+1)}[(1-\nu)(\varepsilon_\theta - \varepsilon_\theta^p) + \nu(\varepsilon_r - \varepsilon_r^p) + \nu(\varepsilon_z - \varepsilon_z^p) - (\nu+1)\alpha\Delta T] \qquad (10.b)$$

$$\sigma_z = \frac{E}{(1-2\nu)(\nu+1)}[(1-\nu)(\varepsilon_z - \varepsilon_z^p) + \nu(\varepsilon_r - \varepsilon_r^p) + \nu(\varepsilon_\theta - \varepsilon_\theta^p) - (\nu+1)\alpha\Delta T] \qquad (10.c)$$

Applying similar procedures as in the elastic analysis, the following differential equation is obtained

$$\frac{d^2\varepsilon_\theta}{dr^2} + \frac{3}{r}\frac{d\varepsilon_\theta}{dr} = \frac{(1-2\nu)}{(1-\nu)r}\frac{d\varepsilon_r^p}{dr} + \frac{(1-2\nu)(\varepsilon_r^p - \varepsilon_\theta^p)}{(1-\nu)r^2} + \frac{(1+\nu)}{(1-\nu)r}\frac{d(\alpha\Delta T)}{dr} \qquad (11)$$

In the case of uniform temperature distribution, the solution for the tangential strain takes the form

$$\varepsilon_\theta = \frac{(1-2\nu)}{(1-\nu)r^2}\int r\varepsilon_r^p dr - \frac{(1-2\nu)}{2(1-\nu)r^2}\int r(\varepsilon_r^p - \varepsilon_\theta^p)dr + \frac{(1-2\nu)}{2(1-\nu)}\int \frac{(\varepsilon_r^p - \varepsilon_\theta^p)}{r}dr - \frac{C_1}{2r^2} + C_2 \tag{12.a}$$

the radial strain is obtained from eqs. (4) and (12.a) as

$$\varepsilon_r = \frac{(1-2\nu)}{(1-\nu)}\varepsilon_r^p - \frac{(1-2\nu)}{(1-\nu)r^2}\int r\varepsilon_r^p dr + \frac{(1-2\nu)}{2(1-\nu)r^2}\int r(\varepsilon_r^p - \varepsilon_\theta^p)dr + \frac{(1-2\nu)}{2(1-\nu)}\int \frac{(\varepsilon_r^p - \varepsilon_\theta^p)}{r}dr + \frac{C_1}{2r^2} + C_2 \tag{12.b}$$

and the displacement

$$u = \frac{(1-2\nu)}{(1-\nu)r}\int r\varepsilon_r^p dr - \frac{(1-2\nu)}{2(1-\nu)r}\int r(\varepsilon_r^p - \varepsilon_\theta^p)dr + \frac{(1-2\nu)r}{2(1-\nu)}\int \frac{(\varepsilon_r^p - \varepsilon_\theta^p)}{r}dr - \frac{C_1}{2r} + C_2 r \tag{13}$$

is obtained from the strain-displacement relationship. Note that the solutions reduce to those of the elastic case when the plastic strains become zero.

4 Boundary Conditions

The previously obtained elastic and elastoplastic solutions are applied to the fiber and matrix, respectively. There are altogether six unknowns: two constants A_1 and A_2 in the elastic solution, two constants C_1, C_2 and the plastic strains ε_r^p and ε_θ^p in the elastoplastic solution. These unknowns are determined by satisfying the following six boundary conditions:

1. The axial strains in the fiber and matrix equal and constant:

$$\varepsilon_{zf} = \varepsilon_{zm} = \varepsilon_z = D_2 \tag{14}$$

where subscripts f and m denote fiber and matrix, respectively.

2. There exists no singularity in the displacement field at the center of the cylinder, i. e.,:

$$A_1 = 0 \tag{15}$$

This leads to a simpler form of the elastic displacement field

$$u_f = A_2 r \tag{16}$$

$$\varepsilon_{rf} = \varepsilon_{\theta f} = A_2 \tag{17}$$

3. Displacements are continuous at the fiber and matrix interface:

$$u_f(a) = u_m(a) \tag{18}$$

and from eqs. (8.a) and (13) it follows that

$$\begin{aligned} aA_2 + \frac{C_1}{2a} - aC_2 = & \frac{(1-2\nu_m)}{(1-\nu_m)a}\int_0^a r\varepsilon_r^p dr - \frac{(1-2\nu_m)}{2(1-\nu_m)a}\int_0^a r(\varepsilon_r^p - \varepsilon_\theta^p)dr \\ & + \frac{(1-2\nu_m)a}{2(1-\nu_m)}\int_0^a \frac{(\varepsilon_r^p - \varepsilon_\theta^p)}{r}dr \end{aligned} \tag{19}$$

4. Radial stresses are continuous at the fiber and matrix interface:

$$\sigma_{rf}(a) = \sigma_{rm}(a) \tag{20}$$

Substituting eqs. (14) and (17) into eq. (10.a) and eqs. (12) into eq. (10.a), equation (20) is rewritten in the form

$$\begin{aligned} & \frac{E_f A_2}{(1-2\nu_f)(\nu_f+1)} - \frac{E_m C_1}{2(\nu_m+1)a^2} - \frac{E_m C_2}{(1-2\nu_m)(\nu_m+1)} \\ & + [\frac{\nu_f E_f}{(1-2\nu_f)(\nu_f+1)} - \frac{\nu_m E_m}{(1-2\nu_m)(\nu_m+1)}]\varepsilon_z \\ & = \frac{(\nu_f+1)E_f\alpha_f\Delta T}{(1-2\nu_f)(\nu_f+1)} - \frac{(\nu_m+1)E_m\alpha_m\Delta T}{(1-2\nu_m)(\nu_m+1)} \\ & + \frac{E_m}{(1-2\nu_m)(\nu_m+1)}[-\frac{(1-2\nu_m)^2}{(1-\nu_m)a^2}\int_0^a r\varepsilon_r^p dr + \frac{(1-2\nu_m)^2}{2(1-\nu_m)a^2}\int_0^a r(\varepsilon_r^p - \varepsilon_\theta^p)dr \\ & + \frac{(1-2\nu_m)}{2(1-\nu_m)}\int_0^a \frac{(\varepsilon_r^p - \varepsilon_\theta^p)}{r}dr \end{aligned} \tag{21}$$

5. The radial stress vanishes at $r = b$:

$$\sigma_{rm}(b) = 0 \tag{22}$$

or

$$\begin{aligned}
&\frac{(1-2\nu_m)C_1}{2b^2} + C_2 + \nu_m \varepsilon_z \\
&= (\nu_m + 1)\alpha_m \Delta T + \frac{(1-2\nu_m)^2}{b^2(1-\nu_m)}\int_0^b r\varepsilon_r^p dr - \frac{(1-2\nu_m)^2}{2b^2(1-\nu_m)}\int_0^b r(\varepsilon_r^p - \varepsilon_\theta^p)dr \\
&- \frac{(1-2\nu_m)}{2(1-\nu_m)}\int_0^b \frac{(\varepsilon_r^p - \varepsilon_\theta^p)}{r}dr
\end{aligned} \tag{23}$$

6. Force equilibrium in the fiber direction yields

$$\int_0^a \sigma_{zf} r dr + \int_a^b \sigma_{zm} r dr = \frac{\sigma_0 b^2}{2} \tag{24}$$

or

$$\begin{aligned}
&\frac{\nu_f E_f a^2 A_2}{(1-2\nu_f)(\nu_f+1)} + \frac{\nu_m E_m (b^2 - a^2) C_2}{(1-2\nu_m)(\nu_m+1)} \\
&+ [\frac{(1-\nu_f)E_f a^2}{2(1-2\nu_f)(\nu_f+1)} + \frac{(1-\nu_m)E_m(b^2-a^2)}{2(1-2\nu_m)(\nu_m+1)}]\varepsilon_z \\
&= \frac{\sigma_0 b^2}{2} + \frac{E_f \alpha_f \Delta T a^2}{2(1-2\nu_f)} + \frac{E_m \alpha_m \Delta T (b^2 - a^2)}{2(1-2\nu_m)} \\
&+ \frac{E_m}{(1-2\nu_m)(\nu_m+1)}\{-\frac{\nu_m(1-2\nu_m)}{2(1-\nu_m)}[b^2\int_0^b \frac{(\varepsilon_r^p - \varepsilon_\theta^p)}{r}dr - a^2\int_0^a \frac{(\varepsilon_r^p - \varepsilon_\theta^p)}{r}dr] \\
&- \frac{(1-2\nu_m)(2-\nu_m)}{2(1-\nu_m)}\int_a^b r(\varepsilon_r^p + \varepsilon_\theta^p)dr\}
\end{aligned} \tag{25}$$

where σ_0 is the applied stress.

5 Successive Approximation Method

The prescribed boundary conditions are not expressed in explicit form so that it is difficult to obtain exact solutions. However, approximate solutions were found numerically by introducing the successive approximation scheme that was used to solve various similar problems by many investigators; Mendelson and Spero (1962), Davis (1963), and Tuba (1965).

Since the matrix behaves in a highly nonlinear fashion, it is often necessary to express the stress-strain curve in empirical equational form for the theoretical prediction of composite behavior. Figure 2 illustrates two simple forms of broadly used curve fittings: linear and power law strain hardening models, in which the stress-strain curve is fitted as:

$$\sigma = \begin{cases} \sigma_Y + \dfrac{\beta E_m}{1-\beta}\varepsilon_p & \text{(linear law)} \\ \sigma_Y + kE_m\varepsilon_p^n & \text{(power law)} \end{cases} \tag{26}$$

where k, n, and β are material constants, and σ_Y the elastic limit or the yield stress. It was found from experience that the power law strain hardening model fits aluminum reasonably well.

Following is the step-by-step procedure of the method used in computing the effective plastic strain distribution.

1. Assign number of equidistant stations (N) along the radial direction from the center of the cylinder as illustrated in Fig. 1.
2. Assume that ε_r^p and ε_θ^p are zero at every station, as a first approximation.
3. Determine four unknowns A_2, C_1, C_2 and ε_z from eqs. (19), (21), (23), and (25). Perform integration numerically by using simple trapezoidal or

Simpson's rule.

4. Compute strains for fiber and matrix from eqs. (9) and (12), and obtain the corresponding stresses from eqs. (5) and (10).

5. Calculate equivalent stresses in the matrix ($\overline{\sigma}_m$) at each station from eq. (A13) in the Appendix.

6. For all stations at which the equivalent stress exceeds the elastic limit, calculate the equivalent total strain in the matrix from eq. (A10):

$$\overline{\varepsilon}_m = \frac{1}{3}\sqrt{2[(\varepsilon_{rm} - \varepsilon_{\theta m})^2 + (\varepsilon_{\theta m} - \varepsilon_{zm})^2 + (\varepsilon_{zm} - \varepsilon_{rm})^2]} \tag{27}$$

7. Plot the experimentally obtained stress-strain curve of the matrix and fit it into an appropriate strain hardening model to it, e.g., the power law model. Determine the constants k and n and compute the equivalent plastic strain $\overline{\varepsilon}_m^p$ from the relationship:

$$\overline{\varepsilon}_m^p = \overline{\varepsilon}_m - \frac{2(1+\nu_m)\overline{\sigma}_m}{3E_m} \tag{28}$$

8. Obtain the next approximate plastic strains from eq. (A12) as:

$$\begin{aligned} \varepsilon_r^p &= \frac{\overline{\varepsilon}_m^p}{3\overline{\varepsilon}_m}(2\varepsilon_{rm} - \varepsilon_{\theta m} - \varepsilon_{zm}) \\ \varepsilon_\theta^p &= \frac{\overline{\varepsilon}_m^p}{3\overline{\varepsilon}_m}(2\varepsilon_{\theta m} - \varepsilon_{rm} - \varepsilon_{zm}) \\ \varepsilon_z^p &= \frac{\overline{\varepsilon}_m^p}{3\overline{\varepsilon}_m}(2\varepsilon_{zm} - \varepsilon_{rm} - \varepsilon_{\theta m}) \end{aligned} \tag{29}$$

Use these values as the second approximation for the stations where yielding has occurred and use zero for the remaining stations.

9. Repeat the steps above until the strains at all stations converge.

6 Experimental Procedure

The experimental characterization of the material in this study consists of (1) mechanical characterization of the composite at ambient temperature, (2) characterization of the fiber, (3) thermomechanical characterization of the matrix at various temperatures, and (4) measuring the stress-strain behavior of the unidirectional composite at corresponding temperatures. The detailed procedure is described below.

The mechanical characterization procedures are described in Whitney *et al.* (1985). These test methods were used for preliminary characterization of the material and the measured properties are shown in Table 1.

The fiber was characterized by measuring its elastic modulus and tensile strength following the ASTM D3379-75 standard procedure. A special miniature tensile testing device was designed and used to provide good control and accuracy of measurements (See Daniel *et al.* (1989,1993), Luo *et al.* (1994)). After a careful center-line alignment of a single filament on the special slotted tabs, the specimen was loaded up to failure. During testing, the load and displacement were continuously monitored from the load cell and the LVDT, respectively. The filament cross-sectional area was determined from the highly magnified photomicrographs. The apparent compliance obtained directly from the load-displacement curve should be corrected to obtain the true compliance by repeating tests for various gage lengths from 25.4 mm (1.0 in.) to 61.0 mm (2.4 in.) from the slope of the apparent compliance curve plotted against the gage length.

Since it is extremely difficult to measure the in-situ properties of the matrix, it was only possible to measure them from the bulk form material. Selection of the heat treatment state that correspond to the condition of the matrix was a problem because the matrix properties, particularly those of metal matrix composites, are significantly changed by the temperature history during the manufacturing process. The properties of the as-fabricated aluminum matrix are similar to those of the near O temper (annealed state) characteristics, according to Pindera and Lin (1989). Furthermore, the specimen, during the curing process of bonding of the tabs at an elevated temperature, experiences a temperature history similar to that of the annealing process of aluminum. It is believed that property changes due to the repeated heat treatment is negligible. Assuming that the in-situ properties of the matrix are reasonably close to those of the fully annealed state, the 6061 aluminum, heat treated by the standard annealing procedure (See Alloy Digest), was characterized at various operating temperatures.

The as-obtained 1.42mm (0.056in.) thick composite plate was cut into 12.7mm (0.5in.) wide 152.4mm (6.0in.) long coupons and tabbed with high strength adhesive for testing at elevated temperatures. Two types of adhesive were used for different temperature ranges. For the temperature range between 24°C (75°F) and 288°C (550°F), a polyimide adhesive film (FM36, American Cyanamid) was used; while an aluminum filled condensation type polyimide adhesive film (FM680) was used for the temperature range of 288°C (550°F) to 399°C (750°F). Both types are supported by a glass cloth carrier for better shear and peel-off strengths. These adhesives provide

sufficiently high strength for testing provided the bonded tabs are sufficiently long (38.1mm(1.5in.)).

The high temperature tests were conducted in a thermal chamber. For strain measurement, the specimens were instrumented with commercially available strain gages for high temperature applications (WK-gages from Micro Measurements and RKO-gages from J. P. Technology). The strain readings from the gages were compensated for temperature by using a dummy gage technique and were verified by measuring the axial strain by means of a water-cooled clip-on extensometer. The specimen surface temperature was monitored with K-type thermocouple bonded on the surface with ceramic adhesive. To minimize the error due to convection heat loss, the thermocouple was shielded with Kapton tape. The temperature signal was also used as a feedback to the temperature controller. Tests were conducted at the temperatures of 24°C (75°F), 121°C (250°F), 177°C (350°F), 288°C (550°F), and 399°C (750°F).

7 Results and Discussion

Constituent materials were thermomechanically characterized and shown in Table 2. Figure 3 shows the measured apparent compliances obtained from the SCS-2 single fiber testing as a function of gage length. The true compliance of the fiber is determined from the slope of the curve. In addition, the coefficient of thermal expansion (CTE) measured by Tsai and Daniel (1994) was used in this study. The stress-strain curves of 6061-0 aluminum obtained at various temperatures are shown in Fig. 4. As the temperature increases, the elastic limit stress decreases significantly and the stress-strain

behavior becomes close to that of an elastic perfectly-plastic solid. These curves are fitted by the power law strain hardening model of eq. (26). The temperature dependent parameters, k, n, and σ_Y from this fit are tabulated in Table 3.

It was shown from the thermal-strain curve that the CTE of 6061 aluminum is linear up to approximately 93.3°C(200°F) and exhibits slight nonlinearity above that temperature. On the other hand, the CTE of the fiber shows significant nonlinearity in the range between room temperature and 449°C (840°F), but it is linear beyond that up to 1299°C (2370°F), as discussed by Hillmer (1989).

The fiber volume ratio measured from photomicrographic examination was 0.44. The equivalent ratio of the outer to inner cylinder diameters is 1.51 in this case, as determined from the relationship:

$$\frac{b}{a} = \frac{1}{\sqrt{V_f}} \tag{30}$$

The composite behavior was studied by considering the mechanical and thermal loading conditions. From the measured constituent properties, the elastoplastic problem was solved by the successive approximation method with 26 stations assigned along the radial direction. Under longitudinal tensile loading, the state of stresses in the composite is triaxial. Figures 5(a), 5(b), and 5(c) show respectively the radial, tangential, and axial stresses in the fiber and matrix as a function of r/a, that is the radial distance normalized by the fiber radius. As shown in the figures, several different levels of applied stress were chosen up to failure in increments of 275.8 MPa (40 ksi). It is noted that the radial stresses are compressive everywhere while the tangential stresses are compressive in the fiber and tensile in the matrix.

Substitution of eqs. (14)and (17) into eq. (5) yields a condition that the stresses in the fiber, σ_{rf}, $\sigma_{\theta f}$ and σ_{zf} are independent of the radius r. In other words, the stresses in the fiber are uniform. Furthermore, the radial stress component is equal to the tangential stress component. On the other hand, the radial and tangential stresses in the matrix decrease in absolute terms gradually from the fiber-matrix boundary as r increases. These stresses are an order of magnitude smaller than the axial stress but they contribute to the plastic deformation of the matrix. The condition of very high axial stress in the fiber compare to the other stresses implies that the axial deformation of the composite is dominated by the fiber properties.

Because of the plastic deformation of the matrix starting at a certain stress level, the rate of change in the local stresses decreases with respect to the applied stress above the critical yield stress. For example, the radial, tangential and axial stresses at $r = a$ are plotted as a function of applied stress as shown in Fig. 6. The initial portion of the curve is linear at stresses below yielding and then it approaches a plateau as the applied stress increases above the yield point. Also shown in the figure are the stresses in the fiber. Although the fiber properties are purely elastic, the actual stresses in the fiber are influenced by the matrix and show a pattern similar to that of the matrix. However, the axial stress in the fiber is high and not sensitive to the matrix deformation.

The effective strains are computed for prediction of the stress-strain curve of the composite. Figures 7(a), 7(b), and 7(c) show typical stress-strain curves at 24°C (75°F) and 288°C (550°F), respectively. The axial and transverse strains compare favorably experimental measurements.

The case of thermal loading case was also studied in addition to mechanical loading. The effects of residual stresses in the composite were neglected in this study although it is important to understand them for computing the actual stresses at a given temperature. However, it is interesting to study the thermal behavior by computing thermal stress distribution due to a temperature change.

Thermal stress components at various temperatures were computed and shown in Fig. 8. The thermal properties of the matrix at any given temperature can be obtained by linear interpolation of the measured data. Unlike the mechanical loading counterpart, these stresses do not change monotonically with the change in temperature. For example, as shown in Fig.8(a), the stress in the fiber at 177°C (350°F) is higher than that at 65.6°C (150°F) but lower than the one at 121°C (250°F). Figure 9 shows the computed stresses in the fiber and matrix plotted versus temperature. Note that the stresses increase linearly in the initial range of the heating process in the neighborhood of room temperature. The rate of increase slows down above the matrix yielding temperature and then the stresses decrease at higher temperatures. This phenomenon occurs because the internal stresses are affected by two competing factors: Thermal expansion keeps increasing as the temperature rises, while the matrix properties degrade at high temperature. As a result, the stresses increase at lower temperature where the thermal expansion predominates the process. On the other hand, the stresses drop at elevated temperatures where the matrix properties are significantly degraded. This phenomenon should be noted in designing structures for use at high temperatures.

Figure 10 shows the longitudinal and transverse thermal expansions of the composite as a function of temperature. Near room temperature, both fiber and matrix expand linearly with temperature. At a critical temperature where matrix yielding begins, the properties of the fiber contribute more to the longitudinal strains than the matrix. On the other hand, the transverse strains are more influenced by the matrix properties. This is shown in the figure where the slope of the transverse strain increases while that of the longitudinal strain decreases in the temperature range above the yield point. The experimental measurements do not exactly coincide with the prediction. It is believed that this slight deviation is a result of the neglect of residual stresses and of the relatively high fiber volume ratio of the model.

8 Summary and Conclusions

An elastoplastic analysis was developed and applied to the prediction of the thermomechanical behavior of a metal matrix composite based on the coaxial cylindrical model with perfect bonding at the fiber-matrix interface. It was assumed that the fiber is elastic and the matrix elastoplastic following a power law strain hardening model.

Stress distributions in the fiber and matrix due to mechanical and thermal loading conditions were obtained for various stress levels and temperatures. In the case of longitudinal tension, the radial and tangential stresses are approximately an order of magnitude lower than the axial stress. The stresses in the matrix show large variations while the stresses in the fiber are uniform.

In the case of thermal loading, the strain-temperature relationship shows nonlinearity due to matrix yielding and plastic flow. In the last stage of thermal loading, the internal stresses decrease because of the coupling of thermal expansion and matrix softening effects.

The successive approximation method was found to be a useful tool in solving problems where the boundary conditions are not explicitly prescribed. The best advantage of this approach is that the strain and stress fields are computed for any given loads without incrementing the load. However, the method should be refined by considering additional effects such as residual stresses and creep, particularly for studying the composite behavior in the transverse direction

9 Acknowledgment

This work was supported by NASA-Lewis Research Center, Cleveland, OH. We are grateful to Dr. C. C. Chamis of NASA for his encouragement and cooperation.

References

Alloy Digest Al-3, 1952, Engineering Alloys Digest, Inc., Upper Montclare, New Jersey

Alloy Digest Al-205, 1973, Engineering Alloys Digest, Inc., Upper Montclare, New Jersey

ASTM D3379-75, American Society for Testing and Materials, Philadelphia., U.S.A.

Daniel, I. M., Anastassopoulos, G. and Lee, J. W., 1989, "Experimental Micromechanics of Brittle-Matrix Composites," ASME AMD-Vol. 102, ed. by W. N. Sharpe, Jr., pp.133-146.

Daniel, I. M., Lee, J. W. and Anastassopoulos, G., 1993, "The Behavior of Ceramic Matrix Fiber Composites under Longitudinal Loading," *Composite Science and Technology*, Vol. 46, pp. 105-113.

Davis, E. A., 1963, "Extension of Iteration Method for Determining Strain Distributions to the Uniformly Stressed Plate with a Hole," ASME Journal of Applied Mechanics, June, pp. 210-214.

Hillmer, N. J., 1989, "Thermal Expansion of Chemically Vapor Deposited Silicone Carbide Fibers, " *Proceeding of the American Society for Composite*, Dayton, OH, pp. 206-213.

Hoffman, C. A., 1973, "Effects of Thermal Loading on Fiber Reinforced Composites With Constituents of Differing Expansivities," *Journal of Engineering Materials and Technology.*, January, pp 55-62.

Hsueh, C. and Becher, P. F., 1988, "Thermal Expansion Coefficients of Unidirectional Fiber Reinforced Ceramics," *Journal of the American Ceramic Society*, Vol. 71, pp. 438-441.

Iesan, D., 1980, "Thermal Stresses in Composite Cylinders," *Journal of Thermal Stress*, Vol. 3, pp. 495-508.

Ishikawa, T., Koyama, K. and Kobayash, S., 1978, "Thermal Expansion Coefficients of Unidirectional Composites," *Journal of Composite Materials.*, Vol. 12, pp. 153-168.

Luo, J. J., Wooh, S. C., and Daniel, I. M., 1994, "Acoustic Emission Study of Failure Mechanisms in Ceramic Matrix Composite under Longitudinal Tensile Loading," Review of Progress in Quatitative Nondestructive Evaluation, In Press.

Mendelson, A. and Spero, S. W., 1962, "A general Solution for the Elastoplastic Thermal Stresses in a Strain-Hardening Plate with Arbitrary Material Properties," ASME Journal of Applied Mechanics, March, pp. 151-158.

Mikata, Y. and Taya, M., 1985, "Stress Field in a Coated Continuous Fiber Composite Subject to Thermo-Mechanical Loadings," *Journal of Composite Materials*, Vol. 19, pp. 554-578.

Pindera, M.-J. and Lin, M. W., 1989, "Micromechanical Analysis of the Elastoplastic Response of Metal Matrix Composites," *Journal of Pressure Vessel Technology*, Vol. 111, pp. 183-190.

Rosen, B. W., 1970, "Thermomechanical Properties of Fibrous Composites," *Proceeding of the Royal Society of London, A.*, Vol. 319, pp. 79-94.

Schapery, R. A., 1968, "Thermal Expansion Coefficients of Composite Materials Based on Energy Principles," *Journal of Composite Materials.*, Vol. 2, pp. 380-403.

Takao, Y. and Taya, M., 1985, "Thermal Expansion Coefficients and Thermal Stresses in an Aligned Short Fiber Composite with Application to a Short Carbon Fiber/Aluminum," ASME Journal of Applied Mechanics, Vol. 52, pp. 806-810.

Takao, Y., and Taya, M., 1987, "The Effect of Variable Fiber Aspect Ratio on the Stiffness and Thermal Expansion Coefficients of a short Fiber Composite," *Journal of Composite Materials*, Vol. 21, pp. 140-156

Tsai, C-L., and Daniel, I. M., 1994, "Method for Thermo-mechanical Characterization of Single fibers, " *Composite Science and Technology*, Vol. 50, pp. 7-12.

Tuba, S., 1965, "Elastic-Plastic Stress and Strain Concentration Factors at a Circular Hole in a Uniformly Stressed Infinite Plate," ASME Journal of Applied Mechanics, September, pp. 170-171.

Uemura, M., Iyama, H. and Yamaguchi, Y., 1979, "Thermal Residual Stresses in Filament Wound Carbon Fiber-reinforced Composites," *Journal of Thermal Stresses*, Vol. 2, pp. 393-412.

Warwick, C. M. and Clyne, T. W., 1991, "Development of Composite Coaxial Cylinder Stress Analysis Model and Its Application to SiC Monofilament Systems," *Journal of Material Science*, Vol. 26, pp. 3817-3827.

Whitney, J. M., Daniel, I. M., and Pipes, R. B., 1985, *Experimental Mechanics of Fiber Reinforced Composite Materials*, SEM Monograph 4, Second Ed., Bethel, CT.

Appendix

Prandtl-Reuss Relations in terms of Plastic Strain and Total Strain

The Prandtl-Reuss equations express the relationship between the plastic strain increment to the stresses. These relation can be modified using a set of similar equations expressed in strains. These total deformation plasticity relationships are more convenient to use in conjunction with the successive approximation scheme. The general relationships are derived as follows.

The total strain is expressed as a sum of elastic and plastic components

$$\varepsilon_{ij} = \varepsilon_{ij}^{e} + \varepsilon_{ij}^{p} \tag{A1}$$

where ε_{ij} is the total strain, ε_{ij}^{e} the elastic strain, and ε_{ij}^{p} the plastic strain.

Subtracting the mean strain from the diagonal components yields

$$\varepsilon_{ij} - \frac{1}{3}\varepsilon_{kk}\delta_{ij} = \varepsilon_{ij}^{e} - \frac{1}{3}\varepsilon_{kk}\delta_{ij} + \varepsilon_{ij}^{p} \tag{A2}$$

Defining the total deviatoric strain tensor e_{ij}, and elastic deviatoric strain tensor e_{ij}^{e}, equation (A2) becomes

$$e_{ij} = e_{ij}^{e} + \varepsilon_{ij}^{p} \tag{A3}$$

Prandtl-Reuss flow relation gives the relationship

$$\varepsilon_{ij}^{p} = \lambda S_{ij} \tag{A4}$$

where λ is nonnegative constants and S_{ij} the deviatoric stress tensor expressed as

$$S_{ij} = \sigma_{ij} - \frac{1}{3}\sigma_{kk}\delta_{ij} \tag{A5}$$

From the Hook's law and Prandtl-Reuss relationship, the elastic deviatoric tensor is expressed as

$$e_{ij}^{e} = \frac{1}{2G} S_{ij} \tag{A6}$$

or

$$e_{ij}^{e} = \frac{1}{2G} \frac{\varepsilon_{ij}^{p}}{\lambda} \tag{A7}$$

where G is the shear modulus.

Substituting eq. (A7) into (A3) gives

$$e_{ij} = \left(1 + \frac{1}{2G\lambda}\right) \varepsilon_{ij}^{p} \tag{A8}$$

From eq. (A8)

$$\frac{2}{3} e_{ij} e_{ij} = \frac{2}{3} \left(1 + \frac{1}{2G\lambda}\right)^{2} \varepsilon_{ij}^{p} \varepsilon_{ij}^{p} \tag{A9}$$

By defining an equivalent modified total strain

$$\bar{\varepsilon} = \sqrt{\frac{2}{3} e_{ij} e_{ij}} \tag{A10}$$

equation (A9) becomes

$$\frac{\bar{\varepsilon}}{\bar{\varepsilon}^{p}} = 1 + \frac{1}{2G\lambda} \tag{A11}$$

and from eq. (A8)

$$\varepsilon_{ij}^{p} = \frac{\bar{\varepsilon}_{p}}{\bar{\varepsilon}} e_{ij} \tag{A12}$$

Equivalent stress and an equivalent plastic strain are:

$$\bar{\sigma} = \sqrt{\frac{3}{2} S_{ij} S_{ij}} \tag{A13}$$

$$\overline{\varepsilon}^{p} = \sqrt{\frac{2}{3}\varepsilon_{ij}^{p}\varepsilon_{ij}^{p}} \tag{A14}$$

Figure Captions

Fig. 1 Coaxial cylindrical composite model.

Fig. 2 Schematic stress-strain curves of linear and power law strain hardening models.

Fig. 3 Apparent compliance of SCS-2 fiber as a function of gage length.

Fig. 4 Tensile stress-strain curves of 6061-O aluminum at various temperatures.

Fig. 5 Stress distribution in the fiber and matrix as a function of radial distance for longitudinal mechanical loadin: (a) radial, (b) tangential, (c) axial stresses.

Fig. 6 Radial, tangential and axial stresses in the matrix at $r=a$ and radial and tangential stresses in the fiber as a function of applied stress.

Fig. 7 Stress-strain curves of $[0_8]$ unidirectional SiC/Al composite at various temperatures. (a) 24°C (75°F) and (b) 288°C (550°F).

Fig. 8 Stress distribution in the fiber and matrix as a function of radius for various temperature changes: (a) radial, (b) tangential, (c) axial stresses.

Fig. 9 Radial, tangential and axial stresses in the matrix at $r=a$ in the fiber as a function of temperature.

Fig. 10 Longitudinal and transverse thermal strain-temperature curves of unidirectional SiC/Al composite.

Table 1 Properties of SiC/Al composite at room temperature

Property	SiC/Al Composite
Longitudinal modulus, E_1, GPa (Msi)	206.9 (30.0)
Major Poisson's ratio, ν_{12}	0.27
Longitudinal tensile strength, F_t, MPa (ksi)	1620.0 (235.0)
Longitudinal coefficient of thermal expansion, α_1, $\mu\varepsilon/°C$ ($\mu\varepsilon/°F$)	5.94 (3.3)
Transverse coefficient of thermal expansion, α_2, $\mu\varepsilon/°C$ ($\mu\varepsilon/°F$)	16.0 (8.9)
Fiber volume ratio, V_f	0.44

Table 2 Properties of aluminum 6061-O and SCS-2 fiber at room temperature

Property	6061-O Aluminum	SCS-2 Fiber
Elastic modulus, E, GPa (Msi)	69.0 (10)	399.9 (58)
Poisson's ratio, ν	0.33	0.22
Yield stress, σ_y, MPa (ksi)	55.2 (8)	---
Tensile strength, F_t, MPa (ksi)	124.1 (18)	3461- 5309 (502 - 770)
Coefficient of thermal expansion, α, $\mu\varepsilon/°C$ ($\mu\varepsilon/°F$)		
24°C (75°F)	23.4(13.0)	2.25(1.25)
121°C (250°F)	23.6(13.1)	2.34(1.30)
177°C (350°F)	23.9(13.3)	2.81(1.56)
288°C (550°F)	24.8(13.5)	---
450-1300°C (842-2372°F)	---	4.86(2.70)

Table 3 Values of material dependent parameters

Temperature	Modulus E, GPa (Msi)	Elastic limit stress σ_Y, MPa (ksi)	Material constant k ($\times 10^{-5}$)	Material constant n ($\times 10^{-2}$)
24°C (75°F)	68.6 (10)	41.4 (6)	510	45.3
121°C (250°F)	63.8 (9.25)	39.3 (5.7)	450	45.5
177°C (350°F)	60.7 (8.8)	37.4 (5.35)	380	45.6
288°C (550°F)	55.2 (8)	33.1 (4.8)	6.62	45.8
399°C (750°F)	48.3 (7)	15.9 (2.3)	6.12	46.0

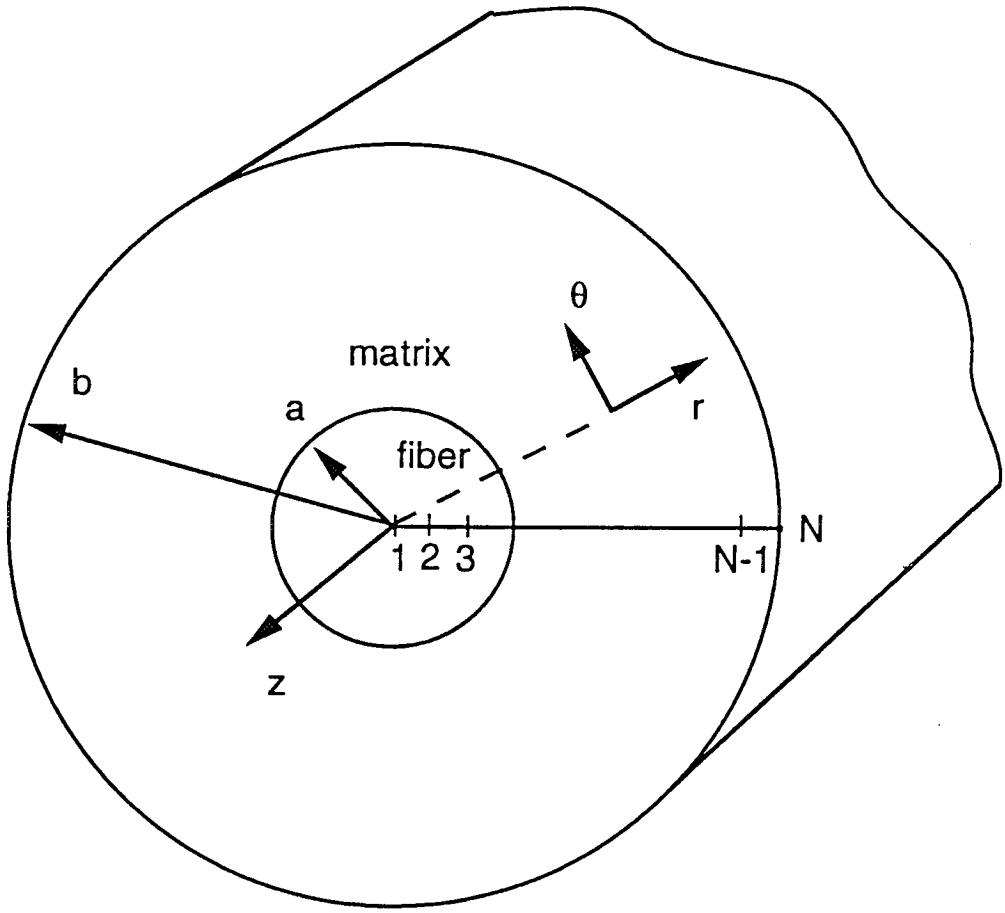
θ
matrix
b
a
r
fiber
N
1 2 3
N-1
z

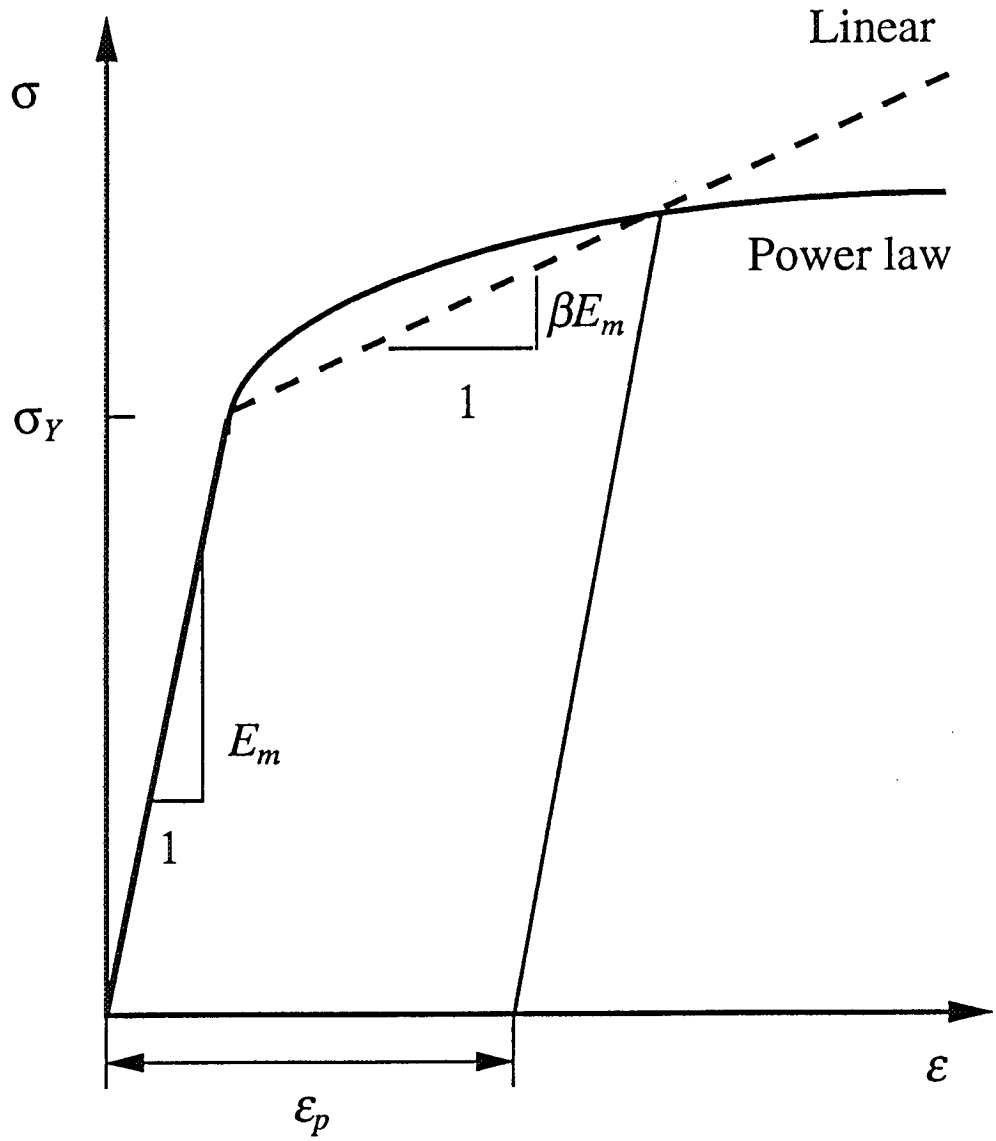
Linear
σ
Power law
βE_m
1
σ_Y
E_m
1
ε
ε_p

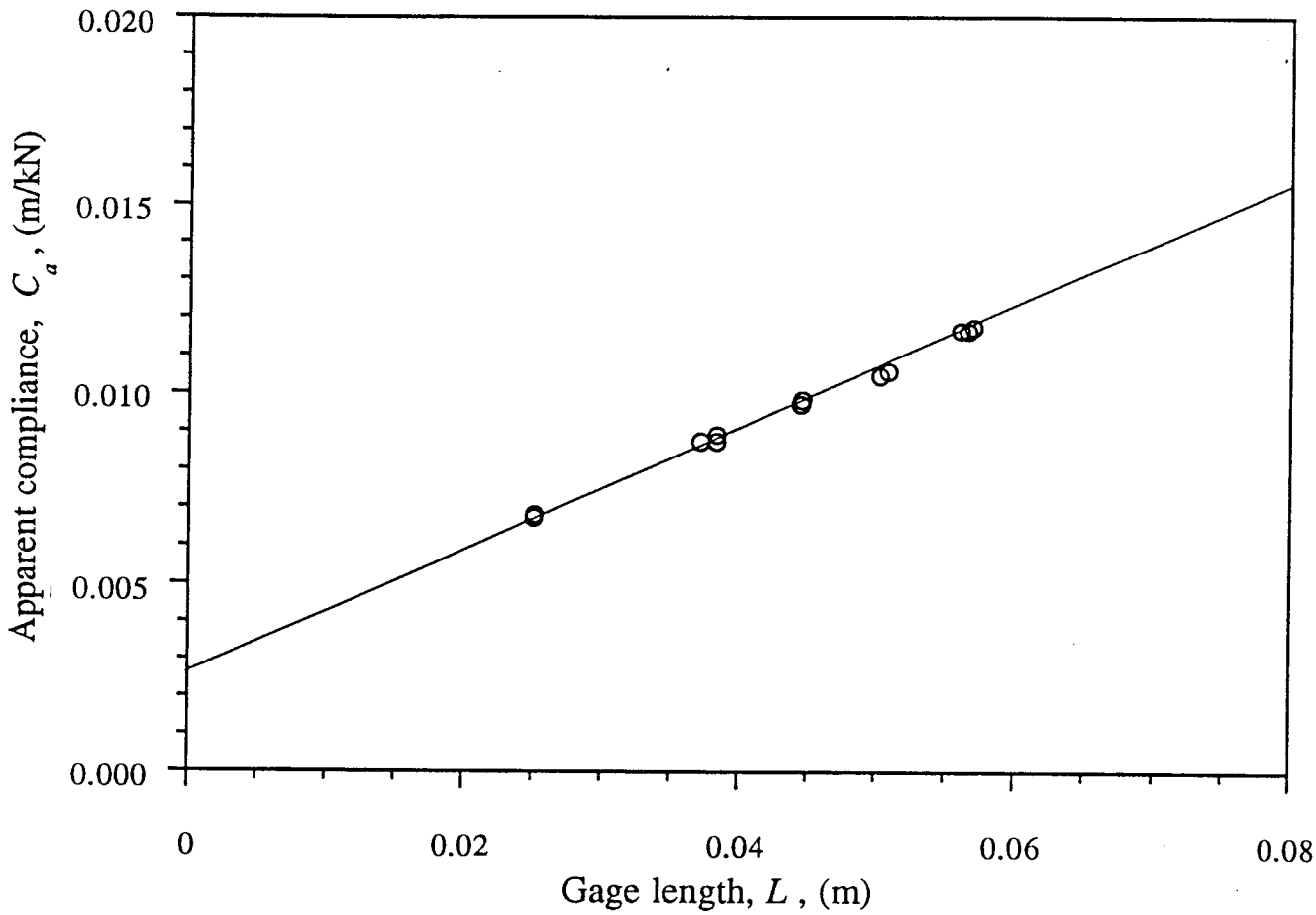
0.020
0.015
0.010
0.005
0.000
Apparent compliance, C_a, (m/kN)
0
0.02
0.04
0.06
0.08
Gage length, L, (m)

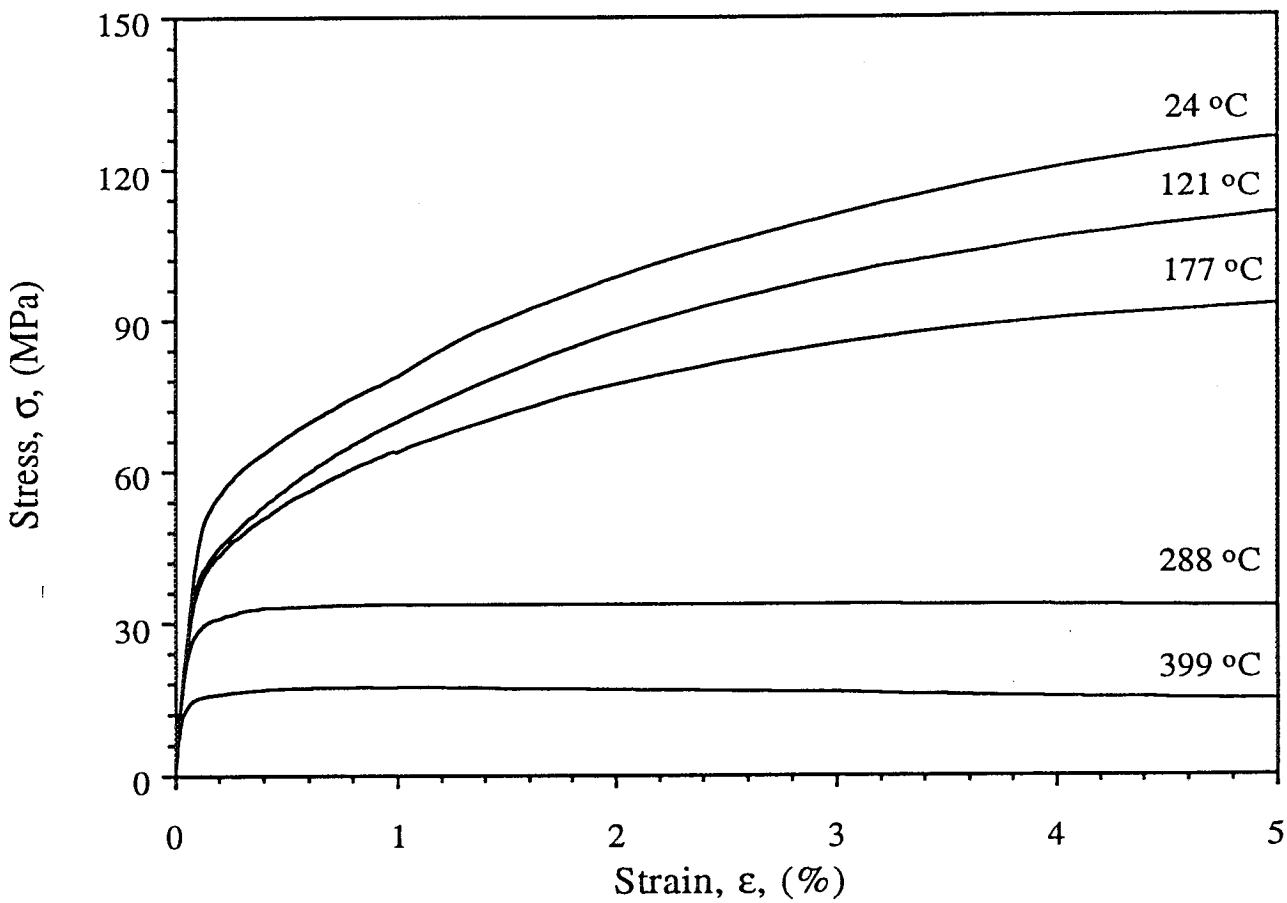
150
120
90
60
30
0
Stress, σ, (MPa)
24 °C
121 °C
177 °C
288 °C
399 °C
0
1
2
3
4
5
Strain, ε, (%)

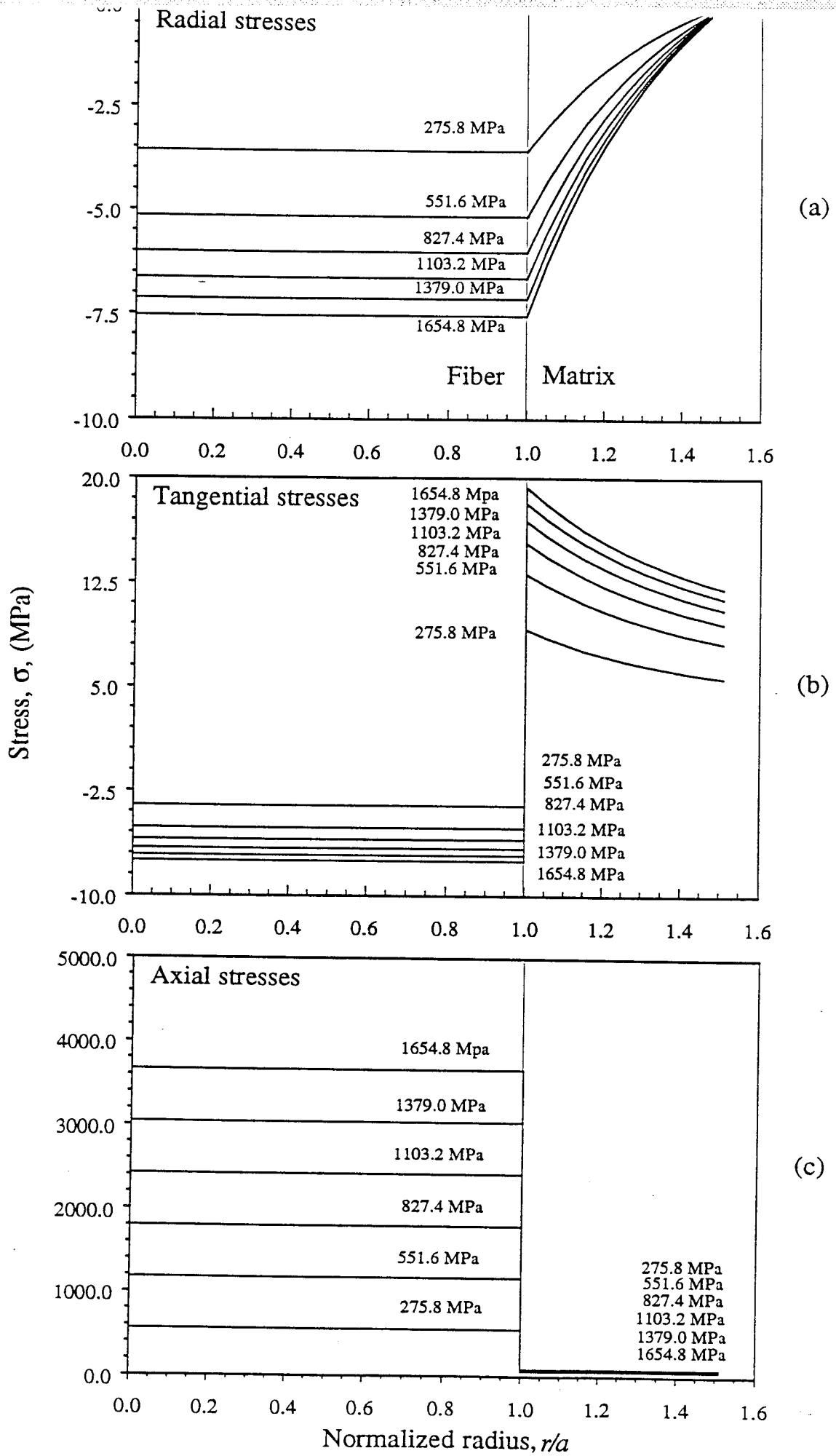
Radial stresses
275.8 MPa
551.6 MPa
827.4 MPa
1103.2 MPa
1379.0 MPa
1654.8 MPa
Fiber
Matrix
(a)
Tangential stresses
1654.8 Mpa
1379.0 MPa
1103.2 MPa
827.4 MPa
551.6 MPa
275.8 MPa
275.8 MPa
551.6 MPa
827.4 MPa
1103.2 MPa
1379.0 MPa
1654.8 MPa
(b)
Axial stresses
1654.8 Mpa
1379.0 MPa
1103.2 MPa
827.4 MPa
551.6 MPa
275.8 MPa
275.8 MPa
551.6 MPa
827.4 MPa
1103.2 MPa
1379.0 MPa
1654.8 MPa
(c)
Stress, σ, (MPa)
Normalized radius, r/a

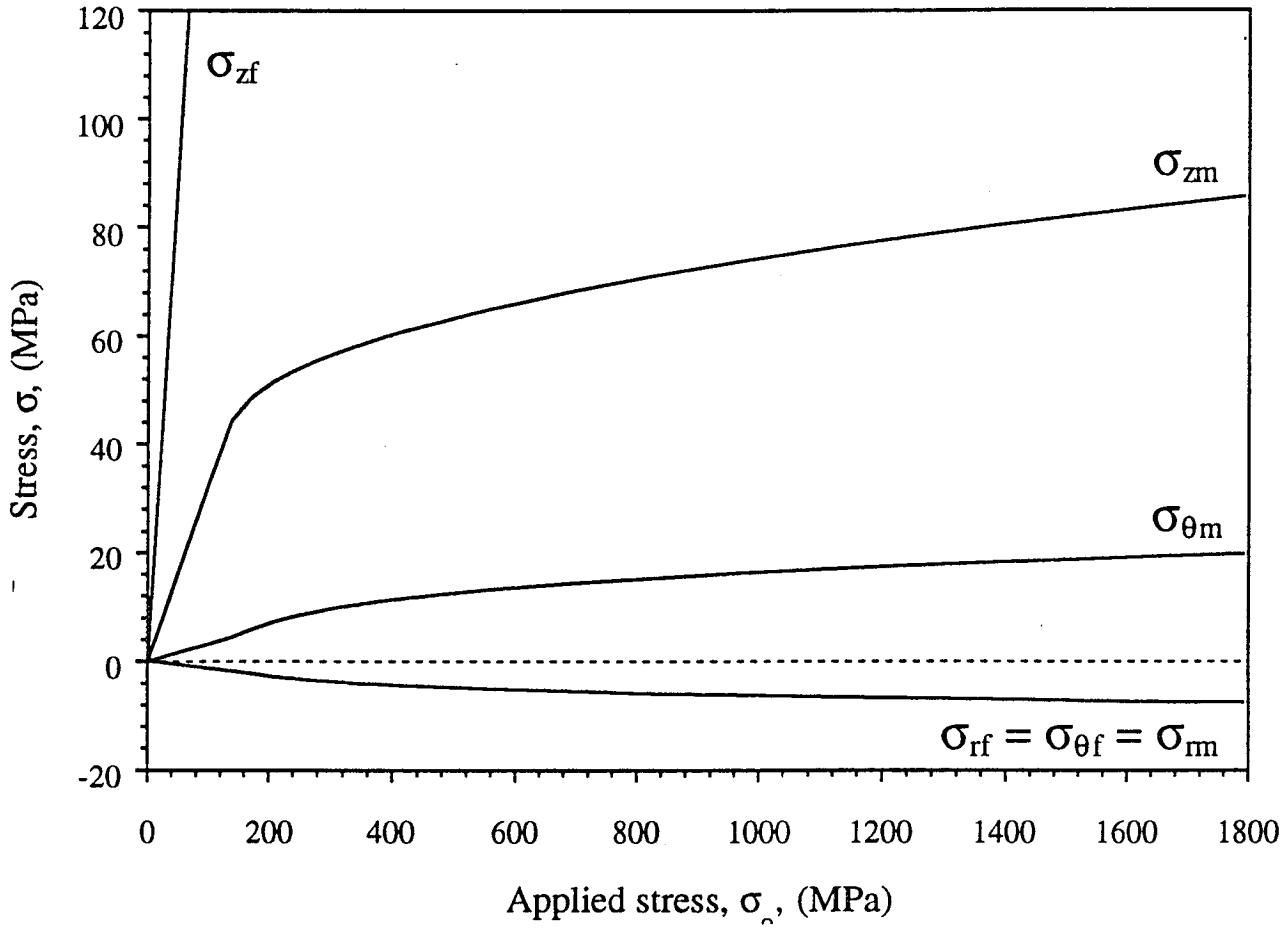
120
100
80
60
40
20
0
-20
Stress, σ, (MPa)
σzf
σzm
σθm
σrf = σθf = σrm
0
200
400
600
800
1000
1200
1400
1600
1800
Applied stress, σ∞, (MPa)

(a)

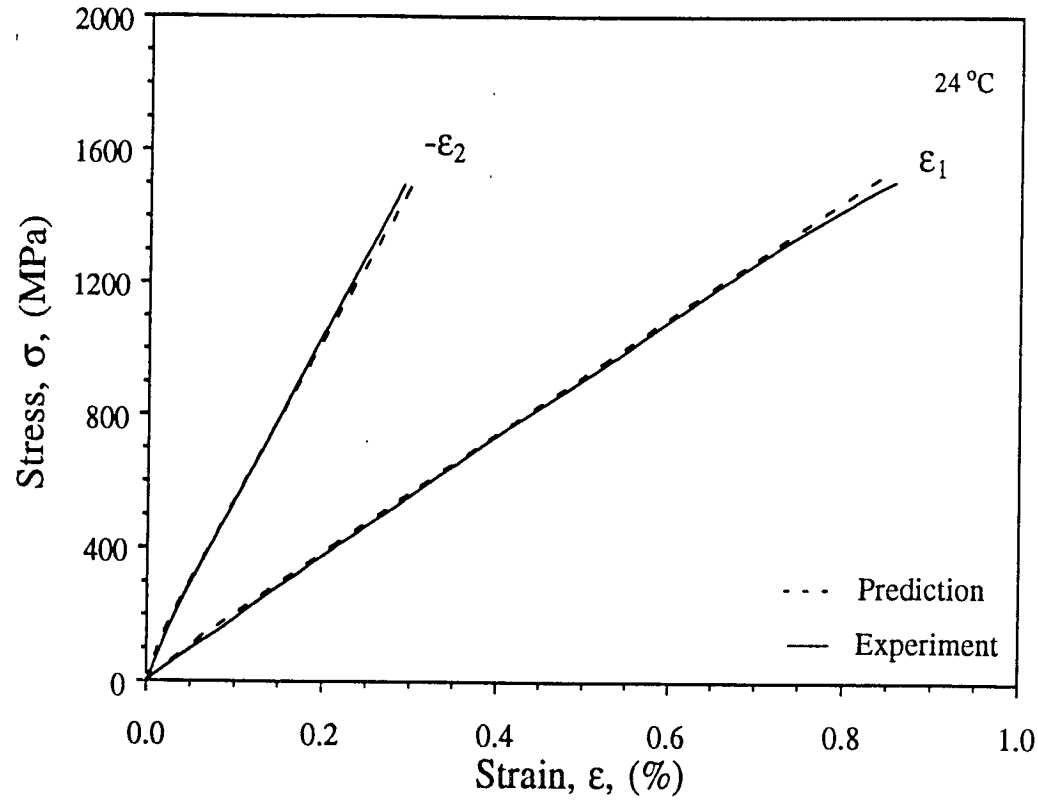
2000
1600
1200
800
400
0
Stress, σ, (MPa)
24 °C
-ε2
ε1
Prediction
Experiment
0.0
0.2
0.4
0.6
0.8
1.0
Strain, ε, (%)

(b)

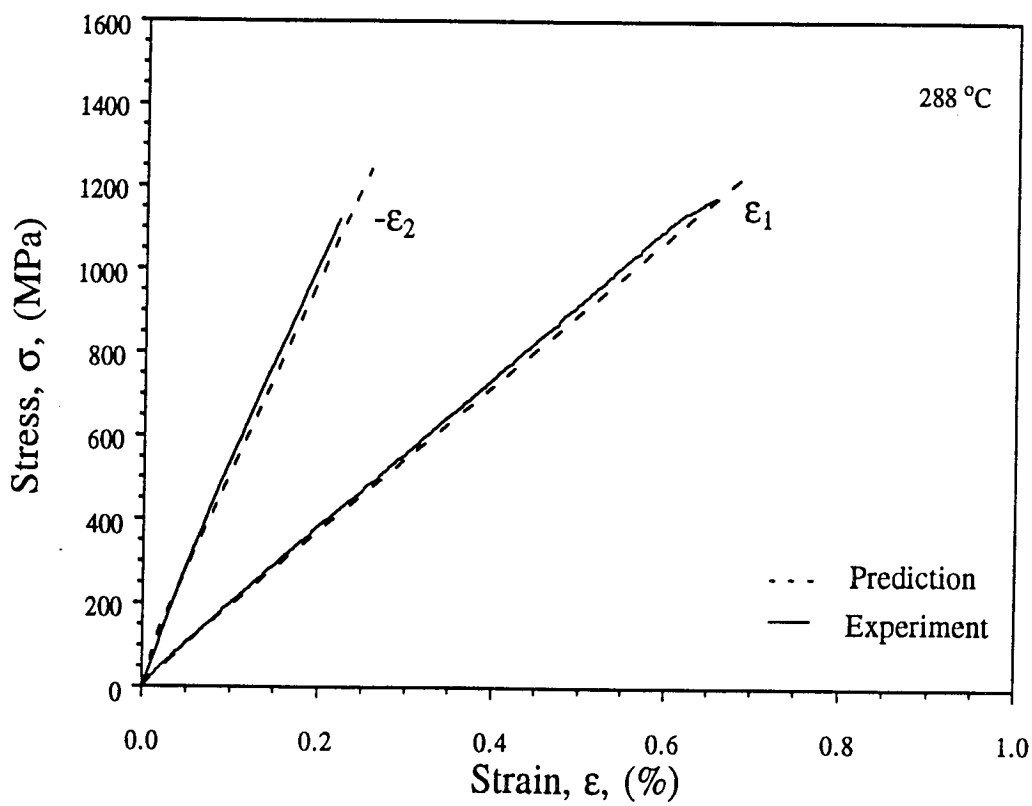
1600
1400
1200
1000
800
600
400
200
0
Stress, σ, (MPa)
288 °C
-ε2
ε1
Prediction
Experiment
0.0
0.2
0.4
0.6
0.8
1.0
Strain, ε, (%)

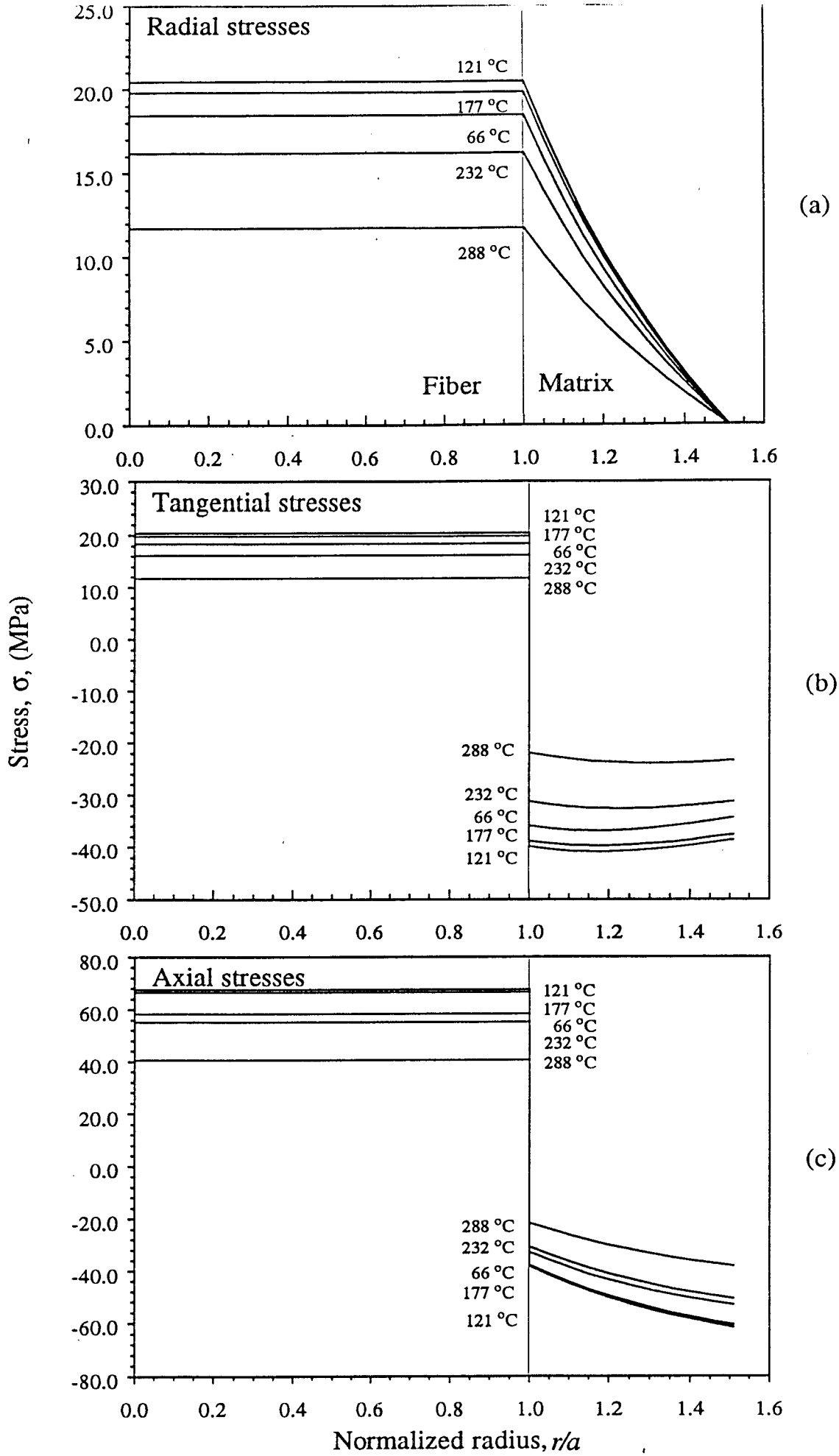
Radial stresses
121 °C
177 °C
66 °C
232 °C
288 °C
Fiber
Matrix
(a)
Tangential stresses
121 °C
177 °C
66 °C
232 °C
288 °C
288 °C
232 °C
66 °C
177 °C
121 °C
(b)
Axial stresses
121 °C
177 °C
66 °C
232 °C
288 °C
288 °C
232 °C
66 °C
177 °C
121 °C
(c)
Stress, σ, (MPa)
Normalized radius, r/a

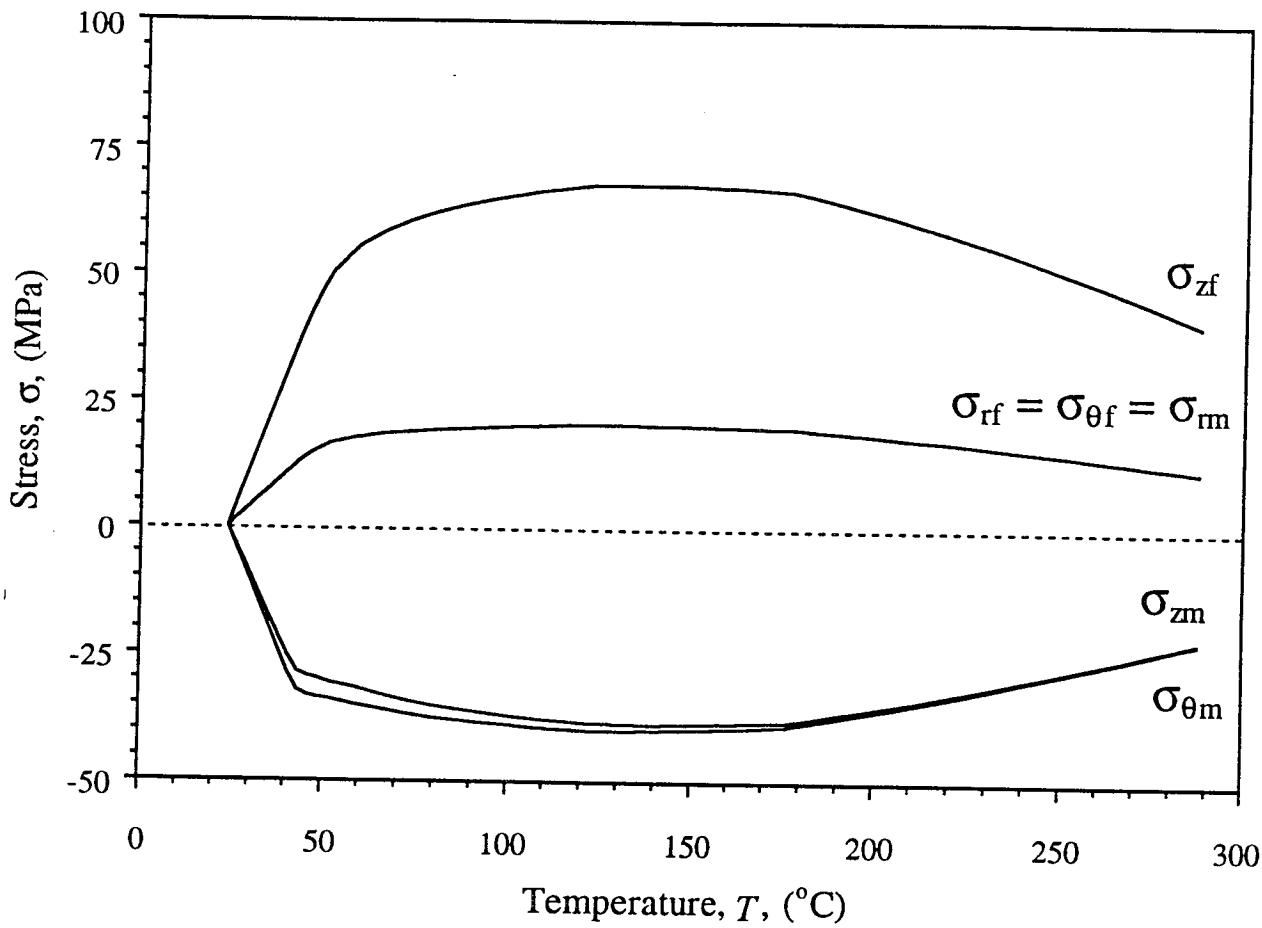
100
75
50
25
0
-25
-50
Stress, σ, (MPa)
0
50
100
150
200
250
300
Temperature, T, (°C)
σzf
σrf = σθf = σrm
σzm
σθm

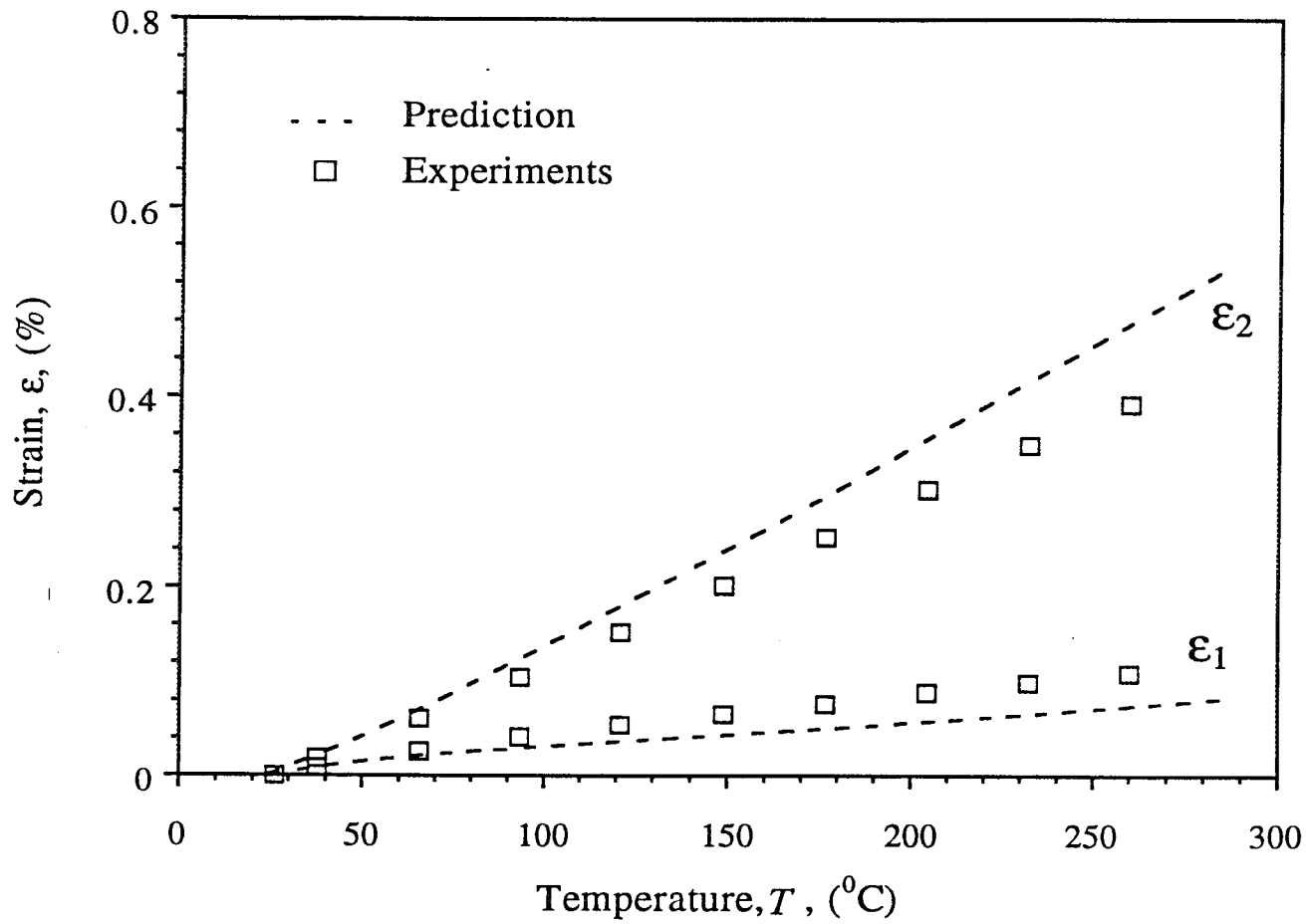
0.8
0.6
0.4
0.2
0
Strain, ε, (%)
Prediction
Experiments
ε2
ε1
0
50
100
150
200
250
300
Temperature, T , (°C)

APPENDIX D

Unidirectional SiC/Al Composite Behavior under Thermomechanical Loading

Heoung-Jae Chun, Research Assistant

Isaac M. Daniel, Professor

Robert R. McCormick School of Engineering and Applied Science

Northwestern University,

Evanston, Illinois 60208

Abstract

The thermoelastoplastic behavior of unidirectional SiC/Al composite was studied with a micromechanical model based on the average field theory. The continuous elastic fibers are assumed consistently scattered in the thermoelastoplastic matrix in the model. The thermoelastoplastic analysis of the composite is achieved by introducing the concept of secant properties of the matrix. The average stresses of the matrix, fiber and the effective strain of the composite are expressed as functions of the secant modulus of the matrix. The stress-strain curves under transverse and longitudinal tensile loading at different temperatures and the thermal strain-temperature curves of the composite were predicted and compared satisfactorily with experimental results.

Introduction

Metal matrix composites (MMC's) are in demand even though their fabrication process is more complex and less cost effective than that of polymer based composites because of their superior performance in operating environments involving high temperature and moisture. They also posses other merits such as high toughness, impact resistance, resistivity to temperature change or thermal shock, surface durability, low sensitivity to surface flaws, and high electrical and thermal conductivity. The unidirectional composite is the easiest to manufacture and has the best properties in the fiber direction. However, its transverse strength is much lower than that of unreinforced matrix. This makes it difficult to use the material in unidirectional form and is important to understand its behavior especially under transverse loading.

A micromechanical model was adopted to predict thermoelastoplastic behavior of composite materials. In the past, most investigations were focused on the elastic behavior of the composite and only a limited number of studies was carried out on elastoplastic behavior due to its complicated nature. In the case of MMC, the matrix undergoes a plastic flow and is sensitive to the environmental temperature. Thus, it is imperative to study the MMC behavior using the thermoelastoplastic solution.

A number of investigations of different micromechanics were carried out. For a low fiber volume ratio Eshelby's method (1957) was used successfully to predict average behavior of the composite. For intermediate fiber volume ratio the coaxial cylinder model (CCM) was introduced by Ishikawa *et al.* (1978), Unemura *et al.* (1979), Iesan (1980), Mikata and Taya (1985), and Warwick and Clyne (1991), by assuming elastic constituents, particularly elastic matrix. The model was extended to include elastoplastic behavior of the matrix by Hecker *et al.* (1970), Gayda and Ebert (1979), and Chun *et al.* (1994). But the applications of CCM are restricted to the axisymmetric problems. To overcome this restriction, attention was paid to a model which is based on Eshelby's solution with Mori and Tanaka's (1973) average field theory incorporating Eshelby's equivalence principle. This model is not only applicable to non axisymmetric loading conditions but also gives reasonable results for larger fiber volume ratios (See Lin *et al,* 1992). This method has been used by Taya and Chou (1981), Taya and Mura (1981), Takao and Taya (1987), Benveniste(1987), Tandon and Weng (1988), and Lin *et al.* (1992).

The theory proposed by Tandon and Weng (1988) was extended to the thermoelastoplastic analysis of a unidirectional composite in this paper. In the analysis, the thermoelastoplastic behavior of the composite is described by introducing the concept

of secant moduli to the Mori and Tanaka's method (1973). This method simplifies the thermoelastoplastic analysis without recourse to the plastic strain components from the plastic flow rule. The theoretical predictions were compared with experimental results.

Theoretical background

The representative volume of the composite consists of a number of long fibers in a matrix block. The fibers and matrix are assumed fully bonded. The model provides the following constutive relations for the effective response of a unidirectional elastoplastic composite referred to a Cartesian coordinate system (x_1, x_2, x_3) where x_3 is aligned with the fiber direction as shown in Fig. 1.

The fiber behaves elasticly up to failure and the matrix behaves thermoelastoplasticly. The fiber volume ratio is denoted by f. The secant moduli of the matrix and fiber are denoted as C_m and C_f, respectively.

According to Mori and Tanaka (1973), the average disturbed strain field exists only inside the fiber in the representative volume if the shape of the representative volume and fiber are taken similar because the average disturbed strain field due to the existence of the fiber vanishes outside the inhomogenity. This method has an advantage because no boundary condition is needed to determine overall behavior of the system. External tractions or external displacements can be assigned to the boundary of the system which yield the same result. In this paper, the analysis was carried out when the external traction is applied to the boundary of the representative volume. This method is based on analysis of two systems, one is a reference model of a pure matrix under the same external load as the second system that contains the fibers.

The external traction applied to the boundary produces a uniform stress σ_0 and strain ε_0 if the body does not contain any reinforcement. They are related by

$$\sigma_0 = C_m \varepsilon_0 \tag{1}$$

where C_m is the secant modulus of the matrix at the applied stress σ_0. The average stress-strain relationship of the matrix in the composite is quite different from equation (1). It is expressed as

$$\sigma_m = \sigma_0 + \tilde{\sigma}_m = C_m(\varepsilon_0 + \tilde{\varepsilon}) \tag{2}$$

where $\tilde{\sigma}_m$ and $\tilde{\varepsilon}$ are matrix disturbance stress and disturbance strain, respectively, due to the presence of reinforcement. The stress-strain relation of the fiber is also different from that of the surrounding matrix. With the help of Eshelby's equivalent inclusion principle the stress in the fibers is expressed as follows

$$\sigma_f = \sigma_0 + \tilde{\sigma}_f = C_f(\varepsilon_0 + \tilde{\varepsilon} + \varepsilon' - \varepsilon_t) = C_m(\varepsilon_0 + \tilde{\varepsilon} + \varepsilon' - \varepsilon_t - \varepsilon^*) \tag{3}$$

where ε_t is the thermal strain introduced due to the mismatch in thermal expansion coefficients between the matrix and fiber, $\tilde{\sigma}_f$ and ε' are disturbance stress and strain fields due to the presence of the fiber and thermal strain, ε^* is a fictitious eigenstrain (See Mura, 1982) which is introduced to relate the present problem to the equivalent inclusion problem. The thermal strain (ε_t) is expressed as

$$\varepsilon_{tij} = (\alpha_m - \alpha_f)\Delta T \delta_{ij} \qquad (i, j=1, 2, 3). \tag{4}$$

where α_m and α_f are the thermal expansion coefficients of the matrix and fiber, respectively and ΔT is the temperature change. According to Eshelby the relationship among the disturbance strain (ε'), thermal strain (ε_t) and eigenstrain (ε^*) is expressed as

$$\varepsilon' = S(\varepsilon_t + \varepsilon^*) \tag{5}$$

where S is Eshelby's secant tensor of the fiber expressed in terms of dimensions of the fiber and secant Poisson's ratio of the matrix. The equilibrium condition in terms of average stress gives

$$\sigma_0 = f\sigma_f + (1-f)\sigma_m \tag{6}$$

where f is the fiber volume ratio. Equation (2), (3) and (6) give

$$\tilde{\sigma}_m = \frac{f}{(f-1)}\tilde{\sigma}_f \tag{7}$$

From eqs. (2), (3) and (7) the disturbance strain of the matrix is obtained as

$$\tilde{\varepsilon} = C_m^{-1}\sigma_0 - \varepsilon_0 + f(I-S)(\varepsilon_t + \varepsilon^*) \tag{8}$$

where I is the identity tensor.

From eqs. (3) and (8) the eigenstrain is expressed as

$$\varepsilon^* = J^{-1}(C_f - C_m)\{C_m^{-1}\sigma_0 + (1-f)(S-I)\varepsilon_t\} \tag{9}$$

where

$$J = (f-1)C_m(I-S) + C_f\{f(S-I) - S\} \tag{10}$$

The average stress in the matrix is calculated from eq. (2) as

$$\begin{aligned}\sigma_m = \sigma_0 &- fC_m(S-I)J^{-1}(C_f - C_m)C_m^{-1}\sigma_0 \\ &- fC_m(S-I)\{(1-f)J^{-1}(C_f - C_m)(S-I) + I\}\varepsilon_t\end{aligned} \tag{11}$$

The average stress in the fibers is calculated from eq. (3) as

$$\begin{aligned}\sigma_f = \sigma_0 &+ (1-f)C_m(S-I)J^{-1}(C_f - C_m)C_m^{-1}\sigma_0 \\ &+ (1-f)C_m(S-I)\{(1-f)J^{-1}(C_f - C_m)(S-I) + I\}\varepsilon_t\end{aligned} \tag{12}$$

The stress-strain relation for the composite is obtained from following relationship

$$\bar{\varepsilon} - \bar{\varepsilon}_t = f\varepsilon_f + (1-f)\varepsilon_m \tag{13}$$

where

$$\bar{\varepsilon}_{tij} = \{f\alpha_f + (1-f)\alpha_m\}\Delta T\delta_{ij} \qquad (i, j=1, 2, 3) \tag{14}$$

From eq. (13), the effective strain of the composite due to the mechanical and thermal loading is given as

$$\bar{\varepsilon} = \{C_m^{-1} + fJ^{-1}(C_f - C_m)C_m^{-1}\}\sigma_0 + f(1-f)J^{-1}(C_f - C_m)(S-I)\varepsilon_t + \bar{\varepsilon}_t \tag{15}$$

Equation (15) is used to predict the thermoelastoplastic behavior of the composite.

Elastoplastic Analysis

The thermoelstoplastic behavior of the composite is carried out by introducing the concept of secant properties to the Mori-Tanaka method. The thermoelastoplastic analysis is separated into the elastic and plastic parts. At this point it is more convenient to treat the yield condition and plastic analysis with the concept of equivalent stress and strain. This concept enables to reduce the complex three-dimensional stress-strain relations to a single relationship.

The composite behaves elasticly until the equivalent average stress of the matrix from eq. (11) exceeds the yield stress of the matrix.

$$\bar{\sigma} \le \sigma_Y \tag{16}$$

where the equivalent average stress is defined as

$$\bar{\sigma} = \sqrt{\frac{2}{3} S_{mij} S_{mij}} \tag{17}$$

Here S_{mij} is the deviatoric stress tensor of the matrix. The secant moduli of the fiber and matrix and the Eshelby's secant tensors all coincide with the elastic values. The composite,

starts to behave plasticly when the equivalent average stress in the matrix exceeds the yield stress.

$$\bar{\sigma} > \sigma_Y \tag{18}$$

The elastoplastic stress-strain behavior of the matrix is expressed as a power law strain hardening model for the theoretical prediction of composite behavior as an input for constituent properties. The stress-strain curve of the matrix is expressed as

$$\bar{\sigma} = \sigma_Y + kE_m \varepsilon_p^n \tag{19}$$

where k, and n, are material constants, σ_Y is the elastic limit stress or yield stress and ε_p is the equivalent plastic strain of the matrix defined as

$$\varepsilon_p = \sqrt{\frac{3}{2}\varepsilon_{mpij}\varepsilon_{mpij}} \tag{20}$$

where ε_{mpij} are the plastic strains of the matrix. The corresponding secant modulus (See Fig. 2) for a given equivalent plastic strain is express as

$$E_m^{\ s} = \frac{E_m\{\sigma_Y + kE_m\varepsilon_p^{\ n}\}}{\sigma_Y + kE_m\varepsilon_p^{\ n} + E_m\varepsilon_p} \tag{21}$$

Where E_m is the elastic modulus of the matrix. The corresponding secant Poisson's ratio increases in the nonlinear range from its elastic value to the limiting value of 0.5 for an incompressible material. It can be expressed in terms of the secant modulus (see Nadai, 1950) as

$$\nu_m^{\ s} = \frac{1}{2} - (\frac{1}{2} - \nu_m)\frac{E_m^{\ s}}{E_m} \tag{22}$$

where ν_m is the elastic Poisson's ratio of the matrix.

When the matrix yields for a given thermomechanical loading, the combined incremental-search method and bisection method is used to find the corresponding equivalent plastic strain. Then, the secant properties of the matrix are computed from eqs. (21) and (22) to calculate the corresponding effective strain of the composite. Following is the step by step procedure of the method used in computing the equivalent plastic strain under thermomechanical loading following the matrix yielding.

1. An equivalent plastic strain is first assumed then the corresponding secant Modulus and Poisson's ratio of the matrix are computed from eqs. (21) and (22).
2. From eqs. (11) and (17) the equivalent average stress of the matrix under the thermomechanical loading is obtained from the secant properties.
3. If the equivalent average stress of the matrix from the above procedure is matched with the result from equation (19) then the solution is obtained. If not, then, the above procedure is repeated until the solution is found.
4. Known secant properties of the matrix are used to calculate the effective strain of the composite from eq. (15) under thermomechanical loading.

Experimental Procedure

The composite material studied in this paper is SiC/Al composite. This composite material consists of 6061 aluminum matrix reinforced with 140 μm (0.00551 in.) diameter SCS-2 fiber (Textron Specialty Materials, Inc.). The fiber volume ratio measured from photomicrographic examination was 0.44. The composite material was made by diffusion bonding consolidation. The specimens, cut from 1.42mm (0.056in.) thick unidirectional

eight-ply composite plate, were 12.7mm (0.5in.) wide 152.4mm (6.0in.) long and were tabbed with 38.1mm (1.5in.) steel tabs with high strength adhesive for use at elevated temperatures. Two types of adhesives were used for different temperature ranges. For the temperature range between 24°C (75°F) to 288°C (550°F), a polyimide adhesive film (FM36, American Cyanamid) was used; while an aluminum filled condensation type polyimide adhesive film (FM680, American Cyanamid) was used for the temperature range of 288°C (550°F) to 399°C (750°F). Both types are supported by a glass cloth carrier for better shear and peel strengths.

Elevated temperature tests were conducted in an Instron 1331 servo-hydraulic testing system equipped with a thermal chamber. The specimens were instrumented with commercially available strain gages for high temperature applications (WK-gages from Micro Measurements and RKO-gages from J. P. Technology). The strain readings from the gages were compensated for temperature by using a dummy gage technique and were verified by measuring the axial strain by a high temperature water-cooled clip-on extensometer. The specimen surface temperature was monitored by a K-type thermocouple bonded on the surface with ceramic adhesive. The temperature signal was also used as a feedback to the temperature controller. All tests of the composite were repeated at three temperatures, 24°C (75°F), 288°C (550°F), and 399°C (750°F).

For micromechanical prediction of thermomechanical behavior of the composite, the thermomechanical properties of matrix were needed. Selection of the heat treatment state that corresponds to the in-situ properties of the matrix was a problem because the matrix properties, particularly those of metal matrix composites, are significantly changed by the temperature history during the manufacturing process. Furthermore, the specimen,

during curing of the adhesive at an elevated temperature, experiences a temperature history similar to that of the annealing process of aluminum. It is believed that the property change due to the repeated heat treatment is negligible. It is assumed that the in-situ properties of the matrix are reasonably close to those of the fully annealed material (See Pindera and Lin, 1989). Prismatic 20.32 cm (8.0 in.) long, 1.27 cm (0.5 in.) wide, and 0.16 cm (0.062 in) thick aluminum specimens were prepared. Elevated temperature tests were conducted on 6061-O aluminum. Stress-strain curves of 6061-O aluminum up to 5% strain at various temperatures ranging from 24°C (75°F) to 399°C (750°F) are shown Fig. 3. The fiber was characterized by measuring its elastic modulus and tensile strength following the ASTM D3379-75 standard procedure. The elastic modulus measured is 400 GPa (58 Msi). The fiber behaves elasticly up to failure and is assumed isotropic and temperature independent.

The thermal strains of composite and 6061-O aluminum were measured by strain gages. The specimens were instrumented with WK-00 (Micro Measurements) gages for measuring longitudinal or transverse thermal strains of the composite and 6061 aluminum. At least three thermocouples were attached to the specimen to monitor temperature. A programmable hot press (MTP-14, Tetrahedron) was used for controlling temperature change step by step. The specimens were heated up to 288°C (550°F) with the gages at increments of 14°C (25°F) at half hour intervals to stabilize the temperature and expansivity of the specimen. A strain gage bridge conditioner BC-8SSG (KAYE Instruments) and data logger (Digistrip, KAYE) were used to record time, temperature and strain. The obtained apparent strains were corrected to give true thermal strains. Similar gages are attached to a reference titanium silicate specimen that has a known

stable coefficient of thermal expansion of 0.0306×10^{-6} /° C (0.017×10^{-6} /° F). The reference specimen is included in the test chamber together with the test specimens. The true thermal strain ε_{true} is obtained by correcting the apparent strain ε_a by the reference strains as follows (See, Daniel and Ishai, 1994)

$$\varepsilon_{true} = \varepsilon_a - (\varepsilon_r - \varepsilon_{tr}) \tag{23}$$

where ε_r is the measured gage output from the reference specimen and ε_{tr} is the known thermal expansion of titanium silicate. Figure 4 shows the thermal strain - temperature curve of 6061 aluminum.

Results and Discussion

Constituent materials were thermomechanically characterized and the properties at room temperature are shown in Tables 1 and 2. The coefficient of thermal expansion (CTE) of SCS-2 in the table is adopted from the measurement of Tsai and Daniel (1994). The stress-strain curves of 6061-O aluminum at various temperatures are shown in Fig. 3. These curves are fitted into a power law strain hardening model which is expressed in eq. 19. The corresponding temperature dependent parameters k, n and σ_Y are given in Table 3. The elastoplastic analysis was performed using the constituent properties given in the tables.

The composite behavior was studied under mechanical and thermal loading conditions. According to the elastoplastic analysis based on this model the matrix is considered as an elastic material with varying secant modulus and secant Poisson's ratio depending on the amount of plastic deformation. The variations of secant modulus and Poisson's ratio of the matrix under the transverse tensile loading at room temperature are

shown in Fig. 5. It can be noticed that the secant modulus of the matrix decreases from its elastic value of 68.6 Gpa (10 Msi), while the secant Poisson's ratio increases from its elastic value of 0.33 toward the limiting value of 0.50. The stresses in the constituents and effective strain of the fiber are influenced by the change of these matrix secant properties.

Under transverse tensile loading the triaxial state of average stresses in the fiber and matrix are calculated from the model. Figure 6 shows the average stresses in the fiber and matrix as a function of applied stress. It is noted that all the average stresses in the matrix and fiber stress σ_{f2} are tensile while fiber stresses σ_{f1} and σ_{f3} are compressive. The maximum stresses in the matrix and fiber were along the loading axis. The stresses vary linearly with applied stress before yielding of the matrix. The model shows that the average stresses other than σ_{m2}, increase in rate after yielding. As shown in the figure, the fiber behaves purely elasticly but the average stresses in the fiber are influenced by the plastic flow of the matrix and show a similar behavior. Note also that the larger portion of load is transmitted to the fiber because of its higher stiffness. Although, the stresses along the x_1 and x_3 axes are an order of magnitude lower than that along the loading axis (x_2), they contribute to the plastic deformation of the matrix.

The effective strains were computed for transverse tensile loading to obtain stress-strain curves at three different temperatures. Figure 7 shows the comparison between the predicted and experimental stress-strain curves at 24°C (75°F), 288°C (550°F), and 399°C (750°F). It shows that the predicted stress-strain curve at room temperature matches favorably the experimental one. However, the other two predicted stress-strain curves at higher temperatures show some deviation from the experiments in the early stages of yielding. There are three major possible reasons for this deviation. The first is

creep. The two high temperature tests were conducted at a rather slow stroke rate at well above the homologous temperature. The low temperature strengthening mechanism no longer holds in this case and creep deformation under tensile loading is inevitable. The composite experiences three different modes of deformation at high temperature: elastic, plastic, and creep. The creep activity is affected by its prior mechanical deformation. Usually, plastic and creep behavior of the composite are modeled separately, although many creep theories obviously were generalized from plasticity. But within certain stress and temperature ranges when both plastic and creep activities are of comparable significance, both types of strains must be considered simultaneously to fully assess the extent of inelastic deformation. To be physically consistent such a consideration requires inclusion of creep effect in the model. The second possible reason is the inability of the model to incorporate the high heterogeneous local deformation field in the ductile matrix and to account for the local stress field in the initial elastic state and during the subsequent plastic deformation. In the average field model the complicated local yielding in the matrix cannot be taken into consideration so that the prediction tends to significantly underestimate the extent of plastic flow in the case of transverse loading. The third possible reason is the interfacial effect since high transfer of load from matrix to fiber is observed. The degradation of interfacial properties also affects the transverse behavior of the composite. These phenomena are expected to be more pronounced at high temperatures.

The effective strains of the composite were also computed for longitudinal loading and were compared with the experiments. Figures 8(a), 8(b) and 8(c) show stress-strain curves under longitudinal loading. The stress-strain curves under transverse loading were

also shown in the figures for comparison purposes. The predictions show better match with the experiments because the behavior of the composite is dominated by the fiber and the complex inelastic behavior of the matrix at high temperature plays a smaller role under longitudinal loading.

The longitudinal and transverse thermal expansion of the composite was also computed. The temperature effect on the matrix is fully considered. The material properties of the matrix at a given temperature were obtained by linear interpolation between known properties at a few temperatures. Figure 9 shows the thermal expansions of the composite as functions of temperature. As seen in the figure, both thermal strains show nonlinear behavior after the temperature reaches a critical temperature This characteristic can be explained qualitatively by following events. As the temperature increases from room temperature, both fiber and matrix tends to expand linearly. At a certain critical temperature the matrix starts to yield due to the thermal internal stresses caused by the difference in expansion between fiber and matrix. The thermal strain in the axial direction is more influenced by the fiber and in the transverse direction more by the matrix because less constraint is imposed between fiber and matrix due to the plastic flow of matrix. This leads to reduction of thermal expansion in the longitudinal direction and increase in the transverse direction.

Summary and Conclusions

The effective strain response of a unidirectional composite under thermomechanical loading was obtained by an average field theory. The fiber is elastic and temperature independent and the matrix is thermoelastoplastic that is fitted into series

of power law strain hardening model. The thermoelastoplastic analysis was carried out by introducing the concept of secant properties to the average field theory.

Under transverse tensile loading the secant properties of the matrix and the average stresses in the matrix and fiber at room temperature were obtained as a function of applied stress. It is noticed that the larger portion of the load is transferred to the fibers due to their higher stiffness. The experimental stress-strain curve of the composite at room temperature shows good agreement with prediction under transverse tensile loading. However, the experiments show deviations from predictions at higher temperatures due to inelastic deformations other than plastic flow (creep), higher heterogeneous local deformation of the matrix and degradation for interfacial properties with temperature.

The experimental stress-strain curves of longitudinal tensile loading at different temperatures are also compared with predictions. Favorable agreements are observed at all three temperatures. Because, under longitudinal loading, the behavior of the composite is dominated by the fibers and only a small influence of the complex behavior of the matrix exists.

The experimental longitudinal and transverse thermal strain-temperature curves were also compared with predictions. They show nonlinearity due to matrix yielding and plastic flow. The comparison between predictions and experiments shows good agreement.

The model was found to be a useful tool for predicting thermomechanical behavior of unidirectional metal matrix composites. However, the model should be improved by considering additional inelastic effects, such as creep, particularly in the transverse loading above the homologous temperature of the matrix.

Acknowledgment

This work was supported by NASA-Lewis Research Center, Cleveland, OH. We are grateful to Dr. C. C. Chamis of NASA for his encouragement and cooperation.

References

ASTM D3379-75, American Society for Testing and Materials, Philadelphia., U.S.A.

Benveniste, Y., 1987, "A New Approach to the application of Mori-Tanaka's theory in composite materials, " *Mechanics of Material*, Vol. 6, pp. 147-157.

Chun, H. J., Wooh, S. C., and Daniel, I. M., 1994, "Thermoelastoplastic Behavior of Unidirectional Composite Materials: Successive Approximation Method," *ASME Journal of Applied Mechanics*, Submitted.

Daniel, I. M. and O. Ishai, 1994, *Engineering Mechanics of Composite Materials*, Oxford University Press, New York.

Eshelby, J. D., 1957, "The Determination of the Elastic Field of an Ellipsoidal Inclusion, and Related Problems," Proceedings of the Royal Society, London, Vol. A241, pp. 376-396.

Gayda, J. and Ebert, L. J., 1979, "The Effect of Cryogenic Cooling on the Tensile Properties of Metal-Matrix Composites ," *Metallurgical Transactions A*, Vol. 10.A, Mar., pp. 349-353.

Hecker, S. S., Hamilton, C. H., and Ebert, L. J., 1970, "Elastoplastic Analysis of Residual Stresses and Axial Loading in Composite Cylinders," *Journal of Materials*, JMLSA, Vol. 5, No. 4, pp. 868-900.

Iesan, D., 1980, "Thermal Stresses in Composite Cylinders," *Journal of Thermal Stress*, Vol. 3, pp. 495-508.

Ishikawa, T., Koyama, K. and Kobayash, S., 1978, "Thermal Expansion Coefficients of Unidirectional Composites," *Journal of Composite Materials.*, Vol. 12, pp. 153-168.

Lin, S. C., Yang, C. C., Mura, T, and Iwakuma T., 1992, "Average Elastic-Plastic Behavior of Composite Materials," *International Journal of Solids and Structures*, Vol. 29, pp. 1859-1872.

Mikata, Y. and Taya, M., 1985, "Stress Field in a Coated Continuous Fiber Composite Subject to Thermo-Mechanical Loadings," *Journal of Composite Materials*, Vol. 19, pp. 554-578.

Mori, T. and Tanaka, K., 1973, "Average Stresses in Matrix and Average Energy of Materials with misfitting inclusions," *Acta Metallurgica*, Vol. 21, pp. 571-574.

Mura, T., 1982, *Micromechanics of Defects in Solids*, Martinus Nijhoff, The Hague.

Nadai, A., 1950, *Theory of Flow and Fracture of Solids*, McGraw-Hill, 2nd Ed., pp. 387.

Pindera, M.-J. and Lin, M. W., 1989, "Micromechanical Analysis of the Elastoplastic Response of Metal Matrix Composites," *Journal of Pressure Vessel Technology*, Vol. 111, pp. 183-190.

Tandon, G. P., and Weng, G. J., 1988, "A Theory of Particle-Reinforced Plasticity," *ASME Journal of Applied Mechanics*, March, Vol. 55, pp. 126-135.

Takao, Y., and Taya, M., 1987, "The Effect of Variable Fiber Aspect Ratio on the Stiffness and Thermal Expansion Coefficients of a short Fiber Composite," *Journal of Composite Materials*, Vol. 21, pp. 140-156

Taya, M. and Chou, T. W., 1981, "On Two Kinds of Ellipsoidal Inhomogeneities in an Infinite Elastic Body: An Application to a Hybrid Composite," *International Journal of Solids and Structures*, Vol. 17, pp. 553-563.

Taya, M. and Mura, T., 1981, "The Stiffness and Strength of an Aligned Short-Fiber Reinforced Composite Containing Fiber-End Cracks Under Uniaxial Applied Stress," *ASME Journal of Applied Mechanics*, Vol. 43, pp. 361-367.

Tsai, C-L., and Daniel, I. M., 1994, "Method for Thermo-mechanical Characterization of Single fibers, " *Composite Science and Technology*, Vol. 50, pp. 7-12.

Uemura, M., Iyama, H. and Yamaguchi, Y., 1979, "Thermal Residual Stresses in Filament Wound Carbon Fiber-reinforced Composites," *Journal of Thermal Stresses*, Vol. 2, pp. 393-412.

Warwick, C. M. and Clyne, T. W., 1991, "Development of Composite Coaxial Cylinder Stress Analysis Model and Its Application to SiC Monofilament Systems," *Journal of Material Science*, Vol. 26, pp. 3817-3827.

Figure Captions

Fig. 1 Unidirectional average field composite model subjected to tensile transverse loading.

Fig. 2 Schematic stress-strain curve of power law strain hardening model with corresponding secant modulus.

Fig. 3 Tensile stress-strain curves of 6061-O aluminum at various temperatures.

Fig. 4 Thermal strain-temperature curve of 6061-O aluminum.

Fig. 5 Variation of secant modulus and secant Poisson's ratio of aluminum matrix as functions of applied stress subject to transverse loading.

Fig. 6 Average stresses in the fiber and matrix as functions of applied stress subject to transverse loading.

Fig. 7 Stress-strain curves of $[90_8]$ composite subject to transverse loading at various temperatures.

Fig. 8 Stress-strain curves of $[0_8]$ composite subject to longitudinal loading compare with those of $[90_8]$ composite subject to transverse loading at various temperatures: (a) 24°C (75°F), (b) 288°C (550°F) and (c) 399°C (750°F).

Fig. 9 Longitudinal and transverse thermal strain-temperature curves of unidirectional SiC/Al composite.

Table 1 Properties of 6061-O aluminum and SCS-2 fiber at room temperature

Property	6061-O Aluminum	SCS-2 Fiber
Elastic modulus, E, GPa (Msi)	69.0 (10)	399.9 (58)
Poisson's ratio, ν	0.33	0.22
Yield stress, σ_y, MPa (ksi)	55.2 (8)	---
Tensile strength, F_t, MPa (ksi)	124.1 (18)	3461- 5309 (502 - 770)

Table 2 Coefficients of thermal expansion of 6061-O aluminum and SCS-2 fiber

Temperature, T, °C (°F)	Coefficient of thermal expansion, α, $\mu\varepsilon$/°C ($\mu\varepsilon$/°F)	
24 (75)	23.4(13.0)	2.25(1.25)
121 (250)	23.6(13.1)	2.34(1.30)
177 (350)	23.9(13.3)	2.81(1.56)
288 (550)	24.8(13.5)	---
450-1300 (842-2372)	---	4.86(2.70)

Table 3 Material dependent parameters of matrix

Temperature	Modulus E, GPa (Msi)	Elastic limit stress σ_Y, MPa (ksi)	Material constant k ($\times 10^{-5}$)	Material constant n ($\times 10^{-2}$)
24°C (75°F)	68.6 (10)	41.4 (6)	510	45.3
121°C (250°F)	63.8 (9.25)	39.3 (5.7)	450	45.5
177°C (350°F)	60.7 (8.8)	37.4 (5.35)	380	45.6
288°C (550°F)	55.2 (8)	33.1 (4.8)	6.62	45.8
399°C (750°F)	48.3 (7)	15.9 (2.3)	6.12	46.0

Table 4 Properties of SiC/Al composite at room temperature

Property	SiC/Al Composite
Longitudinal modulus, E_1, GPa (Msi)	206.9 (30.0)
Transverse modulus, E_2, GPa (Msi)	113.8 (16.5)
Major Poisson's ratio, ν_{12}	0.27
Longitudinal tensile strength, F_t, MPa (ksi)	1620.0 (235.0)
Longitudinal coefficient of thermal expansion, α_1, $\mu\varepsilon/°C$ ($\mu\varepsilon/°F$)	5.94 (3.3)
Transverse coefficient of thermal expansion, α_2, $\mu\varepsilon/°C$ ($\mu\varepsilon/°F$)	16.0 (8.9)
Fiber volume ratio, V_f	0.44

Appendix

The secant moduli tensor of fiber (C_f)and matrix (C_m) are expressed by 6×6 matrix forms.

$$C_f = \begin{bmatrix} C_{f1111} & C_{f1122} & C_{f1133} & & & \\ C_{f2211} & C_{f2222} & C_{f2233} & & 0 & \\ C_{f3311} & C_{f33222} & C_{f3333} & & & \\ & & & C_{f1212} & & \\ & 0 & & & C_{f2323} & \\ & & & & & C_{f3131} \end{bmatrix} \tag{A.1}$$

where

$$C_{f1111} = C_{f2222} = C_{f3333} = \frac{(1-\nu_f)E_f}{(1-2\nu_f)(\nu_f+1)}$$

$$C_{f1122} = C_{f1133} = C_{f2211} = C_{f2233} = C_{f3311} = C_{f3322} = \frac{\nu_f E_f}{(1-2\nu_f)(\nu_f+1)} \tag{A.2}$$

$$C_{f1212} = C_{f2323} = C_{f3131} = \frac{E_f}{2(\nu_f+1)}$$

$$C_m = \begin{bmatrix} C_{m1111} & C_{m1122} & C_{m1133} & & & \\ C_{m2211} & C_{m2222} & C_{m2233} & & 0 & \\ C_{m3311} & C_{m33222} & C_{m3333} & & & \\ & & & C_{m1212} & & \\ & 0 & & & C_{m2323} & \\ & & & & & C_{m3131} \end{bmatrix} \tag{A.3}$$

where

$$C_{m11} = C_{m22} = C_{m33} = \frac{(1-\nu_m^s)E_m^s}{(1-2\nu_m^s)(\nu_m^s+1)}$$

$$C_{m12} = C_{m13} = C_{m21} = C_{m23} = C_{m31} = C_{m32} = \frac{\nu_m^s E_m^s}{(1-2\nu_m^s)(\nu_m^s+1)} \tag{A.4}$$

$$C_{m44} = C_{m55} = C_{m66} = \frac{E_m^s}{2(\nu_m^s+1)}$$

Eshelby's secant tensor (S) is expressed as

$$S = \begin{bmatrix} S_{1111} & S_{1122} & S_{1133} & & & \\ S_{2211} & S_{2222} & S_{2233} & & 0 & \\ S_{3311} & S_{3322} & S_{3333} & & & \\ & & & S_{1212} & & \\ & 0 & & & S_{2323} & \\ & & & & & S_{3131} \end{bmatrix} \tag{A.5}$$

where

$$\begin{aligned} S_{1111} = S_{2222} &= \frac{(5-4\nu_m^s)}{8(1-\nu_m^s)} \\ S_{3333} &= 0 \\ S_{1122} = S_{2211} &= \frac{(4\nu_m^s-1)}{8(1-\nu_m^s)} \\ S_{1133} = S_{2233} &= \frac{\nu_m^s}{2(1-\nu_m^s)} \\ S_{3311} = S_{3322} &= 0 \\ S_{1212} &= \frac{(3-4\nu_m^s)}{2(1-\nu_m^s)} \\ S_{2323} = S_{3131} &= \frac{1}{4} \end{aligned} \tag{A.6}$$

The thermal strains ($\varepsilon_t, \bar{\varepsilon}_t$) have the following form

$$\varepsilon_t = \{\varepsilon_{t11}, \varepsilon_{t22}, \varepsilon_{t33}, 0, 0, 0\} \tag{A.7}$$

and

$$\bar{\varepsilon}_t = \{\bar{\varepsilon}_{t11}, \bar{\varepsilon}_{t22}, \bar{\varepsilon}_{t33}, 0, 0, 0\} \tag{A.8}$$

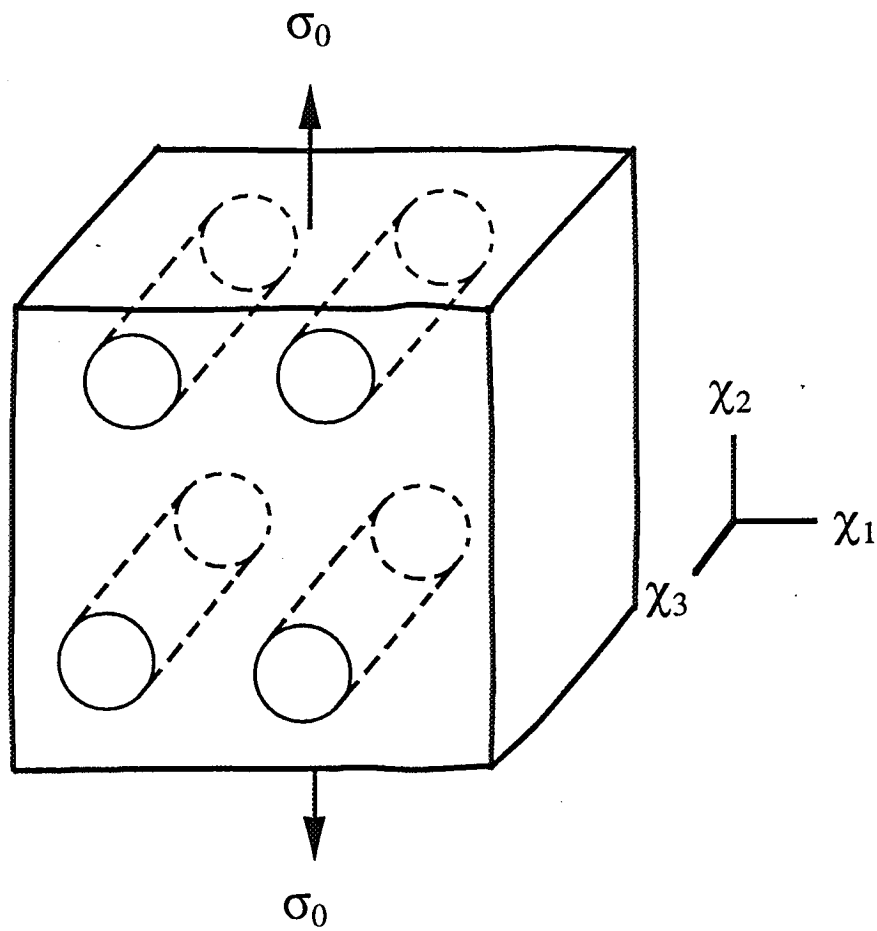
σ0
χ2
χ1
χ3
σ0

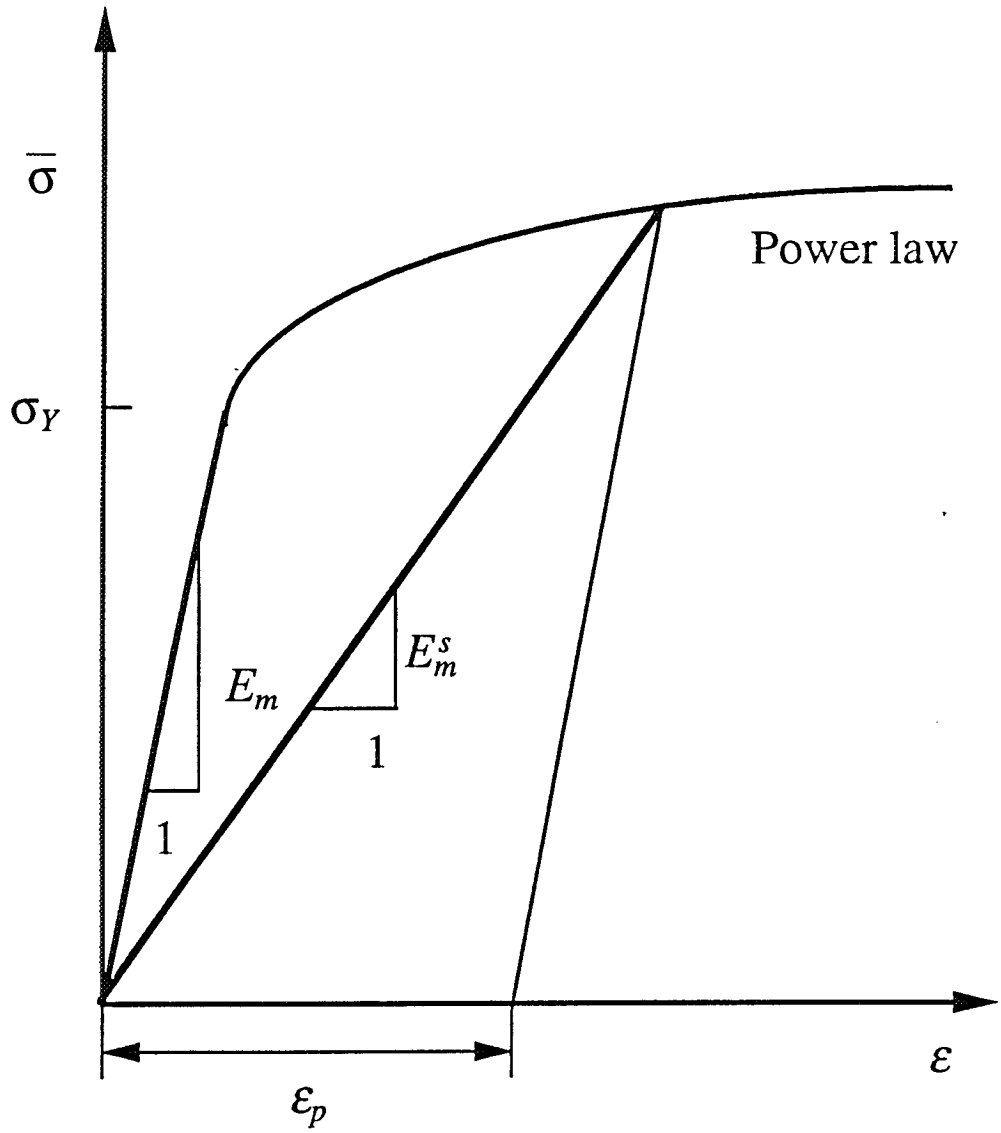
$\bar{\sigma}$
Power law
σ_Y
E_m
E_m^s
1
1
ε
ε_p

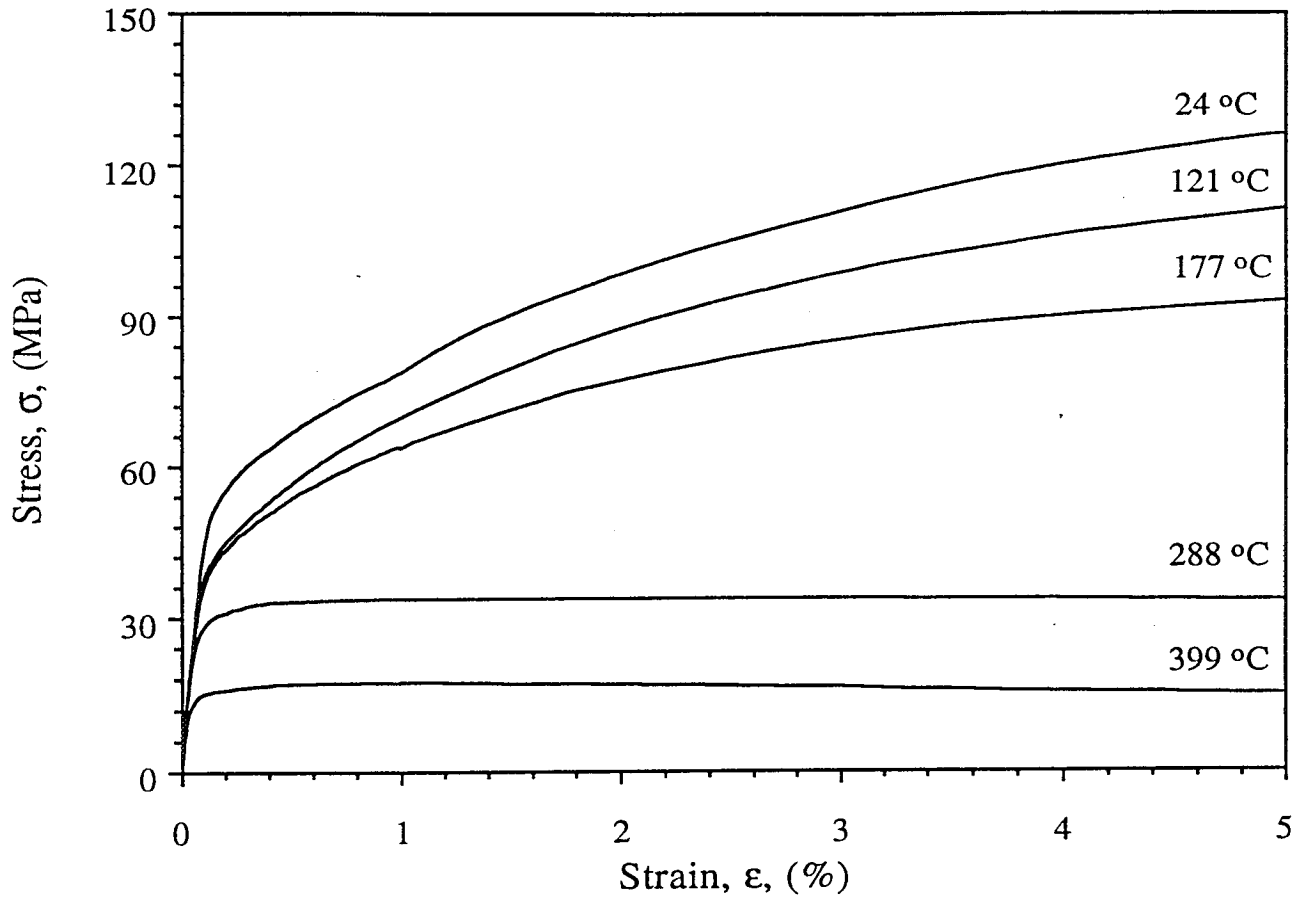
150
120
90
60
30
0
Stress, σ, (MPa)
24 °C
121 °C
177 °C
288 °C
399 °C
0
1
2
3
4
5
Strain, ε, (%)

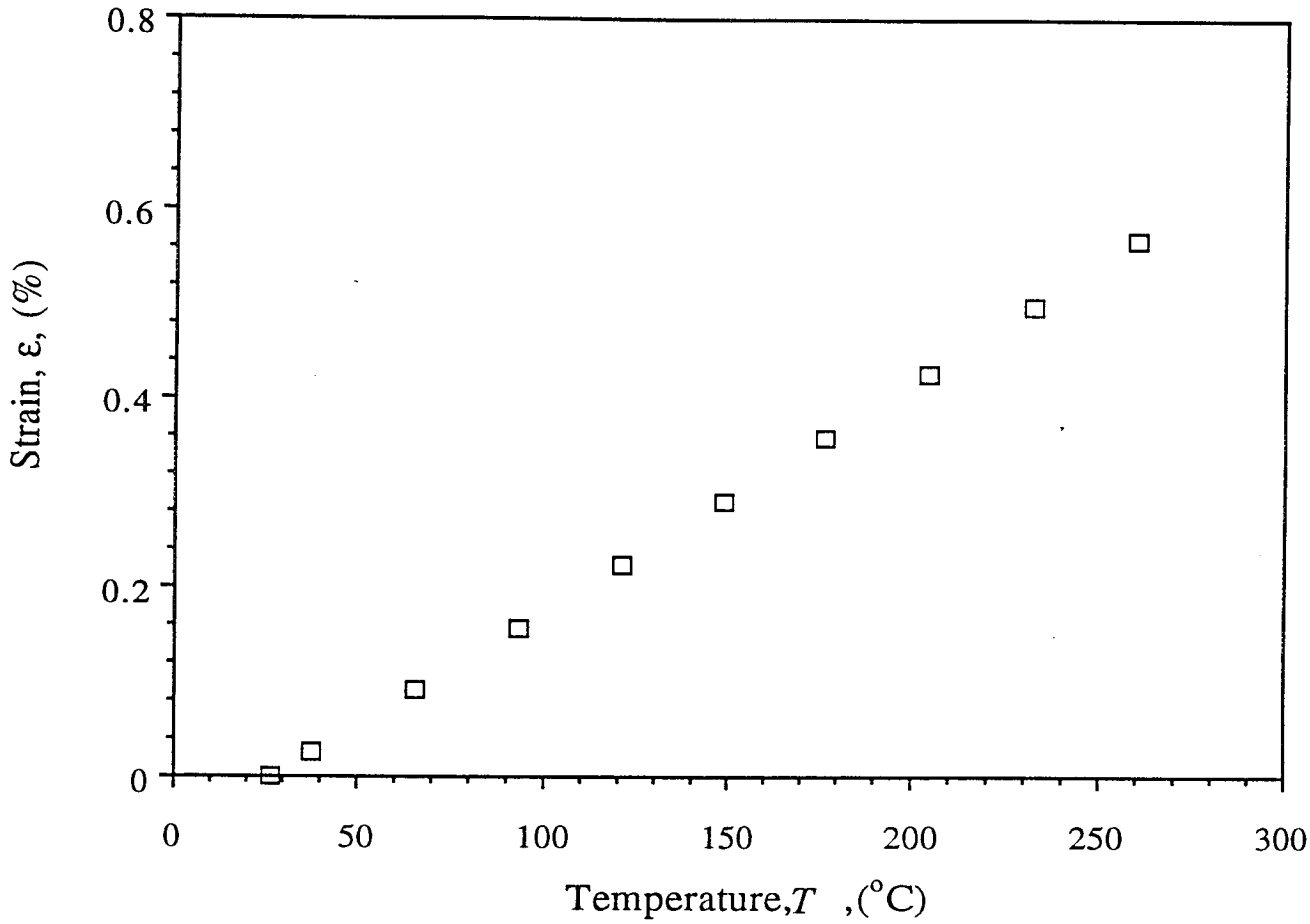
0.8
0.6
0.4
0.2
0
Strain, ε, (%)
0
50
100
150
200
250
300
Temperature,T ,(°C)

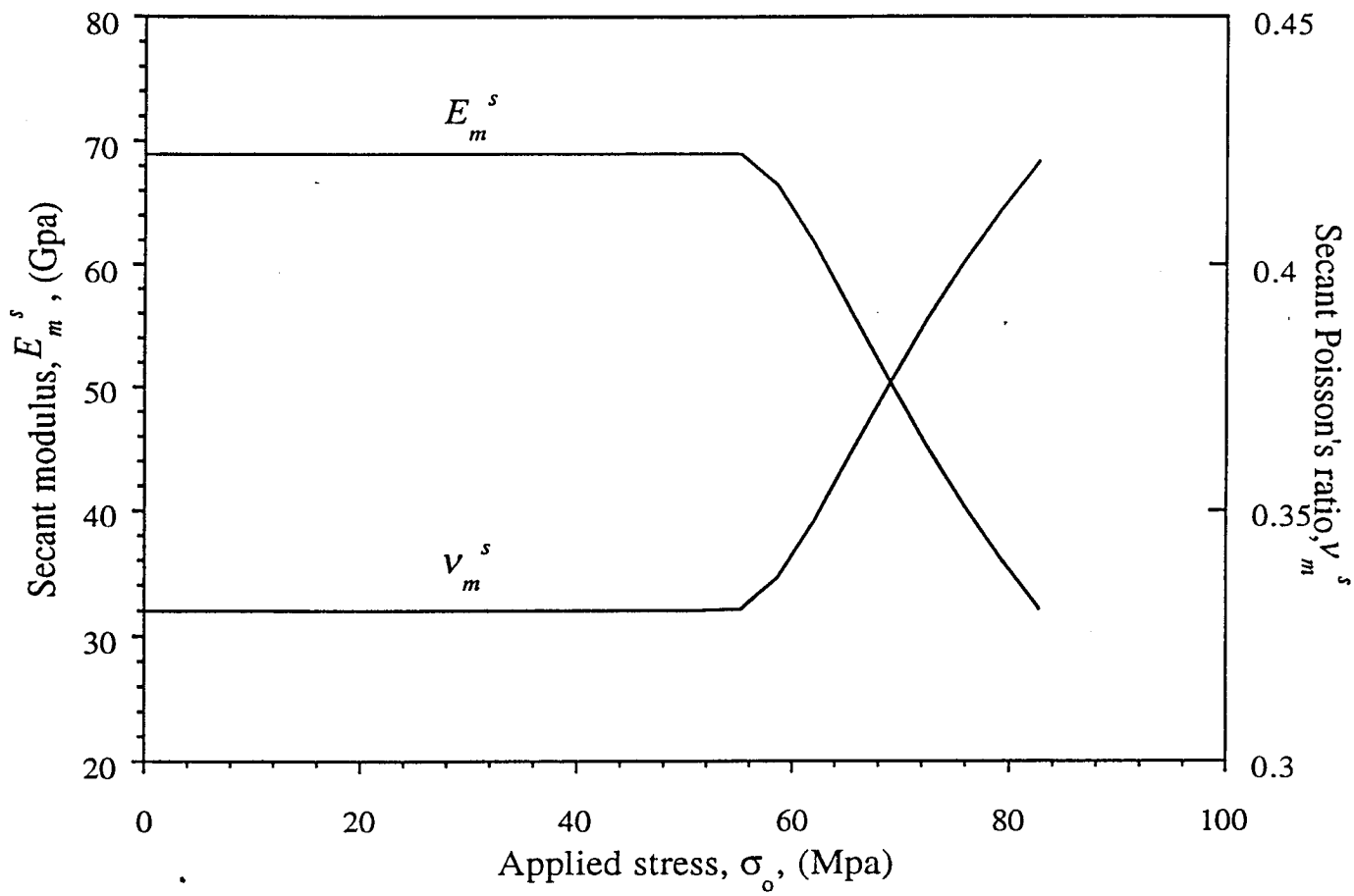
80
70
60
50
40
30
20
0.45
0.4
0.35
0.3
0
20
40
60
80
100
E_m^s
ν_m^s
Secant modulus, E_m^s, (Gpa)
Secant Poisson's ratio, ν_m^s
Applied stress, σ_o, (Mpa)

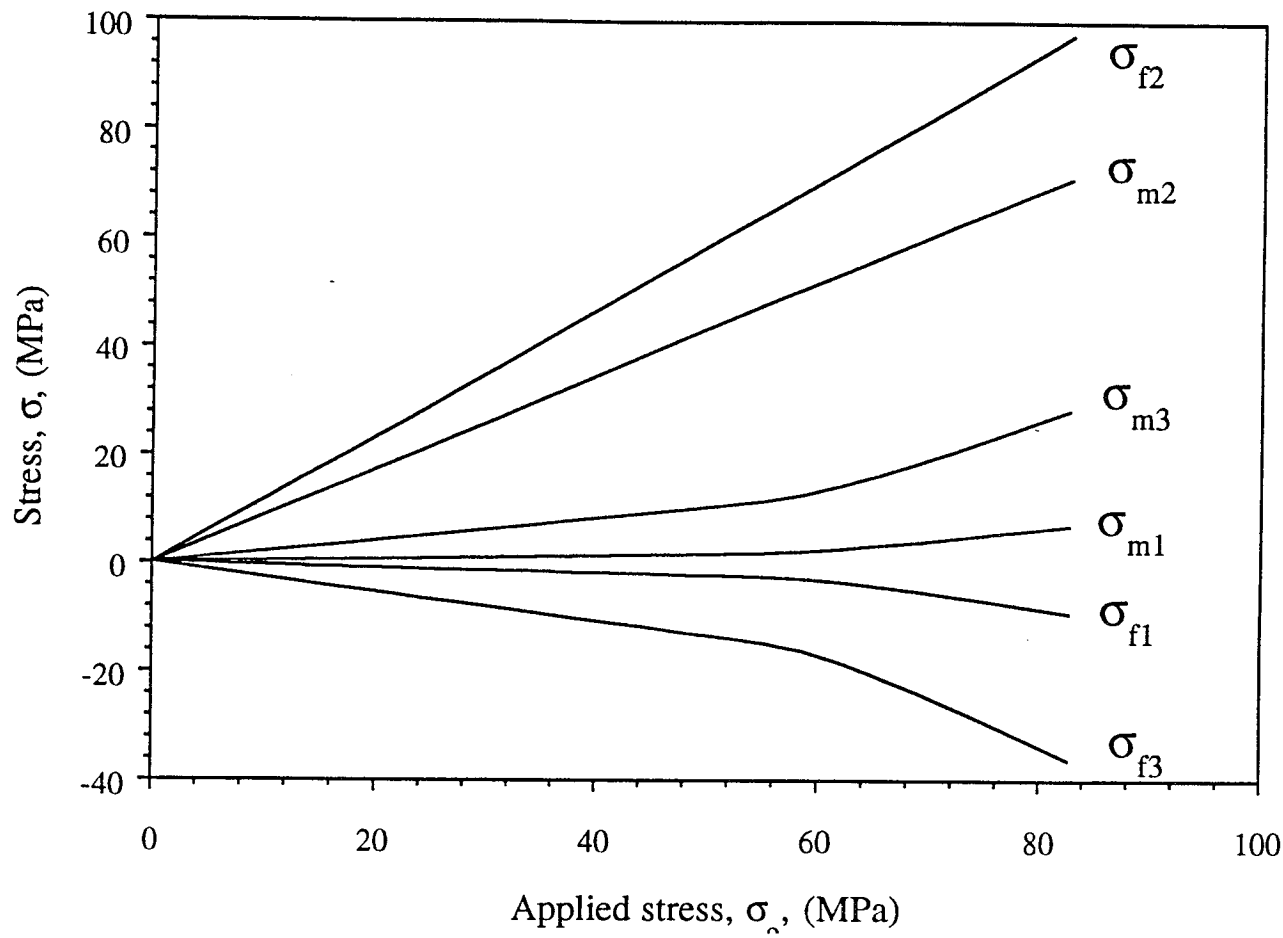
100
80
60
40
20
0
-20
-40
Stress, σ, (MPa)
0
20
40
60
80
100
Applied stress, σ, (MPa)
σf2
σm2
σm3
σm1
σf1
σf3

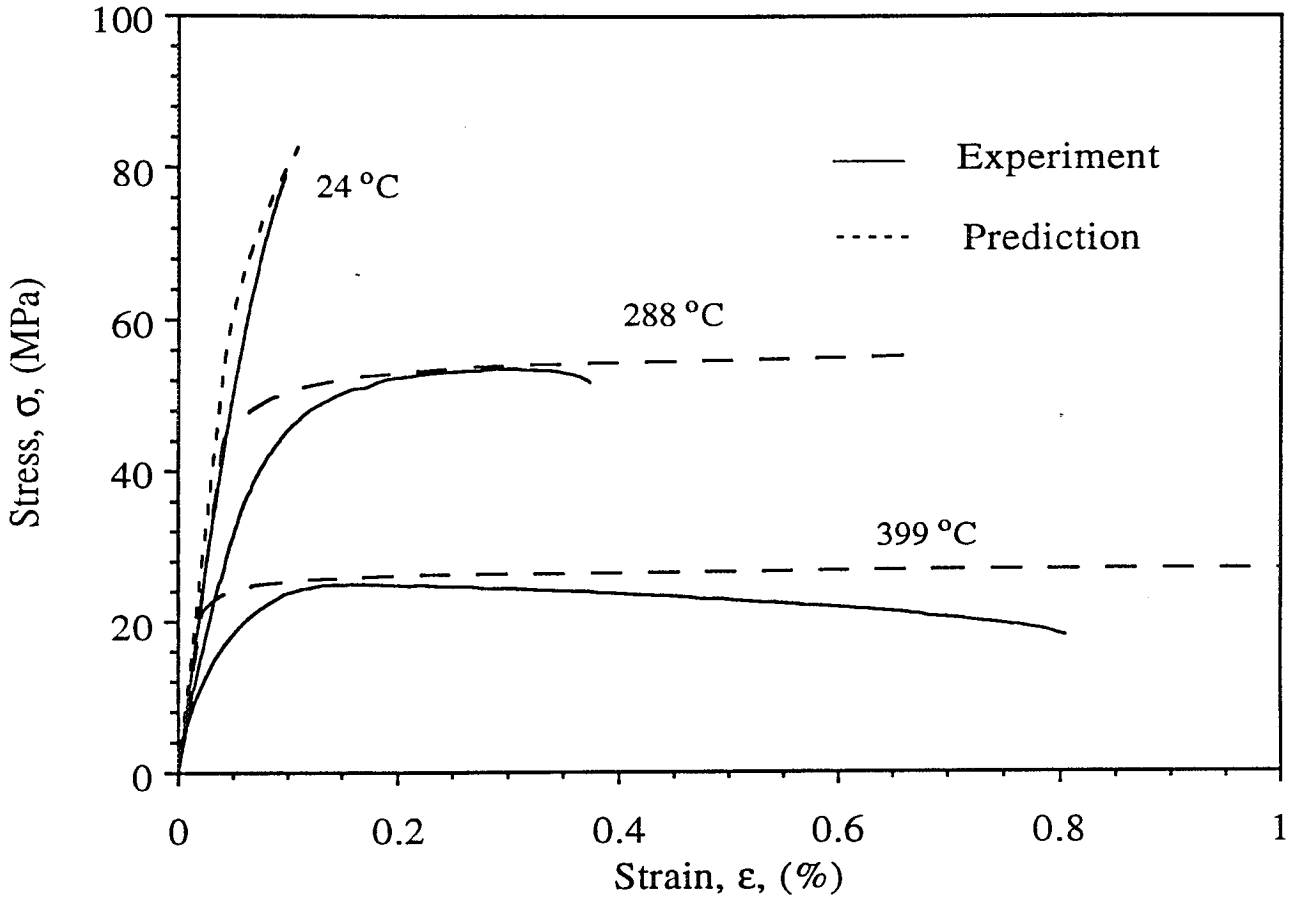
100
80
60
40
20
0
Stress, σ, (MPa)
0
0.2
0.4
0.6
0.8
1
Strain, ε, (%)
24 °C
288 °C
399 °C
Experiment
Prediction

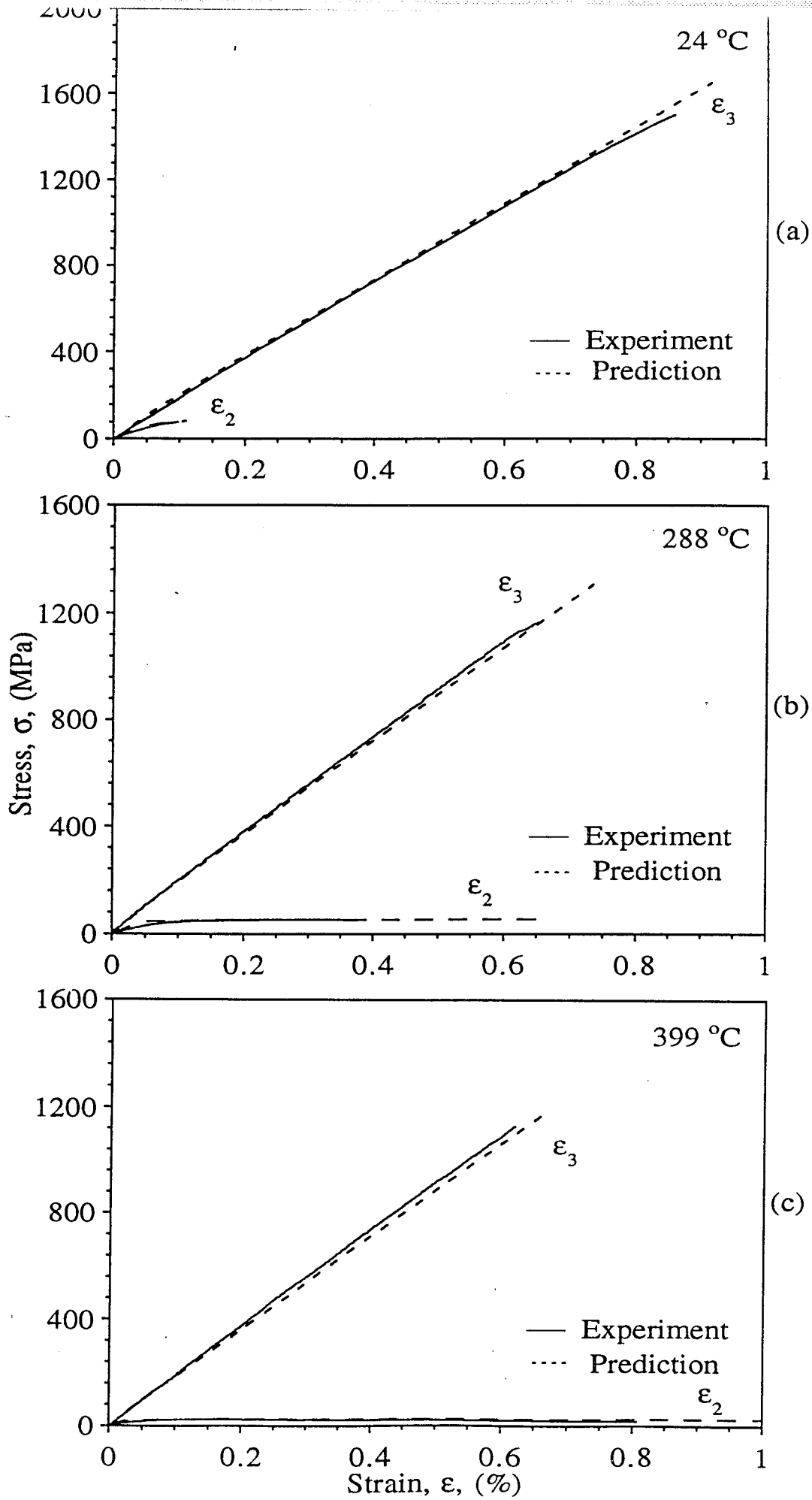
24 °C
(a)
Experiment
Prediction
ε_3
ε_2
288 °C
(b)
399 °C
(c)
Stress, σ, (MPa)
Strain, ε, (%)
0
400
800
1200
1600
0.2
0.4
0.6
0.8
1

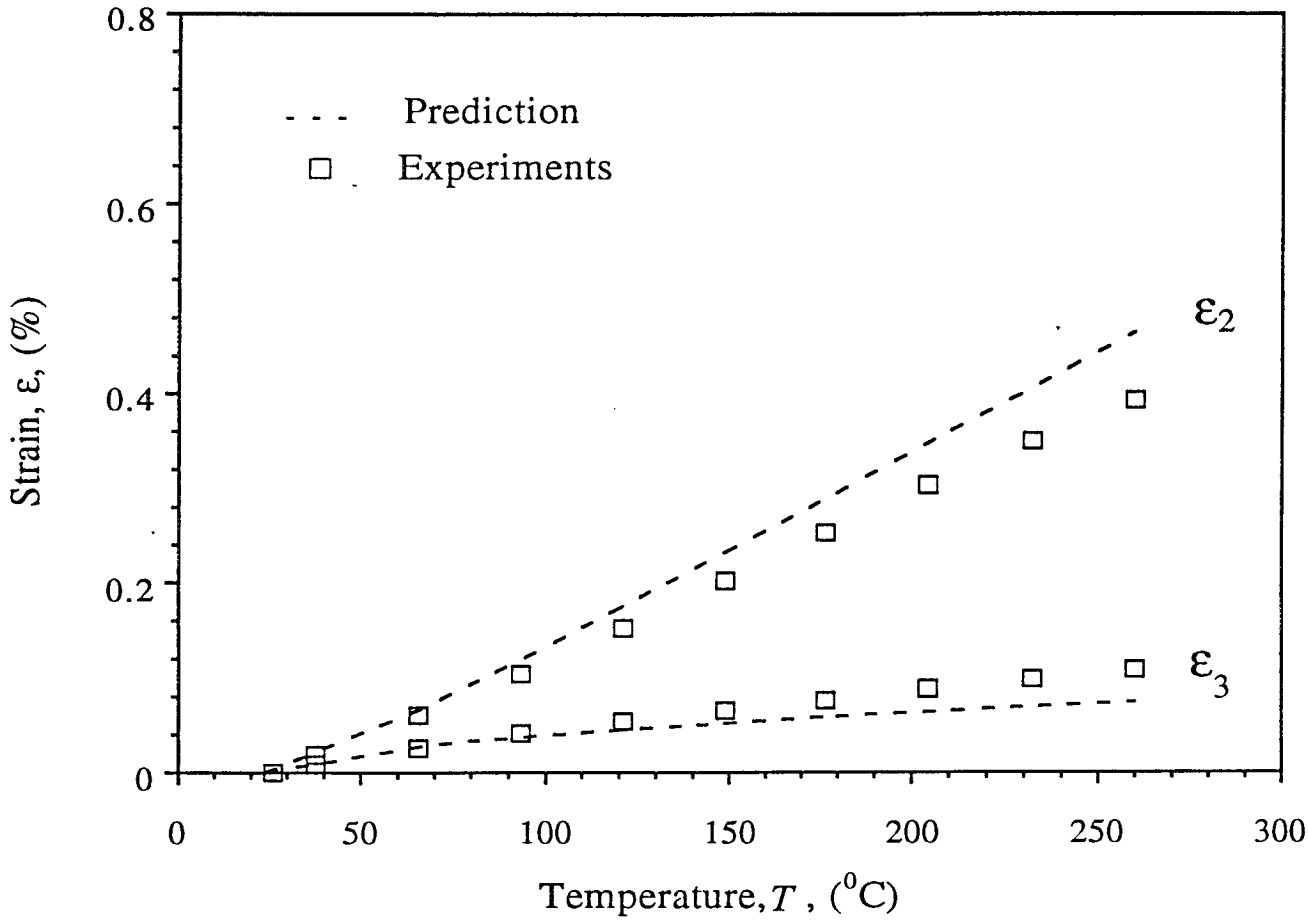
0.8
0.6
0.4
0.2
0
Strain, ε, (%)
Prediction
Experiments
ε2
ε3
0
50
100
150
200
250
300
Temperature, T , (°C)

REPORT DOCUMENTATION PAGE

Form Approved
OMB No. 0704-0188

Public reporting burden for this collection of information is estimated to average 1 hour per response, including the time for reviewing instructions, searching existing data sources, gathering and maintaining the data needed, and completing and reviewing the collection of information. Send comments regarding this burden estimate or any other aspect of this collection of information, including suggestions for reducing this burden, to Washington Headquarters Services, Directorate for Information Operations and Reports, 1215 Jefferson Davis Highway, Suite 1204, Arlington, VA 22202-4302, and to the Office of Management and Budget, Paperwork Reduction Project (0704-0188), Washington, DC 20503.

1. AGENCY USE ONLY (*Leave blank*)	2. REPORT DATE	3. REPORT TYPE AND DATES COVERED
	November 1994	Final Contractor Report

4. TITLE AND SUBTITLE

Characterization of Metal Matrix Composites

5. FUNDING NUMBERS

WU–505–63–5B
G–NAG3–950

6. AUTHOR(S)

I.M. Daniel, H.J. Chun, and D. Karalekas

7. PERFORMING ORGANIZATION NAME(S) AND ADDRESS(ES)

McCormick School of Engineering and Applied Science
Northwestern University
Evanston, Illinois 60208

8. PERFORMING ORGANIZATION REPORT NUMBER

E–9121

9. SPONSORING/MONITORING AGENCY NAME(S) AND ADDRESS(ES)

National Aeronautics and Space Administration
Lewis Research Center
Cleveland, Ohio 44135–3191

10. SPONSORING/MONITORING AGENCY REPORT NUMBER

NASA CR–195381

11. SUPPLEMENTARY NOTES

Project Manager, C.C. Chamis, Structures Division, NASA Lewis Research Center, organization code 5200, (216) 433–3252.

12a. DISTRIBUTION/AVAILABILITY STATEMENT

Unclassified - Unlimited
Subject Category 24

12b. DISTRIBUTION CODE

13. ABSTRACT ***(Maximum 200 words)***

Experimental methods were developed, adapted and applied to the characterization of a metal matrix composite system, namely, silicon carbide/aluminum (SCS–2/6061 A*l*), and its constituents. The silicon carbide fiber was characterized by determining its modulus, strength and coefficient of thermal expansion. The aluminum matrix was characterized thermomechanically up to 399° C (750° F) at two strain rates. The unidirectional SiC/A*l* composite was characterized mechanically under longitudinal, transverse and in-plane shear loading up to 399° C (750° F). Isothermal and non-isothermal creep behavior was also measured. The applicability of a proposed set of multifactor thermoviscoplastic nonlinear constitutive relations and a computer code was investigated. Agreement between predictions and experimental results was shown in a few cases. The elastoplastic thermomechanical behavior of the composite was also described by a number of new analytical models developed or adapted for the material system studied. These models include the rule of mixtures, composite cylinder model with various thermoelastoplastic analyses and a model based on average field theory. In most cases satisfactory agreement was demonstrated between analytical predictions and experimental results for the cases of stress-strain behavior and thermal deformation behavior at different temperatures. In addition, some models yielded detailed three-dimensional stress distributions in the constituents within the composite.

14. SUBJECT TERMS

Silicon fibers; Aluminum matrix; High temperature; Isothermal; Non-isothermal; Creep; Micromechanics; Stresses; Displacements; Nonlinear models

15. NUMBER OF PAGES

338

16. PRICE CODE

A15

17. SECURITY CLASSIFICATION OF REPORT	18. SECURITY CLASSIFICATION OF THIS PAGE	19. SECURITY CLASSIFICATION OF ABSTRACT	20. LIMITATION OF ABSTRACT
Unclassified	Unclassified	Unclassified	